

CONTRACT: NAS 8-2630

NASA PHASE II REPORT  
DECEMBER 1963

FACILITY FORM 602

N66 23706  
(MISSION NUMBER) (THRU)

15  
(PAGES) (CODE)

15  
(NASA CR OR TMX OR AD NUMBER) (CATEGORY)

**THEORETICAL AND EXPERIMENTAL  
EVALUATION OF HIGH ENERGY  
FORMING OF HEMISPHERICAL SHAPES  
IN METALS**

P. D'AGUANNO  
G. PFANNER

GPO PRICE \$ \_\_\_\_\_  
CFSTI PRICE(S) \$ \_\_\_\_\_  
Hard copy (HC) # 5.00  
Microfiche (MF) 1.50

# 653 July 65

REPUBLIC AVIATION CORPORATION  
MANUFACTURING RESEARCH

PHASE II REPORT  
PERIOD: APRIL 1963 - DECEMBER 1963

MANUFACTURING ENGINEERING DIVISION  
GEORGE C. MARSHALL SPACE FLIGHT CENTER  
HUNTSVILLE, ALABAMA

*RJ 365/14*

## FOREWORD

This Engineering Phase II Report covers the work performed under Contract NAS 8-2630 from May 1963 to December 1963 and is identified as Republic Aviation Corporation report RAC 1893. It is published for technical information only and does not necessarily represent the recommendations, conclusions or approval of the National Aeronautics and Space Administration.


The contract with Republic Aviation Corporation, Farmingdale, New York, was initiated by the Manufacturing Engineering Division and administered by the Contracts Branch, Procurement and Contracts Office, National Aeronautics and Space Administration, George C. Marshall Space Flight Center, Huntsville, Alabama. The project is monitored by Messrs: William A. Wilson, Chief, Methods Development Branch - R-ME-MM, and Earl A. Hasemeyer, Chief, Metal Processing Section - R-ME-MMP.

At Republic Aviation Corporation, Mr. P. D'Aguanno performed the experimental work while Mr. G. Pfanner was responsible for the overall supervision of the program. Messrs. P. D'Aguanno and G. Pfanner prepared this report.

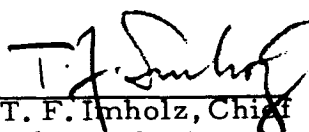
Grateful acknowledgement is given to Messrs. T.A. Renshaw, S. Bogdan and H. Sieber (all of Republic Aviation Corporation Materials Development Research Laboratory) for their contributions on Transmission Electron Microscopy, X-ray Diffraction, and Stress Corrosion, respectively. The authors also wish to extend their thanks to Mr. P. Seese, Manufacturing Process Mechanic, for his invaluable assistance during many of the experiments.

Comments are solicited relative to the possible utilization of the information contained in this report to other production programs. Suggestions concerning additional Manufacturing Methods development required on this or other subjects will be appreciated.

Approved by:

  
Robert W. Husa, Ass't. Chief  
Manufacturing Research Engr.

Approved by:

  
T. F. Inholz, Chief  
Mfg. Rsch. Engr.



## TABLE OF CONTENTS

	<u>Page</u>
INTRODUCTION	1
Experimental Program	1
Phase I	1
Phase II (Original)	2
Phase II Revised	2
EXPERIMENTAL PROCEDURE AND TECHNIQUES	4
A. Overall Procedure	4
B. Experimental Techniques to Measure Strain Rate	5
C. Method of Calculating Strain Rate	6
D. Techniques Employed to Evaluate Formed Specimens	9
1. Mechanical Property Testing	9
2. Gauge Reduction	10
3. X-Ray Diffraction	11
4. Electron Transmission Microscopy	12
5. Stress Corrosion Testing	13
E. Pressure Measurements	15
F. Preliminary Testing to Determine Forming Conditions	17
TOOLING, EQUIPMENT, AND FORMING PROCEDURE	56
A. Electrohydraulic Forming	56
1. Equipment	56
2. Tooling	56
3. Forming Procedure	57
B. Explosive Forming	58
1. Equipment	58
2. Tooling	59
3. Forming Procedure	59
C. Magnetic Forming	60
1. Equipment and Tooling	60
2. Forming Procedure	60
D. Hydrostatic Forming	61
1. Equipment and Tooling	61
2. Forming Procedure	61
E. Hydroforming	61
1. Equipment and Tooling	62
2. Forming Procedure	62

	<u>Page</u>
DISCUSSION OF RESULTS	93
A. Mechanical Property Testing	93
B. X-Ray Diffraction	94
C. Electron Transmission Microscopy	98
D. Stress Corrosion	99
E. Pressure Measurements	100
F. Dimensional Evaluation	102
1. Efficiency	102
2. Thinout	103
3. Discharge Energy and Dome Depth	103
 CONCLUSIONS	 122
APPENDIX A   Preliminary Electron Microscopic Study of Metals Deformed at High Strain Rates	 A-1

## INTRODUCTION

Electrohydraulic, Explosive and Magnetic Repulsion forming are high energy rate forming processes which are adapted to forming of sheet metal parts. Electrohydraulic forming uses stored electrical energy, which when discharged through a wire located between underwater electrodes, causes the wire to explode thus creating pressure wave energy to form parts. Explosive forming, as the name implies, uses chemical explosives which when detonated will likewise create pressure wave energy in the liquid medium to form parts. Magnetic repulsion forming, like electrohydraulic forming uses stored electrical energy which when discharged through a work coil of low inductance will induce a voltage in the closely coupled workpiece (by virtue of the changing high density magnetic field) equal to and opposite in polarity to that which caused it. The high power of the three processes implies forming at high strain rates. In the case of uniaxial tensile tests high strain rates are known to increase the yield strength and delay the strain reaction to stress in deviation from Youngs modulus. It is, therefore, important to inquire what the influence of strain rate is upon other material properties. In this regard, the Phase II of this program was modified from an interest in electrohydraulic phenomena in Phase I, to a comparison of the influence of the high strain rate processes upon properties in Phase II. The properties which were examined were mechanical properties, corrosion resistance, residual stress and micro-structure. Comparison was made with conventional (essentially zero strain rate) processes as a reference.

The following, more fully describes the experimental program and the work accomplished in Phase I and Phase II.

### Experimental Program

The original and revised objectives of Phases I and II are outlined below. Phase I results are reported in the Phase I Final Report dated December 1962. This report, however, contains work conducted in Phase II only.

### Phase I

In Phase I, the following was accomplished:

1. Energy distribution in the die tank assembly was determined from the influence of several parameters such as water level and hydrostatic pressure for the forming of hemispherical shapes.
2. Strain rate was investigated to determine the effect of strain rate on the residual elongation of the workpiece.
3. A comparative analysis was presented between electrohydraulic, hydrostatic and hydroforming to show the thinout obtained and corresponding mechanical properties in forming hemispherical shapes by the three methods used.

## Phase II (Original)

The original objective of this phase (later revised - see below) was to evaluate parameters that influence energy distribution in the workpiece and to determine the relative influence of pressure wave energy versus kinetic energy of the moving water on metal deformation. An objective was to obtain information to permit die-tank designs to be directed toward maximum utilization of the most effective form of energy.

## Phase II (Revised)

The original objective of Phase II above was revised to compare the results of forming three alloys by high energy rate and conventional processes with emphasis on the influence of strain rate on various properties. The alloys and forming processes to be evaluated are shown below:

<u>Forming Process</u>	<u>Alloys</u>
1. Electrohydraulic	1. .090" 321 Stainless Steel Annealed
2. Explosive	2. .090" 2014-0 aluminum
3. Hydrostatic	3. .090" 2219-0 aluminum
4. Hydroform	(4 sheets, 48" x 180" supplied by MSFC)
5. Magnetic *	

\* This process was not called for in the "Work Statement" but was added for strain rate and mechanical property experiments only.

The following work was accomplished:

1. Preliminary electrohydraulic forming experiments to establish blank diameter, energy level, gauge reduction, and dome configuration were performed. A round bottom dome configuration was used for the entire program as it was found that tensile specimens obtained from round bottom domes did not differ significantly from tensile specimens obtained from flat bottom domes. High speed motion picture camera parameters were also established during these preliminary experiments and techniques developed for subsequent measurements of metal strain rate. The method used to measure metal strain was to observe a 1/2" x 1/2" square located at the center of a blank expand during deformation.
2. With the alloys and forming processes mentioned earlier, mechanical properties were obtained from the apex of domes free formed to approximate equal gage reductions. Ultimate, yield, and elongation of all alloys were plotted against percent thickness reduction for all forming processes.

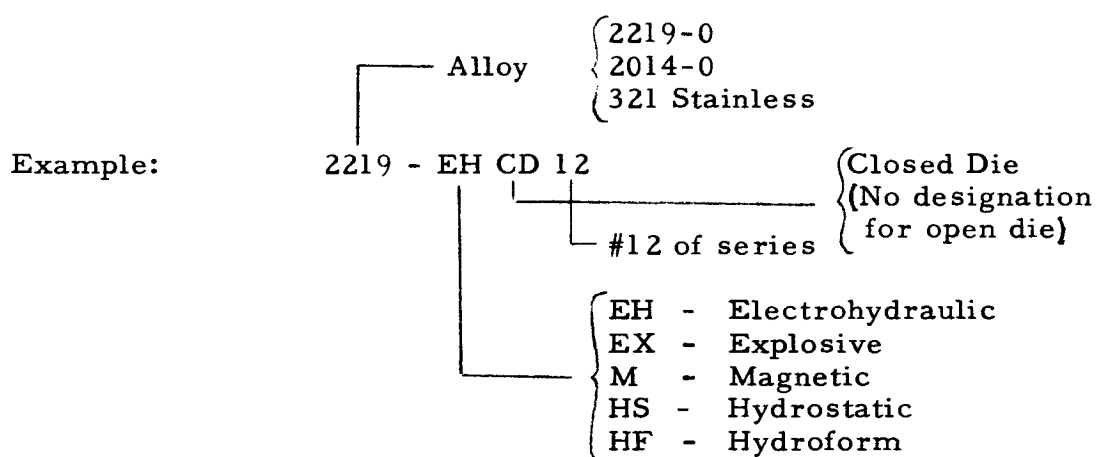
3. Strain rate measurements of all alloys using the Fastax high speed camera were also performed at relatively low and high strains for the electrohydraulic, explosive and magnetic forming processes. In addition, electrohydraulic strain rate values for lubricated and unlubricated 2219-0 blanks were obtained and comparisons made to provide an insight into the true nature of metal strain per unit time. Measurements of dome thickness gradient, depth, and percentage draw-in were also recorded .
4. Experiments with the hemispherical die (closed die) in which all alloys were lightly and highly impacted against die contour, were performed for the electrohydraulic and explosive processes. Tensile specimens were obtained and the influence of die impact on the mechanical properties was determined.
5. Electrohydraulic and explosively free formed and die impacted domes of the 321 stainless steel alloy were subjected to stress corrosion tests for almost 200 continuous hours using a boiling 25 percent magnesium chloride solution. Hydrostatically formed domes were likewise tested. Comparative data was obtained on the resistance to stress corrosion for the above mentioned forming processes.
6. X-ray diffraction analysis was performed on 6 inch diameter specimens obtained from the apex of free form and die impacted domes for all alloys formed by the electrohydraulic, explosive and hydrostatic processes. The sum of the principal stresses was plotted against specimen thickness for comparative purposes.
7. Electron transmission microscopy tests were performed on 1" x 1" specimens likewise obtained from the apex of free formed domes for all alloys formed by the electrohydraulic, explosive, and hydrostatic processes.
8. Pressure-time traces were obtained at various energy levels for the electrohydraulic process using the three materials in the free form configuration as well as under fixed boundary conditions (workpiece supported and restricted from forming.)
9. The efficiency of the electrohydraulic process was determined by comparison of input energy to deformation work obtained from forming of similar domes hydrostatically.

## EXPERIMENTAL PROCEDURE AND TECHNIQUES

### A. Overall Procedure

The overall procedure was to form dome shaped parts of the three materials and four processes mentioned in the "Experimental Program" and to obtain specimens for comparative evaluation.

A system of identifying formed specimens was employed which permitted identification in accordance with the alloy and process used and is explained as follows: The identification number is prefixed by the alloy used, followed by letters indicating the process and finally, by a serial number indicating the relative position in a series of similar parts.



Tensile coupons and specimens obtained for X-ray diffraction and electron microscopy tests were identified in a similar manner with the following additions for tensile coupons:

- T - denotes transverse grain
- L - denotes longitudinal grain
- F - denotes flat bottom dome
- R - denotes round bottom dome  
(or no letter)

A, B or C - denotes location in cases where more than one coupon was taken from subject dome

The four processes of interest covered a relatively wide range of strain rates. An additional process (not called for in the original work statement) was added - namely, "Magnetic Repulsion Forming." Of the processes employed, strain rates for the electrohydraulic, explosive and magnetic forming processes were measured as discussed in Section C.

The hydrostatic process served as a reference to which the processes were compared with regard to mechanical properties, gage reduction, X-ray diffraction, electron transmission microscopy, and stress corrosion tests. These tests or techniques are discussed more fully as items 1 through 5 in Section D to follow. Items 3, 4 and 5 were not performed for the magnetic process.

Pressure pulse traces were taken for the electrohydraulic process only and is discussed in Section E.

## B. Experimental Techniques to Measure Strain Rate

In order to determine strain rate developed in free forming domes, a  $1/2'' \times 1/2''$  square was painted on the center of the blank before installation into the 10" diameter die contained in the closed tank. High speed movies taken during the forming operation, recorded the increase in the size of the square and provided a time/dimension relationship which was used to calculate rate of strain.

The Fastax camera used in these experiments has a maximum speed of approximately 7,000 frames per second, which is attained at or near the end of its run of 100 feet of film. It is controlled by a timing device (Goose Control) which is also capable of initiating the discharge of the capacitor bank, making it possible to have the event occur near the end of the camera run where it has attained near maximum speed. The experimental setup is shown in Figure 1. A series of test runs gave timer settings which assured that the event would be photographed at approximately 20 feet from the end of the 100 ft. roll of film. The camera contains a timing light, which flashes at a rate of 120 times per second, and these flashes are photographed on the margin of the film. Thus it is possible to determine film speed at any given point by counting the number of frames between flashes and multiplying by 120, giving camera speed in frames per second. The entire forming action takes place in 1.5 milliseconds or less, which corresponds to a maximum of 12 frames of metal movement. See Figure 2 for typical film sequence of metal strain.

The center square was produced by applying a coating of "Turco #505" masking compound to the center of a blank, covering an area approximately 3 inches in diameter.

By using a  $1/2'' \times 1/2''$  square template, the perimeter of the square was cut through the coating and the area within the lines was peeled off, leaving a  $1/2'' \times 1/2''$  square of bare metal surrounded by the coating. This gave the contrast, and edge definition necessary for accurate square measurements. Other substances such as layout dye, black lacquer, and zinc chromate primer were tried but proved unsatisfactory because of lack of adhesion and elasticity, or loss of definition due to metal stretch to the extent that the image could not be measured. The "Turco 505" compound is used in industry as a protective coating brushed, dipped, or sprayed on parts requiring chemical milling. Having a rubber base, it offers good elasticity and bonding qualities. The compound is black and is dissolved with talnol. Experiments in which

this coating was applied to a tensile coupon which was subsequently pulled to the point of fracture, revealed that the coating stretched with the metal without peeling or fraying to 50% of its original size.

A more elaborate design consisting of concentric circles encompassing the square was used on some blanks for the purpose of determining whether there was a significant difference in metal stretch along horizontal and vertical axes. Measurements showed that differences in diameters were very slight. Therefore, this method was discontinued.

Measurements of the size of the actual image on film were made on an optical comparator. This comparator is shown in Figure 3. The film was positioned between two glass slides which were mounted on the stage of the comparator, which can be moved laterally by two micrometer-type adjusting heads located 90° apart. Projection of the image on a screen containing horizontal and vertical hairlines made it possible to accurately measure the image size, by aligning first one side of the image with the hairline, reading the setting of the micrometer, then aligning the other side and reading again. The difference in readings then represents the actual size of the projected image. For maximum accuracy, three sets of readings were taken in each position and results averaged, and as the three measured readings were within a range of .0003 inches, it is concluded that the actual square size measurements are correct to .0003 times the minification of 21 or  $\pm .003''$ . Twenty to twenty-five frames of each film were measured in order to determine exactly which frames covered the time of the event, and those which showed no change previous to or subsequent to the event were taken to represent original size of image and final size of image respectively.

Since part of the increase in size of the image is due to camera perspective change brought about by movement of the blank toward the camera, a correction must be made to convert the apparent increase to true increase. This requires a known relationship between camera-to-workpiece distance, (or dome depth), and apparent lineal stretch. A previous set of experiments on blanks of various materials formed to varying depths gives a family of curves showing a depth-stretch relationship used to estimate the depth existing at the time any individual frame was exposed. These curves for the 2219 alloy only, can be seen as Figure 4. A correction factor, proportional to camera-to-workpiece distance can then be applied to reduce film image measurements to dimensions which reflect material stretch only. These resulting dimensions were converted to actual square sizes by multiplying them by the known minification of the lens/distance combination used. The actual square sizes were then used in connection with the time base established by film speed, in frames per second, to compute the rate of strain.

### C. Method of Calculating Strain Rate

The method used to determine strain rate is outlined on the following pages and can be considered typical for all specimens. A typical table of significant values,



applicable to specimen #2219 EH16, has been reproduced and may be seen as Table 12. Frame numbers, assigned to those frames of motion picture film which encompass the event, are listed as 1 through 10 in Column I. Columns 2 and 3 represent the values of horizontal and vertical dimensions of the film images which have been measured by use of the optical comparator previously mentioned, and the product of each horizontal and vertical size, or area of the image, is listed in Column 4. Other data necessary for calculations of strain rate was recorded, including horizontal and vertical measurements of the square both before and after forming, final depth of the formed dome, distance from the camera to the subject, and film speed as determined by examination of the timing light flashes photographed on the film margin.

Using the area values in Column 4, an apparent percent area increase, based on the area of frame 1 only, was computed and listed in Column 5. Since this apparent percent increase included the effect of workpiece toward the camera, a set of values representing only actual percent increase was derived as follows:

Physical measurement of the square before forming showed it to be .495" x .495", giving an area of .245 sq. in. Measurements after forming showed it to be .550" x .550", giving an area of .302 sq. in. Therefore, the actual percent increase  $\left( \frac{a - a_0}{a_0} \times 100 \right)$  was 23.2%, as opposed to the 39%, a total apparent

increase in Column 5. The ratio of these two values, 39/23.2, was recorded in Column 6, and is the corrected percent increase of film image area.

To convert film image sizes to true dimensions, it was necessary to find the subject-to-camera distance for each frame, so that a suitable correction factor could be applied to remove the foreshortening effect produced by the subject moving toward the camera. The family of curves shown as Figure 4 showing relationship of dome depth to percent area change, was used to establish dome depth for each frame, and the resulting values are listed in Column 7. Since dome depth reduces subject distance, these figures are a basis for a correction factor, derived as follows: It has been found by experimentation that each inch of movement toward the camera will produce an apparent increase in size equivalent to .023" per inch of size, when the original subject-to-camera distance is fixed at 48". This gave a correction factor, expressed as  $1 - (\text{dome depth} \times .023)$  and appropriate correction factors were then listed in Column 8.

It was also necessary to find the minification ratio of subject size to image size, in order to convert image size to real or actual size. This was derived by dividing original area of the square, or .245 sq. in. by area of frame #1 image, or .000559 sq. in. Resulting area minification was found to be 438 x. Lineal minification, or  $\sqrt{438}$ , was 21 x. For verification of this value and of the percentage of increase values, division of the final square area, or .302 sq. in., by the corrected image area at frame #10.

.000776 (.931)<sup>2</sup> was found to be 450x, which when reduced to lineal minification was 21.2x. This value is in very close agreement with the base lineal minification of 21x.

Using the proper correction factor from Column 8, and the lineal minification ratio of 21.1x, actual horizontal and vertical square dimensions were calculated and entered in Columns 9 and 10 respectively, as

$$S_a = S_i (c) 21.1 \text{ where: } S_a \text{ is actual size in inches}$$

$S_i$  is image size, horizontal or vertical from Column 1 or 2

C is correction factor from Column 8

21.1 is minification ratio

Square areas were computed from these dimensions and entered in Column 11. From the figures in Columns 9, 10 and 11, values of total increase in horizontal size, vertical size, and area were obtained and entered in Columns 12, 13 and 14 respectively, and these values were also used to plot the graphs shown as Figure 8. Values representing increase (or decrease) in horizontal and vertical size from each frame to the next were recorded in Columns 15 and 16 respectively, for use in the final stage of strain rate computation.

It was necessary at this time to establish a time base for use with the dimension changes. This was accomplished by using the film speed previously determined to be 6,960 frames per second, producing a time interval from one frame to the next of 1/6900 second or .1435 milliseconds.

Finally, true strain rate was calculated by using the formula  $S = \frac{\Delta L}{LT}$

Where: S = True Strain rate (in/in/sec. or units per second)

$\Delta L$  = Strain change (From Column 16 or 17)

L = Size in inches at start of time interval

T = Time interval from frame to frame, in seconds

A typical calculation of the horizontal strain rate from frame #2 to frame #3 is shown below:

$\Delta L$  = .027 in., increase of horizontal size at frame 3 over frame 2 (Column 16)

L = .505 in., horizontal size at frame 2 (Column 9)

T = .0001435 seconds, time interval (constant)

$S = \frac{.027 \text{ in.}}{.505 \times .0001435 \text{ sec.}} = 372.2 \text{ inches/in./sec.}$

Values obtained by these calculations were recorded in Columns 17 and 18 for horizontal and vertical respectively, and used to plot the graph which may be seen as Figure 7.

#### D. Techniques Employed to Evaluate Formed Specimens

##### 1. Mechanical Property Testing

Parent stock materials of 2219-0, 2014-0 and 321 annealed stainless were tested for yield strength, ultimate strength, percent elongation in 2 inches, and Rockwell hardness. Tensile coupons included specimens of both transverse and longitudinal grain directions, and values obtained served as a base or reference for which succeeding results obtained from various processes were compared. The reference data is shown in Table I and includes handbook values for further comparison. Since grain direction did not greatly influence material strength, all subsequent property tests were performed with tensile coupons taken in the transverse direction. A standard coupon configuration used for all transverse mechanical property tests performed in this program is shown in Figure 23.

Experiments in which flat bottom and round bottom domes were electrohydraulically formed served to establish that mechanical properties of curved specimens did not appreciably differ from flat specimens of equal thickness. Further information regarding this experiment can be seen in Section F entitled, "Preliminary Testing to Determine Forming Conditions." As a consequence of this experiment, round bottom domes were used throughout the program providing curved specimens which were subsequently straightened for mechanical property tests.

Tensile coupons of the three materials used were obtained from specimens free formed by the electrohydraulic, explosive, magnetic, and hydrostatic processes. The three materials were formed at relatively high and low forming rates and provided a range of gauge reductions for each forming process for mechanical property tests. Mechanical properties obtained under these conditions are tabulated in Table 5 and are also graphically represented in Figures 15, 16 & 17. Yield strength, ultimate strength, and percent elongation were plotted against percent thinout for each of the three alloys and reveals changes in the mechanical properties as a result of the various forming processes and strain rates employed.

An important experiment in which domes were either highly impacted (coined) or lightly impacted (just seated) against a die surface was performed to establish if discernible differences in mechanical properties exist. Electrohydraulic and explosive overpressure experiments were performed for all materials using a hemispherical die configuration similar in shape to the free formed dome specimens. Tensile specimens were taken from an area adjacent to the dome center as the dome center contained a small protuberance resulting from the die vacuum outlet port. Mechanical property test results may be seen in Table 7.

## 2. Gauge Reduction

One of the major objectives of the program was to observe metal strain at the region of maximum strain, that is, at the dome center. By means of high speed photographic observation of the dome center during forming, the relatively balanced biaxial strain at the dome center was directly obtained. After forming the thickness (gauge) reduction of the domes was also measured. Thickness reduction is related to balanced biaxial strain by the following relationship:

$$T = \frac{\alpha}{1 + \alpha} = \frac{2e + e^2}{1 + 2e + e^2}$$

$$\text{where } T = \text{thickness strain} = \frac{\text{reduction in thickness}}{\text{original thickness}}$$

$$\alpha = \text{area stretch} = \frac{\text{surface area increase}}{\text{original area}}$$

$$e = \text{equal biaxial strain} = \frac{\text{elong. in either direction}}{\text{original length}}$$

As the thickness measurement positions move away from the dome center, thickness reduction is less and the biaxial strain becomes unbalanced until at the flange strain is approximately uniaxial. See sketch below. In uniaxial strain, the relation to thickness reduction is:

$$T = \frac{\alpha}{1 + \alpha} = 1 - \frac{1}{e + 1} \quad 1/2$$

$$\text{where } T = \text{thickness strain} = \frac{\text{reduction in thickness}}{\text{original thickness}}$$

$$\alpha = \text{area stretch} = \frac{\text{surface area increase}}{\text{original area}} = e - T - Te$$

$$e = \text{uniaxial strain} = \frac{\text{elong. in tension direction}}{\text{original length}}$$

The rate of strain imbalance with distance from the dome center varies with the degree of flange restriction and the impulsive nature of the forming operation.

Measurements were obtained during forming operations at 17 points located on the diameter of the formed workpiece in the manner shown in Figure 18. Thickness values plotted against their respective position number for the electrohydraulic, explosive, magnetic, hydrostatic and hydroform processes is shown in Figures 19 to 22 respectively.

The entire evaluation work of this program (residual stress, transmission microscopy, and mechanical testing) are concerned with specimens taken near the dome center so that the test specimens were taken from material which was essentially strained equibiaxially. A small imbalance and difference in thickness occurs in the 2" gage length of a tensile specimen. In a conventional tensile specimen the relatively thinner and weaker center tends to strain more rapidly during testing, thereby producing artificially low elongation values. For this reason, the width of the tensile specimens was proportioned to obtain a cross section area only slightly smaller at the center of the 2" gage length.

### 3. X-ray Diffraction

X-ray diffraction gives characteristic reflection lines for the lattice spacing of the surface layers of the specimen. Elastic tension or compression when residual in the material will broaden the lines in opposite directions. The degree of plastic working can also be detected as a function of the number of dislocations each of which in its immediate area, produces elastic strain or lattice size change. Experts generally can distinguish between residual broadening and dislocation broadening, however, when two or more phases are present, alloys become naturally more complex to understand. Specific methods employed to evaluate formed specimens obtained for this program is presented in Section B entitled "Discussion of Results."

The residual stress in a workpiece after forming is dependent on the configuration. A specimen cut from a workpiece will generally contain less stress due to its smaller size which implies free edges closer to the point of measurement. The largest specimen which can be accommodated in the X-ray diffraction equipment is a 6" round. Before proceeding with the bulk of the experimental work, 6" circles cut from the dome center were compared with 1" x 1" squares, also from the dome center. The objective was to establish whether the residual stress due to specimen size was quantitatively significant. The larger specimens would require that additional forming of domes for x-ray diffraction tests be performed whereas the smaller specimens could be taken from domes cut for tensile specimen tests. Experiments HS-1 and HS-3 (1" x 1"), HS-4 and HS-6, (6" round) in Table 13 indicated differences in stress levels of 135,500 psi and 73,700 psi due to the differences in specimen size. Therefore, all further x-ray diffraction tests were performed on 6" diameter specimens.

Twenty-four specimens obtained from domes formed by various processes consisted of eight 6 inch diameter samples for each of the three alloys. These specimens were taken from domes in the manner shown in Figure 23. The specimens were submitted for x-ray diffraction analysis to the Materials Development Research Laboratory located at Republic Aviation Corporation. X-ray diffraction data shown in Table 13, was obtained for the electrohydraulic, explosive, and hydrostatic processes under various dome forming and die impacting conditions.

Typical diffraction patterns for parent stock and formed domes in the three materials are shown as Figures 24, 25 and 26.

#### 4. Electron Transmission Microscopy

Since the principal objective of the forming experiments is to establish the influence of strain rate upon mechanical properties, it was considered advisable to employ electron transmission microscopy rather than conventional optical microscopy. The former offers the decided advantage of permitting observation of the effects of strain upon the crystal lattice structure in terms of dislocation density and distribution. In contrast, conventional microscopy reveals strain only on a gross scale, that is, in terms of grain size, shape, distribution, and phase. See Figure 27.

Also, in contrast to conventional microscopy, preparation of specimens for electron transmission is arduous and time consuming. Special etching techniques are necessary since specimen thickness must range between 200 and 1,000 angstroms ( $7.9 \times 10^{-7}$  to  $3.9 \times 10^{-6}$  inches) to be thin enough to transmit the electrons.

1" x 1" specimens, taken from domes in the manner shown in Figure 23, were submitted for electron transmission microscopy analysis to the Materials Development Research Laboratory located at Republic Aviation Corporation. A total of twelve specimens representing the three alloys free formed by various processes were submitted for comparison. Results of equally reduced specimens, formed by the electrohydraulic and explosive processes at high rates of strain, are compared to the hydrostatic process and parent alloys to determine if changes in the metallurgical structure exist. See Appendix A.

## 5. Stress Corrosion Testing

Stress corrosion cracking is defined as the complex interplay of tensile stress and corrosion which leads to cracking in a metal or alloy. The principal factors are the magnitude of the stress, the nature of the environment, the length of time involved and the internal structure of the alloy. These factors are not independent, but interact, one accelerating the action of another. Their relative importance varies with conditions.

If stress corrosion cracking is to occur, there must be tensile stresses at the surface. The stresses may be internal or applied, the two types being additive. The cracks produced tend to grow in a plane perpendicular to the resultant tensile stress.

Stress corrosion cracks in stainless steel are usually transcrystalline. Intergranular cracking has been observed, but only when the heat treatment has been such as to make the stainless steel susceptible to general intergranular corrosion.

The environment that induces stress-corrosion cracking frequently attacks the metal only superficially if the stresses are absent or extremely low. Many of the environments that cause cracking tend to produce a pitting type of corrosion in the absence of stresses. Most cases of cracking of stainless steels involve the presence of chloride ions, particularly if the solution is acid. Hot concentrated solutions of chloride of magnesium, calcium, barium, cobalt, zinc, lithium, ammonia and sodium all cause rapid cracking.

While the generalized theories advanced to date do not completely account for the complicated interaction of corrosion and stress in all metal systems, a considerable understanding of stress-corrosion cracking is being developed. It is generally agreed that an electrochemical step is involved, in which anodic areas are dissolved away. This is believed to be followed by a mechanical parting of the metal along selective paths which leads to crack initiation and propagation.

An evaluation of the relative stress corrosion performance of 321 stainless steel dome shaped specimens formed by various processes under varying conditions was performed. The domes consisted of two hydrostatic, and eight each of electrohydraulic and explosive formed specimens. Thermal stress relief and rate of energy input to free formed and die impacted domes were introduced as process variables considered significant in stress corrosion susceptibility.

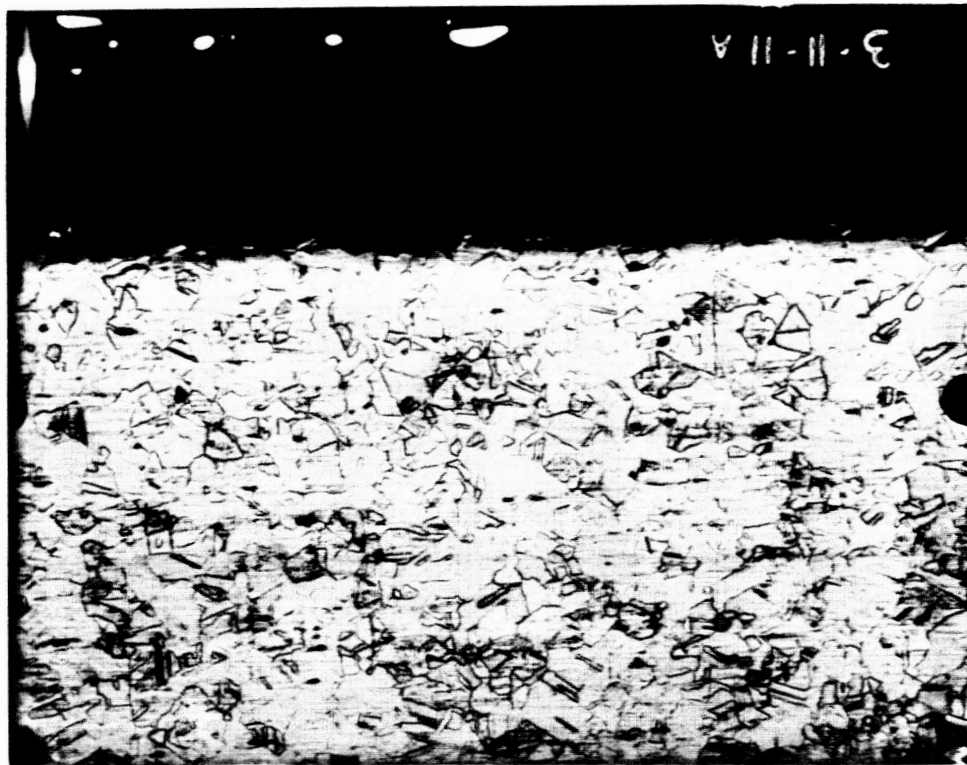
Prior to accelerated corrosion testing, all specimens were brought to a uniform active surface condition by vapor honing. Subsequent procedure consisted of constant immersion in 25 percent aqueous magnesium chloride solution at boiling temperature (217°F). This departure from the standard

42 percent solution was incorporated to extend potential time to failure and provide a more accurate basis of comparison. Mr. C.A. Verbraak \*, in January 1963 Metals Progress article: "Explosive Forming Can Cause Problems" reported failures of explosively formed parts within 24 hours as opposed to three days for those conventionally formed, using the standard test. Since stress corrosion evaluations in artificial environments generally exhibit considerable scatter, it was thought desirable to attempt to produce at least an order of magnitude difference in failure times for the two forming techniques.

An illustration of the test installation is given in Figure 28. Tank working volume was maintained at 80 gallons to provide a high solution volume to specimen area ratio. The first three test series evaluated four specimens simultaneously for total durations of 192 to 216 hours. In the interest of time, the last series was expanded to eight specimens run concurrently. This test was carried to 288 hours to negate influence of the decreased solution volume available to each specimen.

After termination of exposure, the test items were examined visually with low power optics and finally checked by dye penetrant inspection. The surface of an 0.072" thick specimen taken from a dome displaying a general surface attack is shown in the photomicrograph below: Test data for all specimens is provided in Table 14 and a typical dome is shown in Figure 29.

\* Head, Dept. for Basic Research, Metaalinstituut T.N.O., Delft, Netherlands



Etchant: Gamma

250X

Transverse Section Through Dome Showing  
Slight Pitting Attack on Outer Surface.



## E. Pressure Measurements

Electrohydraulic pressure pulses were measured with a Kistler model 617 quartz pressure transducer of 0-30,000 psi range. The transducer contains a quartz element which responds to applied pressures by producing a voltage across the quartz element. The voltage output is applied to an appropriate capacitor, and the resultant microampere current flow is amplified with a Kistler model 655 charge amplifier to a level suitable for further amplification by a Tektronix oscilloscope containing a type K preamp plug-in. The amplifier-calibrator is a transistorized DC differential amplifier with an input impedance greater than 100 megohms and provides an overall time constant which is long relative to the pressure pulse duration. Interconnecting cabling consisted of a special low noise oil filled coaxial cable of very high insulation resistance. Cable and connector ends were sealed from moisture by coating with a room temperature vulcanizing silicone rubber (Dow Corning RTV "Silastic"). Sketch A of Figure 30 shows a block diagram of the pressure measuring system. A specially designed adapter, shown as sketch B of Figure 30, was used to facilitate installation and to electrically isolate the transducer common ground from the discharge electrode common ground. An electrical common ground for the discharge circuit and transducer circuit would introduce a ground loop, inducing an extraneous signal into the transducer circuit. Despite electrical isolation, a voltage signal was induced into the transducer cabling and can be seen at time zero in all pressure traces shown in Figure 31. The induced pickup results from the expanding and collapsing magnetic field occurring during an underwater discharge. This effect was somewhat desirable in that it provided a means of approximating the characteristic discharge waveshape and duration for comparison to the subsequent pressure wave pulse.

Calibration of the 617 Transducer is accomplished by determining the electrical charge output in response to a specific pressure input. The 617 gage is calibrated at the factory and a graph of picocoulombs vs psi is supplied the user. Picocoulombs/psi is the charge sensitivity and is expressed as the ratio of output to input (pCb/psi). The 617 gage has a gage factor of .447 pCb/psi which can be converted to volts/psi by using the simple relation;  $V=QG/C$  where V is voltage, C is the total circuit capacitance (cable plus amplifier input capacitor), Q is the gage factor, and G is the amplifier gain.

The 15 foot cable used has a rating of 20 pfd/ft and the amplifier input capacitor is 40,000 pfd. The amplifier has a gain of 5 and the gage factor is 0.447 pCb/psi.

$$\text{Using these values, } V = \frac{QG}{C} = \frac{0.447 \text{ pCb (5)}}{\text{psi (43,000) pfd}}$$

$$V = \frac{2.234 \text{ Cb}}{4.3 \times 10^4 \text{ psi fds}} = 0.517 \times 10^{-4} \text{ volts/psi or } .0517 \text{ volts/1000 psi}$$

To ascertain this value of voltage sensitivity, it was decided to calibrate the 617 gage using the components previously described. The system was statically calibrated using a manually operated pump to supply a steady state pressure of 0 to 9,000 psig. This pressure was monitored by a 0-10,000 psig standard gage calibrated to  $\pm 1\%$ . The results of this calibration are tabled below:

Standard Gauge Reading (psig)	Oscilloscope Deflection (Volts)
250	.010
500	.030
750	.040
1,000	.055
1,500	.085
2,000	.110
3,000	.180
4,000	.235
5,000	.290
6,000	.355
7,000	.420
8,000	.460
9,000	.500

These values were plotted as E out vs. psi and produced a straight line whose slope is the calibration factor of .0553 volts/psi. It is of interest to note the very close agreement attained between the static calibration method (.0553 V/1000 psig measured) and the voltage sensitivity method (.0517 volts/1000 psig calculated) previously described. All pressure pulse measurements obtained with the Kistler 617 gage and associated equipment in the closed tank were determined using the static calibration factor of .0553V/1000 psig. Test results are shown in Table 15 and plotted in Figure 32.

The influence of standoff distance, chamber reflections, initiation wire size, and energy level upon pulse pressure is discussed in Section E of "Discussion of Results."

## F. Preliminary Testing to Determine Forming Conditions

Preliminary testing in the closed tank using the three materials, was performed to establish operating conditions for subsequent electrohydraulic dome forming experiments. Blank diameter, energy to rupture, gauge reduction and dome configuration (flat or round bottom) were determined. In addition, preliminary testing served to establish high speed motion picture camera parameters and verified the feasibility of determining strain rate by the method described in B of Section II, entitled "Experimental Technique to Measure Strain Rate."

A 17 1/2 inch diameter blank was found to be satisfactory for both aluminum alloys, but produced excessive flange wrinkling in the stainless alloy. This indicated that a larger blank was needed to reduce draw and provide a means of getting a maximum degree of strain for a given depth so that large variations of strain rate would be available for motion picture study. A 20 1/2 inch blank diameter for the stainless steel alloy was selected as suitable, as this size compensated for the relatively lower stretch/draw ratio and also closely matched the draw values found for the aluminum blanks. Total change in blank diameter have ranged from 0.7 to 1.5 inches for all three materials formed to the same depth by multiple discharges. This variation in the ratio of stretch to draw during forming is likely a function of both discharge voltage and flange hold-down pressure. Flange pressure cannot be measured or closely controlled in the experimental setup and the electrohydraulic force reduces the flange restraint. However, these factors do not affect the usefulness of the experiments since strain rate rather than control of stretch/draw ratio is of major concern.

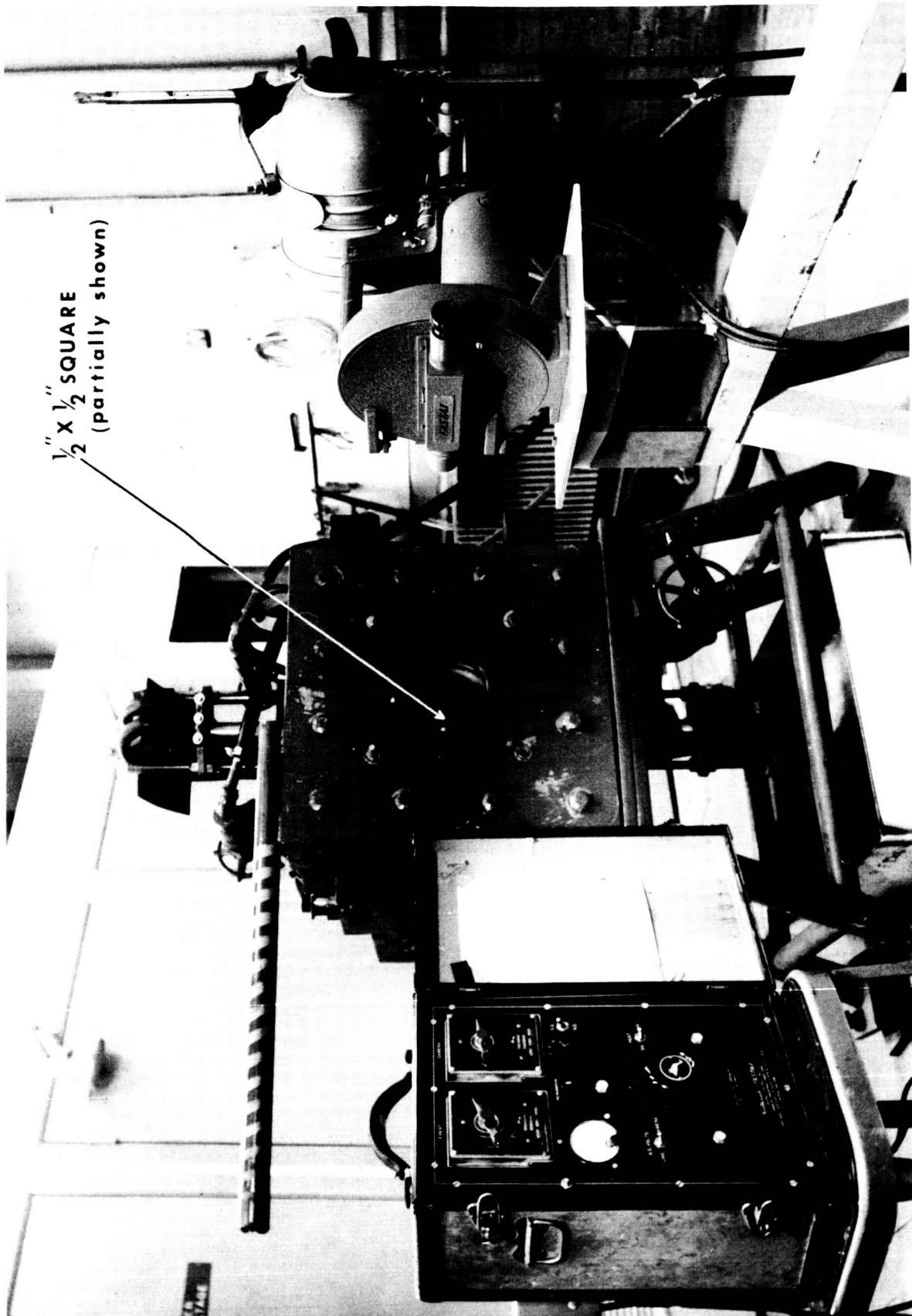
Each alloy was formed to rupture by a series of discharges at various energy levels. The blanks were prepared for measurements by painting a 1/2" square in the center for motion picture study, and marking a diameter with points at 1 inch increments for gauge reduction measurements. The following data was recorded after each shot. Energy level, gauge reduction (at 17 points across the diameter), dome depth, volume, and change in blank diameter (draw). Dome depth at rupture was roughly 5 inches for the 2219 and 321 alloys. For the 2014 alloy, however, only a .3-1/2" depth was possible since elongation and tensile properties are lower. Strain rate measurements were performed for the first shot only for all materials at a relatively low and high discharge level. Studies of the first motion pictures revealed that the event was either entirely missed or occurred too near the start of the film. Subsequently, the camera timer was set to trigger the event 0.75 seconds after the camera start with the result that the event was recorded approximately 70 feet down the 100 foot film.

For determining dome configuration to be used for the balance of the program, a series of flat and round bottom domes were formed to varying depths of approximately equal thicknesses at dome center. The objective of these forming experiments was to establish if the tensile strengths of coupons obtained from round bottom domes differed significantly from those taken from flat bottom domes. See Table 2 for the recorded data, dome shapes,

and the manner in which each configuration was formed. Material chosen for this experiment was 2219-0 aluminum since this alloy is more strain hardenable than 2014-0 and results would be more readily observable. Typical size and location of tensile coupons taken from the center of each dome configuration is shown in Figure 33. Three flat and three round bottom domes having approximately equal center thinout values of 14%, 25% and 47% were formed and tensile coupons obtained for comparison of their tensile properties (see Table 3). It was found that the tensile properties are closely dependent on the degree of thickness reduction and are not appreciably influenced by dome shape (see Figure 34). Also, round bottom domes exhibit a more uniform thinout at the dome center than do the flat bottom domes as shown in Figures 35, 36 and 37. Since the dome center is the region of strain rate observation and mechanical property evaluation, the use of round bottom domes for the balance of the program was considered technically advisable as well as experimentally expedient.

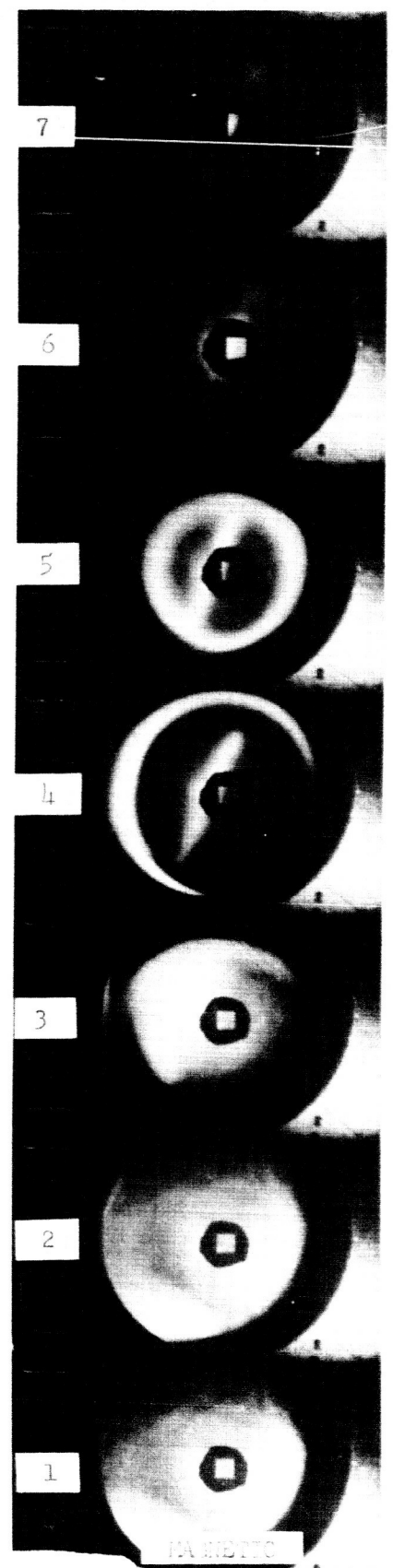
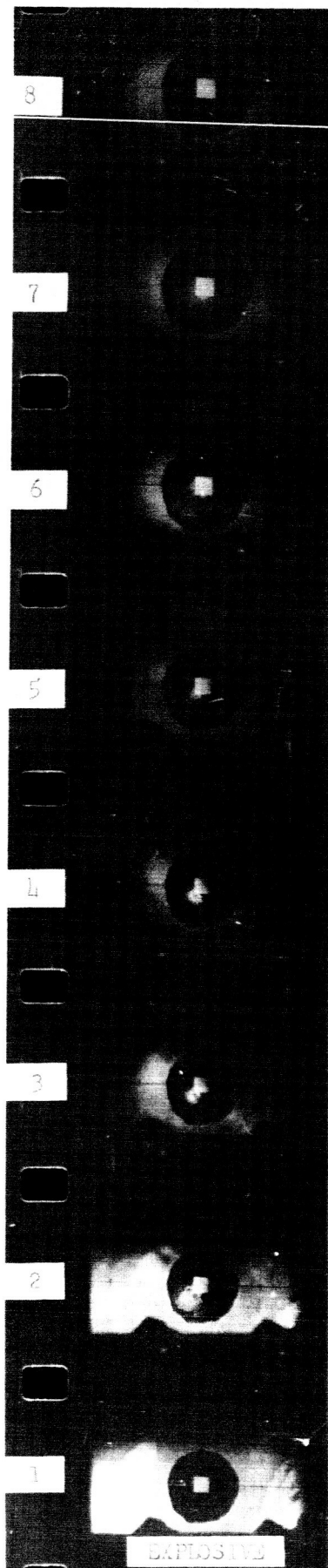
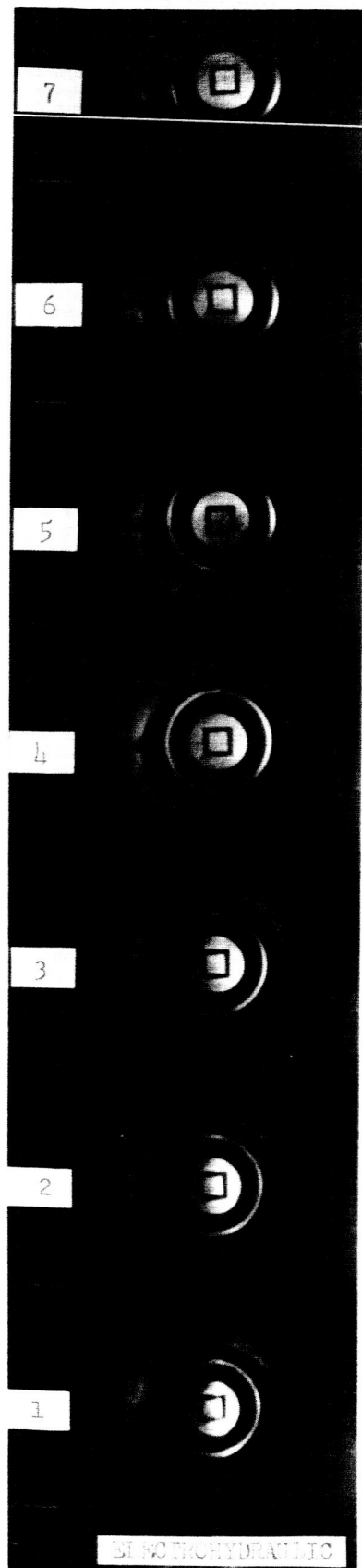
The above experiments also served the purpose of establishing conditions for the high speed camera operation. It was found necessary to use the maximum obtainable camera speed (6,500 frames per second) to obtain metal movement in a reasonable number of frames exposed in the short time of metal movement. Dependent on discharge condition, strain occurred in 4 to 8 frames .

Initially, a 36 inch focal length was used. This was later increased to 48 inches to minimize foreshortening and defocusing.



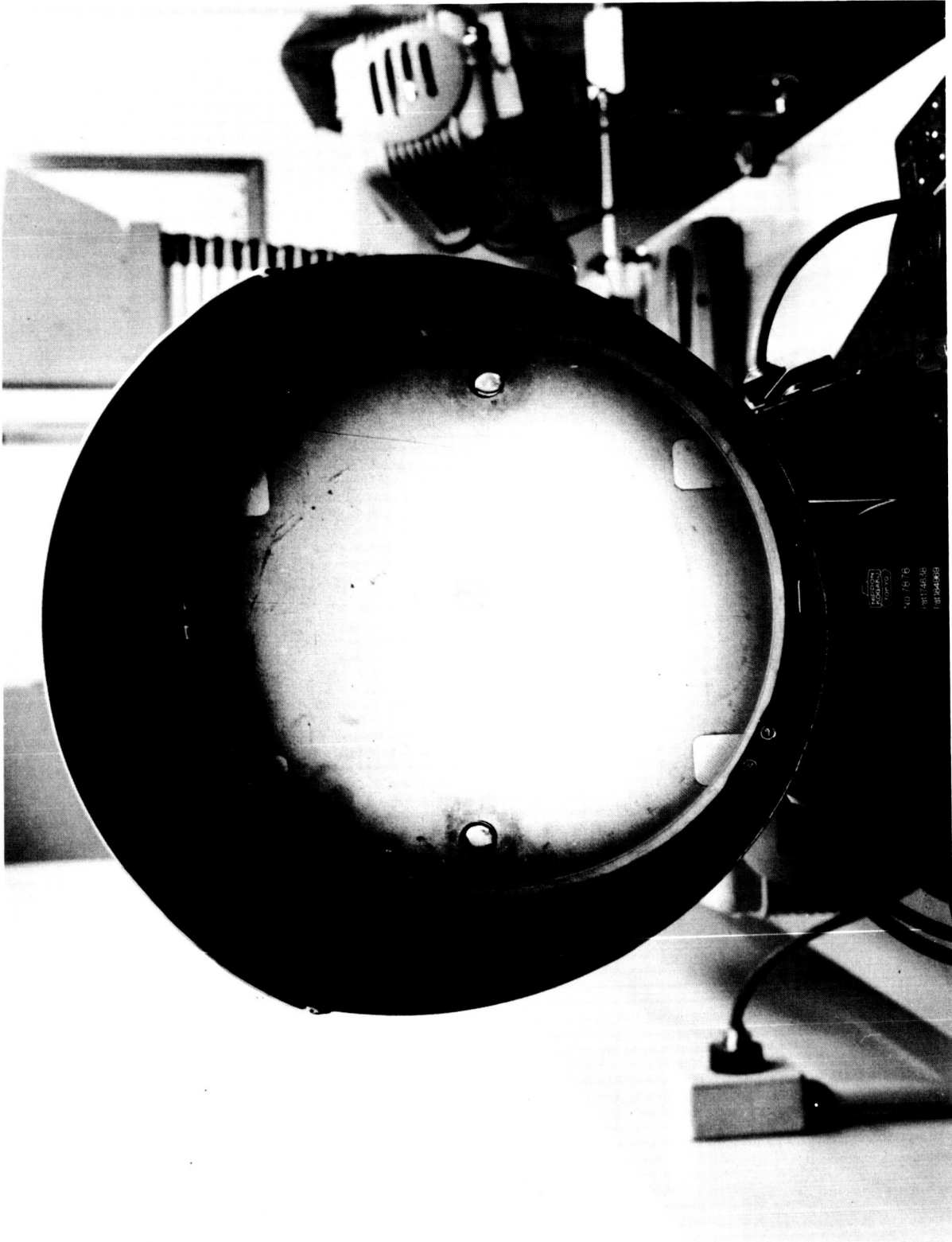
HIGH SPEED CAMERA TECHNIQUE USED TO RECORD EXPANSION OF THE  
 $\frac{1}{2}$ " X  $\frac{1}{2}$ " SQUARE DURING ELECTROHYDRAULIC FREE FORMING OF  
DOMES IN CLOSED TANK.

FIGURE 1



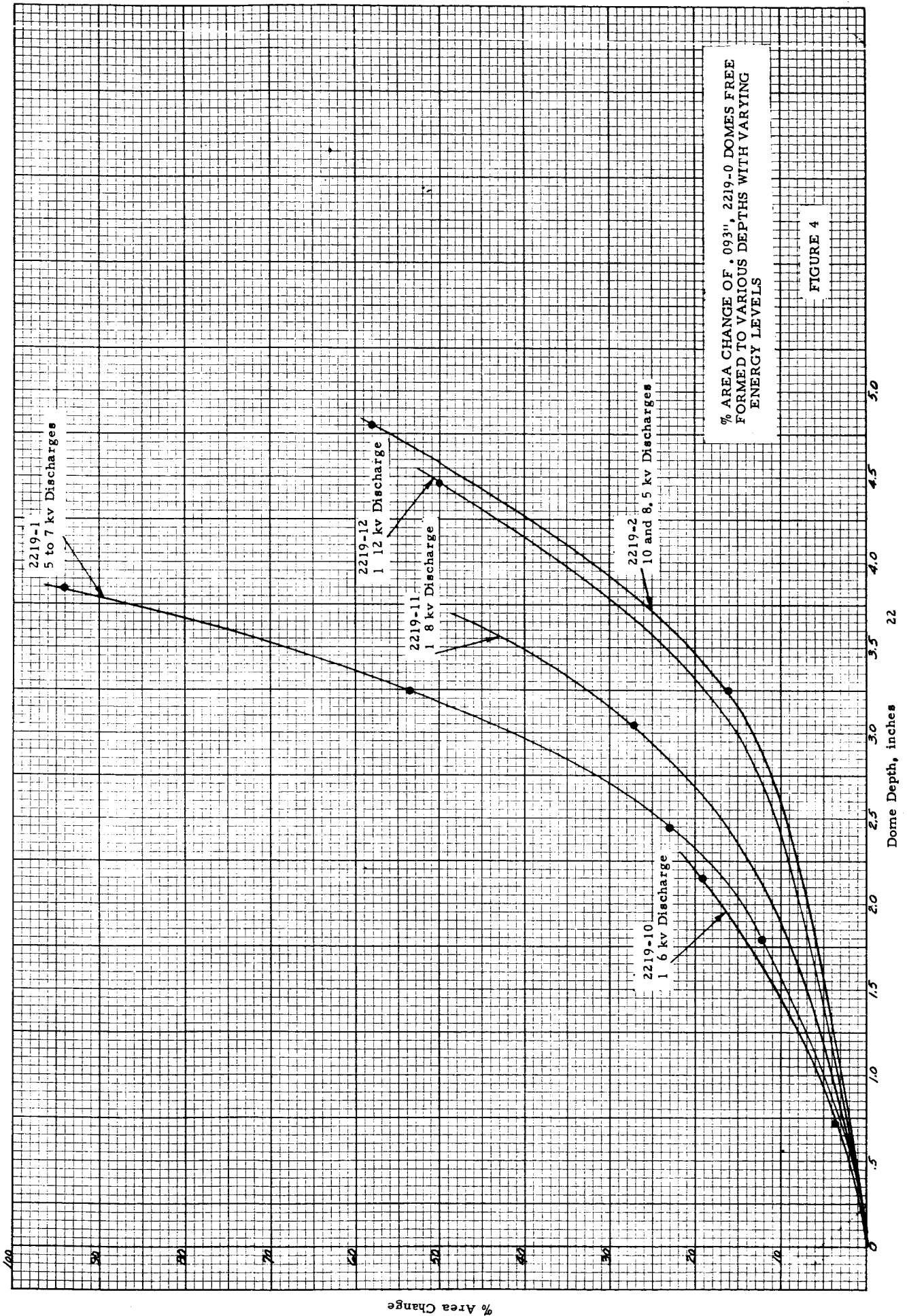
HIGH SPEED FILM SEQUENCE OF METAL STRAIN FOR .092" 2219-O ALUMINUM FORMED BY THE ABOVE PROCESSES

FIGURE 2



OPTICAL COMPARATOR USED TO MEASURE THE HORIZONTAL AND VERTICAL  
FILM IMAGE INCREASE OF THE ORIGINAL  $1/2" \times 1/2"$  CENTER SQUARE FOR  
DETERMINING RATE OF STRAIN.

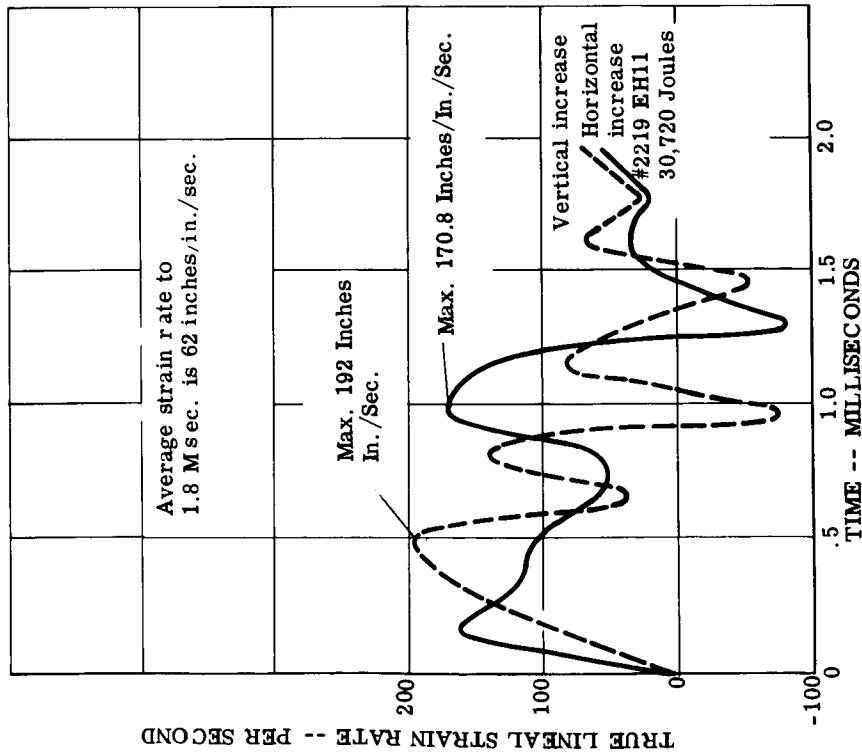
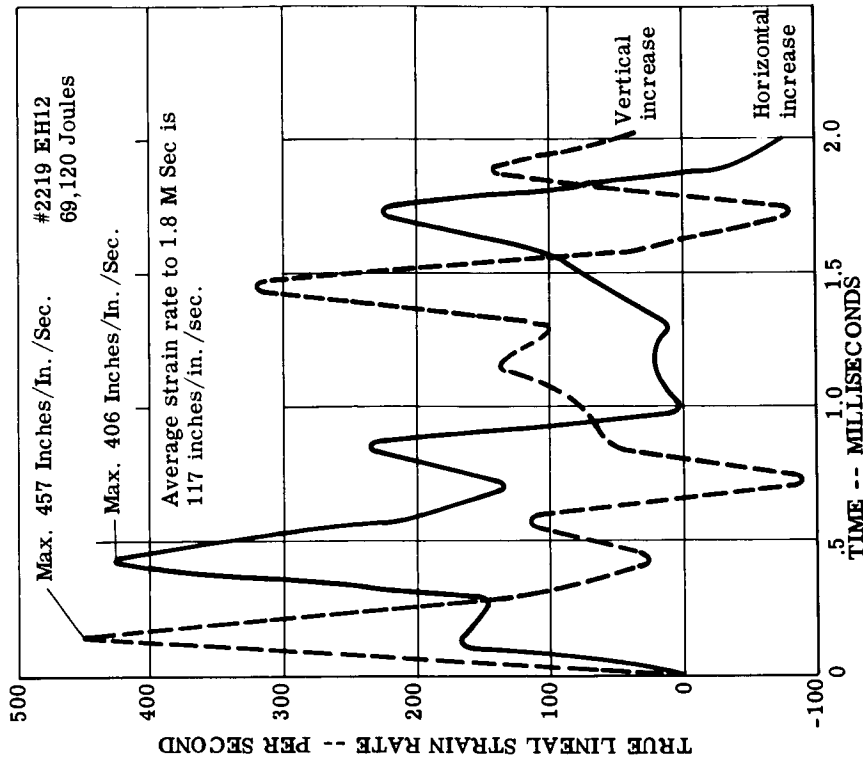
FIGURE 3



% AREA CHANGE OF .093" 2219-0 DOMES FREE FORMED TO VARIOUS DEPTHS WITH VARYING ENERGY LEVELS

FIGURE 4

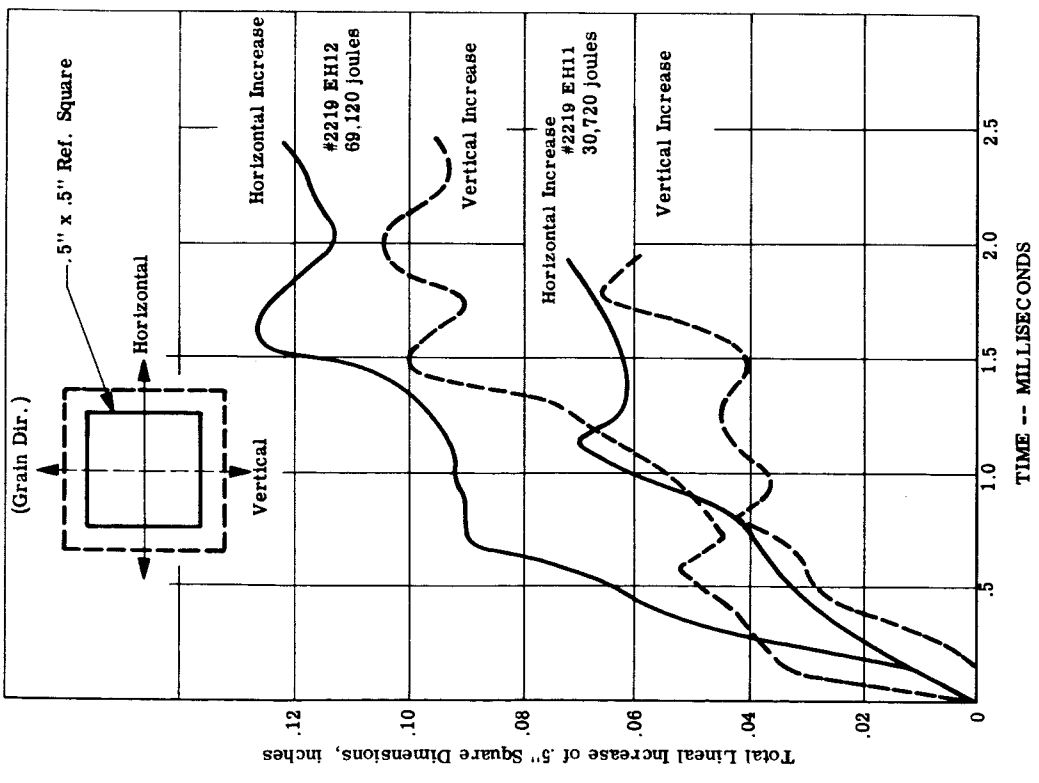
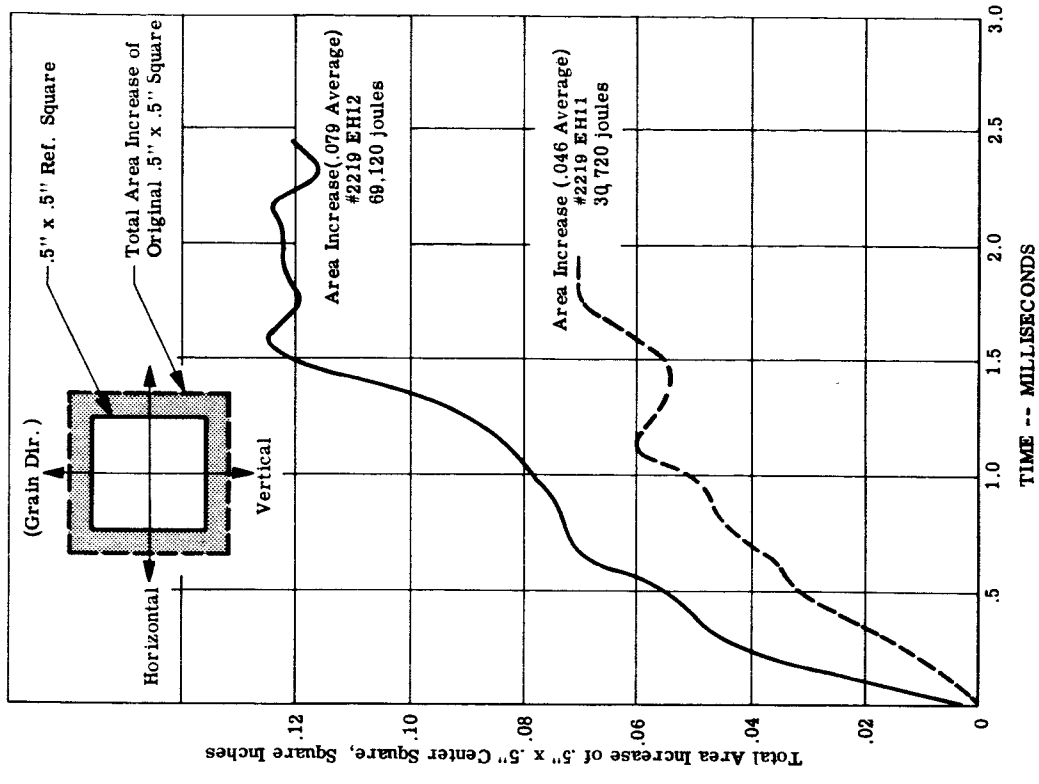




ELECTROHYDRAULIC

ELECTROHYDRAULIC

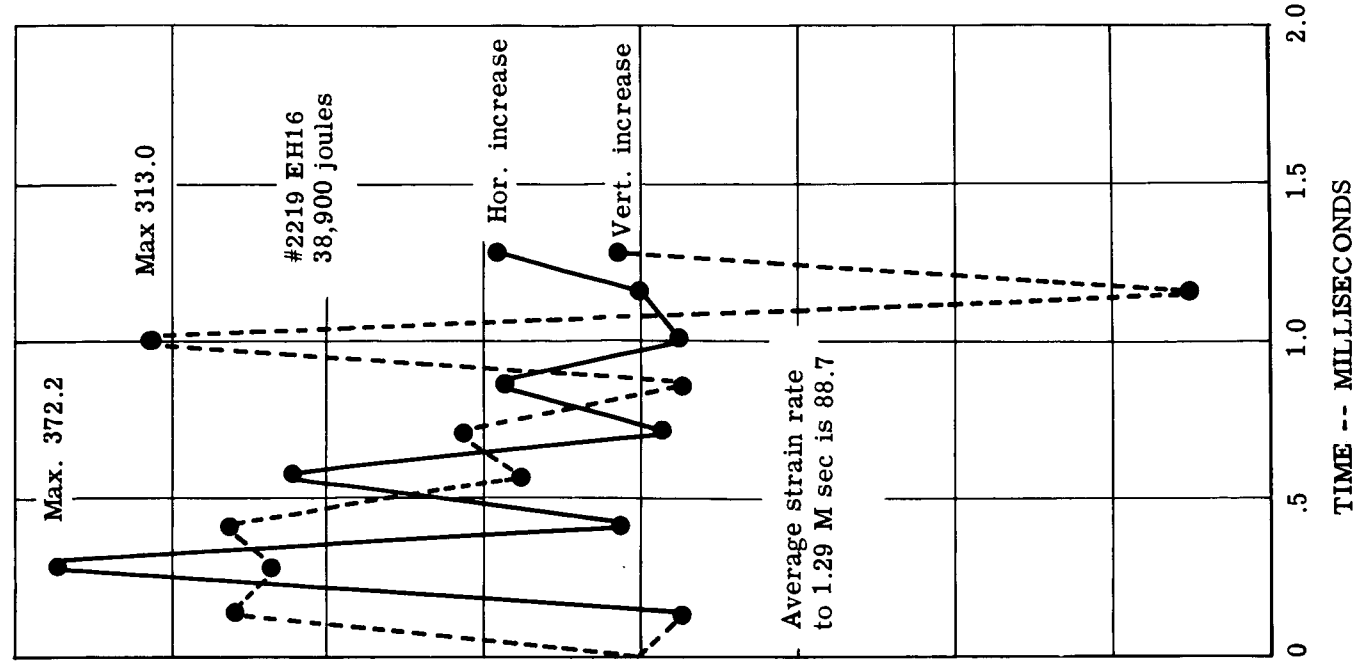
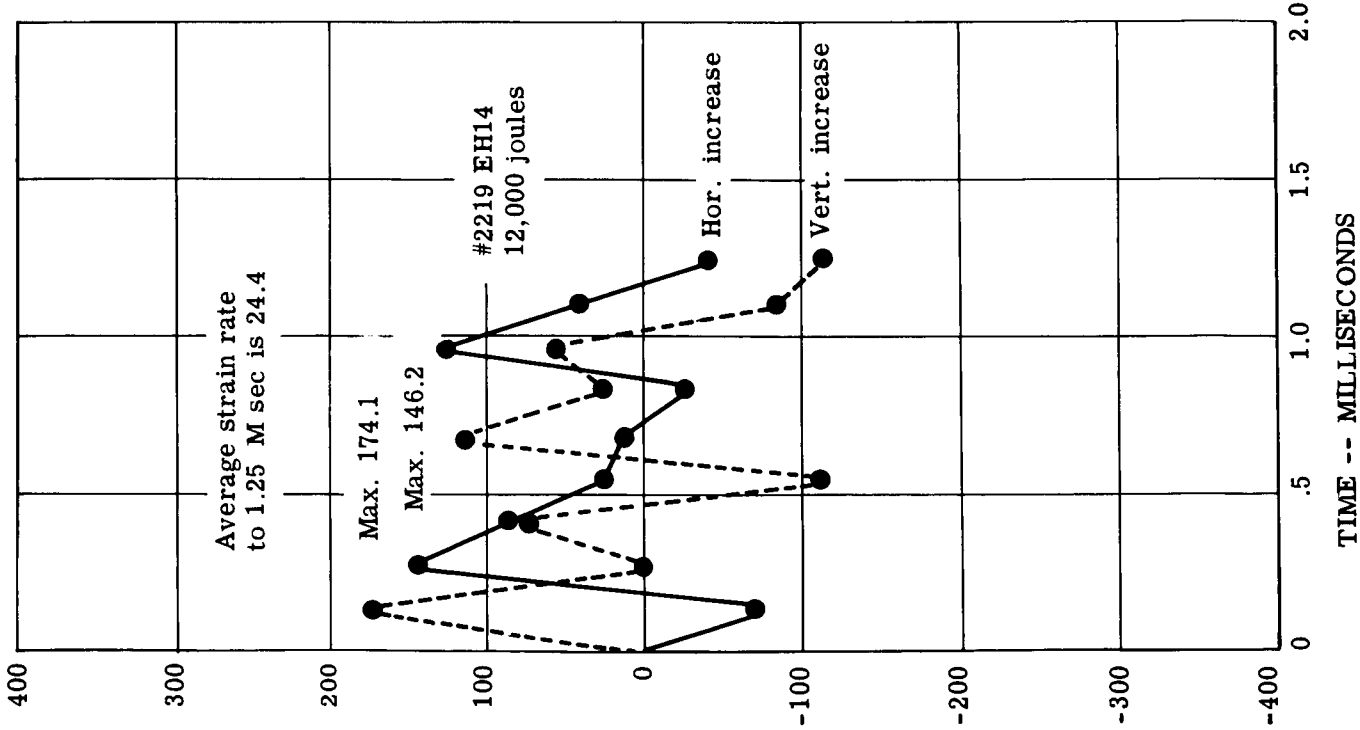
Figure 5 Total Lineal Strain Rate of .5" x .5" Center Square for .092", 2219-0 Aluminum



ELECTROHYDRAULIC

ELECTROHYDRAULIC

Figure 6 Total Lineal Strain and Area Strain of Original .5" x .5" Center Square for .092", 2219-0 Aluminum



TIME -- MILLISECONDS

TIME -- MILLISECONDS

ELECTROHYDRAULIC

Figure 7 True Lineal Strain of .5" x .5" Center Square for .092", 2219-0 Aluminum

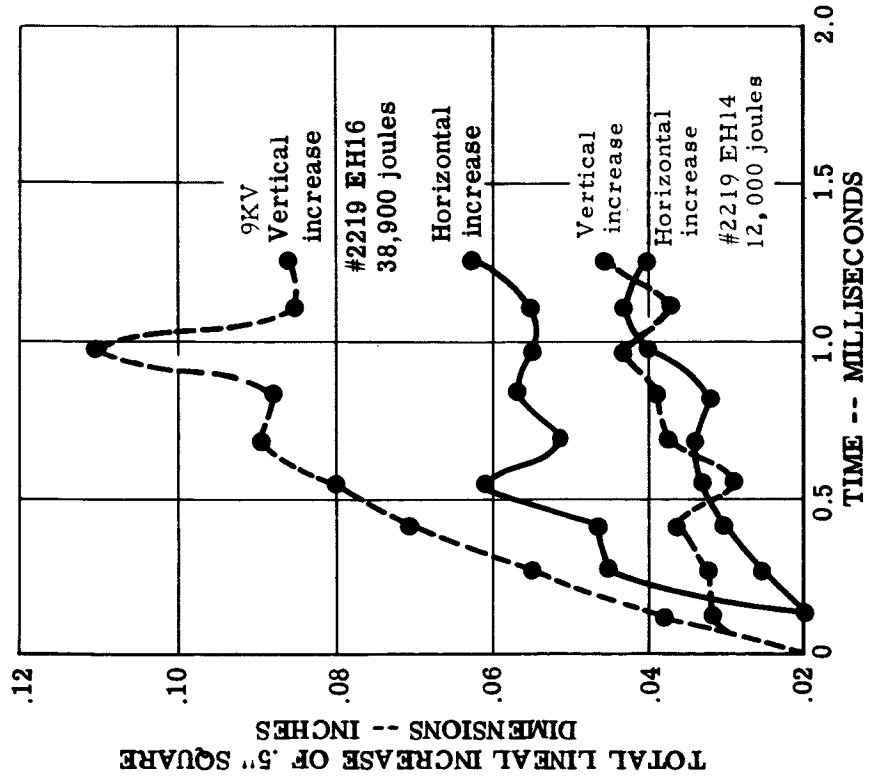
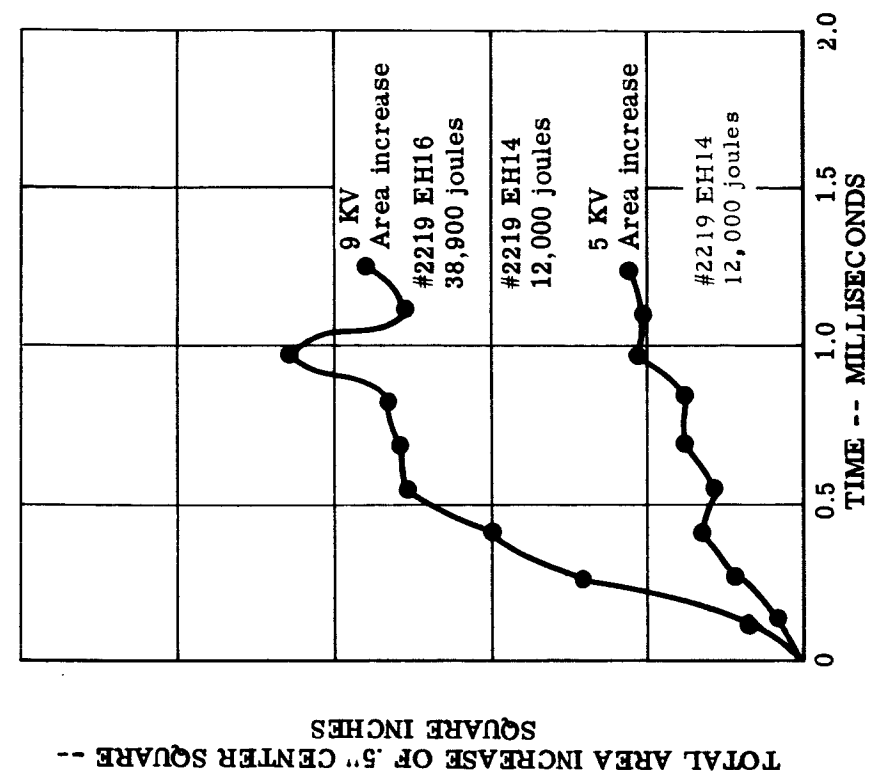


FIGURE 8 TOTAL LINEAL STRAIN AND AREA STRAIN OF ORIGINAL .5" x .5" CENTER SQUARE FOR .092", 2219-0 ALUMINUM

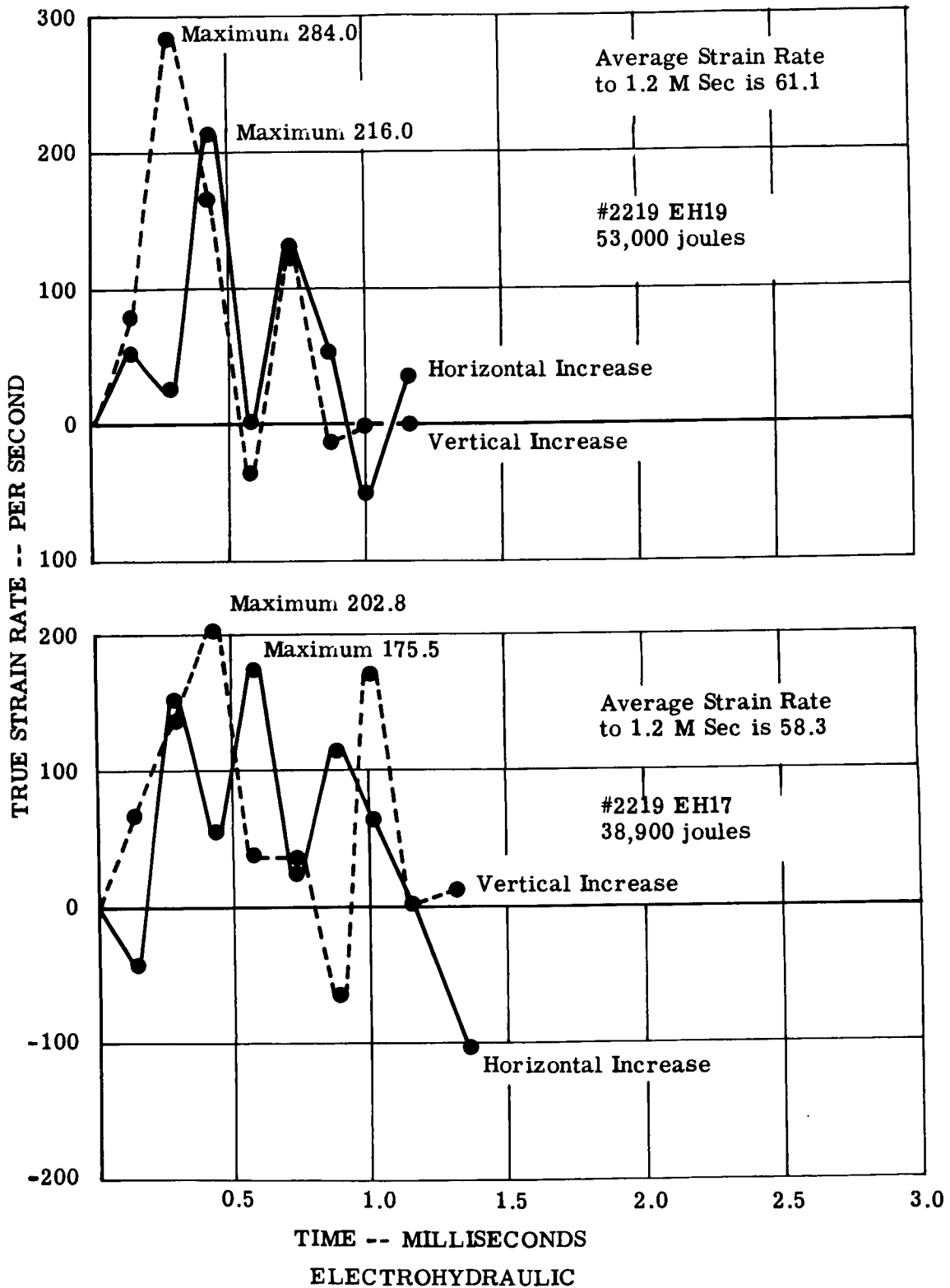


Figure 9 True Lineal Strain Rate of .5" x .5" Center Square for .092", 2219-0 Aluminum, Lubricated Blank

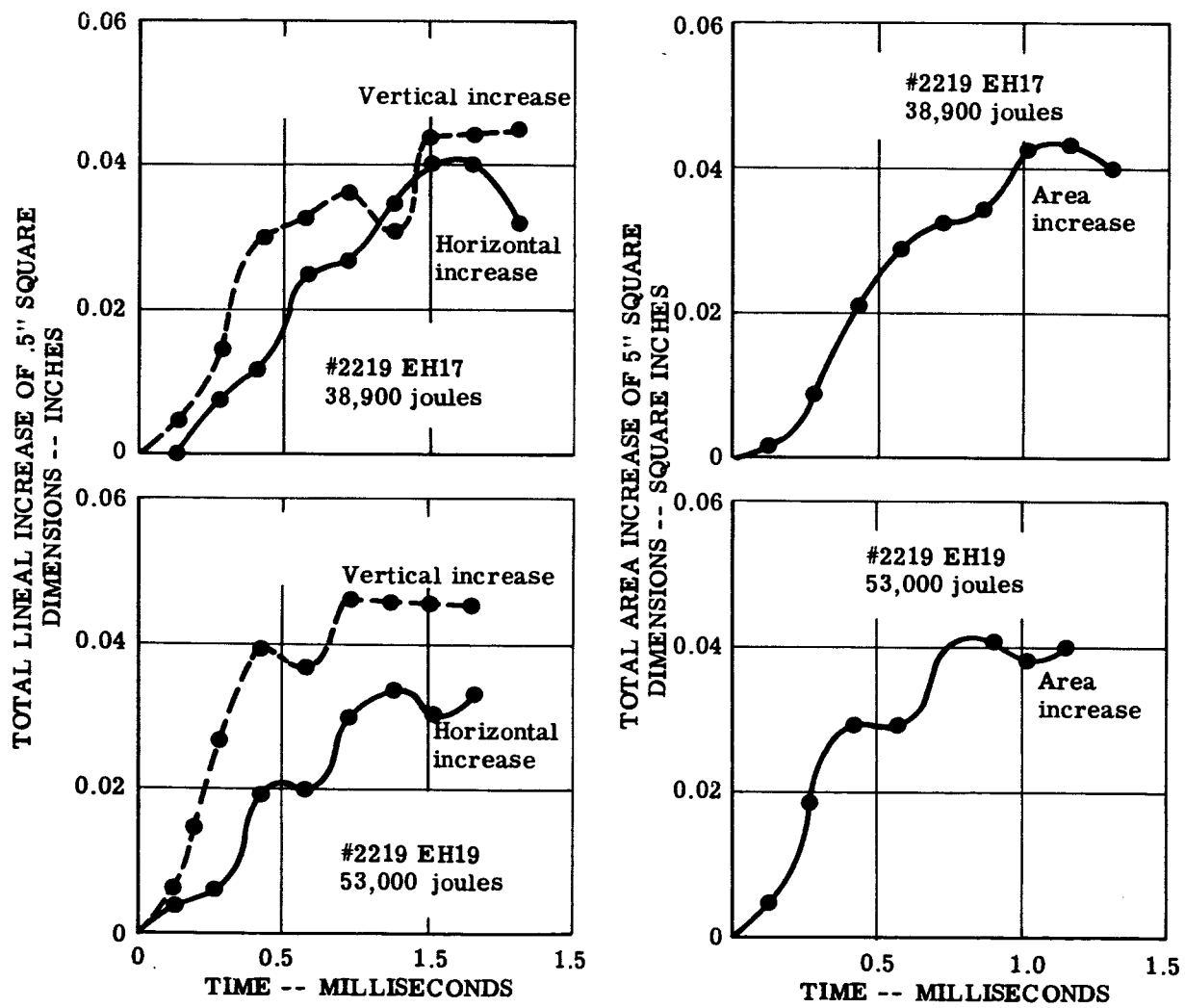
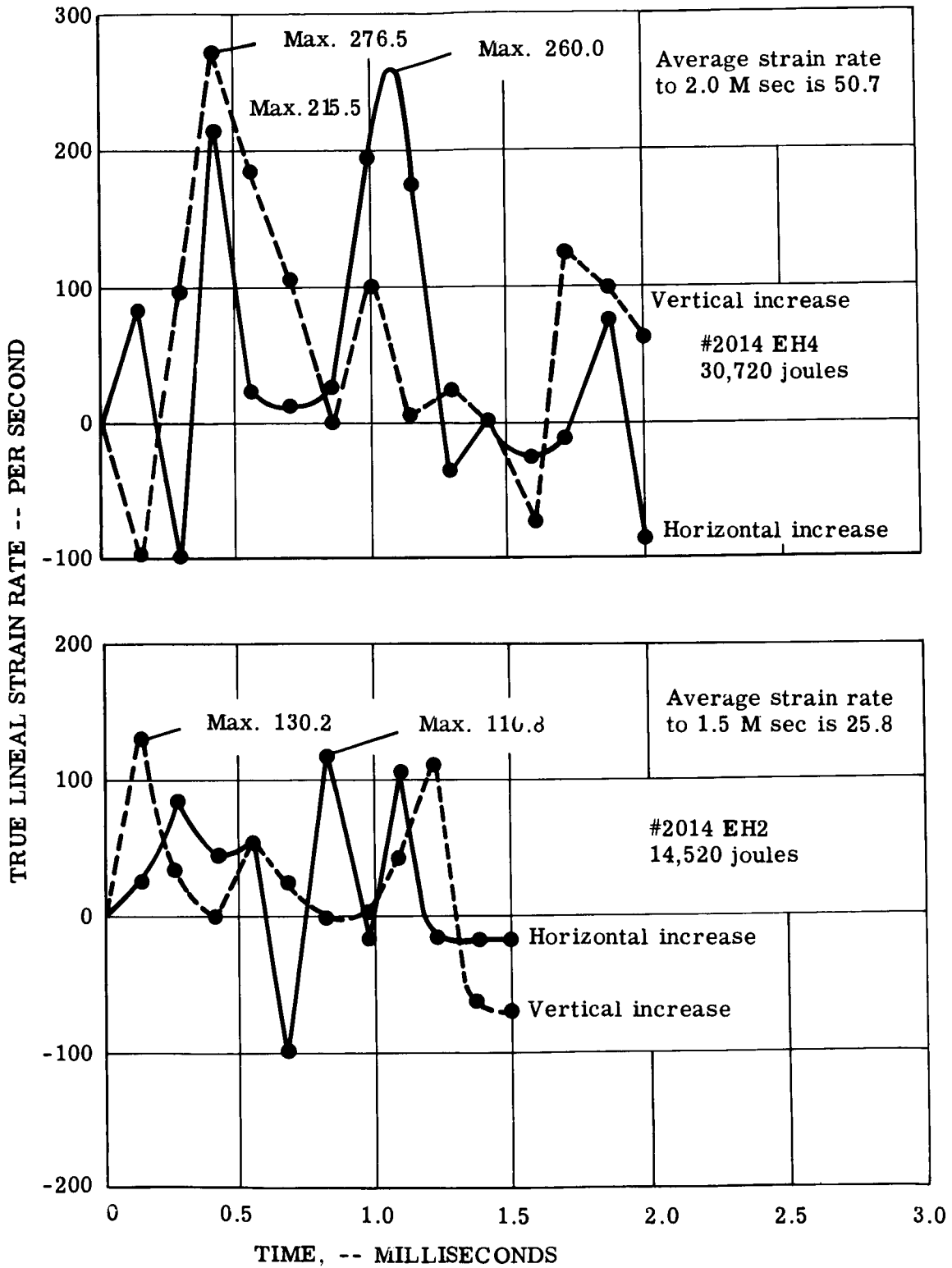


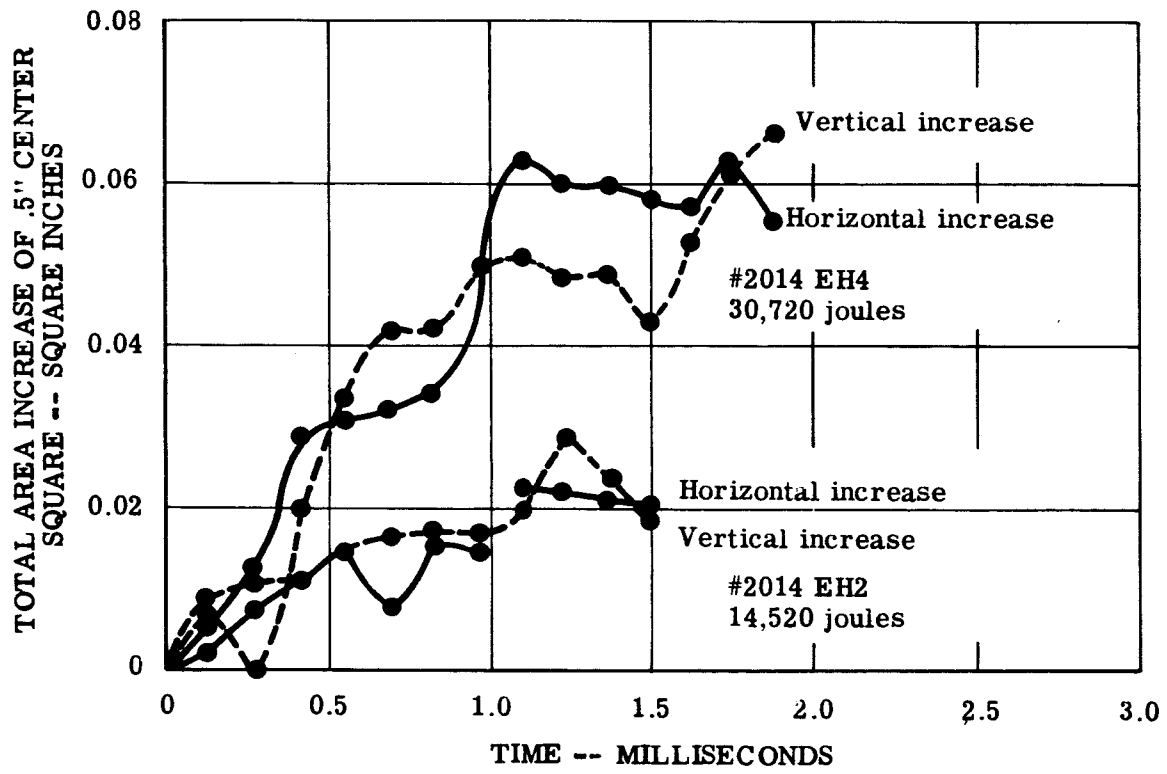
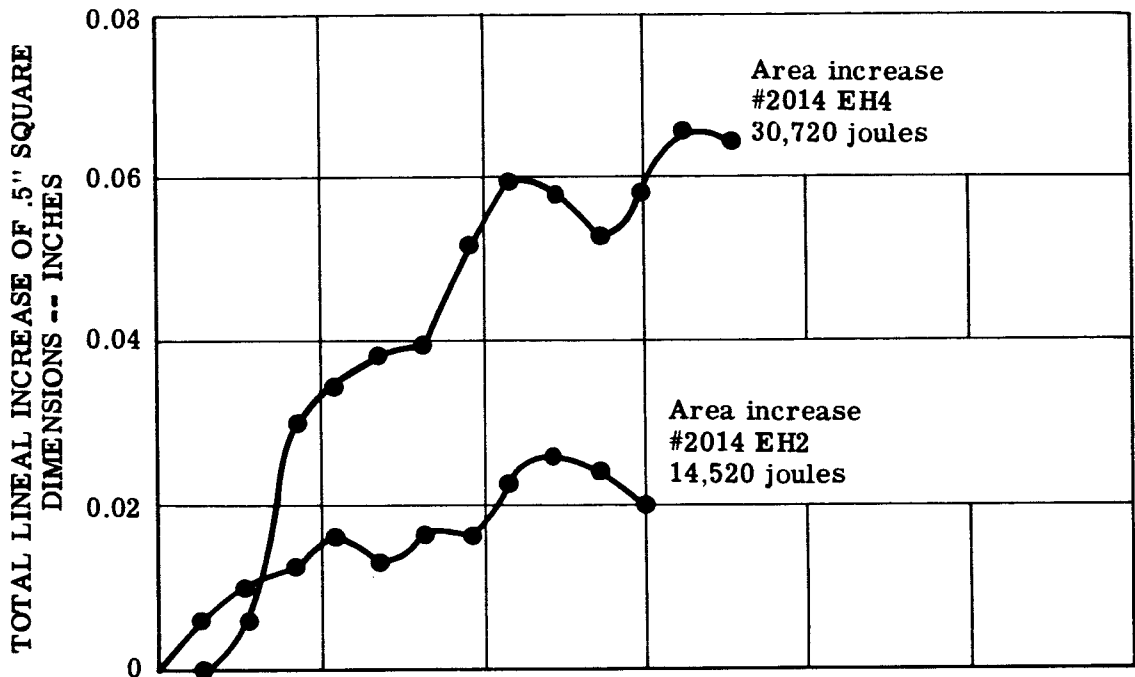
FIGURE 10 TOTAL LINEAL STRAIN AND AREA STRAIN OF ORIGINAL .5" x .5" SQUARE FOR .092", 2219-0 ALUMINUM

ELECTROHYDRAULIC - BLANK LUBRICATED



ELECTROHYDRAULIC

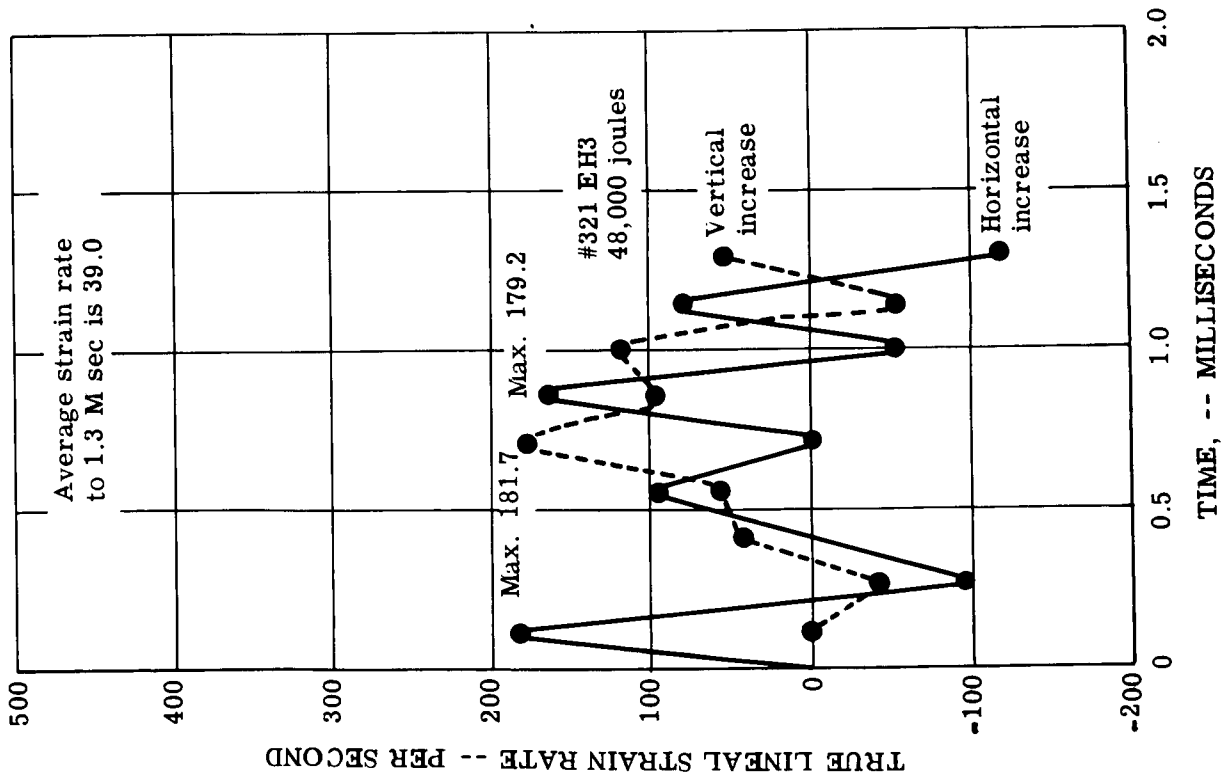
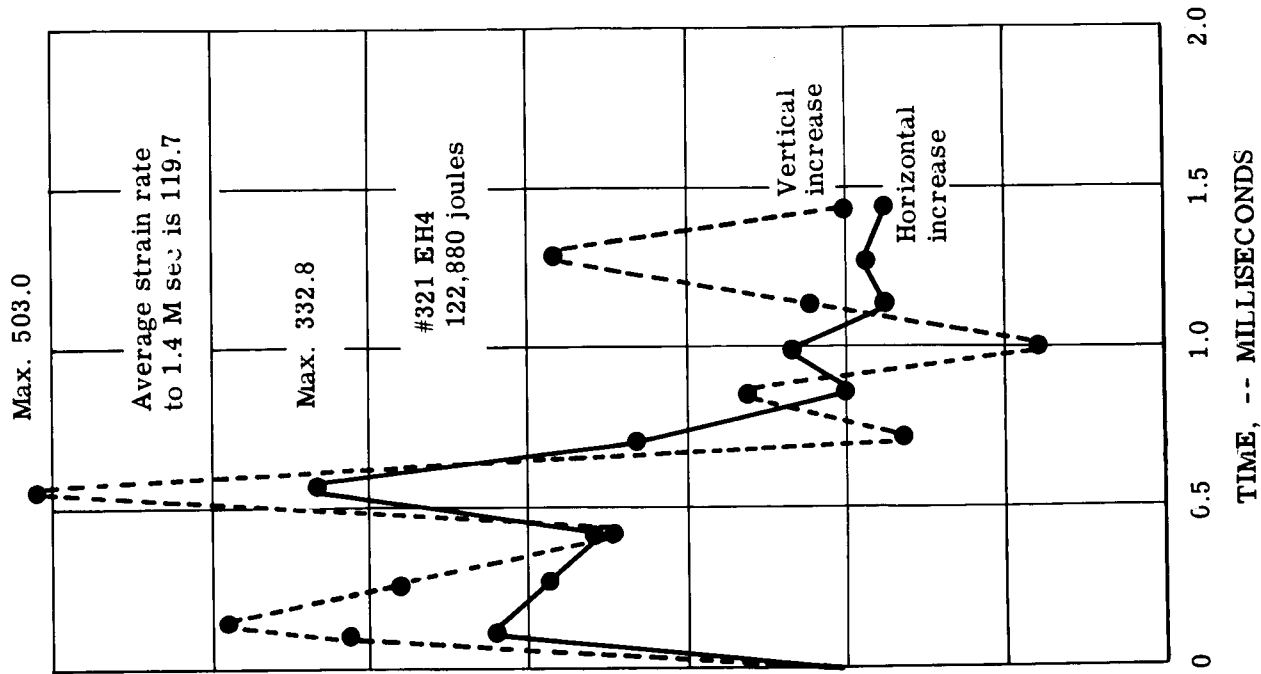
Figure 11 True Lineal Strain Rate of .5" x .5" Center Square for .092", 2014-0 Aluminum



ELECTROHYDRAULIC

Figure 12 Total Lineal Strain and Area Strain of Original .5" x .5" Center Square for .092", 2014-0 Aluminum





ELECTROHYDRAULIC

Figure 13 True Linear Strain Rate of .5" x .5" Center Square for .092", 321 Stainless Steel

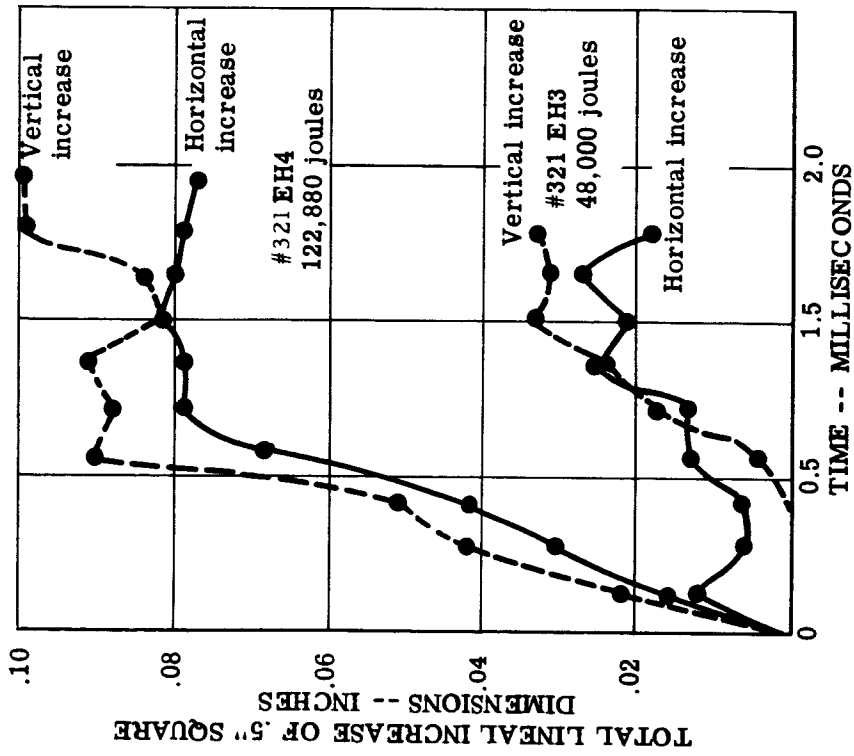
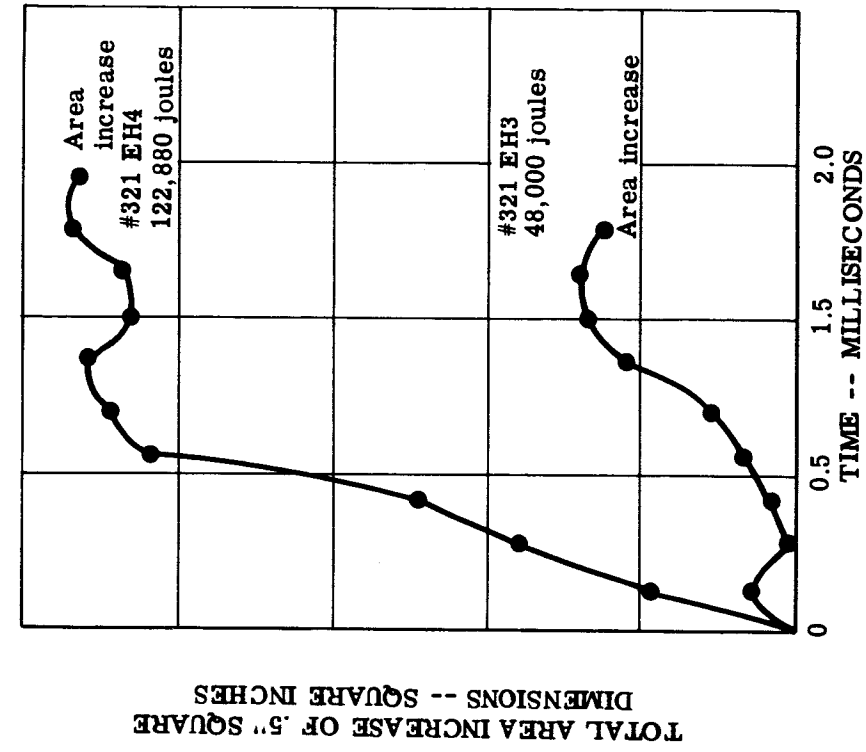
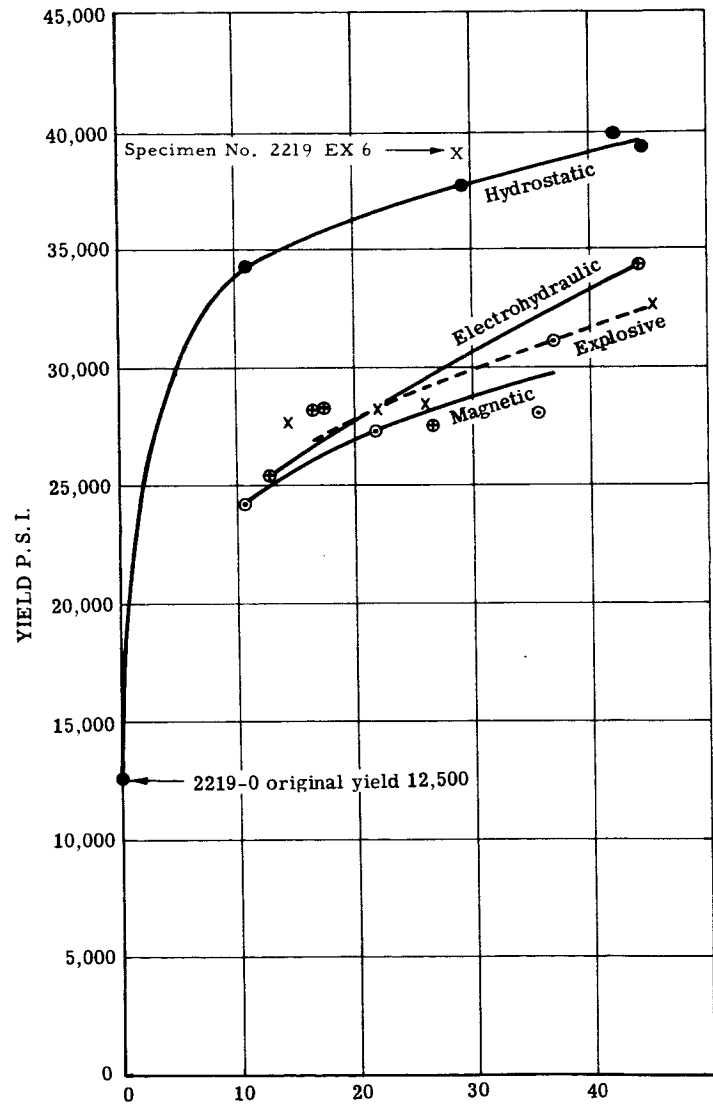
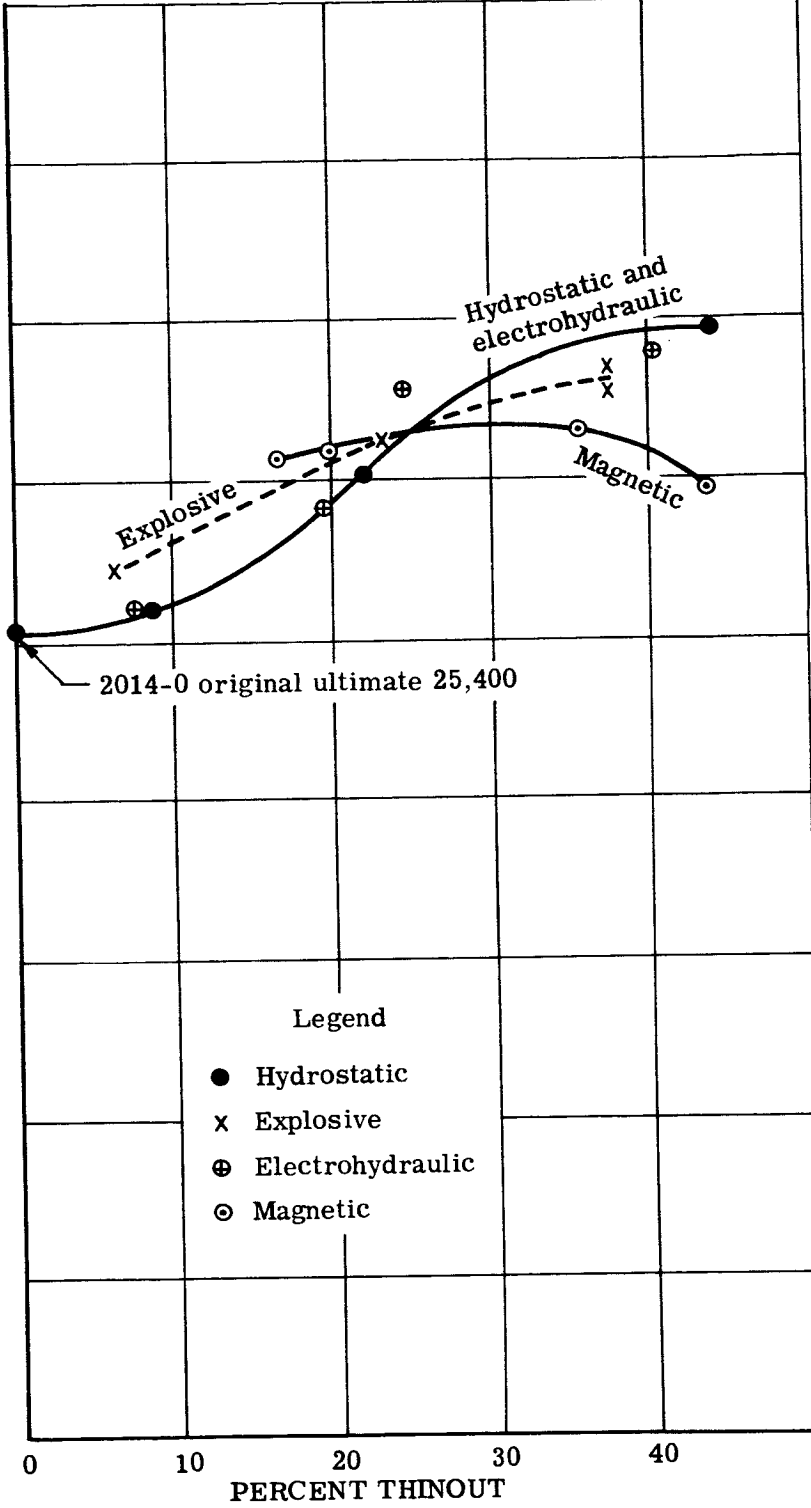


FIGURE 14 TOTAL LINEAL STRAIN AND AREA STRAIN OF .5" x .5" CENTER SQUARE FOR .092", 321 STAINLESS STEEL



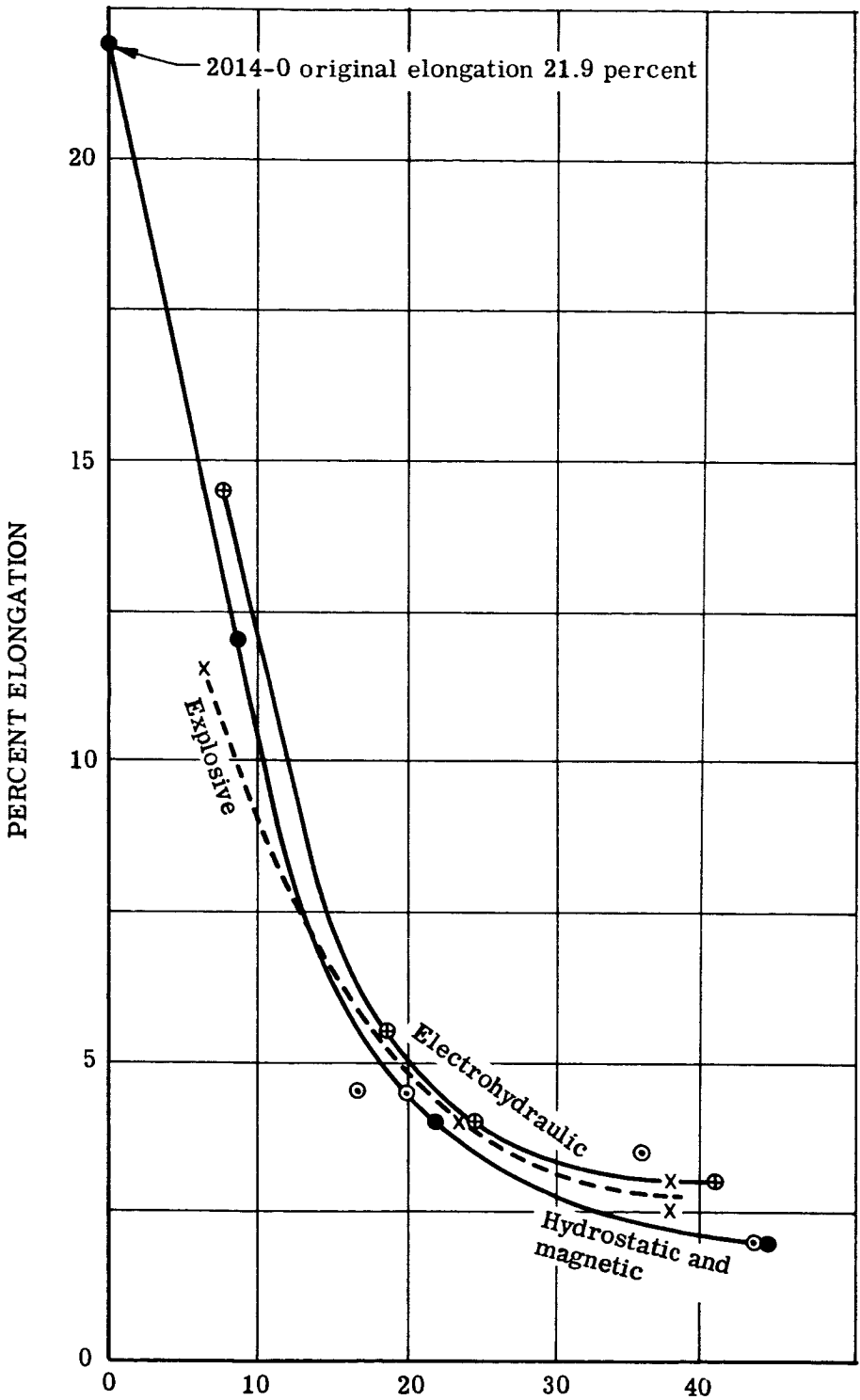
Comparison of mechanical properties and elongation values obtained from 0.092 2219-0 domes at various percentages

ULTIMATE P. S. I.



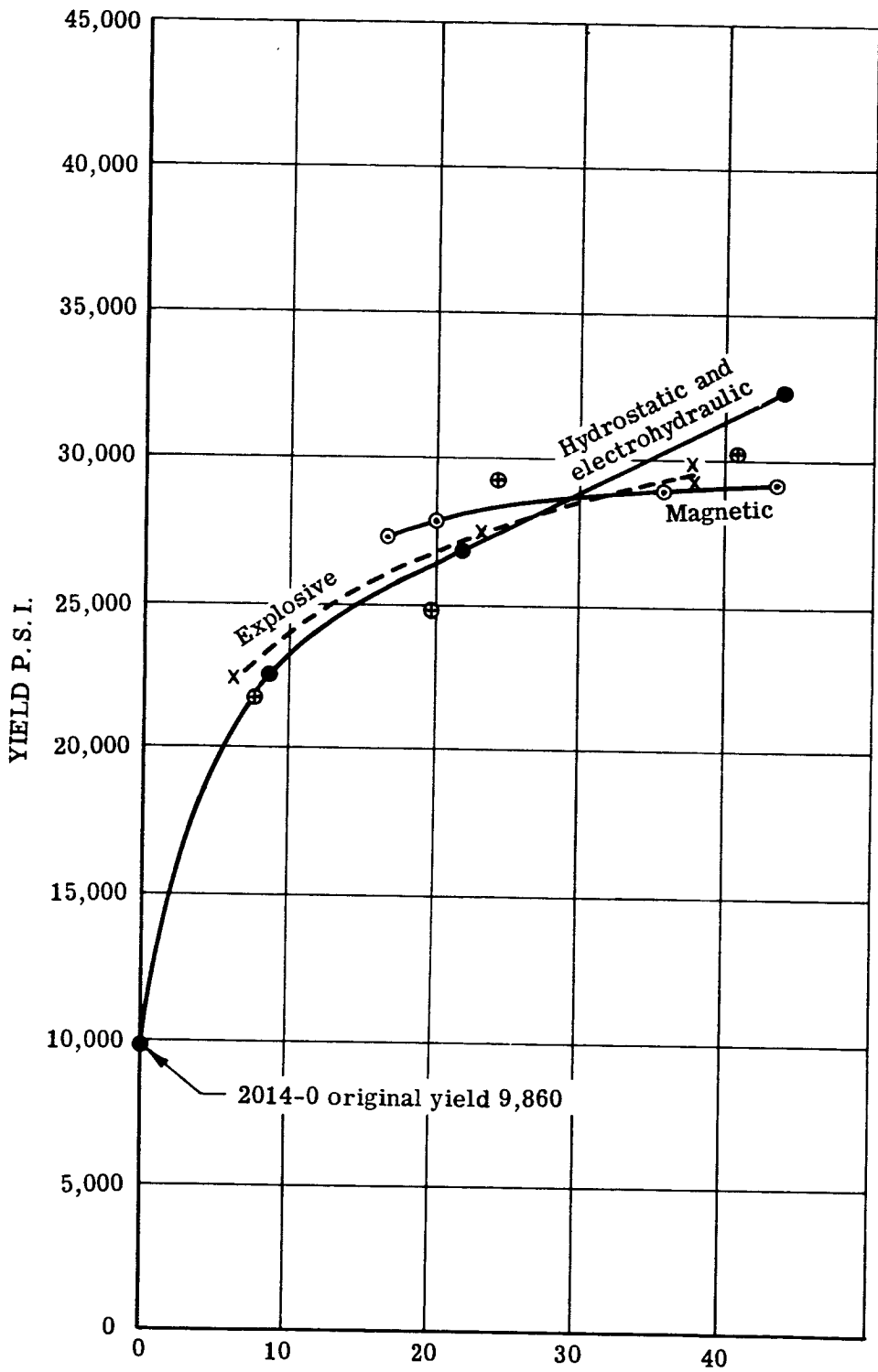
thinout for the hydrostatic, magnetic, explosive and electrohydraulic processes.

FIGURE 16



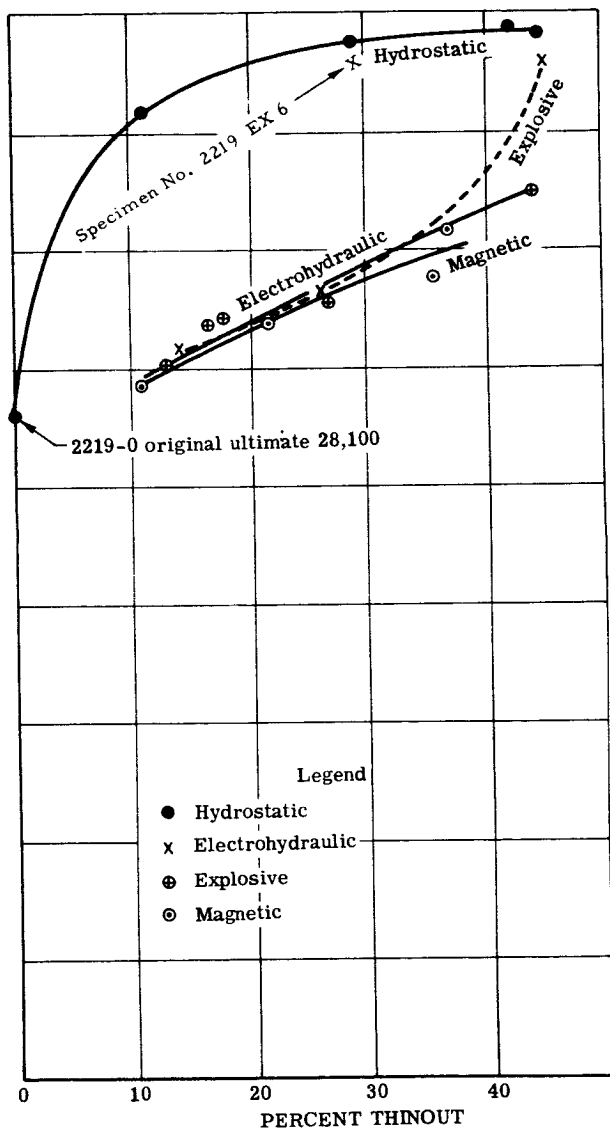
For common forming conditions and recorded data see Tables 4, 8, 10, and 11A. For size, source, and locations of all tensile coupons see figure 23

3



Comparison of mechanical properties and elongation values obtained from 0.092 2014-0 domes at various percentages of

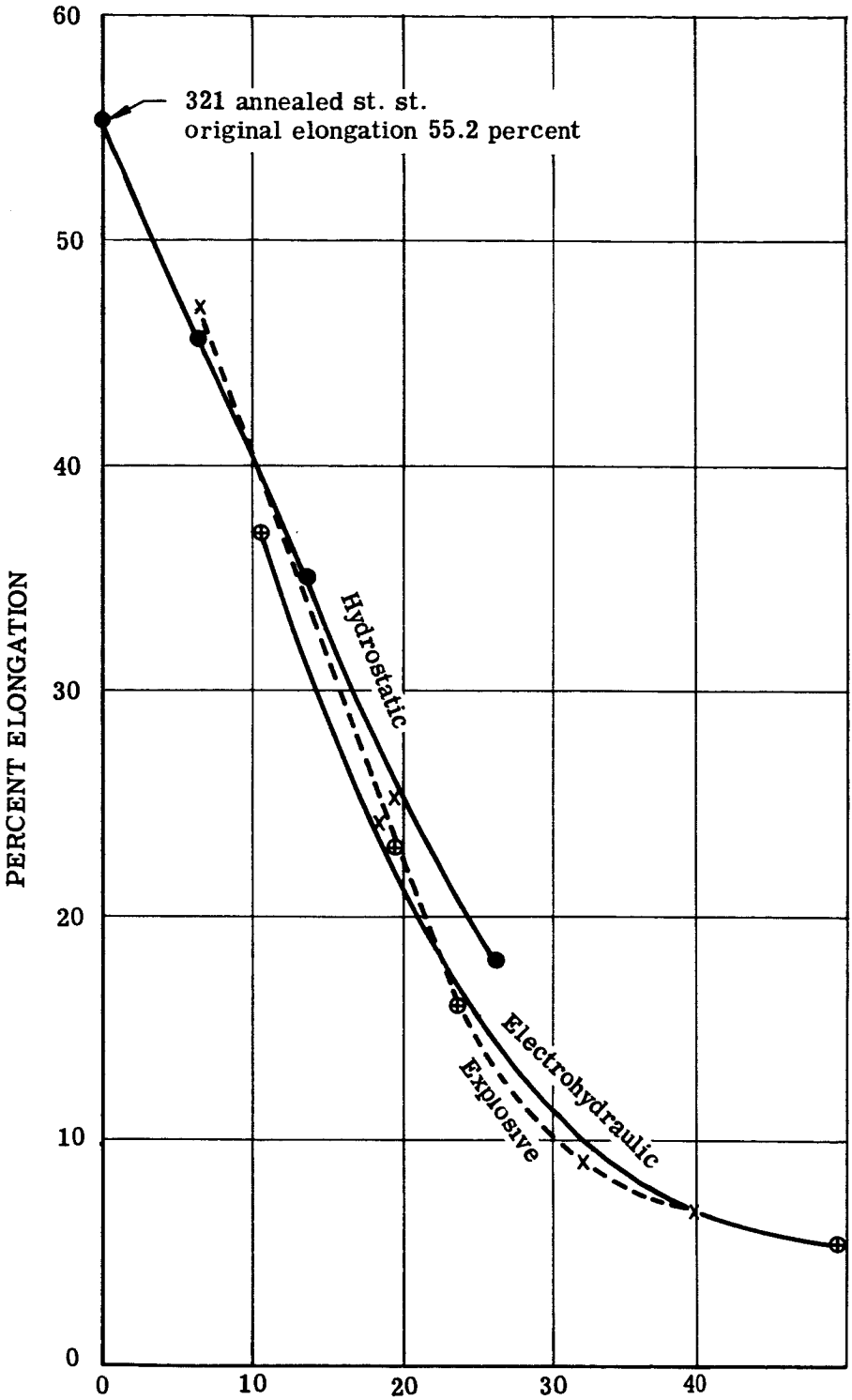
ULTIMATE P. S. I.



of thinout for the hydrostatic, magnetic, explosive, and electrohydraulic processes.

FIGURE 15

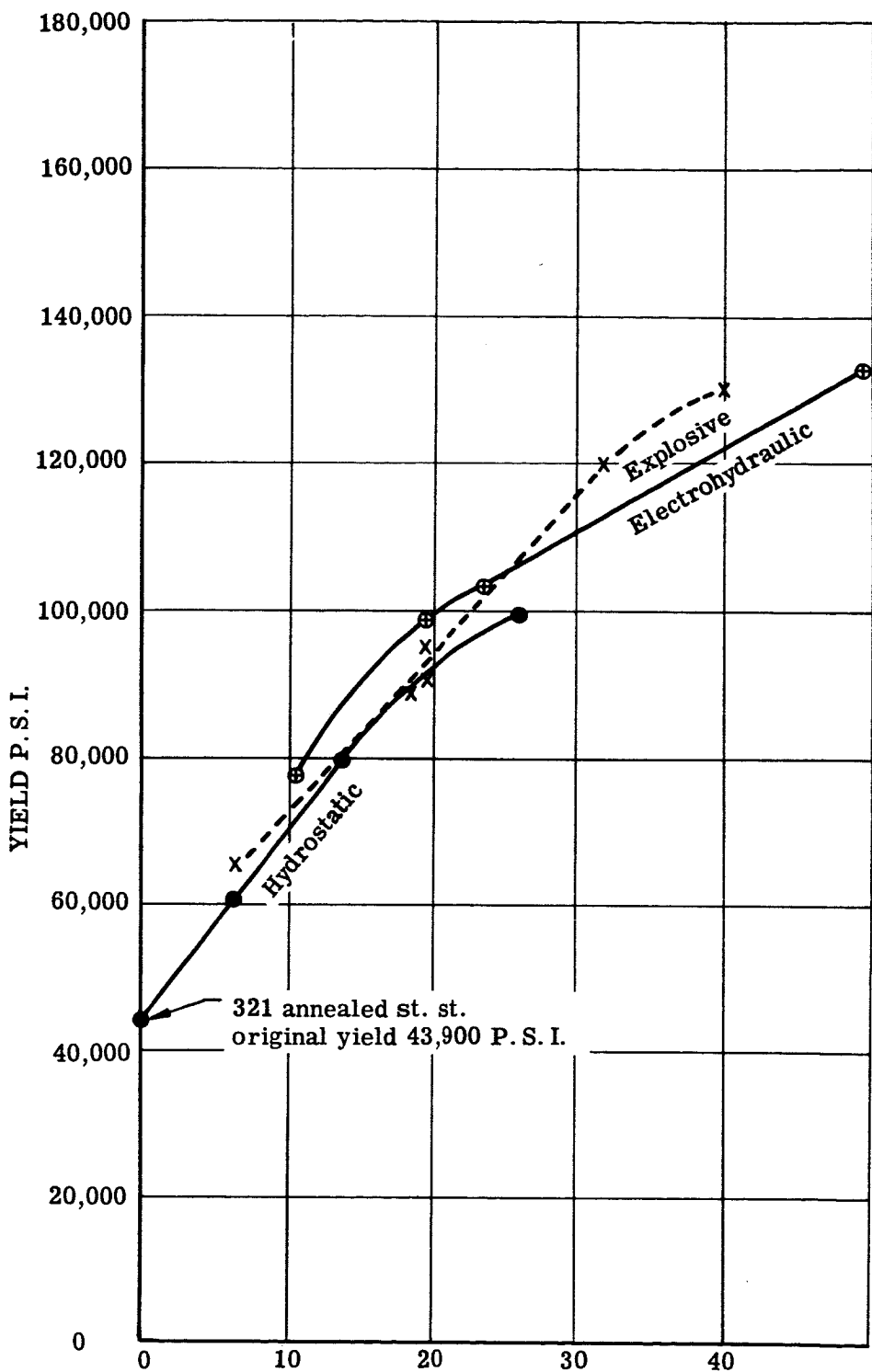




For common forming conditions and recorded data see Tables 4, 8, and 11A. For size, source, and locations of all tensile coupons see figure 23

3

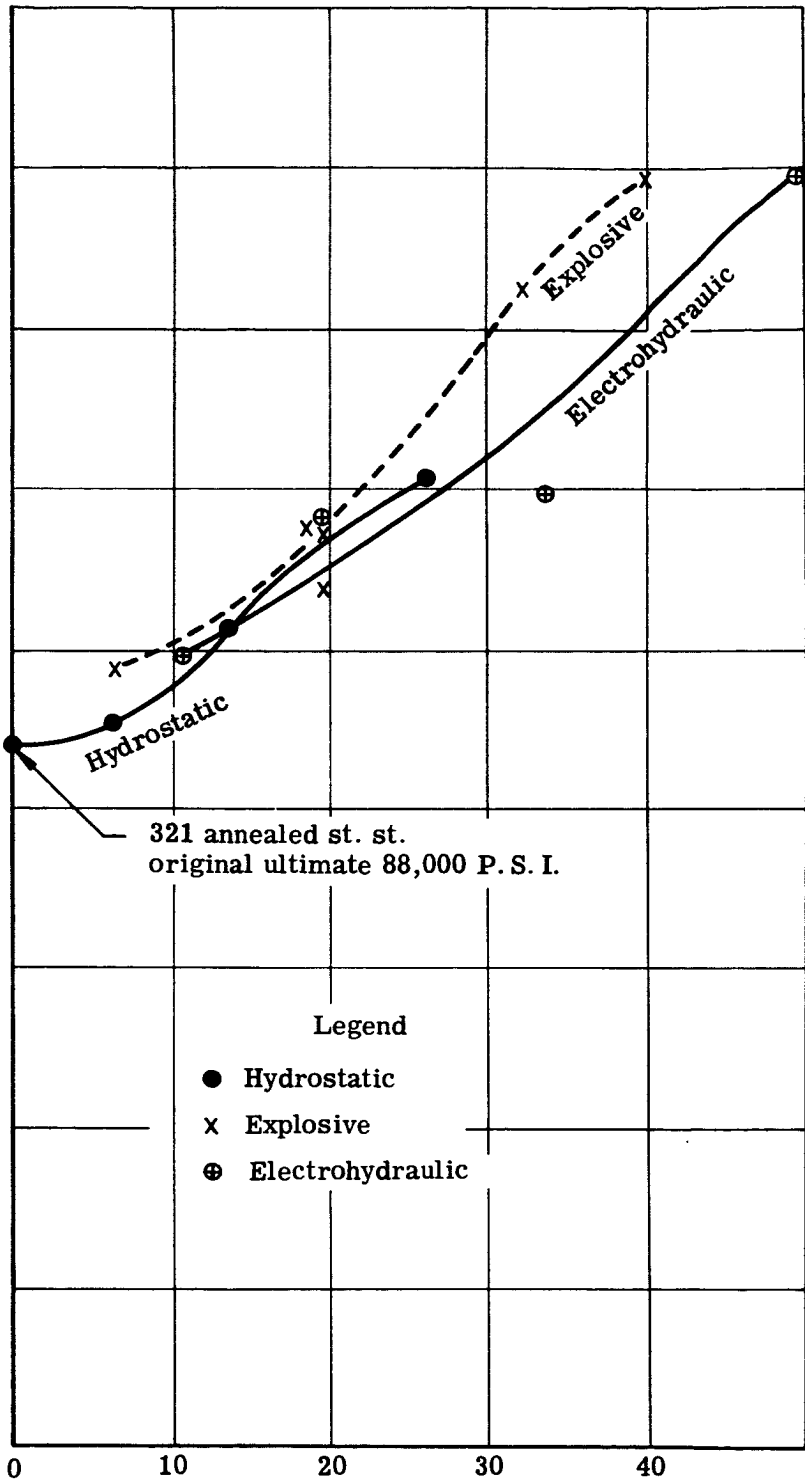




Comparison of mechanical properties and elongation values obtained from 0.092 type 321 annealed stain-

less hydro

ULTIMATE P. S. I.



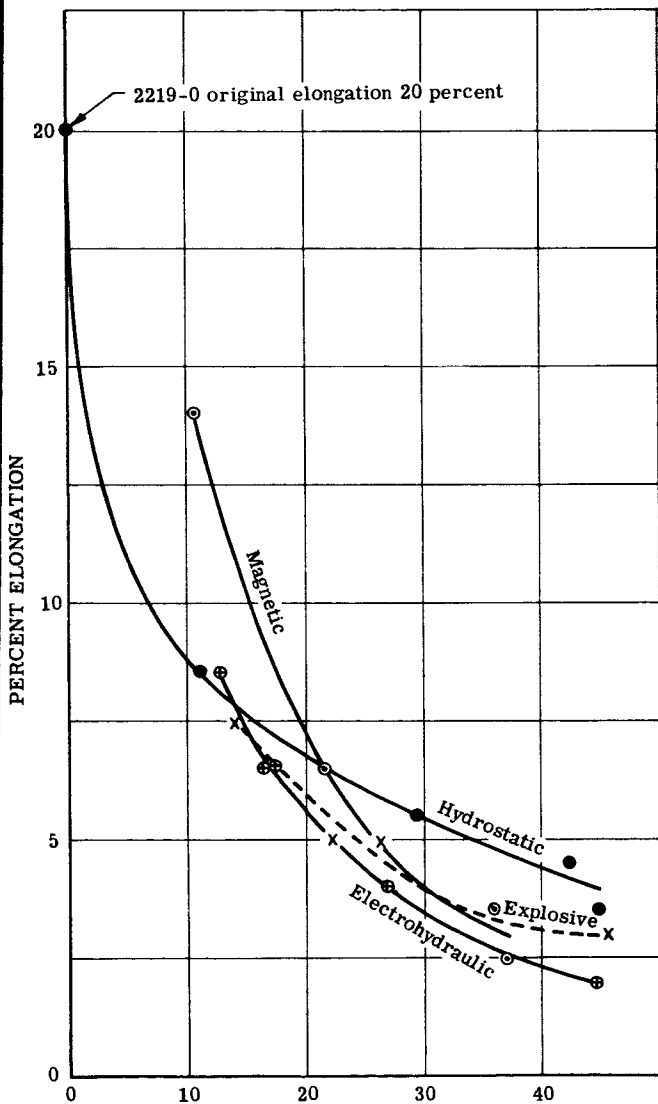
321 annealed st. st.  
original ultimate 88,000 P. S. I.

Legend

- Hydrostatic
- x Explosive
- ⊕ Electrohydraulic

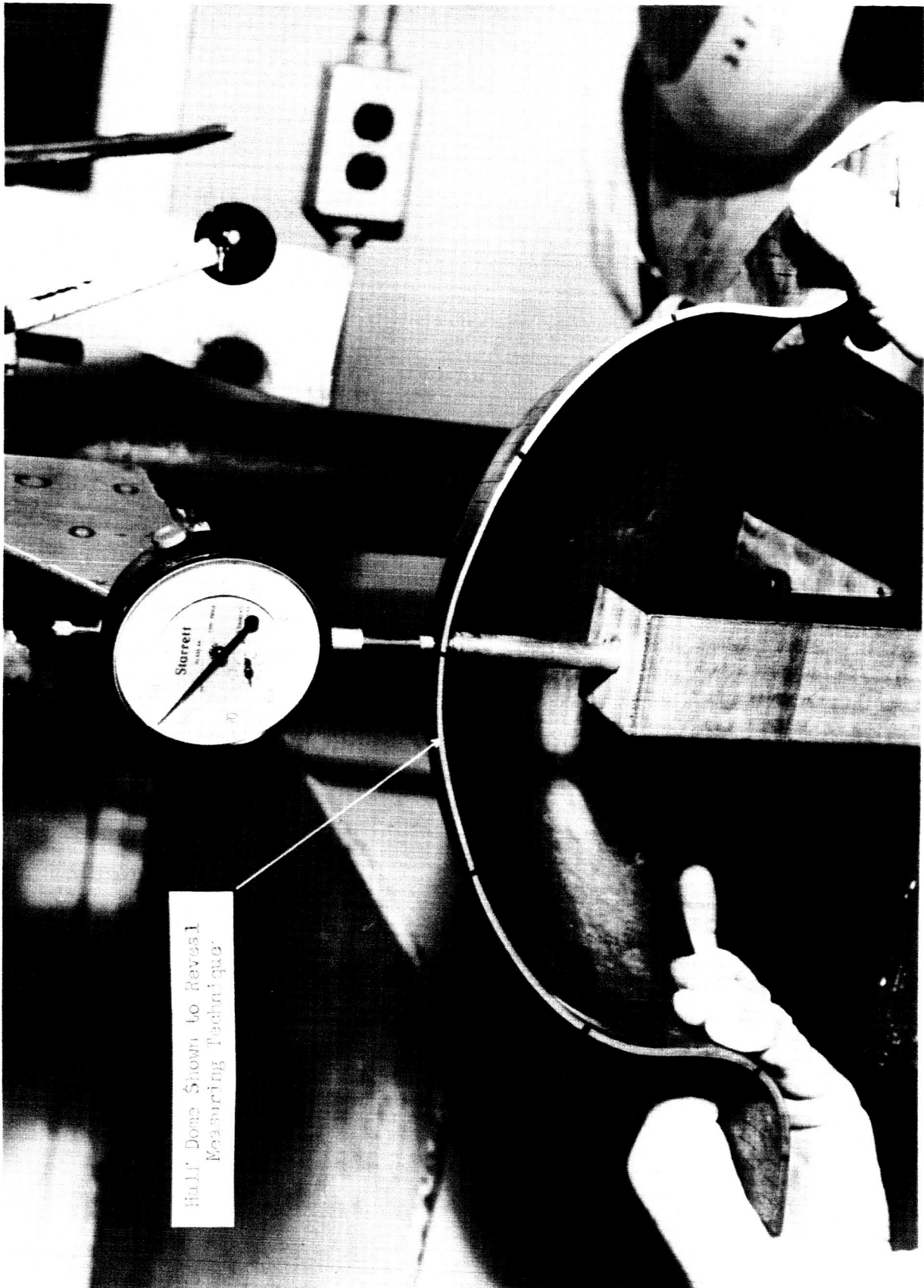
domes at various percentages of thinout for the hydrostatic, explosive, and electrohydraulic processes.

FIGURE 17



For common forming conditions and recorded data see Tables 4, 8, 10, and 11A. For size, source and locations of all tensile coupons see figure 23

3



METHOD USED TO MEASURE GAUGE REDUCTION OF DOME SHAPED PARTS FORMED BY THE ELECTROHYDRAULIC, EXPLOSIVE, MAGNETIC AND HYDROSTATIC FORMING PROCESSES.

FIGURE 18

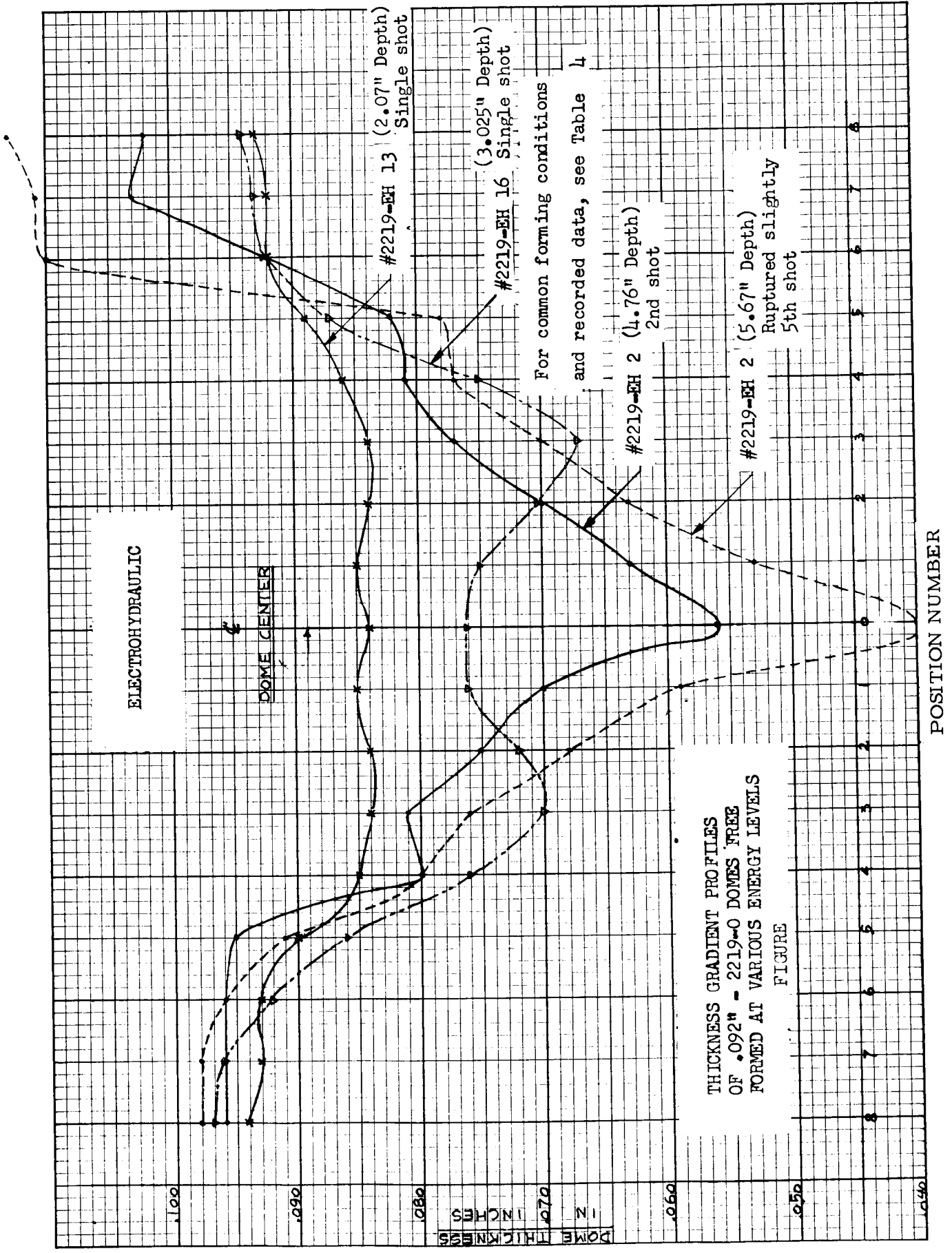


FIGURE 19

For common forming conditions and recorded data, see Table 8

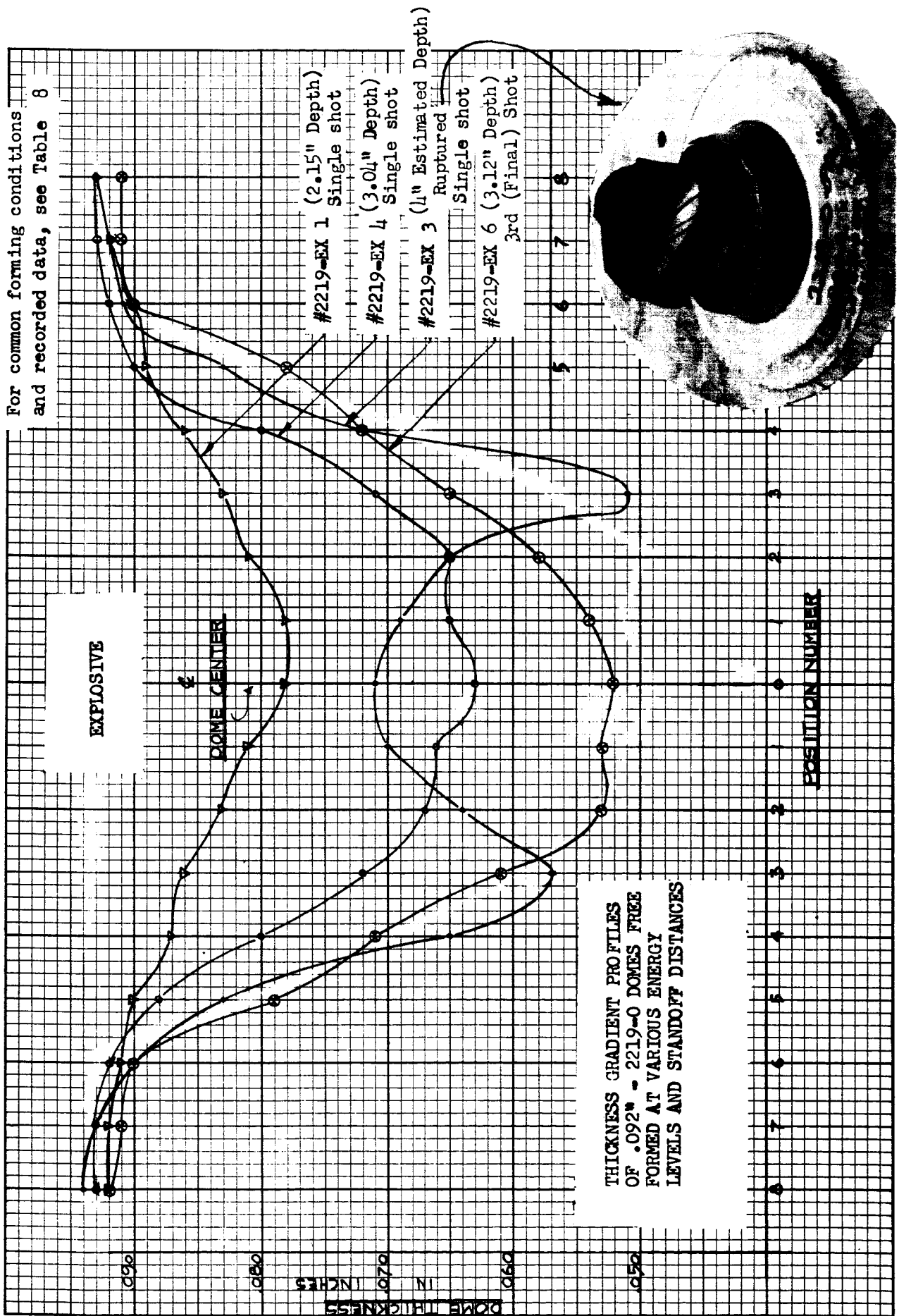


FIGURE 20

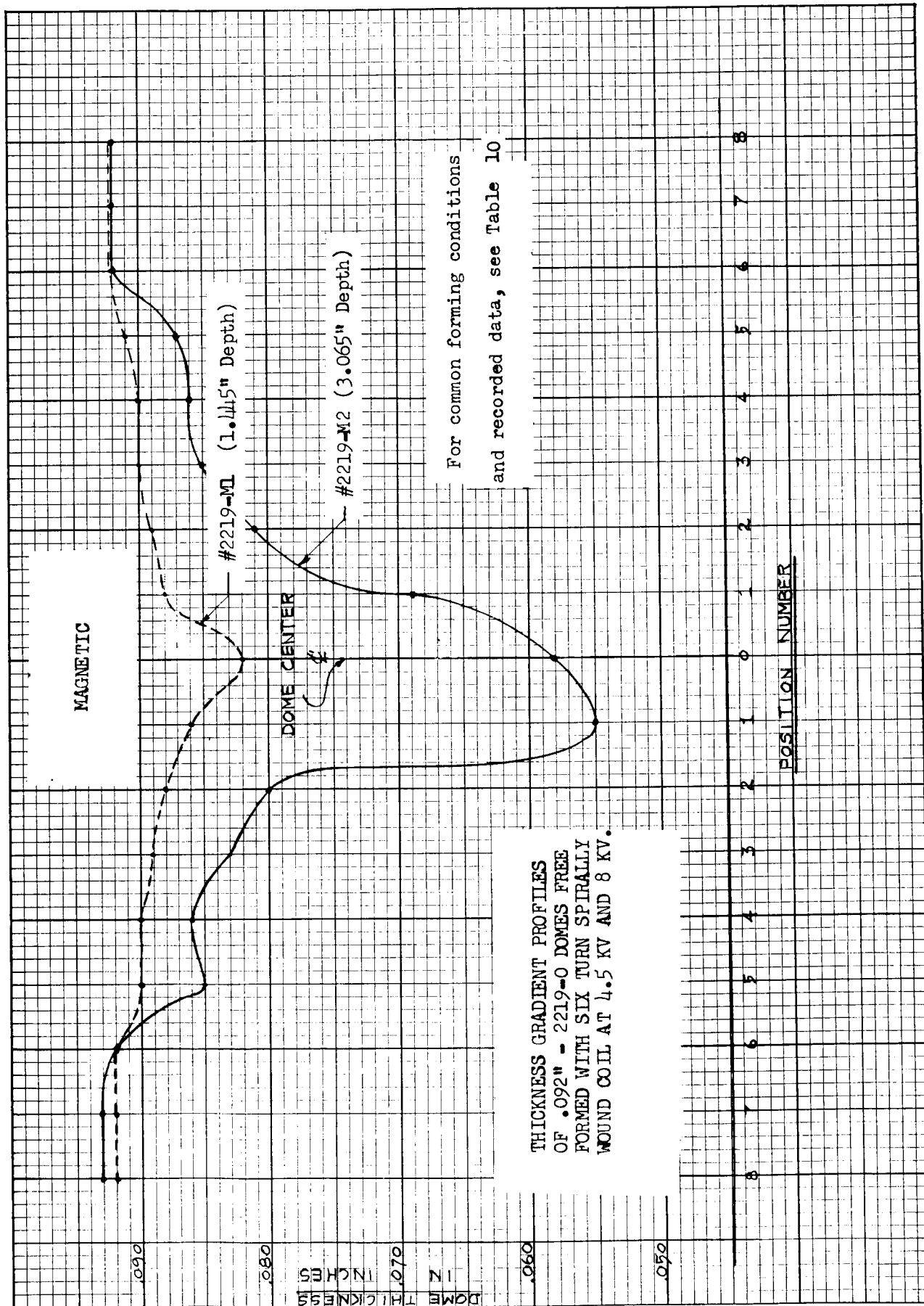


FIGURE 21

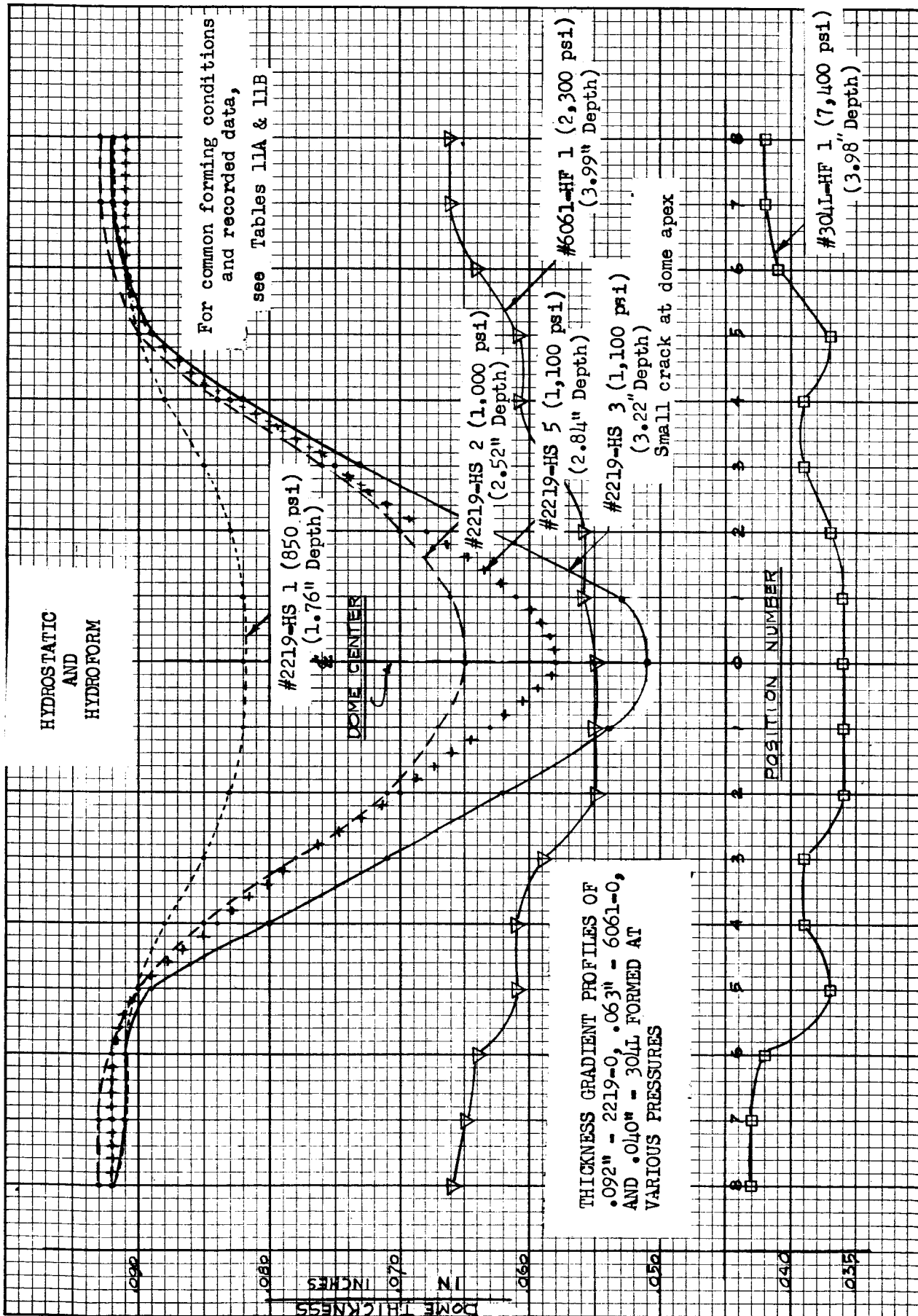
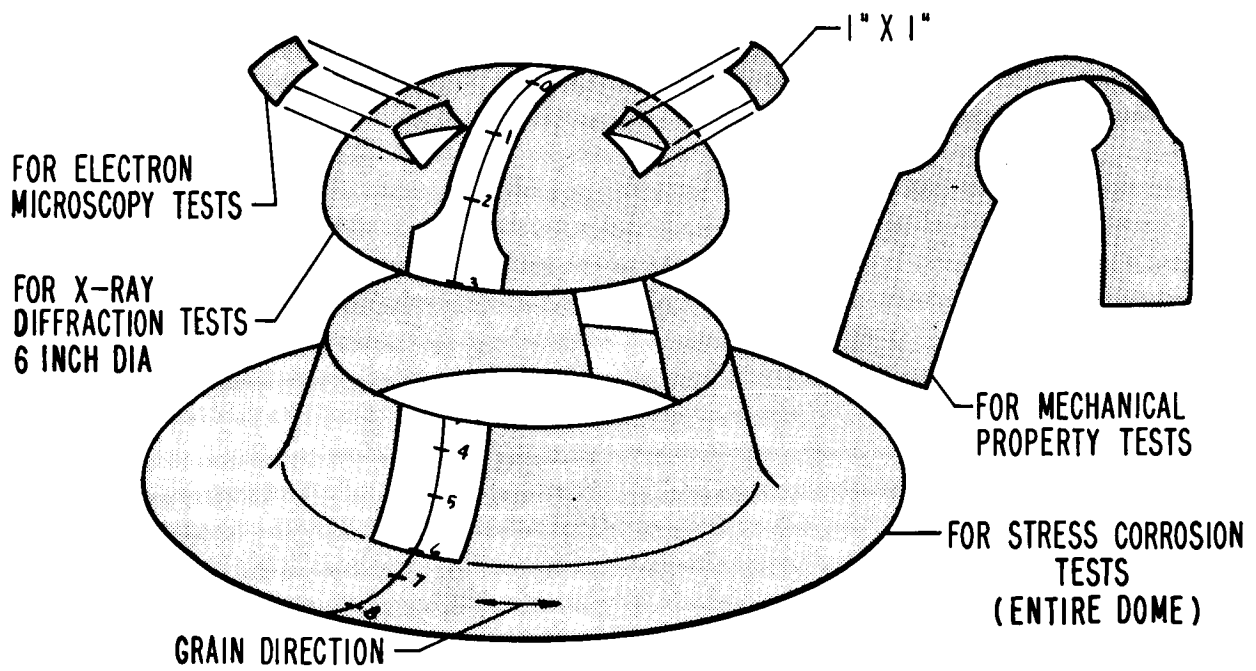


FIGURE 22





Electrohydraulically, Explosively, and Hydrostatically Formed

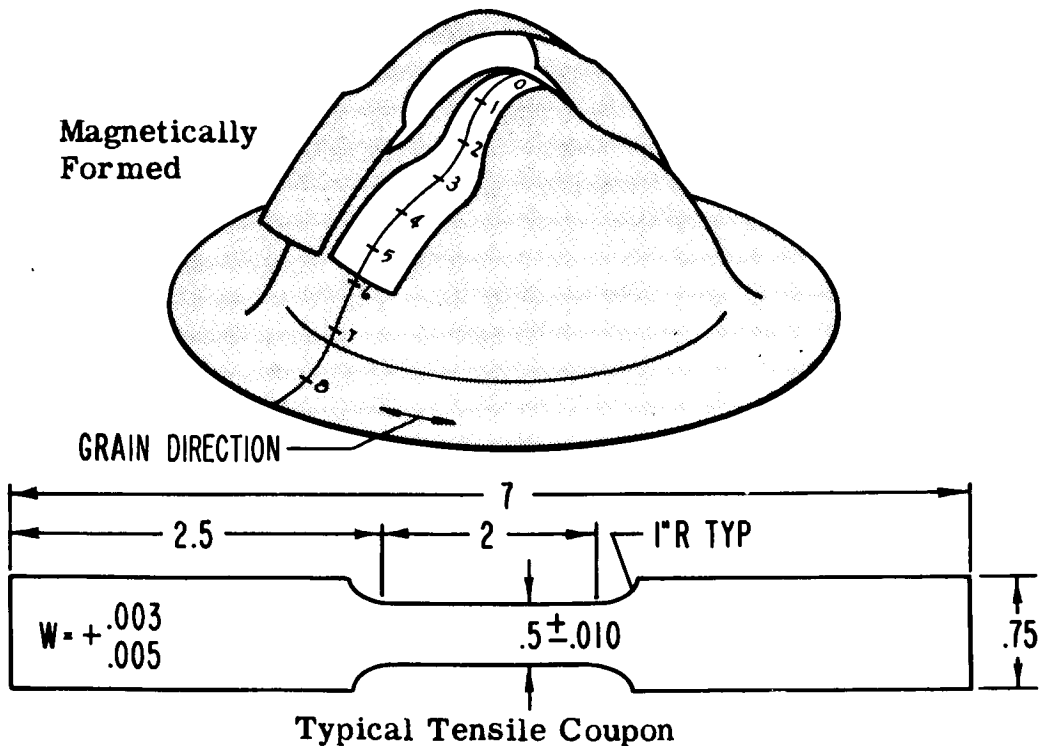
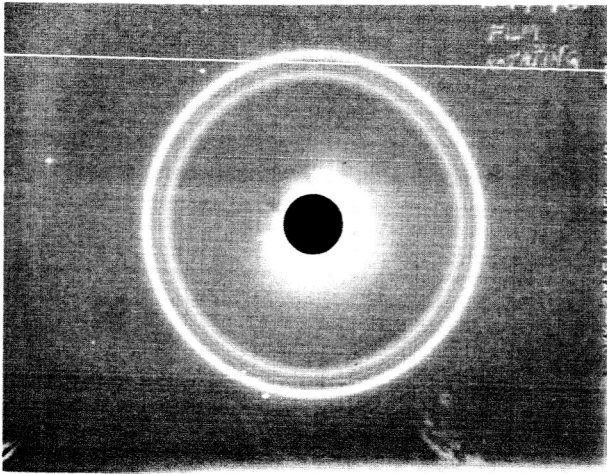
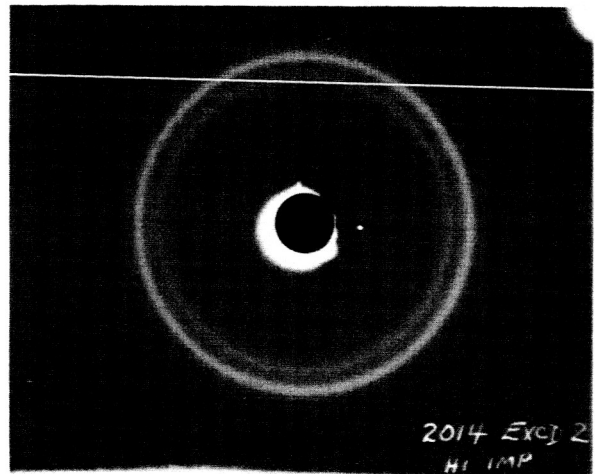


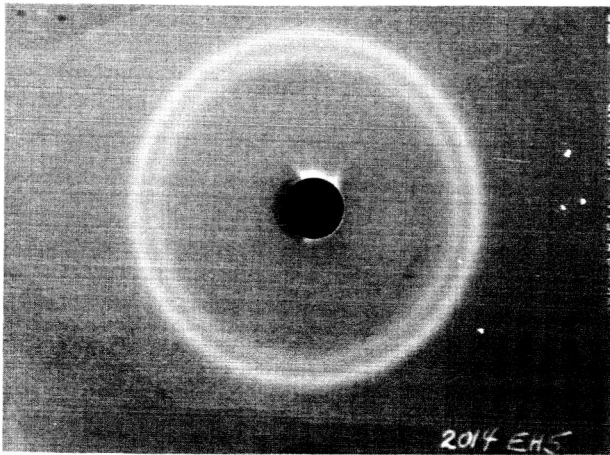
Figure 23 Size, Source and Location of all Specimens Obtained from Domes. Formed by the Electrohydraulic, Explosive, Hydrostatic, and Magnetic Forming Process



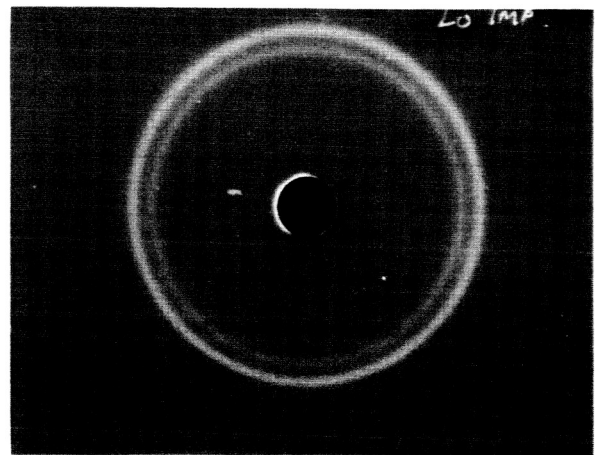
A. Annealed Parent Stock



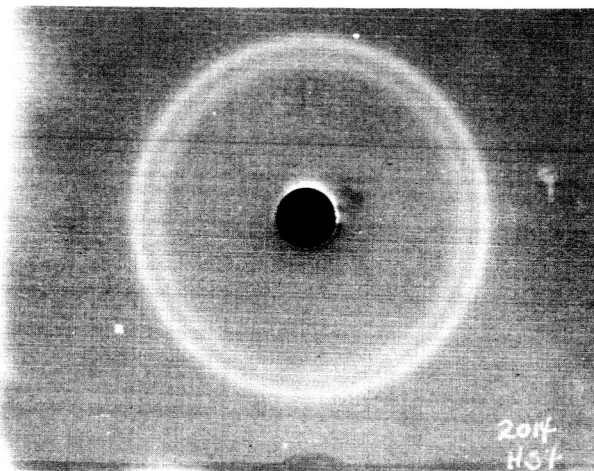
B. Explosively formed to 50% thinout with high die impact.



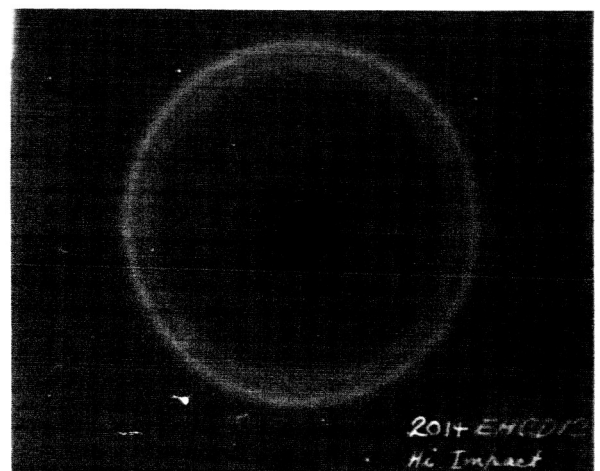
C. Electrohydraulically free formed to 16.1% thinout



D. Explosively formed to 27.8% thinout with low die impact.



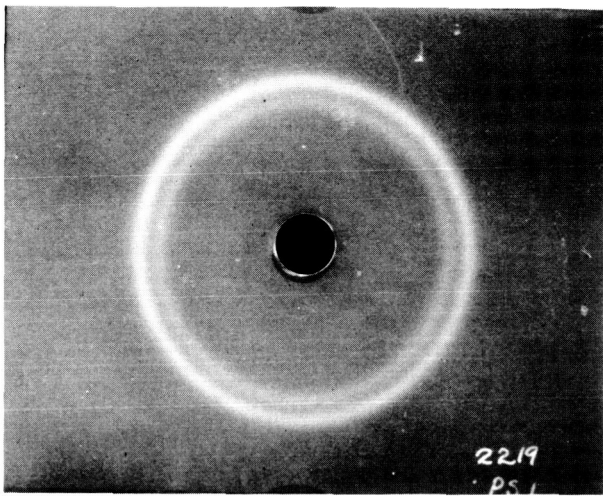
E. Hydrostatically formed to 41.7% thinout



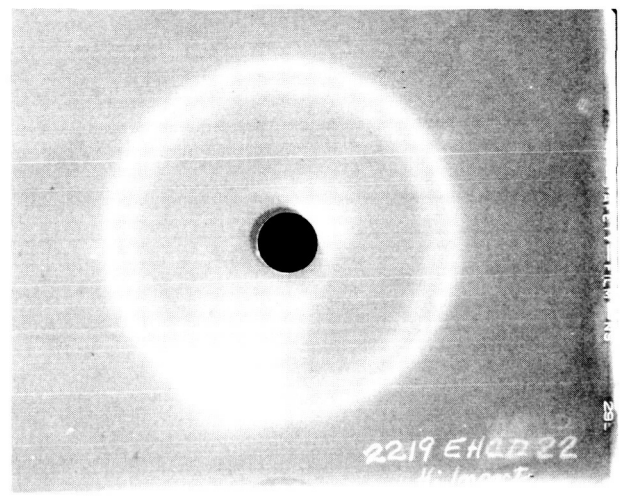
F. Electrohydraulically formed to 36.7% thinout with high die impact.

2014 ALUMINUM ALLOY DIFFRACTION PATTERNS

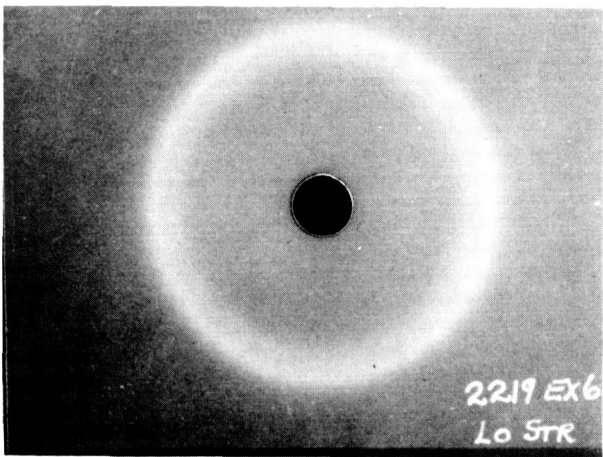
FIGURE 24



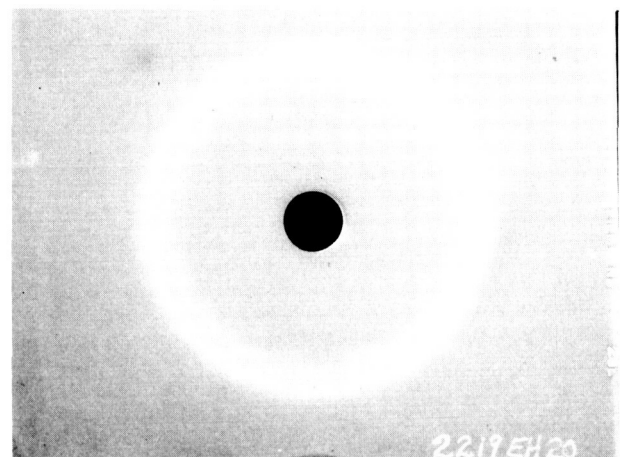
A. Annealed Parent Stock



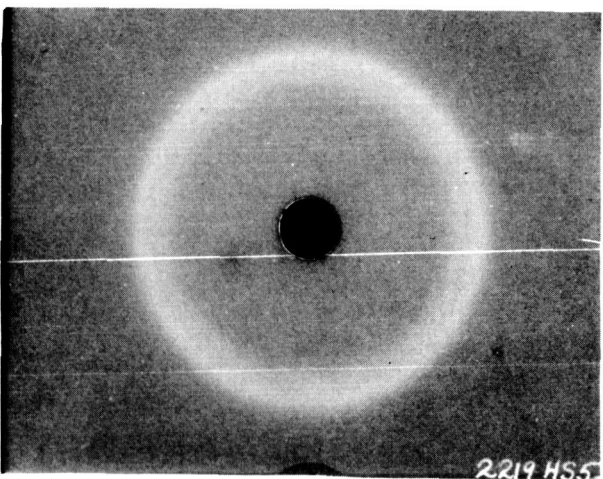
B. Electrohydraulically formed to 29.4% thinout with high die impact.



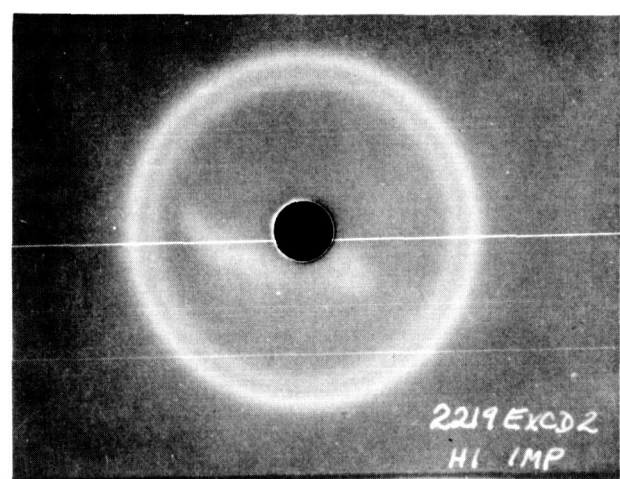
C. Explosively free formed to 29.4% thinout.



D. Electrohydraulically free formed to 21.7% thinout



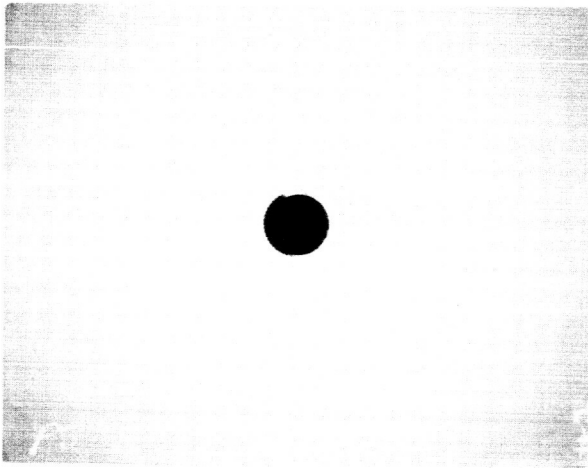
E. Hydrostatically formed to 37% thinout



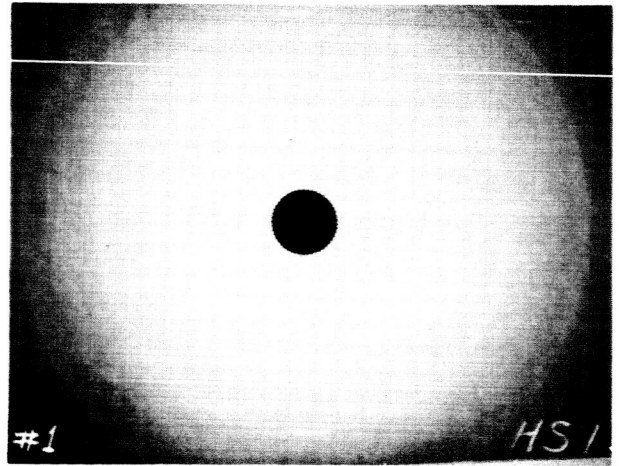
F. Explosively formed to 47.3% thinout with high die impact.

2219 ALUMINUM ALLOY DIFFRACTION PATTERNS

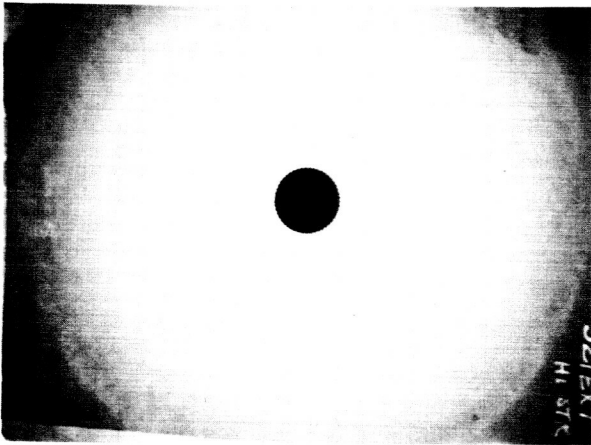
FIGURE 25



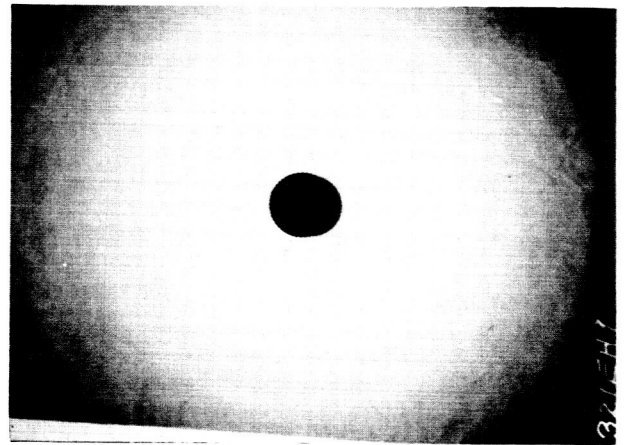
A. Annealed Parent Stock



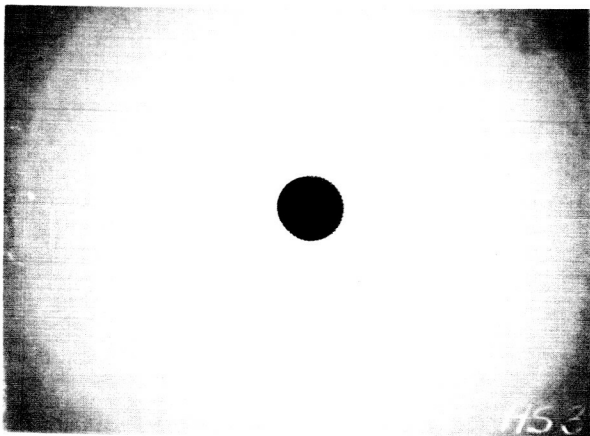
B. Hydrostatically formed to 6.4% thinout



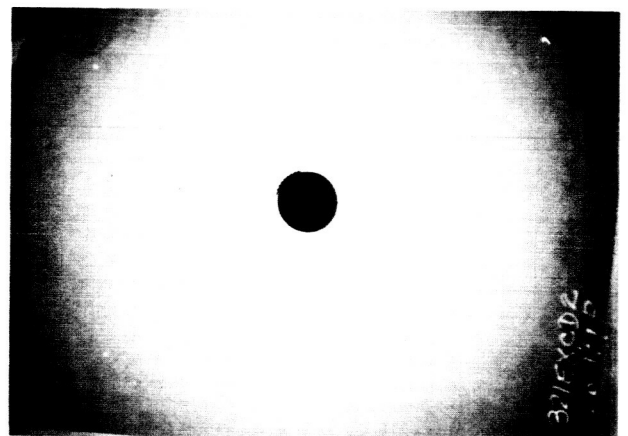
C. Explosively free formed to 17.2% thinout



D. Electrohydraulically free formed to 20% thinout



F. Explosively formed to 28% thinout with low die impact.



E. Hydrostatically free formed to 26.1% thinout

321 STAINLESS STEEL DIFFRACTION PATTERNS

FIGURE 26



321 STAINLESS STEEL DOME SECTION FORMED TO  
48% THINOUT BY THE ELECTROHYDRAULIC PROCESS  
(HARDNESS: ROCKWELL 15T94)

Etchant: Gamma

Mag. 750x



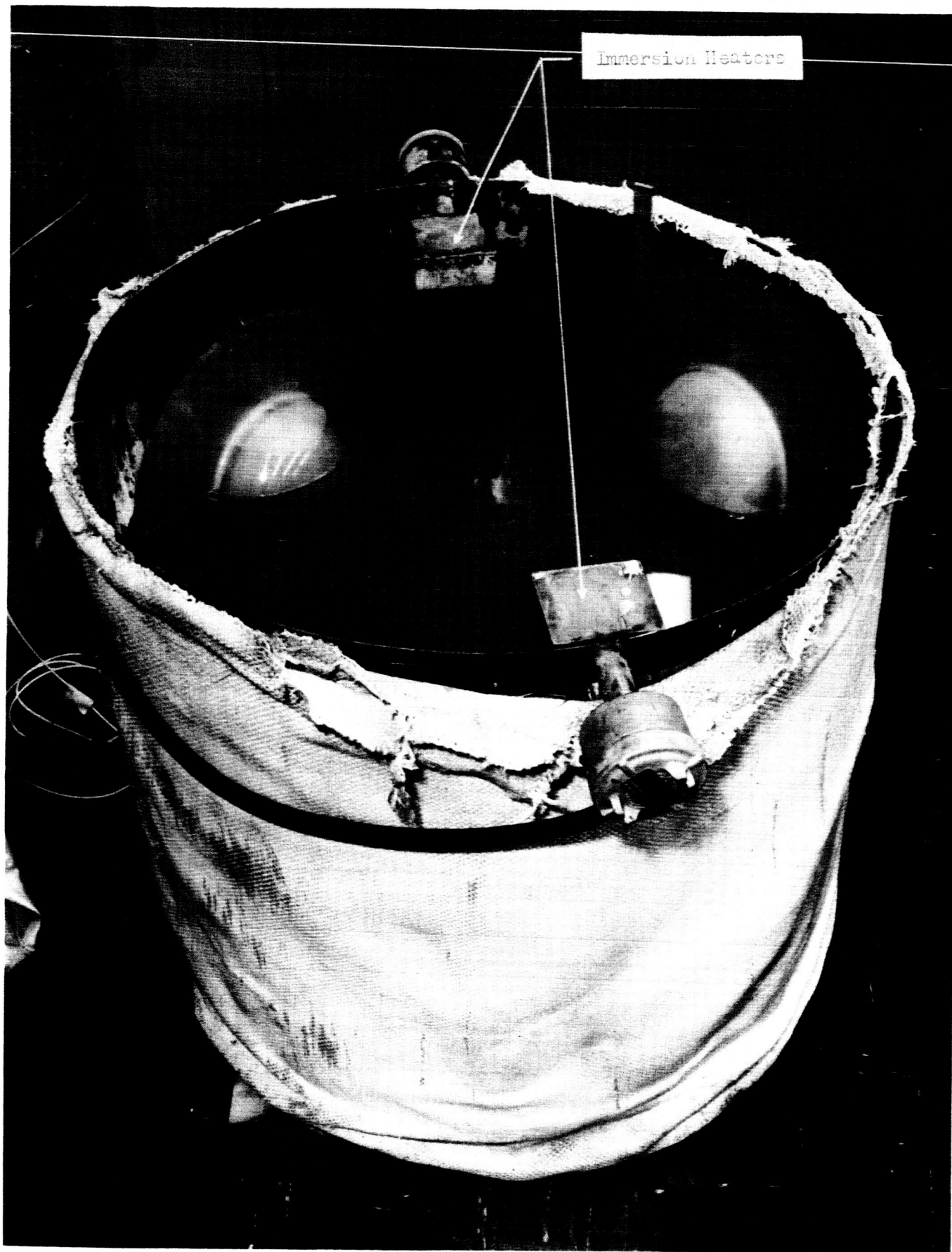
.092", 321 STAINLESS STEEL SECTION BEFORE  
FORMING (HARDNESS: ROCKWELL 15T84)

Etchant: Gamma

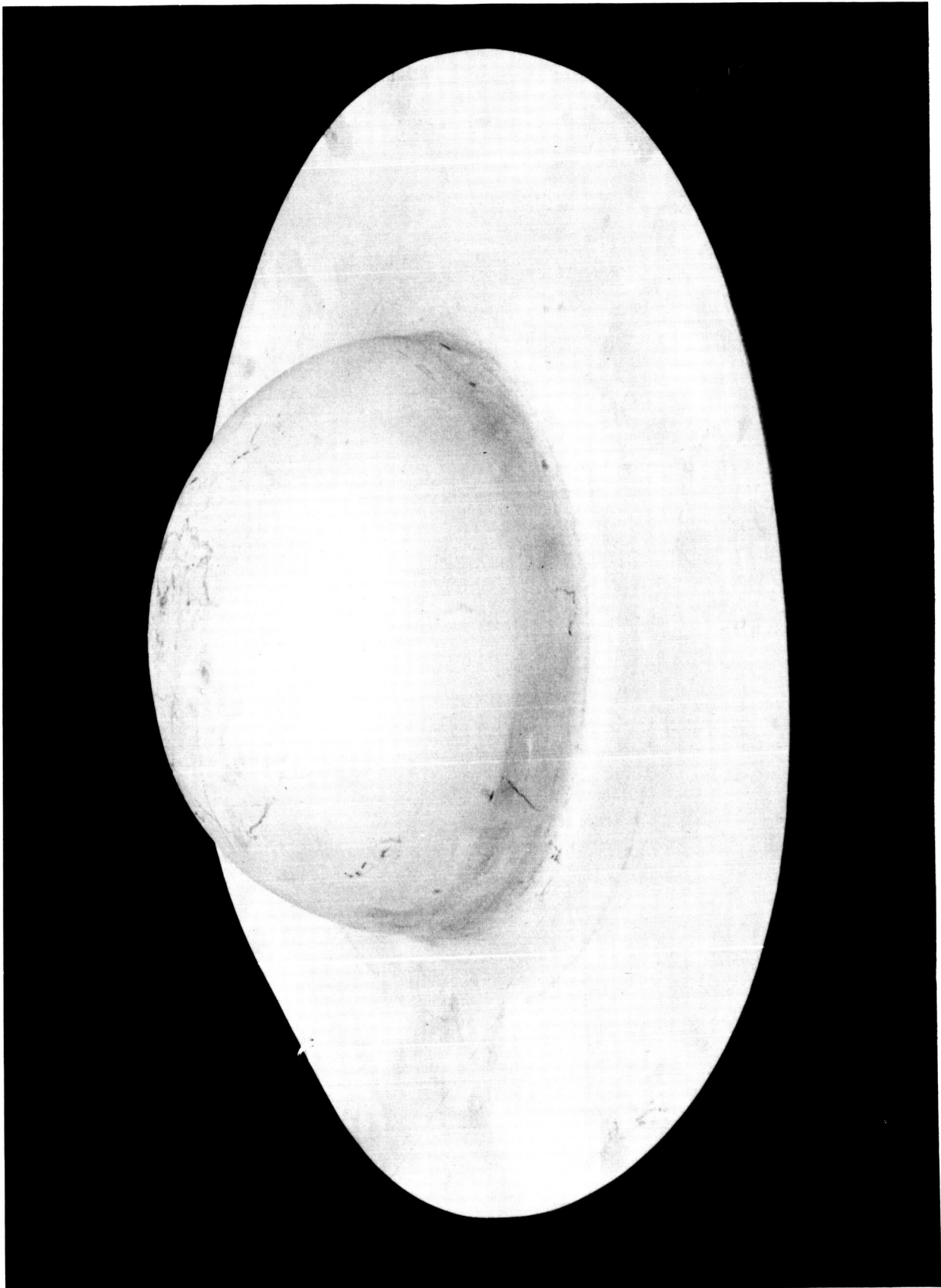
Mag. 750x

FIGURE 27





80 GALLON TANK USED FOR STRESS CORROSION TESTING OF .092" - 321  
STAINLESS DOMES IN A BOILING 25% MAGNESIUM CHLORIDE SOLUTION



TYPICAL 321 STAINLESS STEEL DOME AFTER 288 HOURS OF CONTINUOUS EXPOSURE IN A BOILING (217°F) AQUEOUS MAGNESIUM CHLORIDE SOLUTION

FIGURE 29



View Looking Into Closed Tank Containing Axial Electrodes of 4" Gap And Kistler #617 Gage Housed In Adapter Assembly

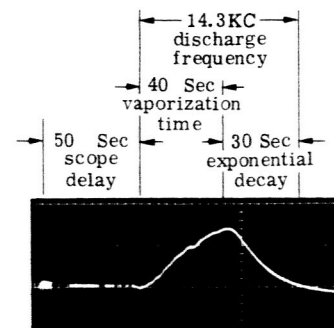
**D**

DISCHARGE CONDITIC

4" Gap, axial electrode  
.096" dia. mag. initiating

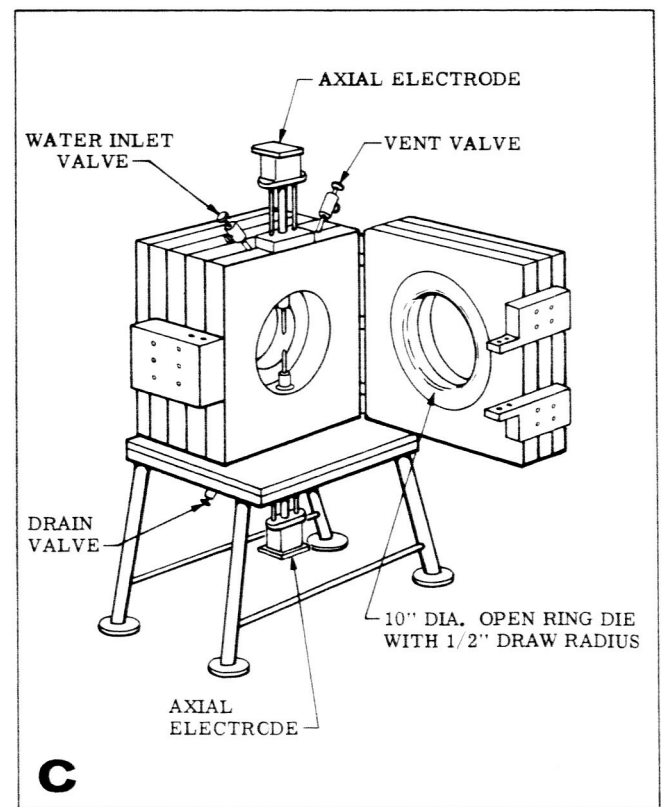
Time - 20 Sec/cm

65,000 Amps Peak Curr  
10KV (48,000 joules)  
Sensitivity - 1V/cm



**E**

Typical single current pulse of the initiating wire diameter is large enough to provide vapor during the 1/2 cycle thereby avoid oscillations after vaporiza



**C**

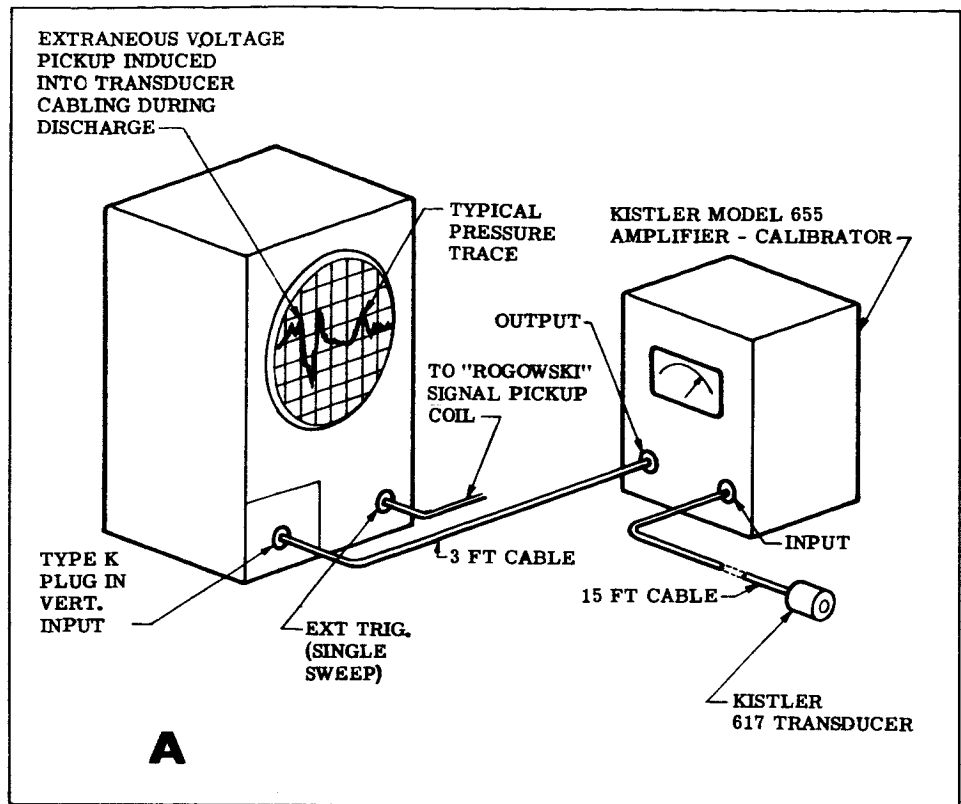
Closed Tank Used For All Electrohydraulic Experiments



NS  
s  
wire

ent

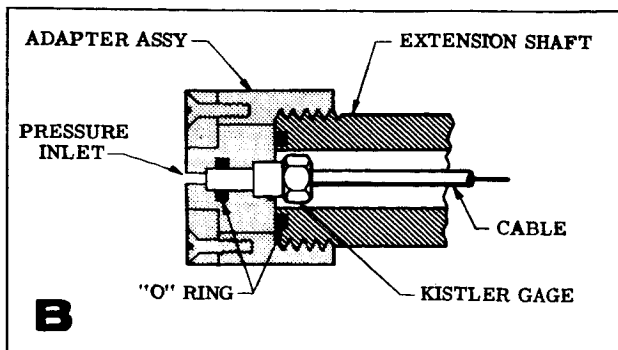
tained when  
selected to  
rization  
oiding cur-  
tion.



Instrumentation Used For All Pressure Measurements

COMMON CONDITIONS

- 960 mfd capacitor bank.
- Closed tank containing axial inline electrodes of 4" gap.
- .096" dia. magnesium initiating wire except for traces 22 and 23.
- 1 1/4" standoff distance.
- Kistler Amplifier-Calibrator, Model 655
- Kistler 617 gage with sensitivity of 0.0557 V/1000 psi.
- Type 555 Tektronix oscilloscope with type K preamp plug in.
- Rogowski pickup coil used to provide sweep trigger signal for pressure measurements. Peak current coil sensitivity is 46,500 Amps/Volt.



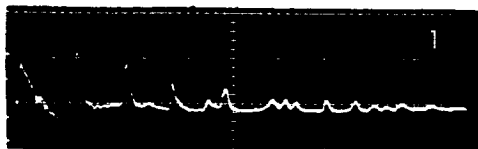
Adapter Housing Assembly For Kistler Model 617 Transducer

INSTRUMENTATION AND TOOLING USED TO OBTAIN ELECTROHYDRAULIC PRESSURE TRACES

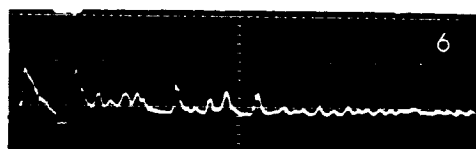
FIGURE 30

2

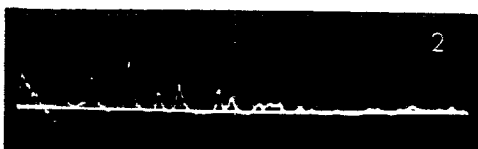
Photos 1-10 5KV - 12,000 Joules



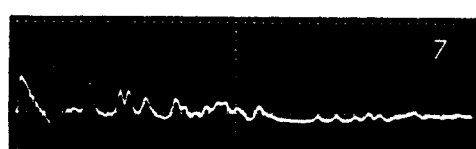
Peak PSI - 10,800 - 2" Gage Distance



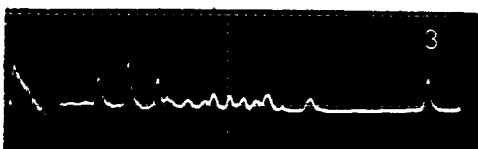
Peak PSI-7,170 2" Gage Distance



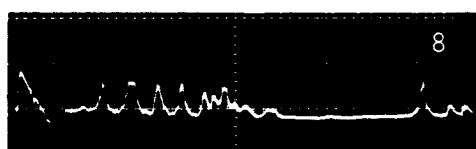
Peak PSI-9,900 4" Gage Distance



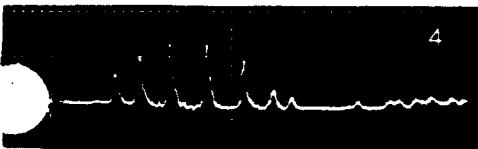
Peak PSI-6,280 4" Gage Distance



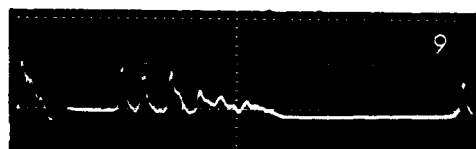
Peak PSI-8,700 6" Gage Distance



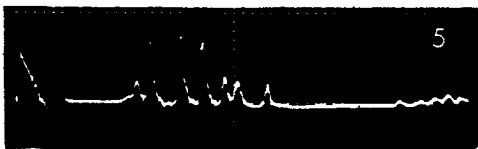
Peak PSI-5,360 6" Gage Distance



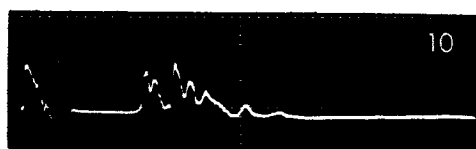
Peak PSI-11,700 8" Gage Distance



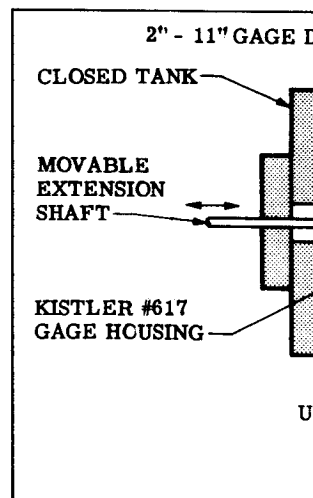
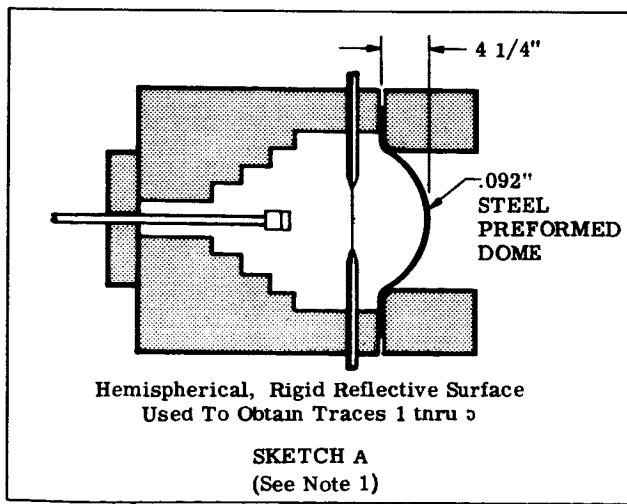
Peak PSI-8,600 8" Gage Distance



Peak PSI-13,500 11" Gage Distance



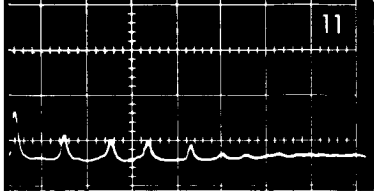
Peak PSI-8,950 11" Gage Distance



SENSITIVITY - 0.5 V/cm (For all traces, except where otherwise noted.) TIME - 100  $\mu$ Sec/cm (All Traces)

Traces 11 - 14 6KV - 17,280 Joules

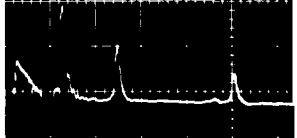
Photos 15, 16, & 20 7 KV - 23,520 Joules



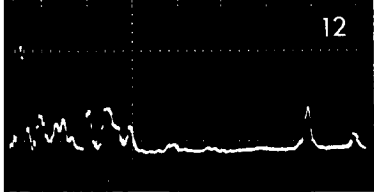
PSI-34,000 2" Gage Distance  
Sensitivity - 1V/cm

(See Trace 20)

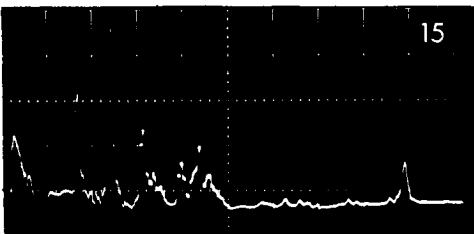
Peak PSI-37,600 2" Gage Distance



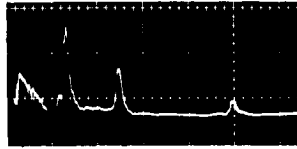
Peak PSI-34,000 Mat'l  
6KV - 17,280 J  
Sensitivity - 1V/cm



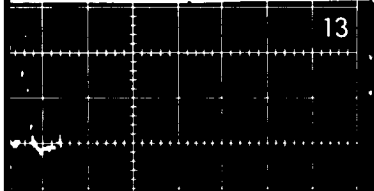
PSI-18,850 5.5" Gage Distance



Peak PSI-32,300 5.5" Gage Distance



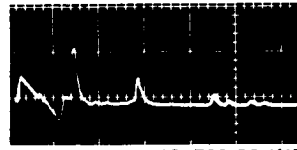
Peak PSI-28,600 Mat'l  
6KV - 17,280 J  
Sensitivity - 1V/cm



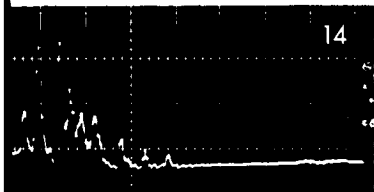
PSI-21,200 8" Gage Distance

(Not measured)

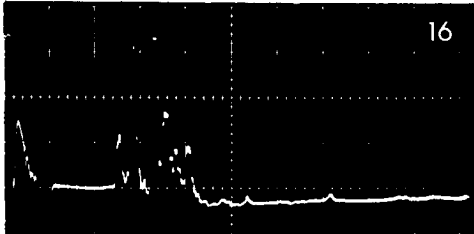
8" Gage Distance



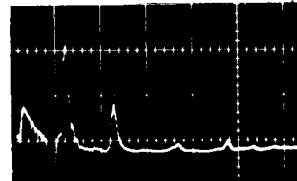
Peak PSI-19,700 Mat'l  
5KV - 12,000 J  
Sensitivity - 1V/cm



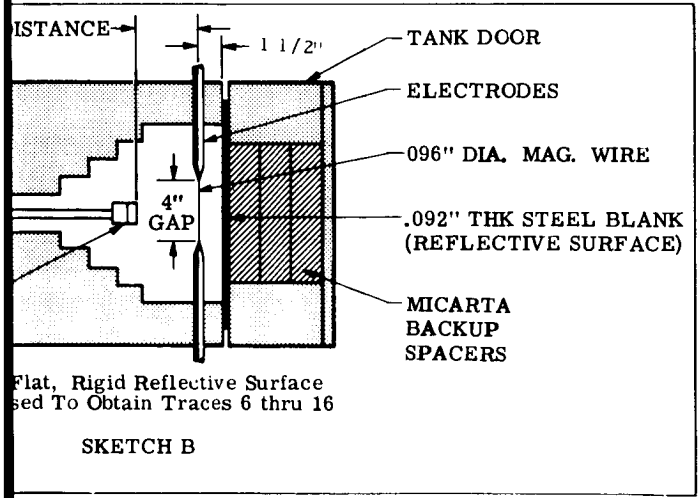
PSI-21,500 11" Gage Distance



Peak PSI-29,600 11" Gage Distance



Peak PSI-37,600 Mat'l  
7 KV - 23,520 Joules Sensitivity - 1V/cm

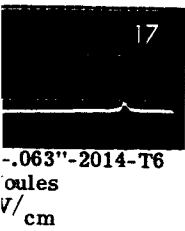


NOTES

- (1) With the exception of the callouts shown, all other conditions were identical to Sketch B
- (2) Approximation of strain rate based on values obtained-not actually measured.
- (3) Peak pressures measured at a 2" gage distance.

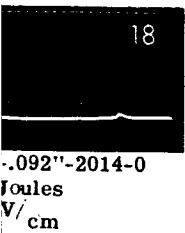
**FIGURE 31**





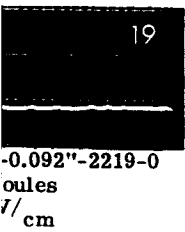
Trial dome ruptured into 4 pcs.  
Depth estimated as 2 5/8"

0.063"-2014-T6  
Joules  
1V/cm



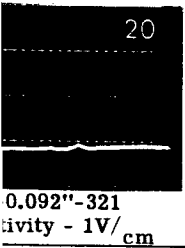
Dome depth of 2.80" formed under conditions which yielded an average strain rate of approx. 35 inches/in./sec. for a 1 1/4" standoff distance (3)

0.092"-2014-0  
Joules  
1V/cm



Dome depth of 2.03" formed under conditions which yielded an average strain rate of approx. 40 inches/in./sec. for a 1 1/4" standoff distance (3)

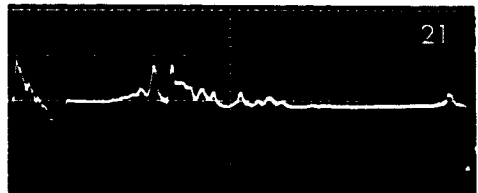
0.092"-2219-0  
Joules  
1V/cm



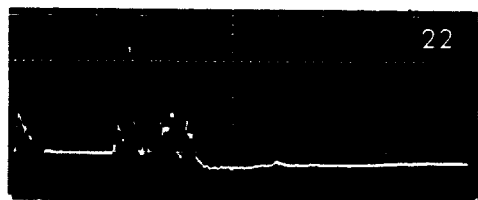
Dome depth of 1.76" formed under conditions which yielded an average strain rate of approx. 25 inches/in./sec. for a 1 1/4" standoff distance (3)

0.092"-321  
Joules  
1V/cm

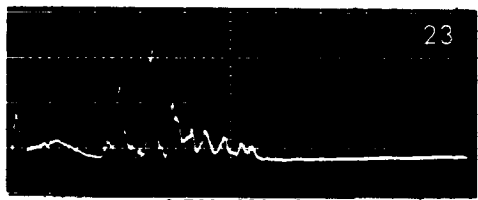
Photos 21-23 5KV-12,000 Joules



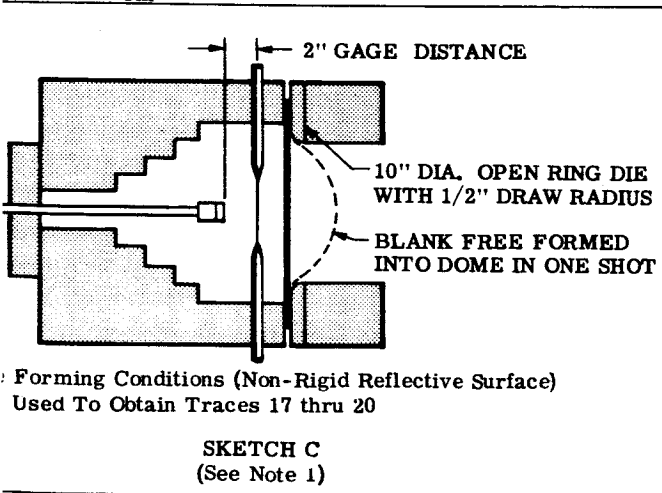
Peak PSI-7,170 .096" dia. mag. wire



Peak PSI 21,500 .062" dia. mag. wire

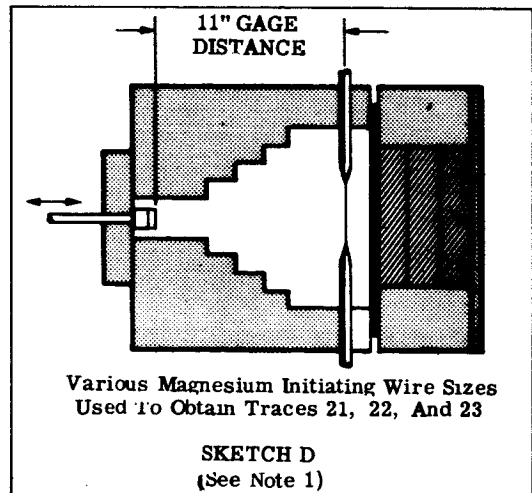


Peak PSI 19,700 .032" dia. mag. wire



Forming Conditions (Non-Rigid Reflective Surface)  
Used To Obtain Traces 17 thru 20

SKETCH C  
(See Note 1)

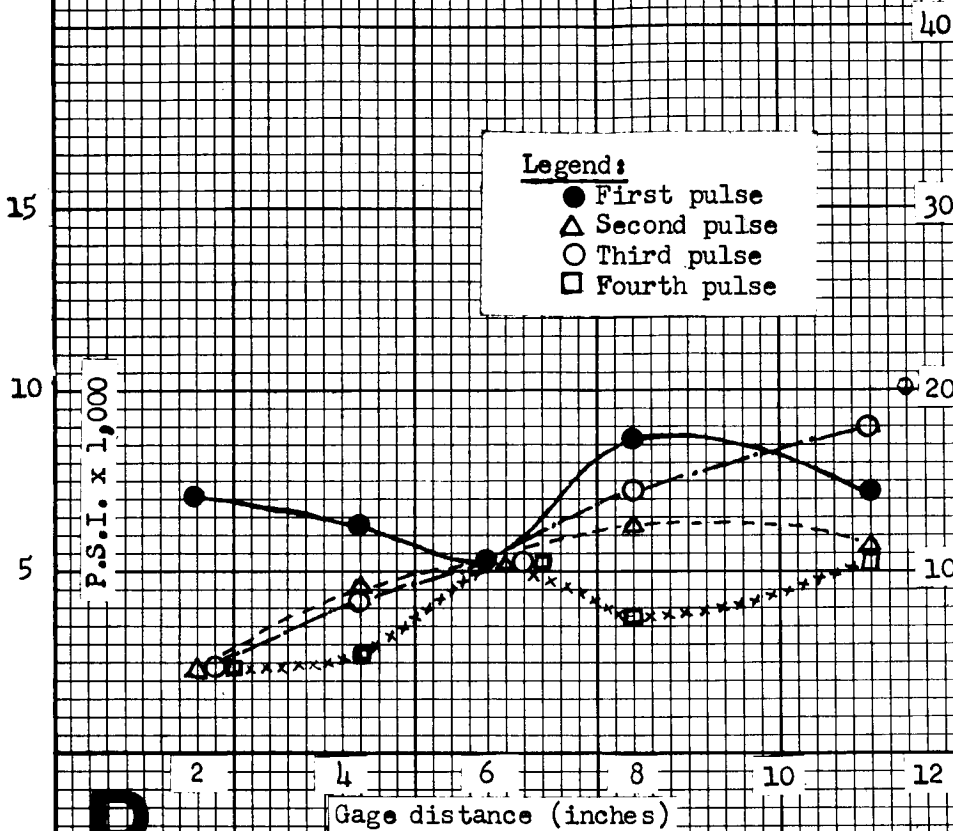


Various Magnesium Initiating Wire Sizes  
Used To Obtain Traces 21, 22, And 23

SKETCH D  
(See Note 1)

ELECTROHYDRAULIC PRESSURE PROFILES OBTAINED WITH THE KISTLER MODEL 617 PRESSURE TRANSDUCER OF 0-30,000 PSI UNDER VARYING TEST CONDITIONS

3

**A**Flat surface  
5 KV (12,000 joules)**B**

40

30

20

10

P.S.I. x 1,000

2

Gage

**E**

P.S.I. x 1,000

10

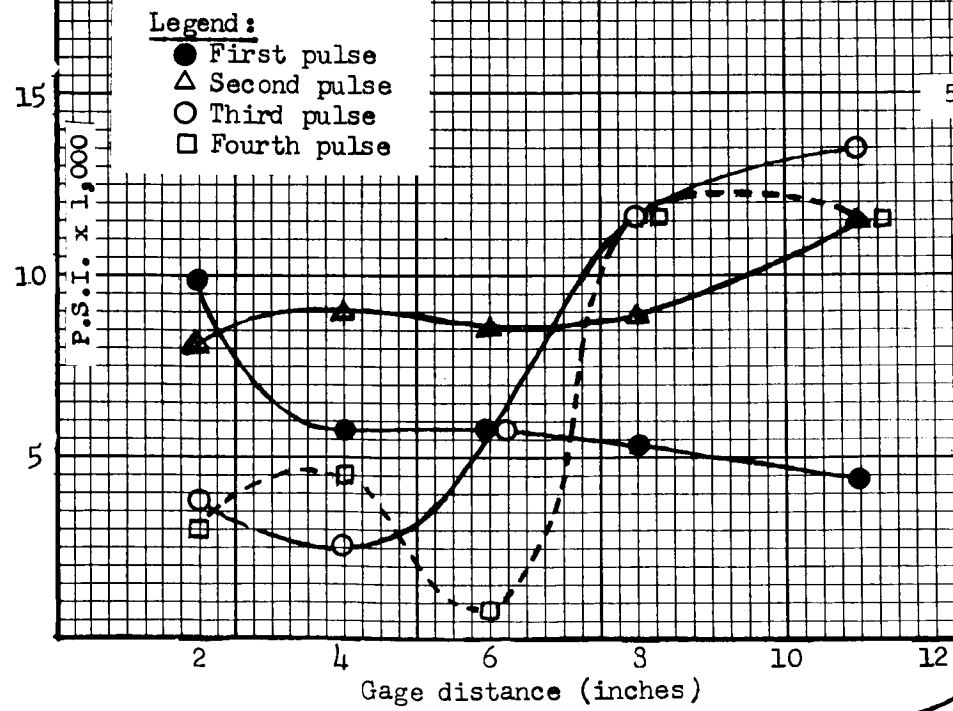
5

0

100

Variation in am  
pressure pul**D**

Gage distance (inches)

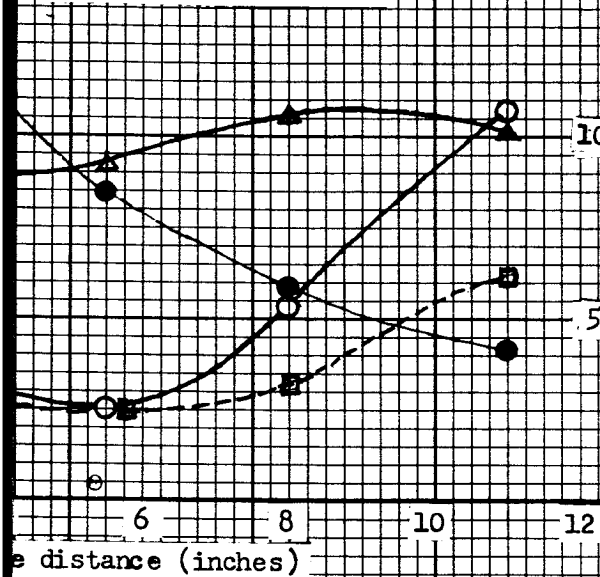
Hemispherical surface  
5 KV (12,000 joules)ELECTROH  
DATA PLOT  
DISTANCE,  
DIAMETER, U

FI

Flat surface  
6 KV (17,280 joules)

**Legend:**

- First pulse
- △ Second pulse
- Third pulse
- Fourth pulse



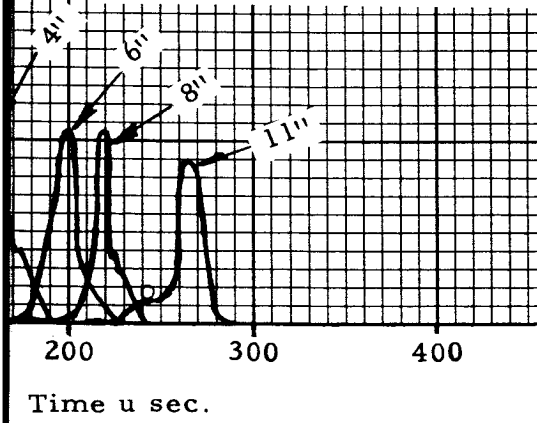
5 KV (12,000 joules) Flat Surface  
11" Gage Distance

Peak PSI x 1,000

**NOTES:**

1. For common test conditions and recorded data, see Table 15
2. For pressure pulse traces, see Figure 31

HEMISPHERICAL SURFACE  
5 KV (12,000 Joules)



Amplitude and delay time of first pulse at different gage lengths.

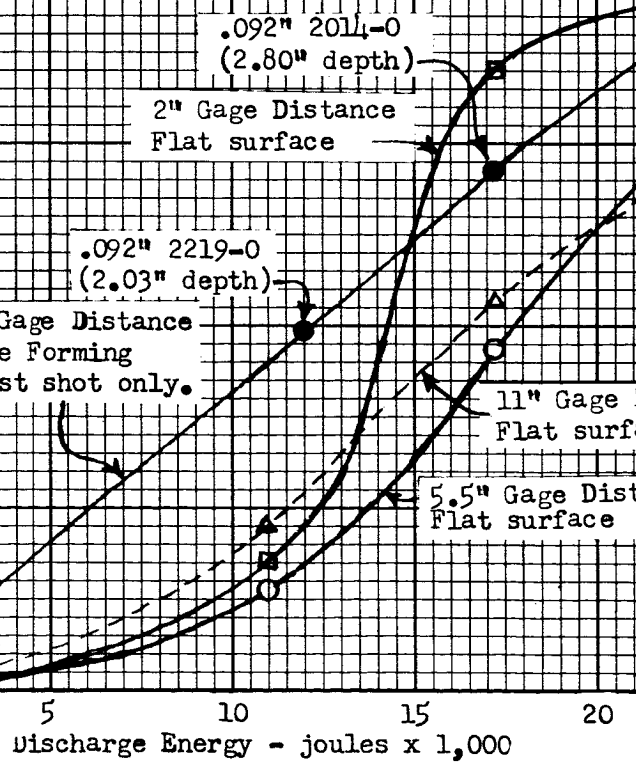
HYDRAULIC PRESSURE PULSE  
RECORDED AS A FUNCTION OF GAGE  
DISTANCE, DISCHARGE ENERGY, AND WIRE  
DIAMETER UNDER VARYING TEST CONDITIONS

**F**

Magnesium Wire Dia. - inches

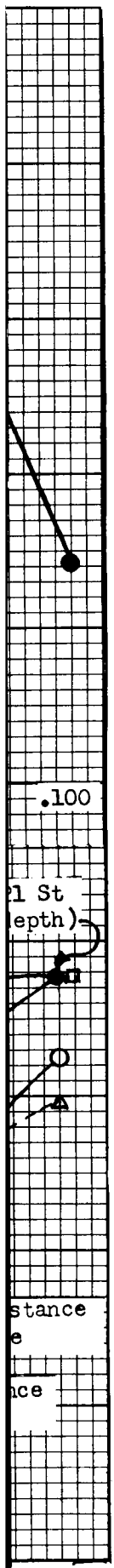
Flat & Dome Forming  
Conditions

Peak PSI x 1,000



Discharge Energy - joules x 1,000

**FIGURE 32**



.100

1 St  
(epth)

distance  
e

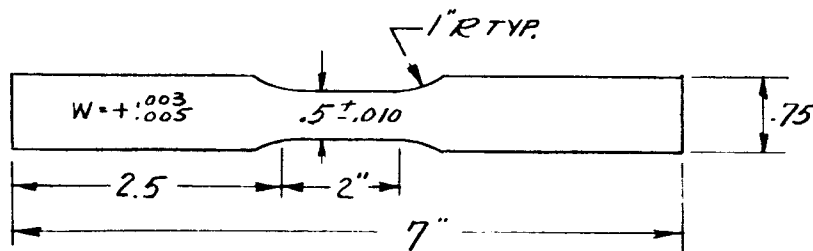
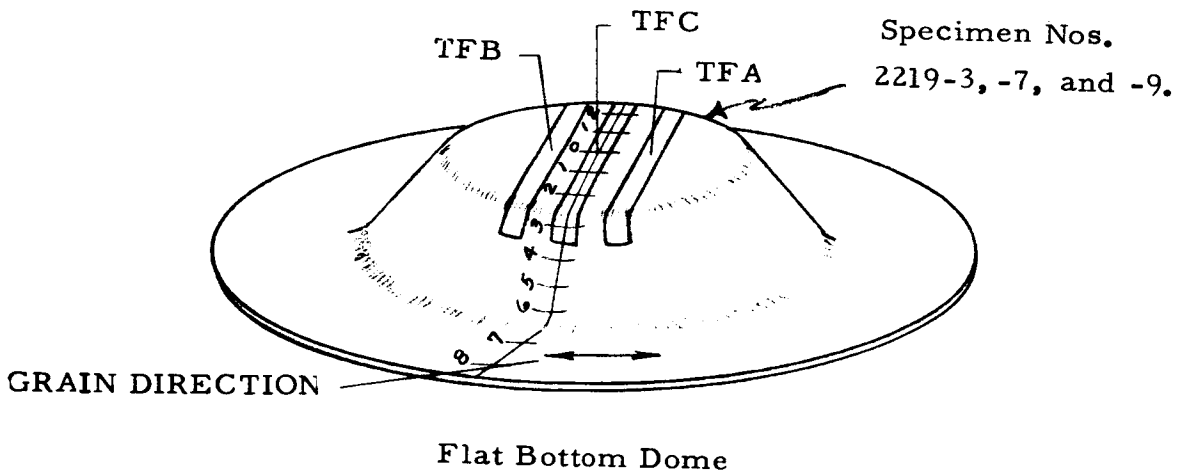
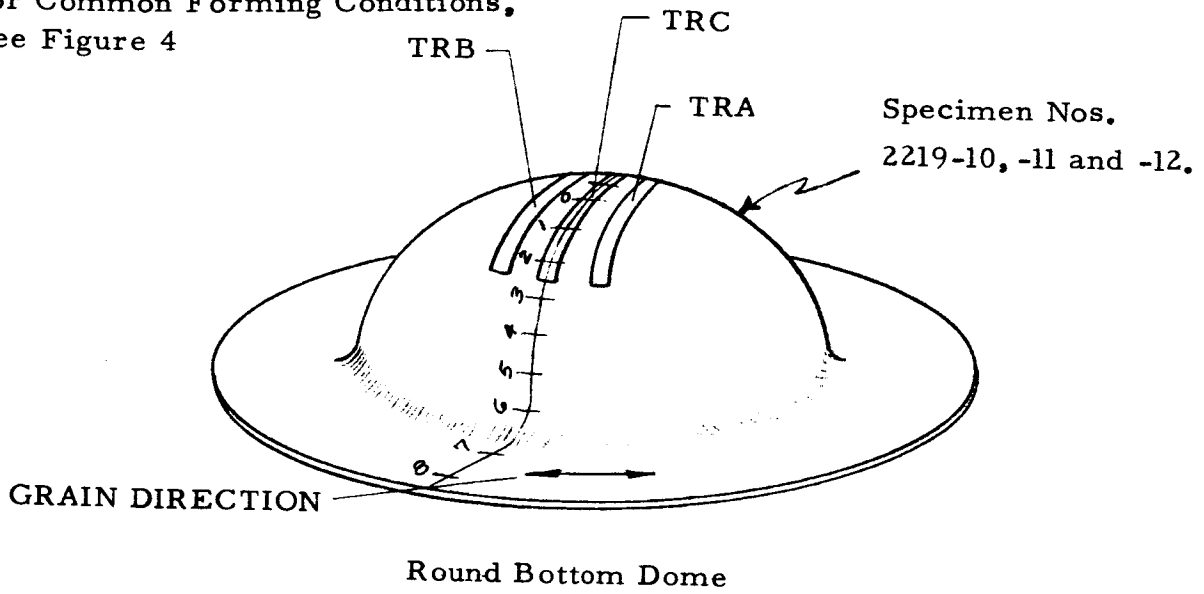
nce

25

3

NOTE: TF Denotes Transverse - Flat Bot.  
 TR Denotes Transverse - Round Bot.

For Common Forming Conditions,  
 see Figure 4



Typical Tensile Coupon

SIZE AND LOCATION OF 2219-0 TENSILE COUPONS  
 OBTAINED FROM THREE FLAT AND THREE ROUND  
 BOTTOM DOMES OF 13%, 25% and 47% AVERAGE  
 THINOUT



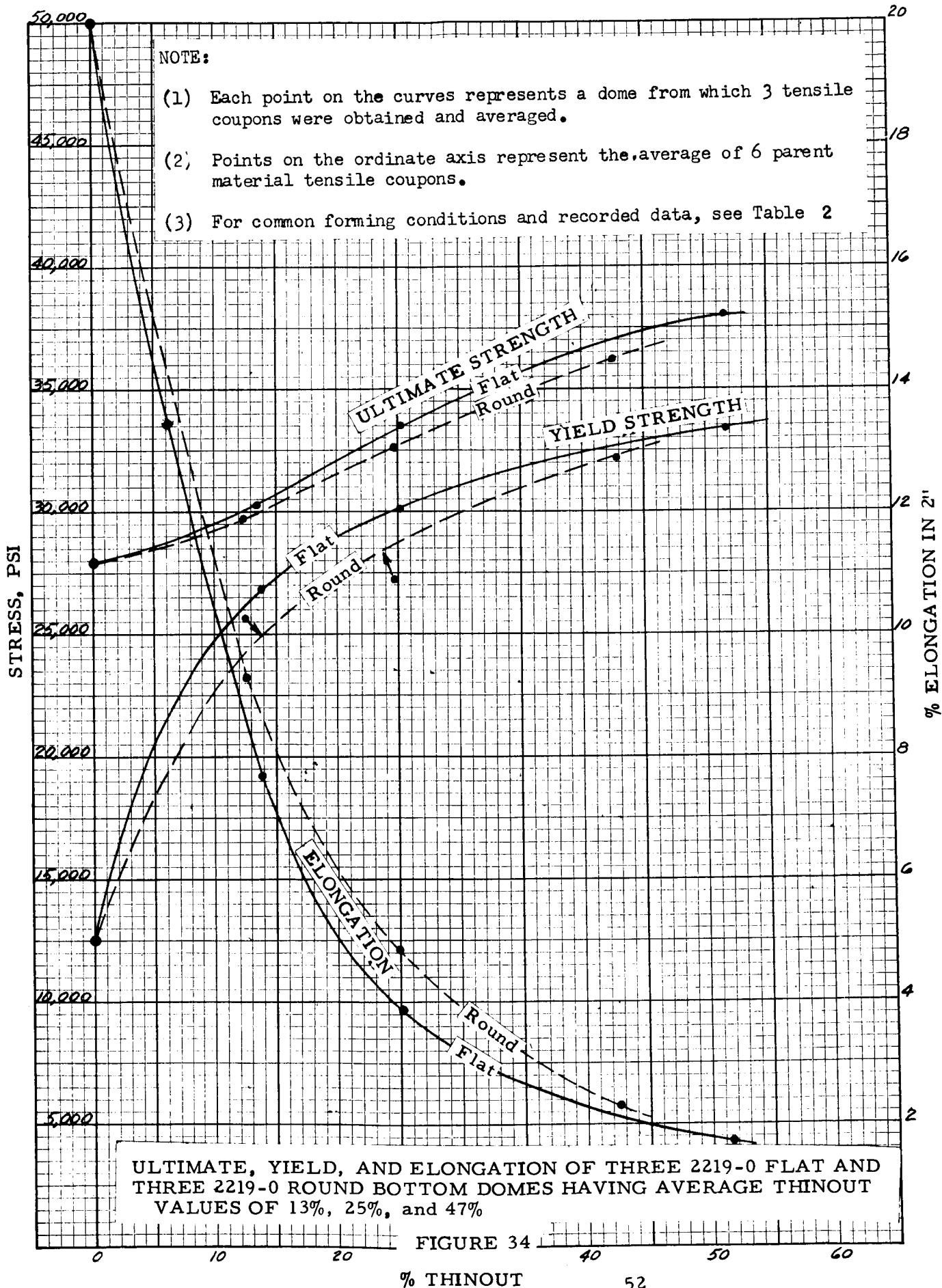
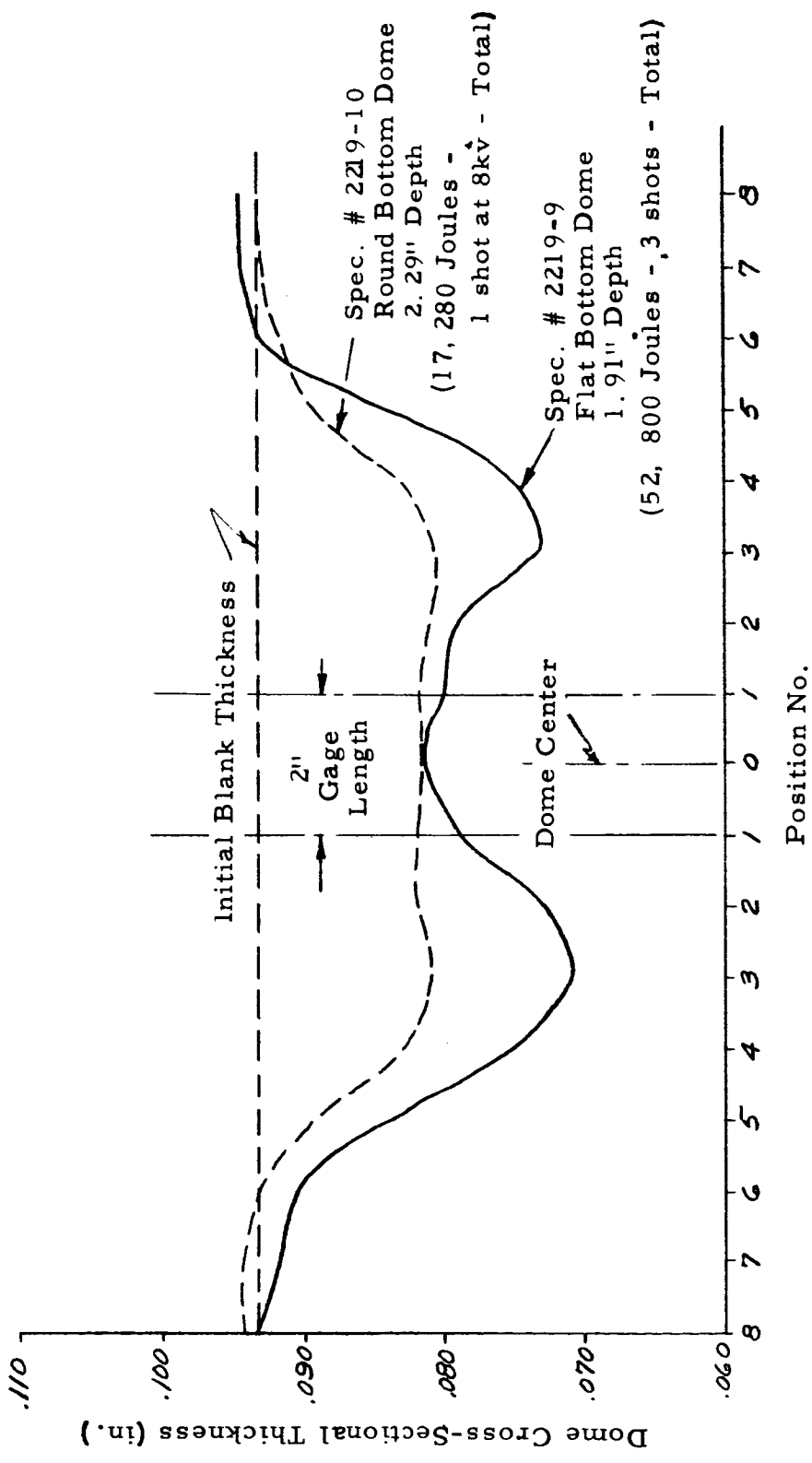


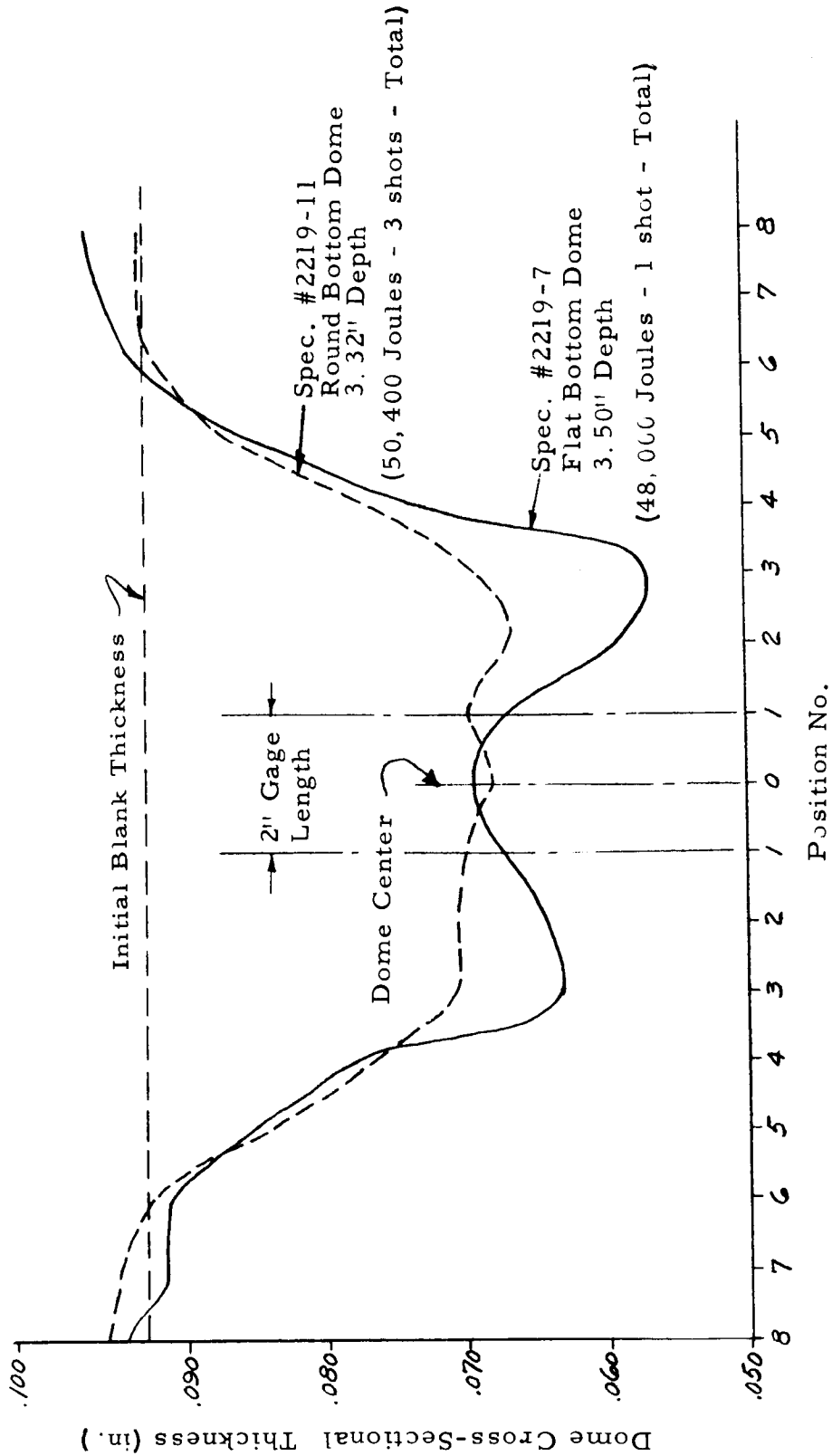
FIGURE 34  
% THINOUT

For common forming conditions and recorded data, see Table 2.



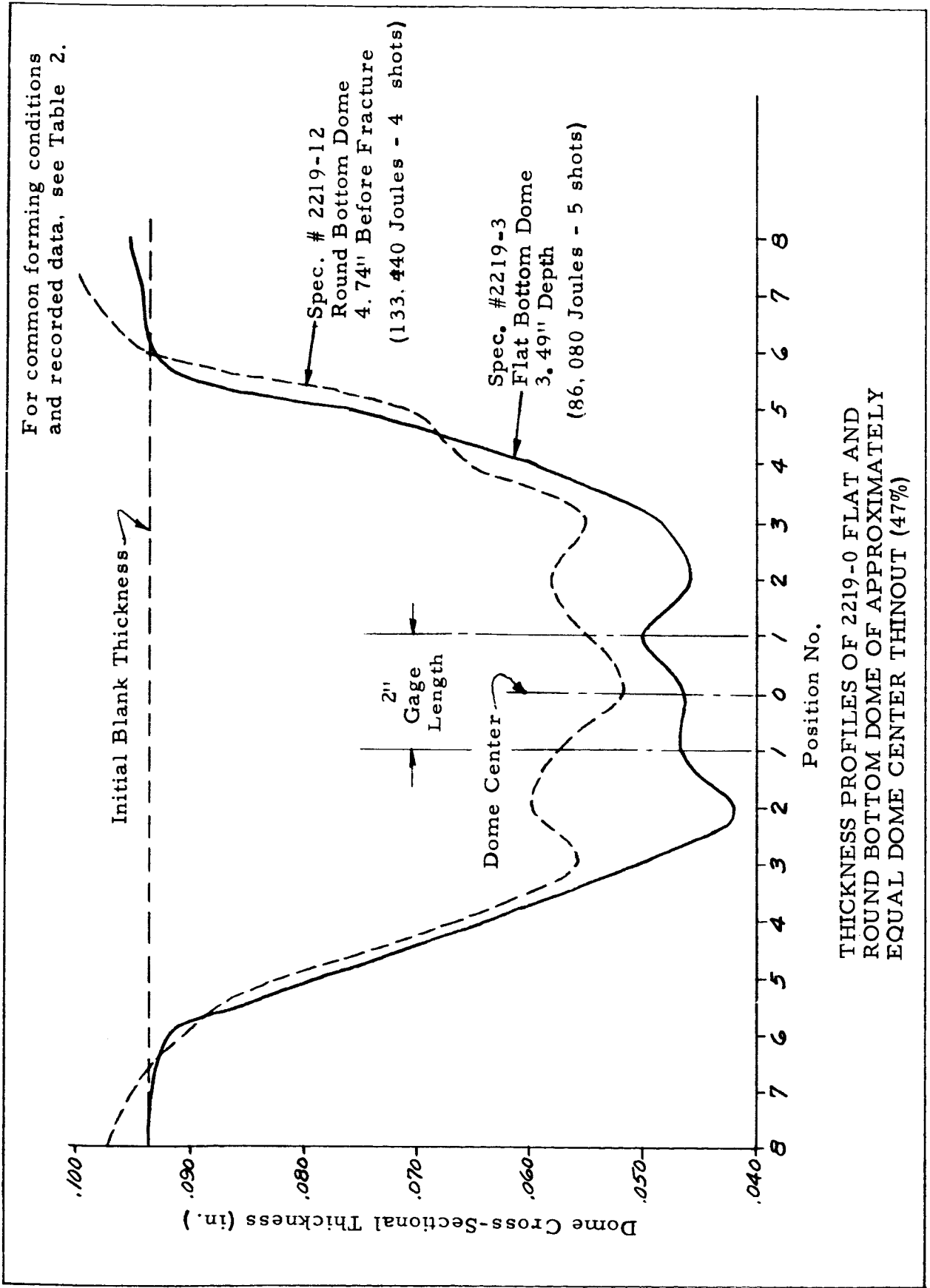
THICKNESS PROFILES OF 2219-0 FLAT AND ROUND BOTTOM DOME OF APPROXIMATELY EQUAL DOME CENTER THINOUT (13%)

For common forming conditions and recorded data, see Table 2.



THICKNESS PROFILES OF 2219-0 FLAT AND ROUND BOTTOM DOME OF APPROXIMATELY EQUAL DOME CENTER THINOUT (25%)

FIGURE 36



## TOOLING, EQUIPMENT, AND FORMING PROCEDURE

The equipment, tooling and forming procedure used for each process is discussed in sections A through E outlined below. The data obtained for these processes is presented in Tables 1 through 17.

### A. Electrohydraulic Forming

#### 1. Equipment

All of the electrohydraulic forming experiments were conducted with the 155,000 joule capacitor discharge forming facility located at Republic Aviation Corporation. The capacitor bank consists of sixty-four (64) 15 ufd capacitors arranged in four (4) groups of sixteen capacitors each for a total capacitance of 960 ufd. When charged to a maximum of 18 kilovolts, the 960 ufd capacitor bank can deliver 155,000 joules of energy to an external load. Capacitors are Cornell Dubilier #214 high energy storage units rated at 15 ufd at 20 KV with an internal inductance of 0.06 u hys. Each capacitor group (module) of sixteen capacitors each is interconnected by flexible coaxial cables at the collector bus. Figure 38 shows two of the four modules where each module consists of four (4) sections, each containing four (4) capacitors connected in parallel with the bus bars.

The capacitor bank is charged by six (6) G.E. K-9207372 power supplies containing bridge type kenetron rectifiers connected in parallel. Charging output current is determined by tap settings of the power transformer which when set at maximum, can continuously deliver 200 milliamps at 18 KV. At this charging rate the 960 ufd capacitor bank can be charged to 18 KV in less than 20 seconds.

The switching apparatus consists of a high vacuum switch and an associated vacuum system. The switch consists of a sealed chamber with a part for connection to the vacuum system which maintains a vacuum level of  $10^{-5}$  mm Hg. Triggering of the switch is accomplished by energizing an ignitor plug which causes ionization by creating a momentary pressure rise. A typical discharge current trace can be seen in Figure 30E.

A schematic of the 960 ufd capacitor discharge facility, shown in Figure 39 includes details of the rectifier units, surface ignitor plug, and the control panel circuitry. A view of the control panel may be seen in Figure 40.

#### 2. Tooling

Details of construction of the closed system pressure vessel (herein referred to as the closed tank) is shown in Figures 30C and D. The door is designed to house either a female die for closed die forming or an open die for free forming experiments. Since the door is hinged to the tank by a single hinge, the open or closed die can be backed with shims to accommodate a wide range of metal thicknesses. The arrangement of hinging

the door at the side of the tank facilitates loading and unloading the work-piece into the tank. Die closure is obtained by keying the door to the tank with a tapered pin which when advanced to a positive stop insures uniform blank restriction.

The die used for all electrohydraulic free forming (open die) experiments was a 10 inch diameter open ring die containing a 1/2 inch draw radius. All electrohydraulic closed die experiments utilized a hemispherical die of 4.75 inch spherical radius. Depth of this die was approximately 4 inches and contained four 1/16 inch diameter vacuum outlet holes located at the die apex. Die impact experiments in which this die was used provided tensile specimens from an area of the dome just outside the vacuum holes. The closed die was designed to have a shape similar to the free formed domes at maximum depth. A photo of the closed die is shown in Table 6.

### 3. Forming Procedure

As discussed in Section F, preliminary tests were conducted to establish energy level, gauge reduction, blank diameter and dome configuration. These tests also served to establish the forming procedures to be employed for all subsequent experiments. All experiments were conducted at a 1 1/2" standoff distance using a 4 inch electrode gap containing an .096" diameter magnesium initiation wire for discharges at 10 KV or less and a .125" diameter wire for discharges greater than 10KV.

To permit a comparison between electrohydraulic and other forming techniques relative to mechanical properties and strain rate, domes were free formed using the open die, at high and low strain rates. The recorded data under these conditions is shown in Table 4. Lineal increase, area increase and strain rate of the original 1/2 inch center square, plotted against time are shown as Figures 5 through 14.

Overpressure experiments in which the closed die was used was also performed to determine the effect of impact on the metallurgical properties of the three alloys used. This data is listed in Table 6. The mechanical properties obtained for the open die and closed die experiments are shown in Tables 5 and 7 respectively. Table 5 and 7 include data obtained from other forming processes for comparative purposes.

For the closed die impact experiments, impact was usually attained at the third or fourth shot where total dome travel distance of approximately 1 inch insured die impact at all points of the die surface. Small circular burn marks found on the dome apex after impact resulted from compression of a small pocket of air trapped between the dome and die surface during

forming despite the initial vacuum level of 29" Hg. Small protuberances, also found on the dome apex, proved to be dome material which was extruded through the vacuum holes. The above factors as well as die marks distributed throughout the dome contour, provided a means of determining the magnitude of die impact for specimen designation of either "high impact" or "low impact." Prior to loading, both sides of a blank were coated with Cimcool lubricant for the electrohydraulic and explosive closed die experiments to facilitate draw rather than stretch, thereby increasing impact velocity.

## B. Explosive Forming

### 1. Equipment

Explosive forming experiments were conducted at the Flare-Northern Division of Atlantic Research Corporation located at West Hanover, Massachusetts approximately 25 miles from Boston. Forming trials, which lasted ten days, were performed at an isolated clearing in woods approximately 4 miles from any building. The forming shed which was located on the test site, contained a four foot thick concrete pad directly over which were poised steel plates arranged in a saw tooth pattern for deflecting the water column.

All forming experiments were accomplished with a high explosive known as RDX, "Cyclonite." This charge is classified as a "Class A" explosive having a composition of 97 1/2 / 2 1/2% RDX/WAX. The 2 1/2% wax is used as a binder and desensitizer. This type, though classified as a high explosive is generally used as a booster explosive for the initiation of other types of high explosives. "Pellets" of various sizes were used. A given quantity of the RDX/WAX composition is compacted to a cylindrically shaped pellet using a Wilson Hydraulic Press of 640 ton capacity. Consolidation pressure required was 25,000 psi. The only criteria in the compacting of these pellets is that the length should not exceed the diameter for a given weight if maximum efficiency is to be attained. This is due to the non-uniform density that would result in the compacting of longer cylindrical pellets. Charge weight ranging from 6 to 75 grams having diameters ranging from 3/4" to 2" respectively have been used. The explosive pellets were fired with a #8 Electric Blasting Cap which contains a thin bridge wire encapsulated in a primary explosive which in turn acts on a secondary explosive contained within the blasting cap.

Firing lines were checked by a "Blasting Galvanometer to insure continuity of the firing circuit prior to detonation. Initiation was accomplished by connecting the firing circuit to a device known as a "Ten Cap Blasting Generator." Maximum rating is for 10 electric blasting caps used with 30 feet of copper wire connected in series only. (one blasting cap was used.) The blasting generator contains two terminals to which the firing line is connected. An actuating handle is inserted into the device and rotated sharply. This action generates 180 - 200 volts DC which is sufficient

to melt the bridge wire contained within the blasting cap. Ohmic resistance of the circuit was found to be 16 ohms. Photos taken at the test site describing various aspects of the explosive forming experiments are shown in Figure 41. Blasting Caps, Generator and Galvanometer were all manufactured by "Hercules Powder Company.

## 2. Tooling

Tooling for the explosive forming experiments consisted of a 4 ft. test stand which housed the open and closed dies. This was accomplished by simply inverting the test stand. Eight large "C" clamps of special design were used to provide the necessary blank restriction by clamping up the restriction ring, workpiece, and open die to the test stand. (Blank drawin was found to range from 2% to 8%.) Supports consisting of 2" angle iron were used to stabilize the test stand during detonation. Sketches of the tooling used may be seen in Figures 42, 43 & 44. All of this tooling was fabricated at Republic Aviation Corporation.

The water container consisted of a 1" mesh chicken wire screen which was fashioned into an open-ended cylinder into which a plastic bag was placed. A typical water container is shown in Figure 41. The container size was 11" in diameter and was 12" high. After each detonation, a new container was required. Water was usually filled to 11" corresponding to a volume of 0.61 cu. ft. or 4 1/2 gallon of water.

## 3. Forming Procedure

After the workpiece was positioned and clamped to the test stand, the plastic bag (located within the water container) was filled with water obtained from an artesian well located just outside the forming shed. The blasting cap open end was next positioned at the center of the RDX pellet flat and firmly taped into position. A 15" length of 1/8" diameter brass rod was used to suspend and centralize the charge with respect to the workpiece. By simply taping the wires of the complete charge assembly to the cross-rod, desired standoff distances would be achieved. The #8 cap contains two 12 foot lengths of #22 AWG wire. These two wires are connected to an additional length of common AC line (Zip Cord). The firing line was run to a firing shack located approximately 65 feet from the main shed where detonation was achieved by the use of the blasting generator previously described. Overall time required for one detonation including workpiece set-up and removal was approximately 15 minutes. Results of the free form and die impact experiments are shown in Tables 8 and 9, respectively.

During strain rate experiments using the Fastax camera, it was found that the event was occurring approximately half way down film. This was due to the insufficient power available to the camera motor at the instant of camera start. The voltage source could not supply the instantaneous power needed and caused momentary voltage drop resulting in slower starts.



To overcome this, the camera voltage was increased to maximum (300 VAC) and the event was further delayed from 0.75 sec. to 0.85 sec. in an effort to provide more time for the camera to come up to speed for its one second running time. A more serious problem, however, was discovered when viewing the films. A total of eight film rolls were viewed and metal movement observed sometimes for only a part of its deformation. After three to four frames, the image would become obscured sometimes briefly re-appearing, sometimes not. The reason for this condition can only be the large amount of smoke and atomized water spray which engulfs the camera lens and mirror. This, however, did not seriously affect the overall strain rate measurements which are shown plotted as Figures 45 through 52.

The camera was protected against water spray by a large plastic shroud, shown in Figure 41. A time exposure Polaroid photo of the attendant smoke and water spray can also be seen in Figure 41. (Note the tripod housing the mirror located under the workpiece being engulfed by smoke and water). A series of exposures showing expansion of the 1/2" x 1/2" center square by the explosive, electrohydraulic, and magnetic forming processes can be seen in Figure 2.

### C. Magnetic Forming

The magnetic forming experiments were performed to obtain higher values of strain rate at the same discharge energies used for the electrohydraulic strain rate experiments. Higher strain rates are not possible with the electrohydraulic discharges since increased discharge energy would produce rupture.

#### 1. Equipment and Tooling

With the exception of the coil, the equipment and tooling used was identical to that used for the electrohydraulic open die forming experiments discussed earlier. The recorded data is presented in Table 10. Coil construction is shown as Figure 53 in Table 10.

#### 2. Forming Procedure

The six turn spirally wound coil was placed into the closed tank with micarta backup spacers serving to provide intimate contact between the coil and workpiece as illustrated in Figure 54 of Table 10. Only the 2219-0 and 2014-0 aluminum alloys were used since higher yield and lower conductivity of the 321 stainless alloy would produce less deformation and, therefore, less strain per discharge. Under these conditions, the maximum magnetic strain rate for the 2219-0 alloy was 723 per second and 877 per second for the 2014-0 alloy. A photo of the coil and a typical formed specimen is shown in Figure 55 of Table 10. Also included in Table 10 are current discharge traces of the coil in a loaded (coupled to workpiece) and unloaded condition. Strain of the original 1/2" x 1/2" center square plotted against time are shown as Figures 56 through 59.

## D. Hydrostatic Forming

### 1. Equipment and Tooling

The domes formed hydrostatically were formed using the setup shown in Figure 60. The same open die as that used for the electrohydraulic, explosive, and magnetic forming experiments was used. A portable Sprague hydraulic power pack Model S-404 was used to supply hydrostatic forming pressure while blank restriction was provided by the Lake Erie Hydraulic Press.

### 2. Forming Procedure

Initial hydrostatic forming trials with the 321 stainless 20 1/2" diameter blank produced a maximum blank drawin of only 0.5%, opposed to 2 to 8% drawin for the electrohydraulic and explosive forming processes. To correct this the 321 stainless blank size was changed from 20 1/2" to 17 1/2" thereby reducing blank restriction to obtain more drawin and to maintain a range of drawin values (2 to 8%) that will permit a fair comparison with the other processes. The aluminum alloy blank sizes were maintained at 17 1/2" A 0.100" outer shim was used which provided a blank clearance of approximately 0.010" between the pressure pad and open draw ring die. Blank drawin under these conditions varied from 2% to 6% and closely matched the drawin values of 2% to 8% found for the high energy rate forming processes. The somewhat higher values of blank drawin experienced for the high rate processes is attributed to the elastic yielding of the restraining structural members during discharge allowing greater blank clearance for drawin. Elastic yielding cannot be tolerated in hydrostatic forming since the increasing gap will impair the effective O ring seal at high pressures.

The recorded data is shown in Table 11A, and tensile properties obtained from tensile coupons taken from dome centers are shown in Table 5. Since the rate of strain of a hydrostatically formed dome can be taken as zero, the tensile data can be used as a basis for comparison with other forming processes.

## E. Hydroforming

Forming of hemispherically shaped domes by the hydroform process was performed during Phase I of this program and is fully discussed in the Phase I technical report dated December 1962. The materials used were .063" - 6061-0 aluminum and .040" 304L annealed stainless steel. All of the hydroform recorded data contained in this report was obtained from the hydroform experiments performed in Phase I. Additional hydroform experiments were not performed since hydroforming does not lend itself for comparison to the other forming methods in a program where the influence of strain rate is of the greatest interest. The hydroform process is essentially a draw process wherein strain is too low for useful comparison to other processes. The hydroform equipment, tooling and forming procedure employed in Phase I is repeated here for convenience.

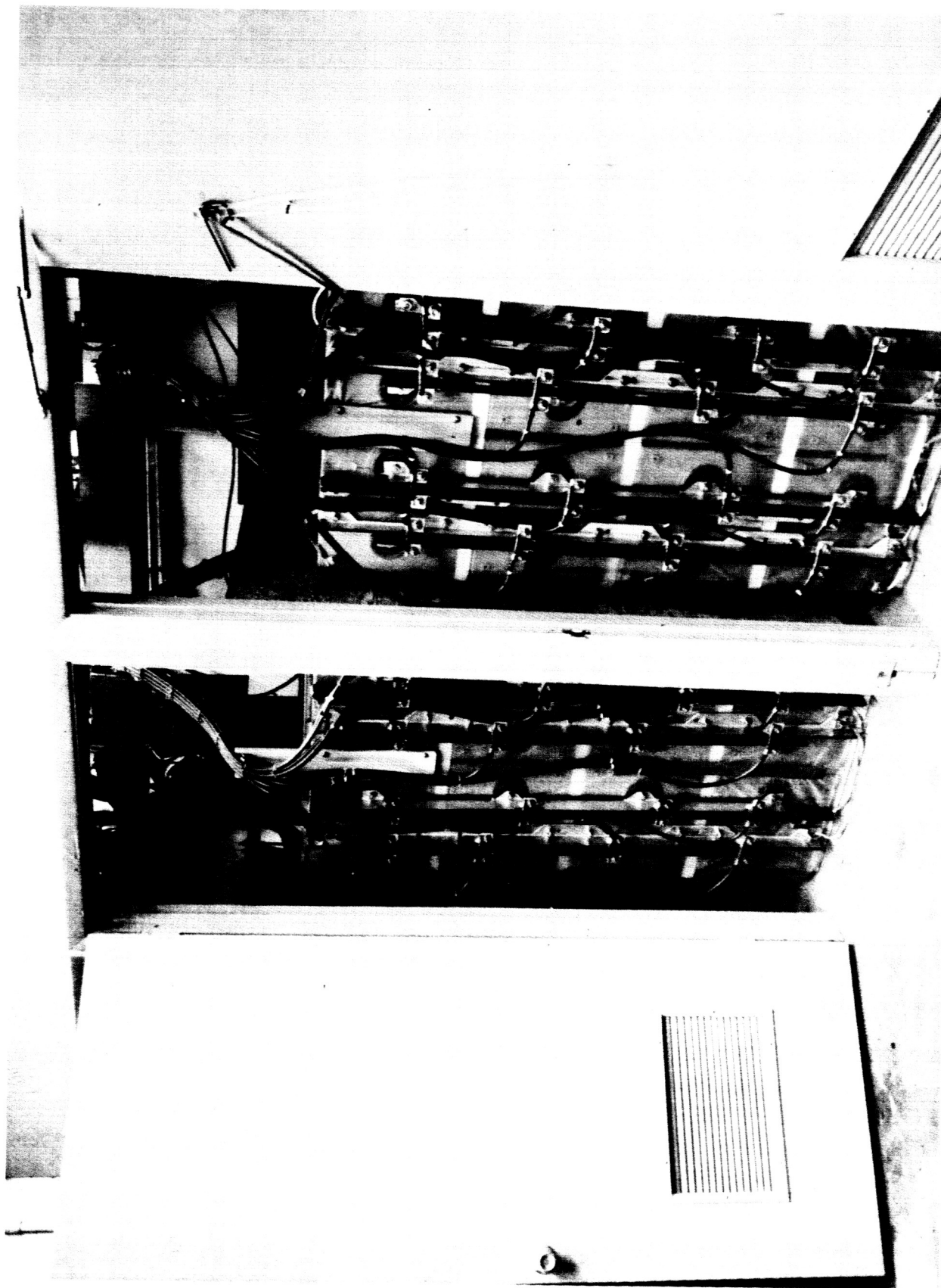
## 1. Equipment and Tooling

The 6061-0 and 304L alloys were formed to a 3 1/2" to 4" depth using the 32" Cincinnati Hydroform. Blanks of 16.4" diameter were formed with a 9 3/4" diameter full hemispherical punch.

## 2. Forming Procedure

The Cincinnati Hydroform forms parts by advancing a male punch against the workpiece which is formed into a flexible die member. The workpiece is placed on a draw ring and an initial hold down pressure is exerted on the blank by a hydrostatic pressure in the forming cavity. The conditions selected for the .063" 6061-0 aluminum alloy were 100 psi initial pressure with a controlled cycle (pressure increased in natural cycle as punch is advanced, but cut off and held constant at 2,000 psi). Drawing compound was used on both sides of the blank. For the .040" 304L annealed stainless steel, the forming conditions selected were 3,700 psi initial pressure with a natural cycle in which the pressure increased with punch advancement to 7,600 psi. Drawing compound was used only on the blank surface in contact with the draw ring. A comparison table of dome center stretch and thinout of stainless steel domes formed to a 3" to 4" depth by the various processes is shown below to illustrate the small stretch to draw ratio obtained for the hydroform process. The hydroform data is shown in Table 11B. The data shown for the hydrostatic electrohydraulic, explosive, and magnetic processes was obtained from Tables 11A, 4, 8 and 10 respectively.

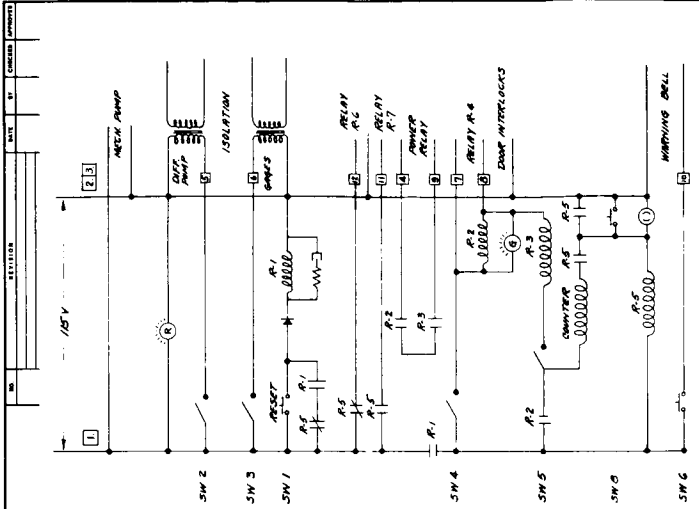
Specimen No.	Alloy	Forming Process	1/2" x 1/2" Center Square Stretch (%)	Dome Center Thinout (%)	Dome Depth (in)
HF-1	304L	Hydroform	14.4	10.0	3.98
HS-3	321	Hydrostatic	-	28.3	3.71
EH-4	321	Electrohydraulic	37.9	25.8	3.42
EX-3	321	Explosive	23.2	20.6	3.24
M-2	2014-0	Magnetic	76.9	36.7	3.36



MR - 2780

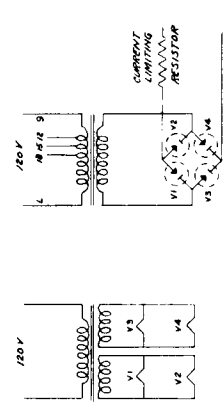
155, 000 JOULE (960 uf AT 18 KV) CAPACITOR DISCHARGE FACILITY  
TWO OF THE FOUR CAPACITOR GROUPS ARE SHOWN

FIGURE 38

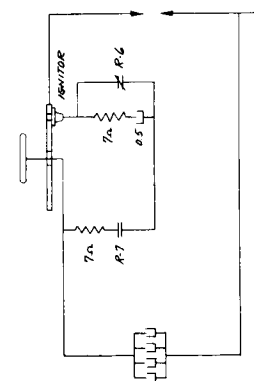


CONTROL CIRCUIT

REV.		DATE		BY		CHECKED		APPROVED	
1									
<b>MRP 2453</b>									
NO.	REV.	DATE	BY	APP. BY	REVISION	QUANTITY	STATUS	REMARKS	SCALE
1		8-2-52			1-1	10	ASSEMBLED	NO BUILT DRAWING	
<b>CAPACITOR DISCHARGE SCHEMATIC CIRCUIT</b>									
<b>FOR SECOND DRAWING</b>									
REPUBLIC AVIATION CORP. MFG. ENGS. DIV.									
FAIRFAXVILLE, N. CAROLINA									
<b>MRP 2453</b>									



DETAIL OF RECTIFIER MODULE



SURFACE IGNITOR - DETAIL OF CIRCUIT

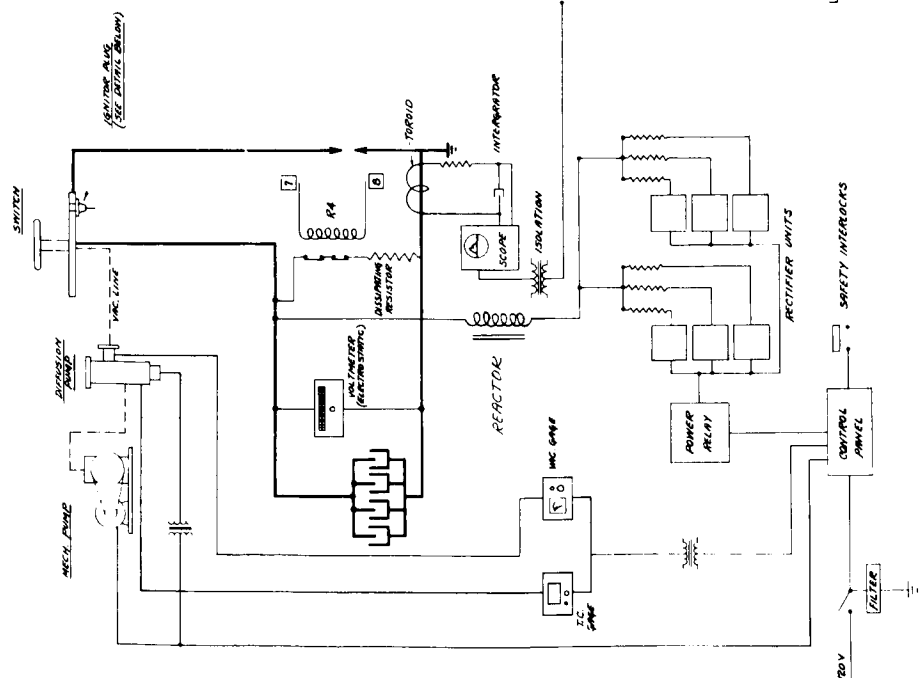
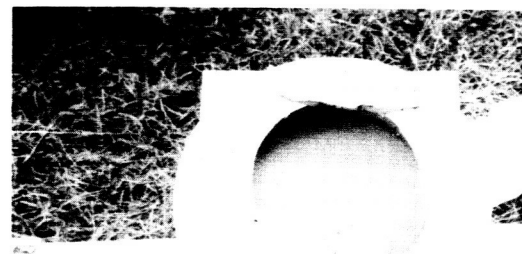
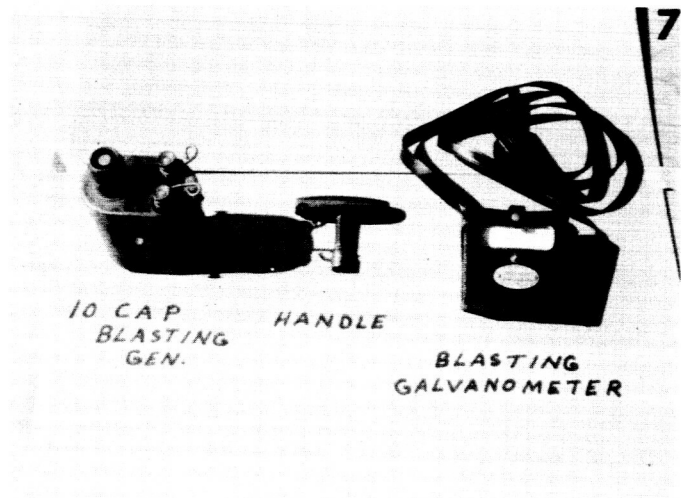
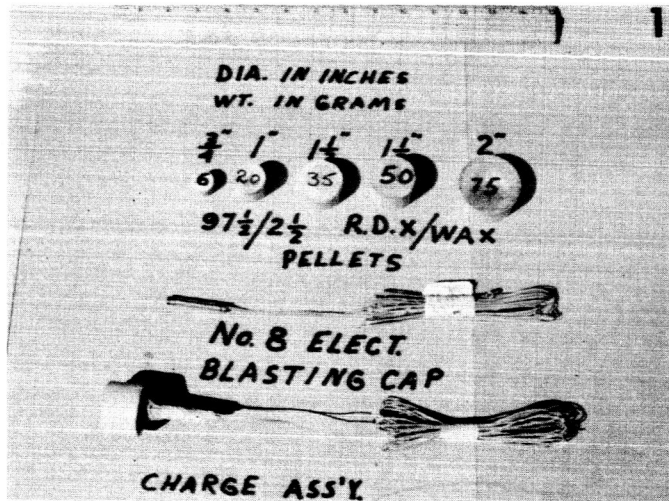
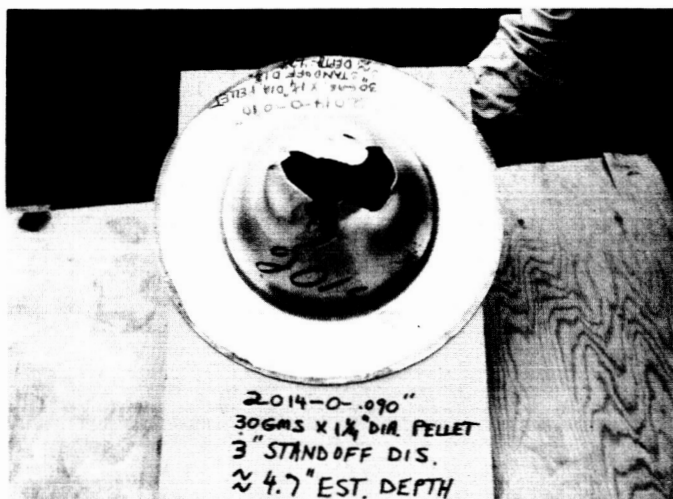
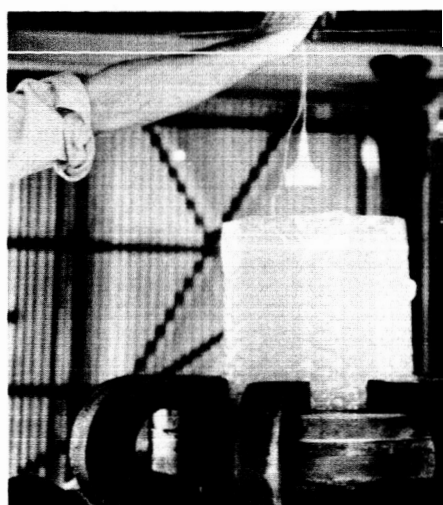
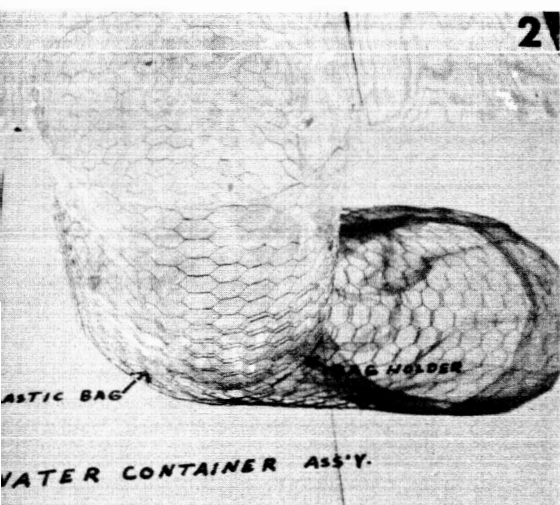


FIGURE 39



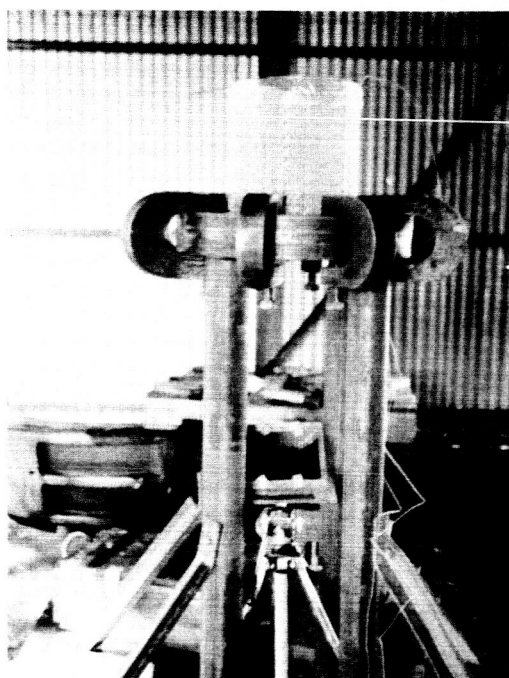
CONTROL PANEL FOR THE 155,000  
JOULE CAPACITOR FORMING FACILITY  
FIGURE 40 65





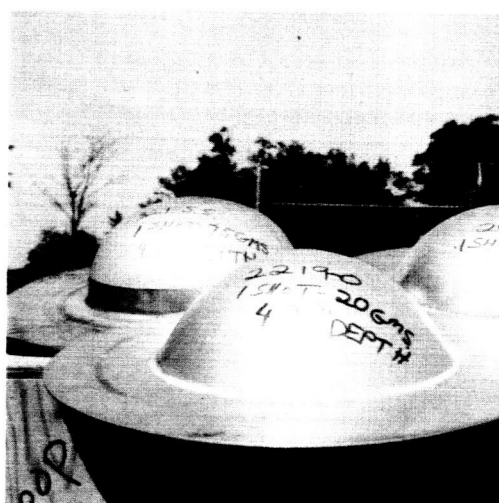
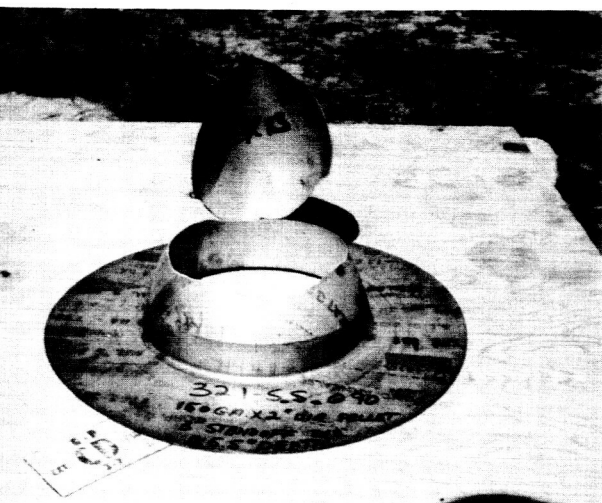
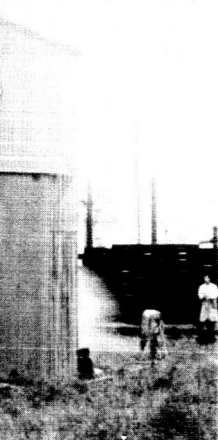
2



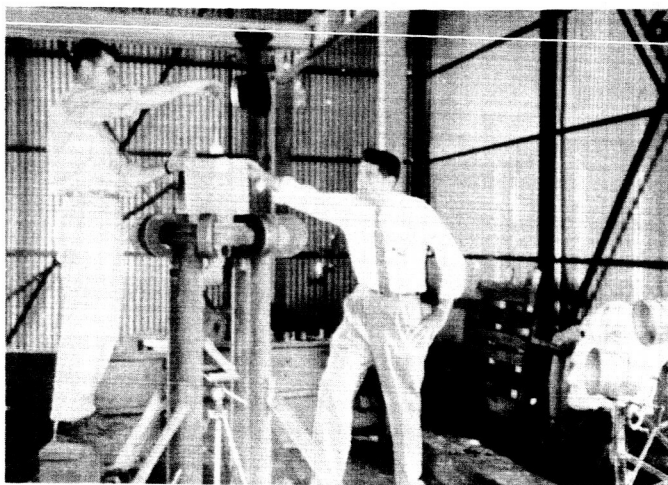
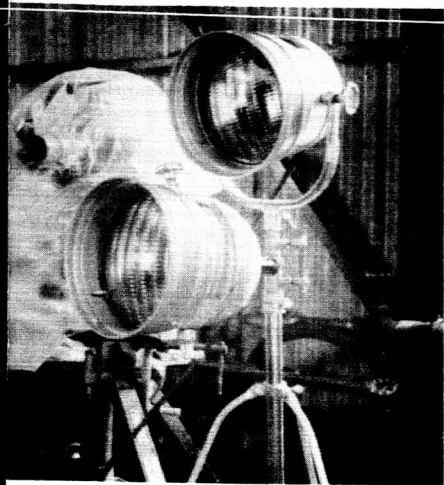


9

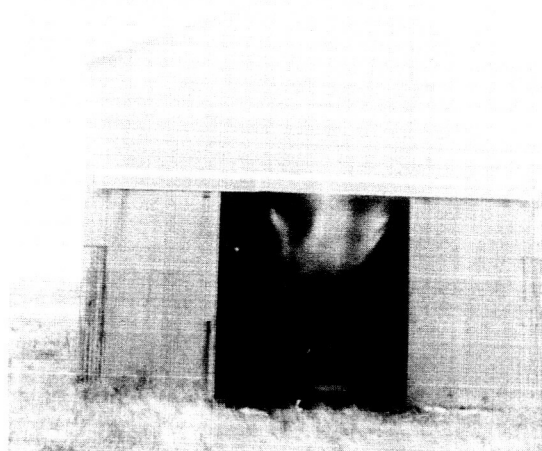
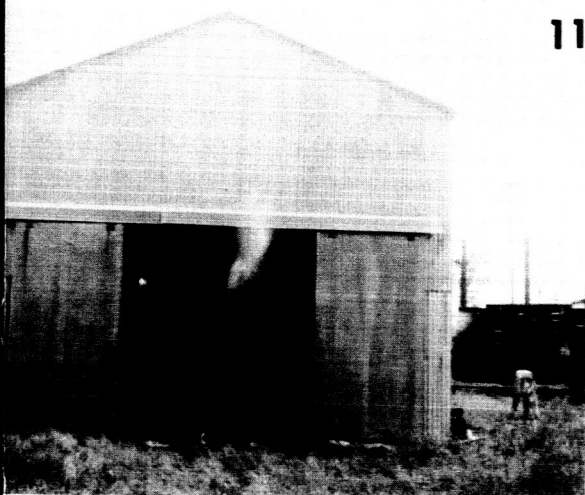
10



3



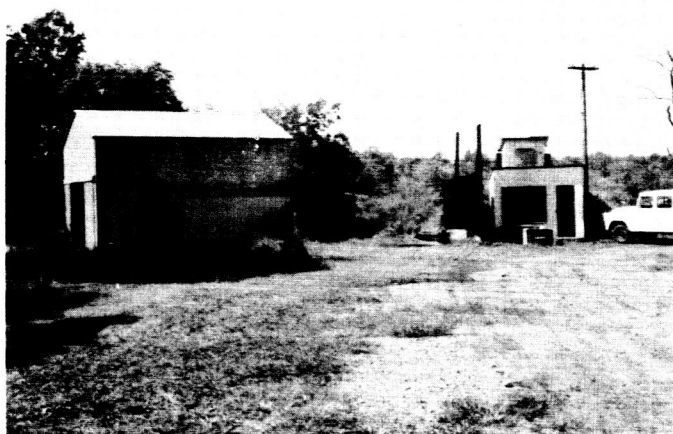
11



16



17



4

<u>Photo No.</u>	<u>Description of Photo</u>
1-2	Elements of the explosive forming experiment.
3	Method of positioning charge and adjusting standoff distance. (Note workpiece sandwiched between restriction ring and open die).
4	Overall view of test set-up prior to detonation. (Note tripod containing mirror angled at $45^{\circ}$ ).
5	Lighting and high speed Fastax camera shrouded with plastic sheet to prevent wetdown.
6	Overall view of test set-up showing camera to workpiece distance (8 ft.).
7-8	Blasting generator and galvanometer as used under actual operating conditions.
9	During detonation of a 20 gram charge at a 3" standoff distance.
10-11-12	Shots 1, 2 and 3 of a 6 gram charge showing how water spray is deflected upwards by placement of the charge within progressively greater dome depths.
13-14-15	Domes formed to rupture to establish charge weight and size.
16	Typical explosively free formed domes.
17	Overall view of test site.

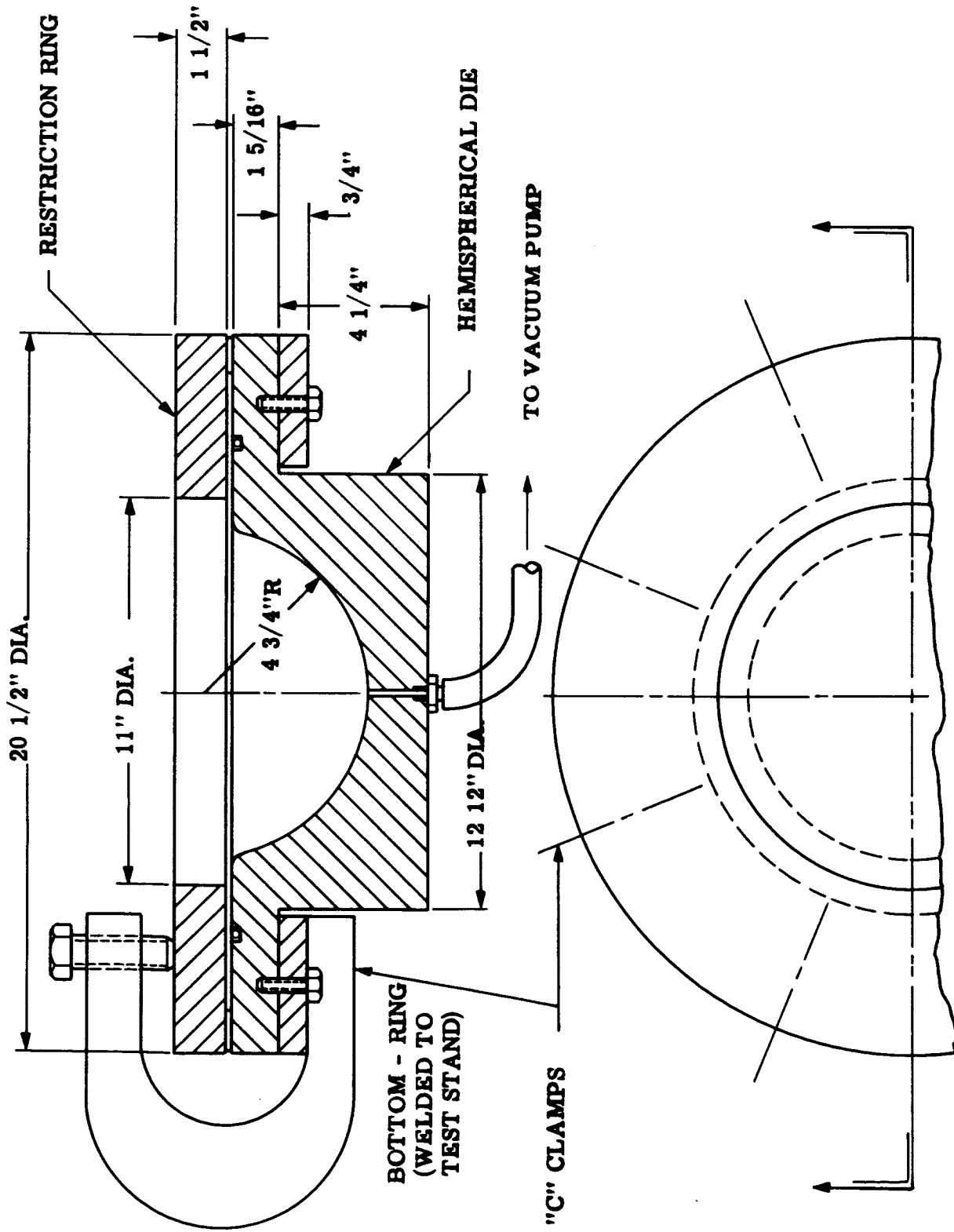
12



5

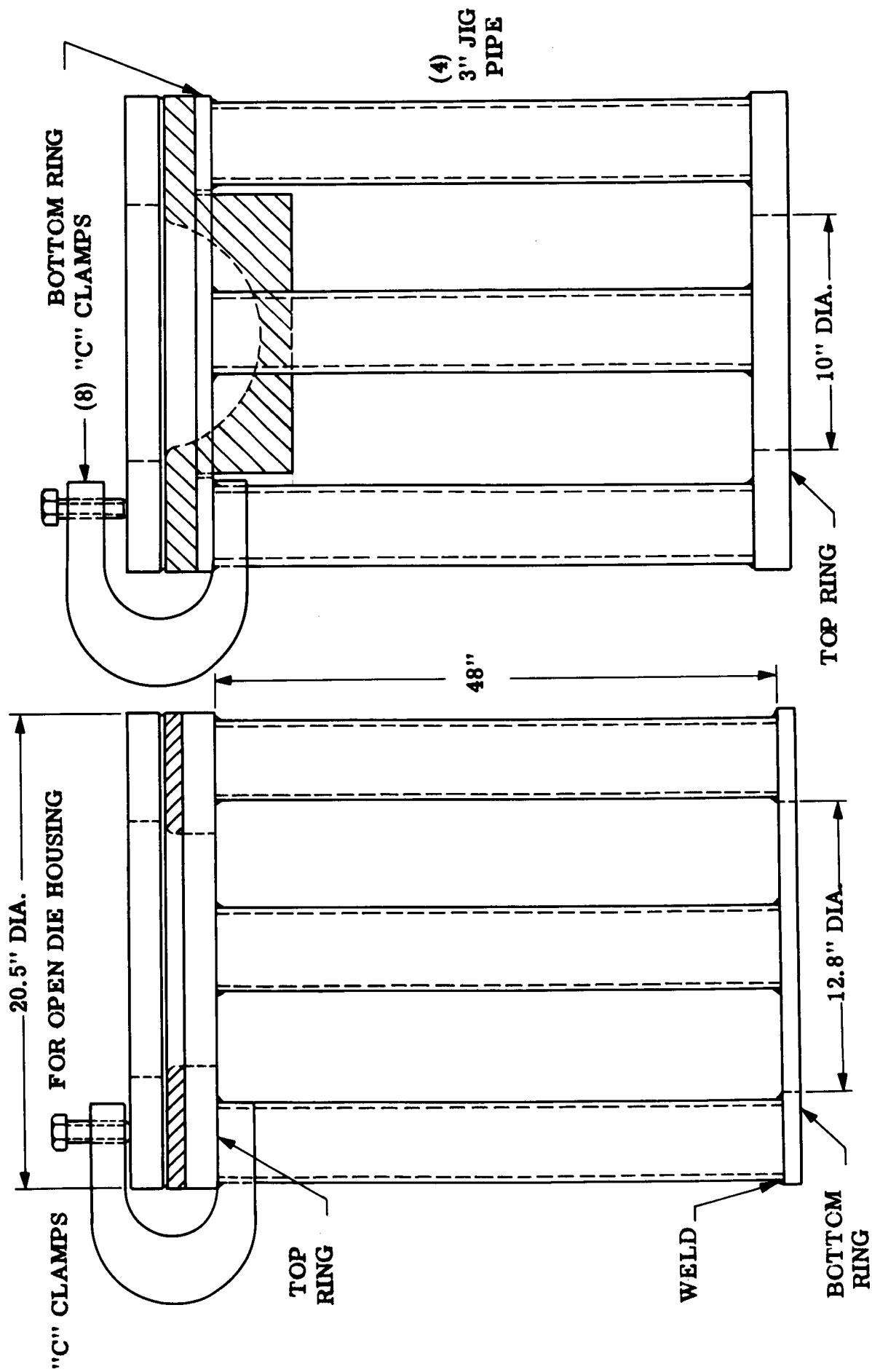
MISCELLANEOUS PHOTOS TAKEN IN THE FIELD  
DURING EXPLOSIVE FORMING EXPERIMENTS

**FIGURE 41**



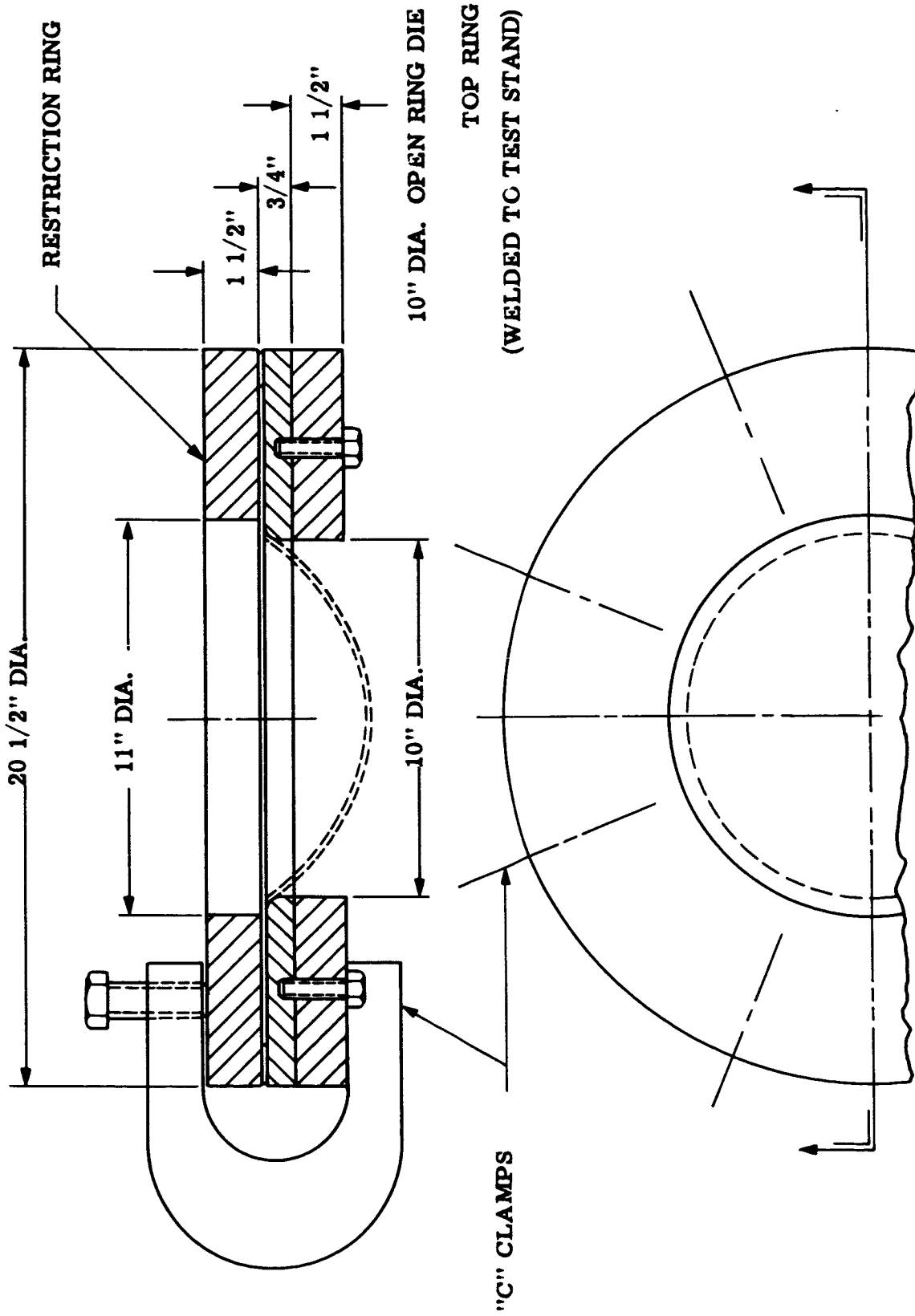
Tooling Used To Explosively "Die Impact" Domes

FIGURE 42



Test Stand Used In Explosive Forming Experiments Showing Compatible Open And Closed Die Housing Methods

FIGURE 43



Tooling Used To Explosively Free Form 10" Dia. Domes

FIGURE 44

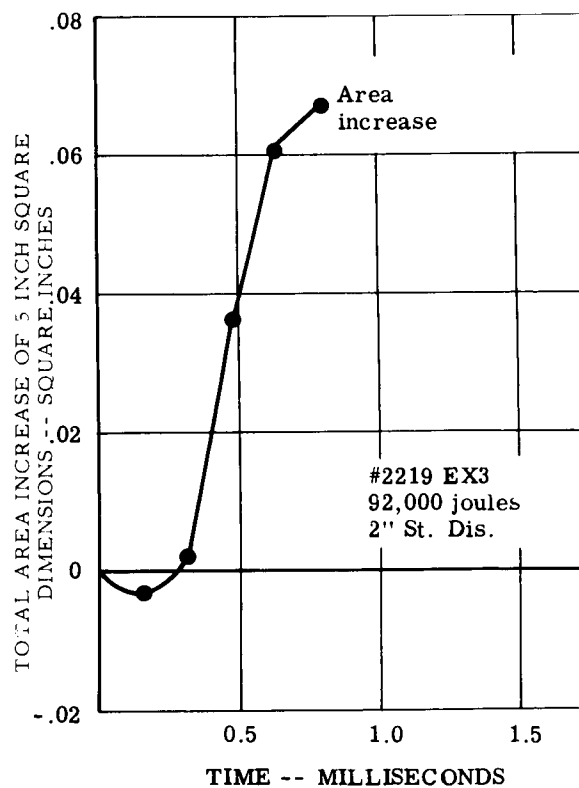
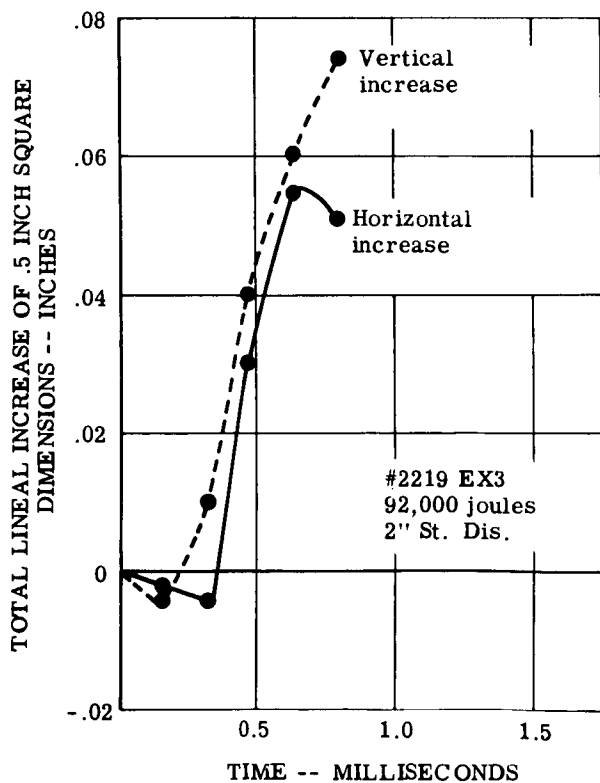
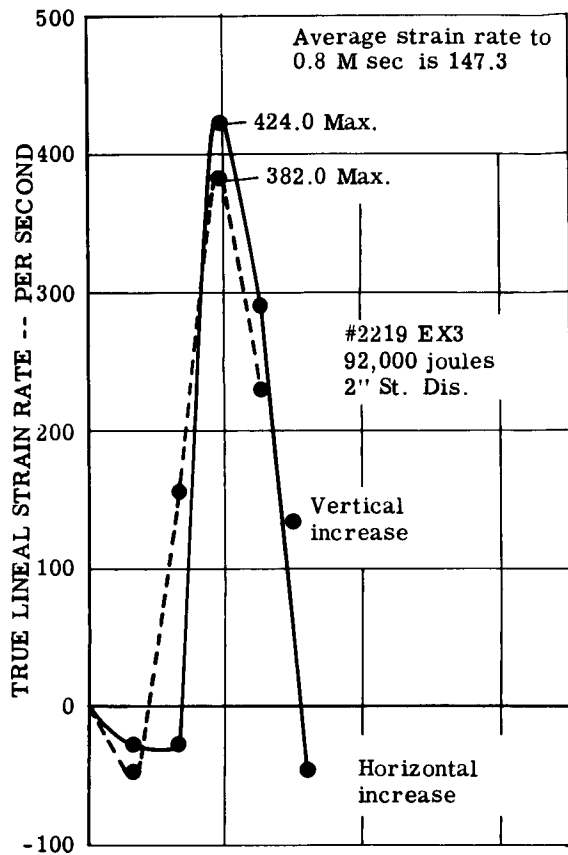


FIGURE 45 TOTAL LINEAL AREA, AND RATE OF STRAIN OF ORIGINAL .5" x .5" CENTER SQUARE FOR .092", 2219-0 ALUMINUM

EXPLOSIVE

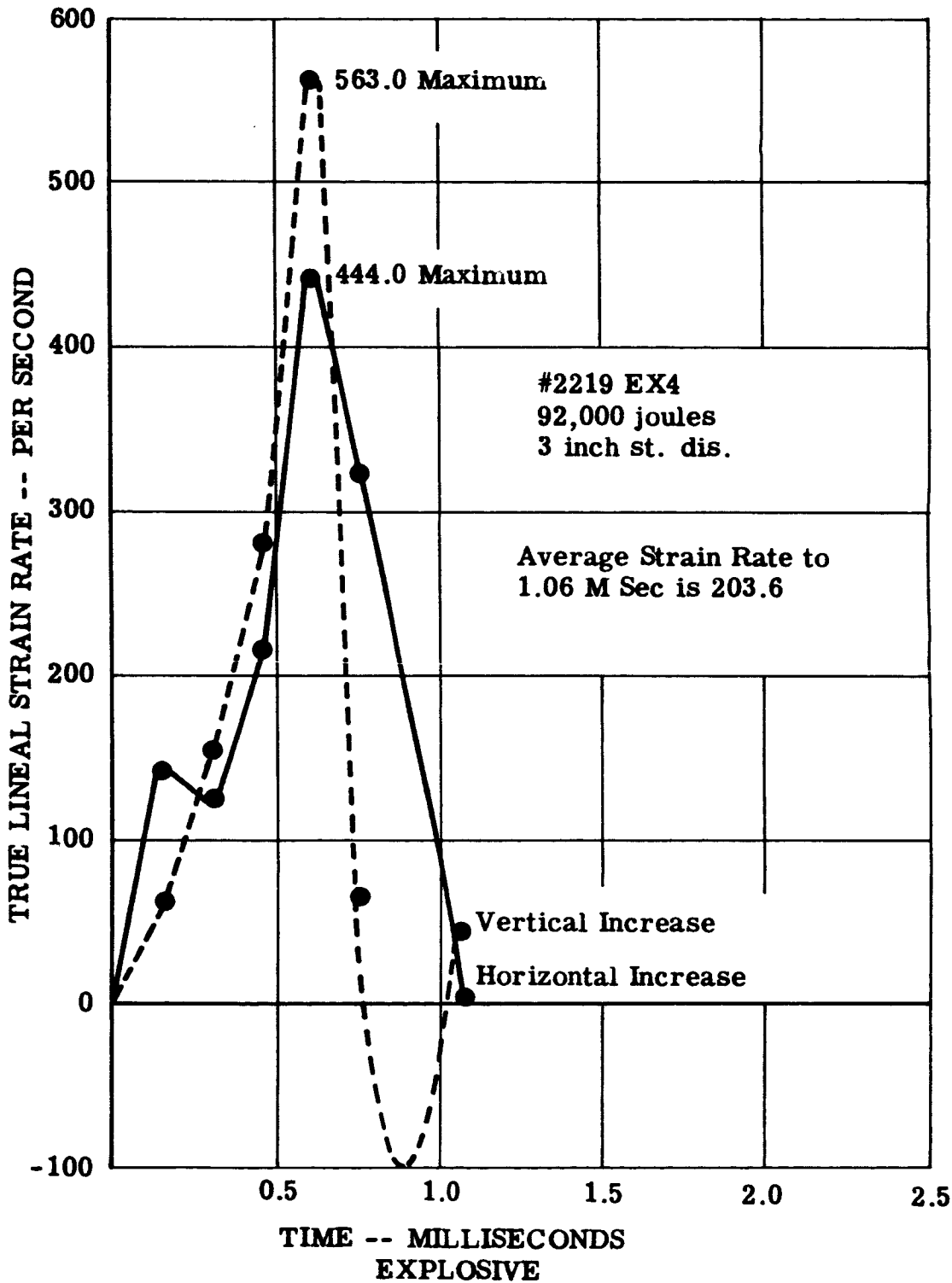


Figure 46 True Linear Strain Rate of .5" x .5" Center Square for .092", 2219-0 Aluminum



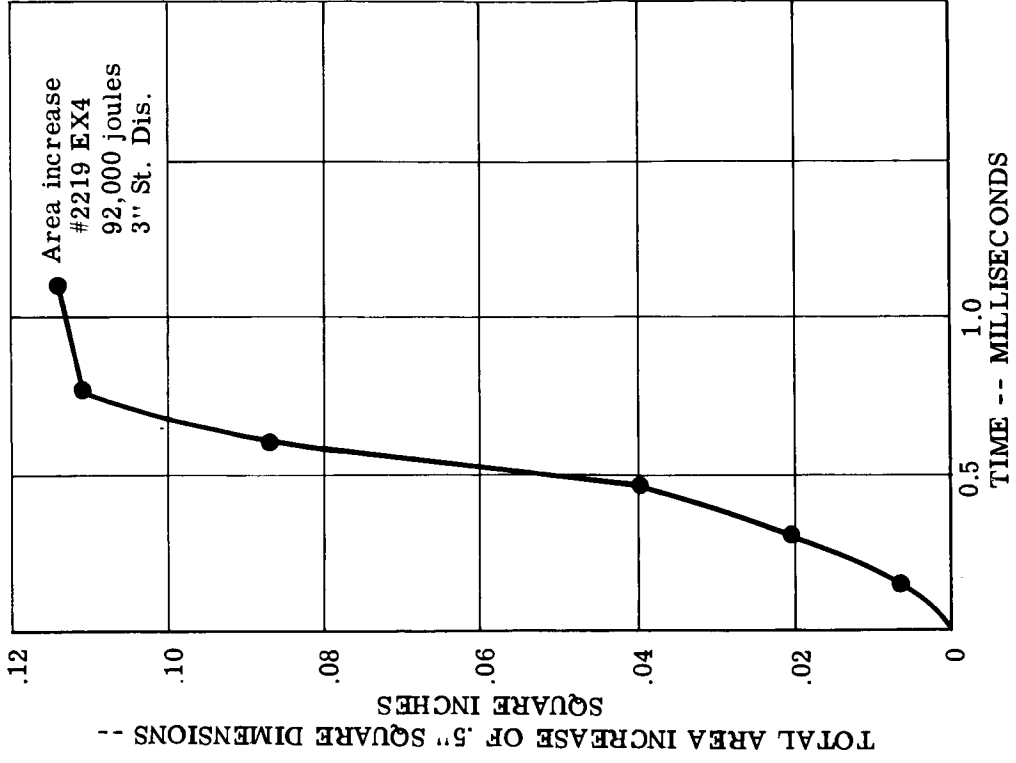
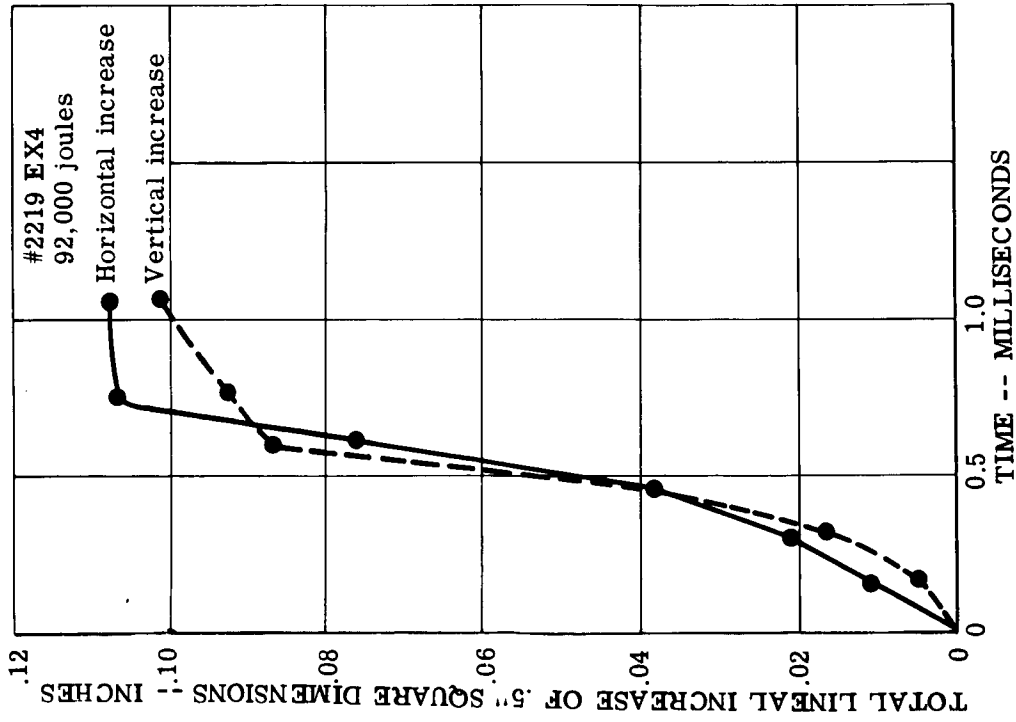


FIGURE 47 TRUE LINEAL STRAIN AND AREA STRAIN OF .5" x .5" CENTER SQUARE FOR .092", 2219-0 ALUMINUM

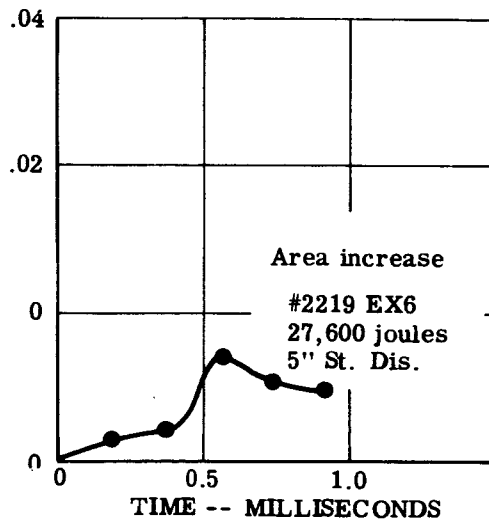
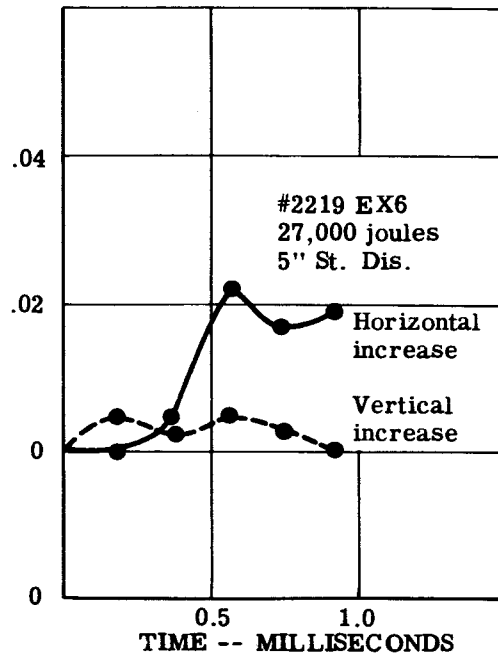
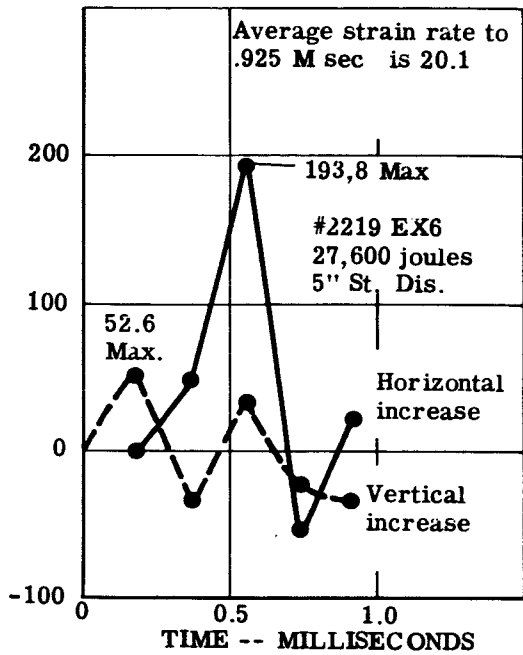


FIGURE 48 TOTAL LINEAL AREA, STRAIN, AND RATE OF STRAIN OF ORIGINAL .5" x .5" CENTER SQUARE FOR 092" 2219-0 ALUMINUM

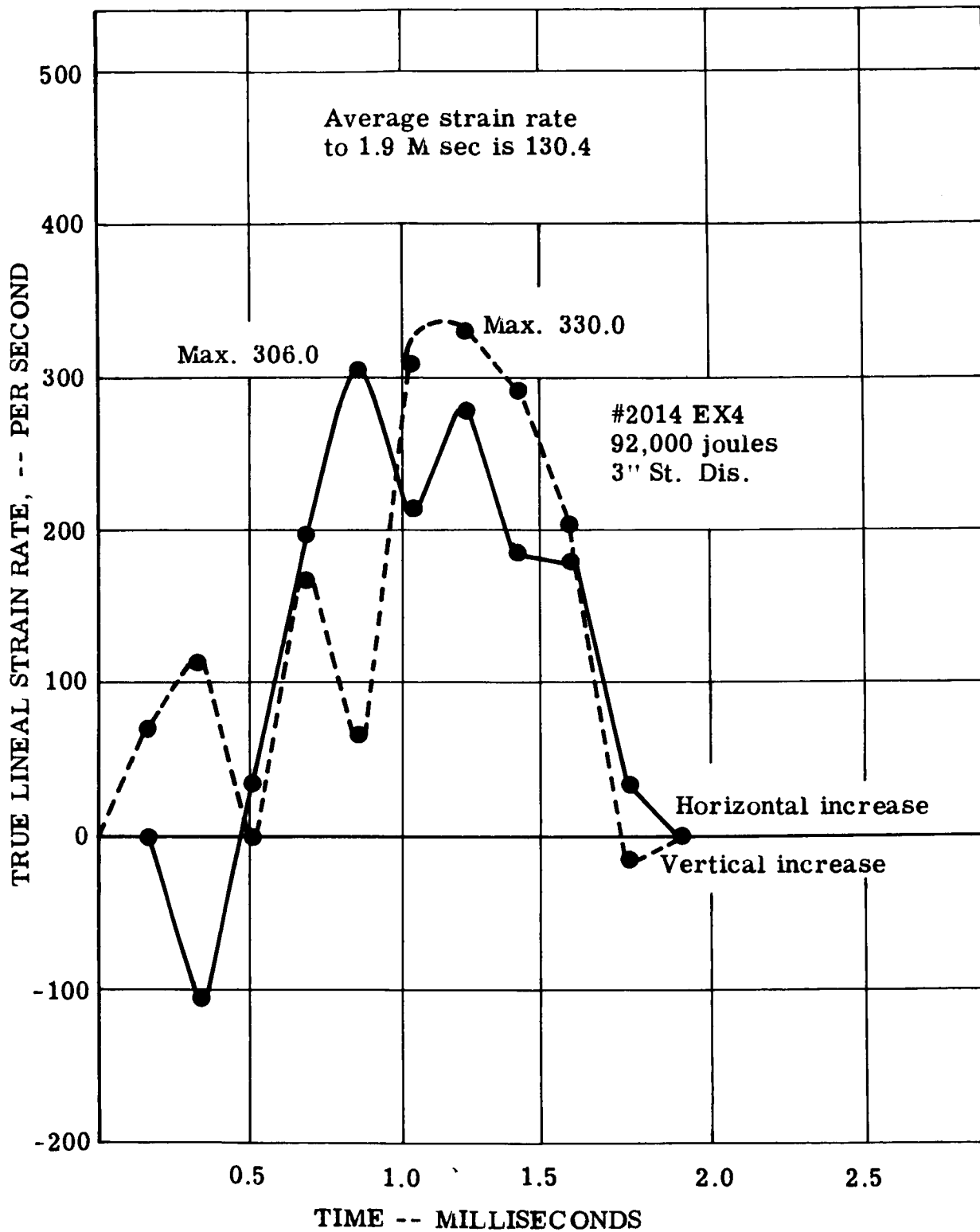


Figure 49 True Lineal Strain Rate of .5" x .5" Center Square for .092", 2014-0 Aluminum

EXPLOSIVE

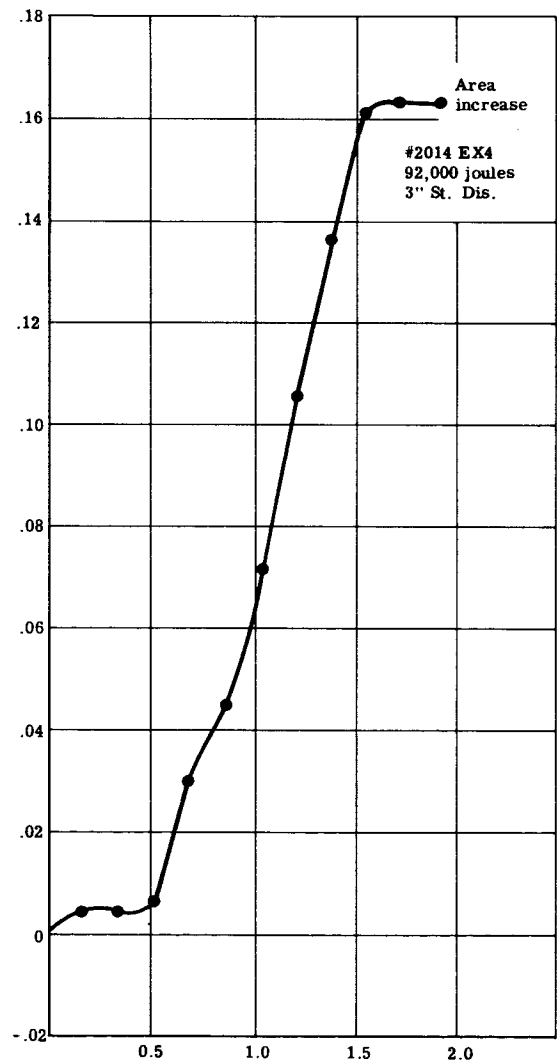
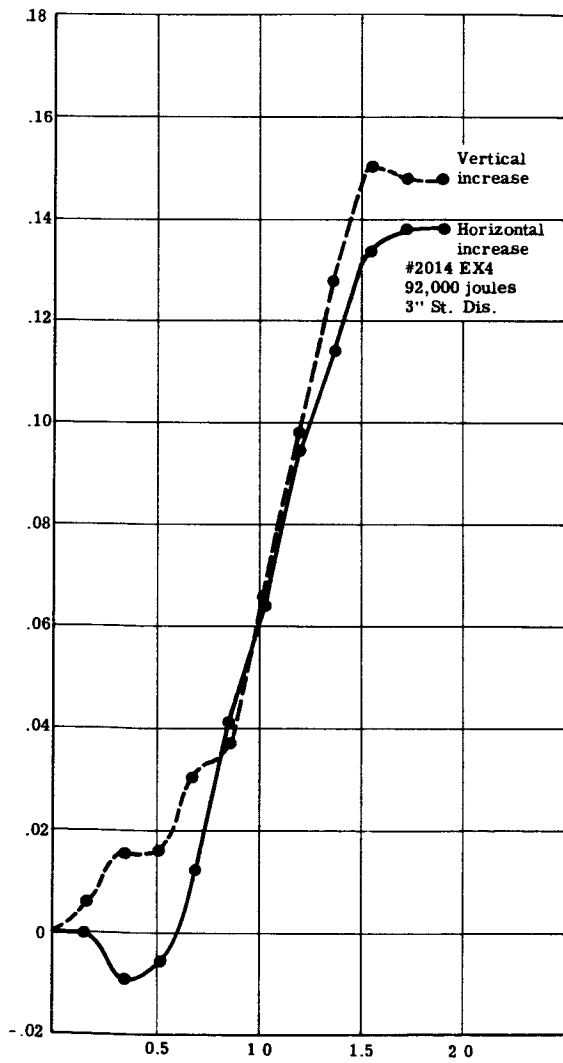
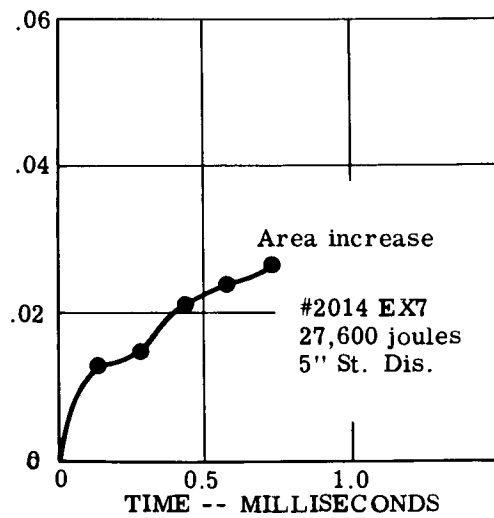
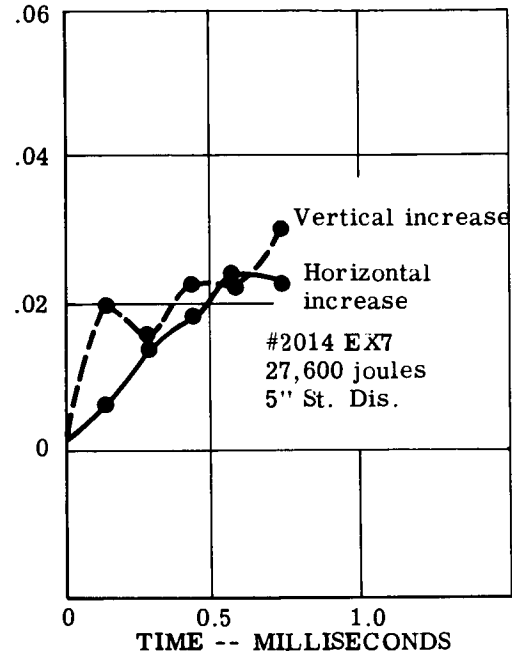
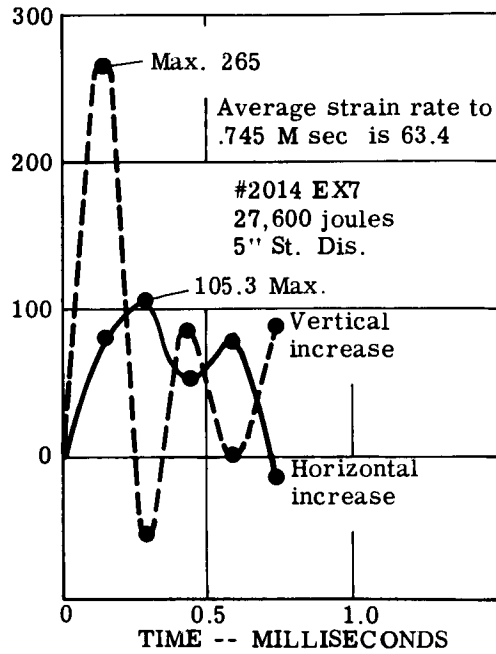


FIGURE 50 TRUE LINEAL STRAIN AND AREA STRAIN OF .5" x .5" CENTER SQUARE FOR .092" .2014-0 ALUMINUM

EXPLOSIVE



**EXPLOSIVE**

FIGURE 51 TOTAL LINEAL AREA STRAIN, AND RATE OF STRAIN OF ORIGINAL .5" x .5" CENTER SQUARE FOR .092", 2014-0 ALUMINUM

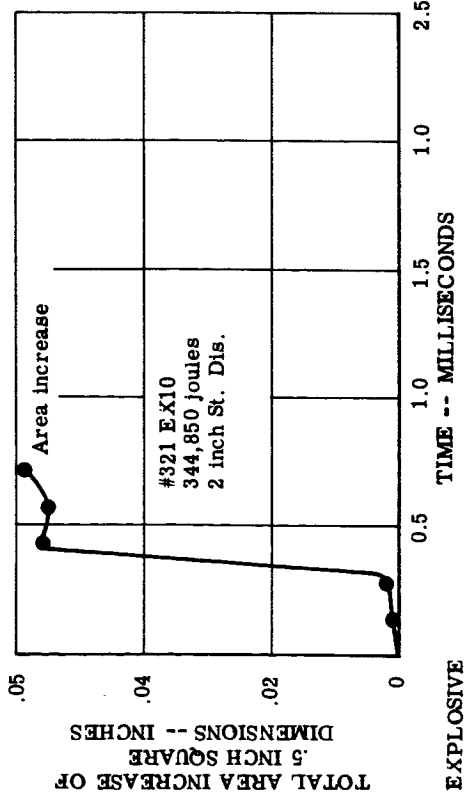
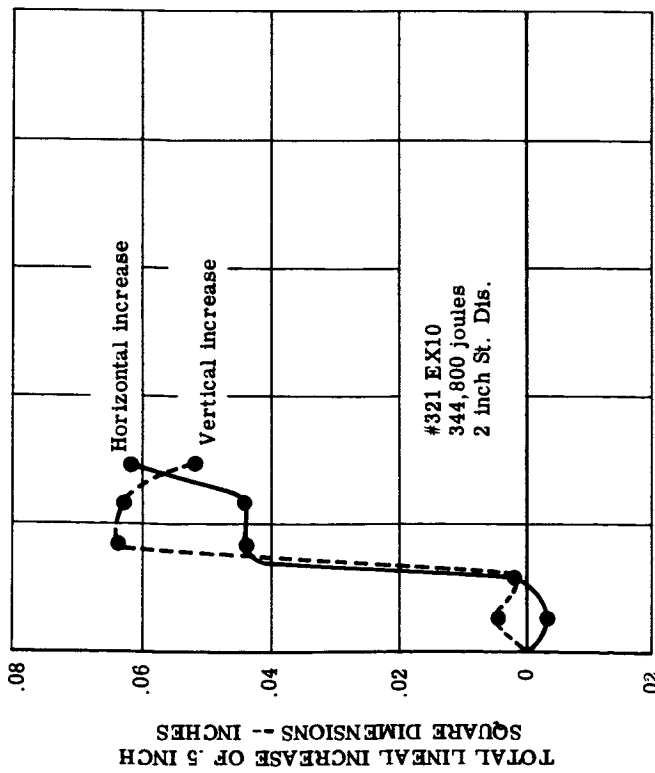
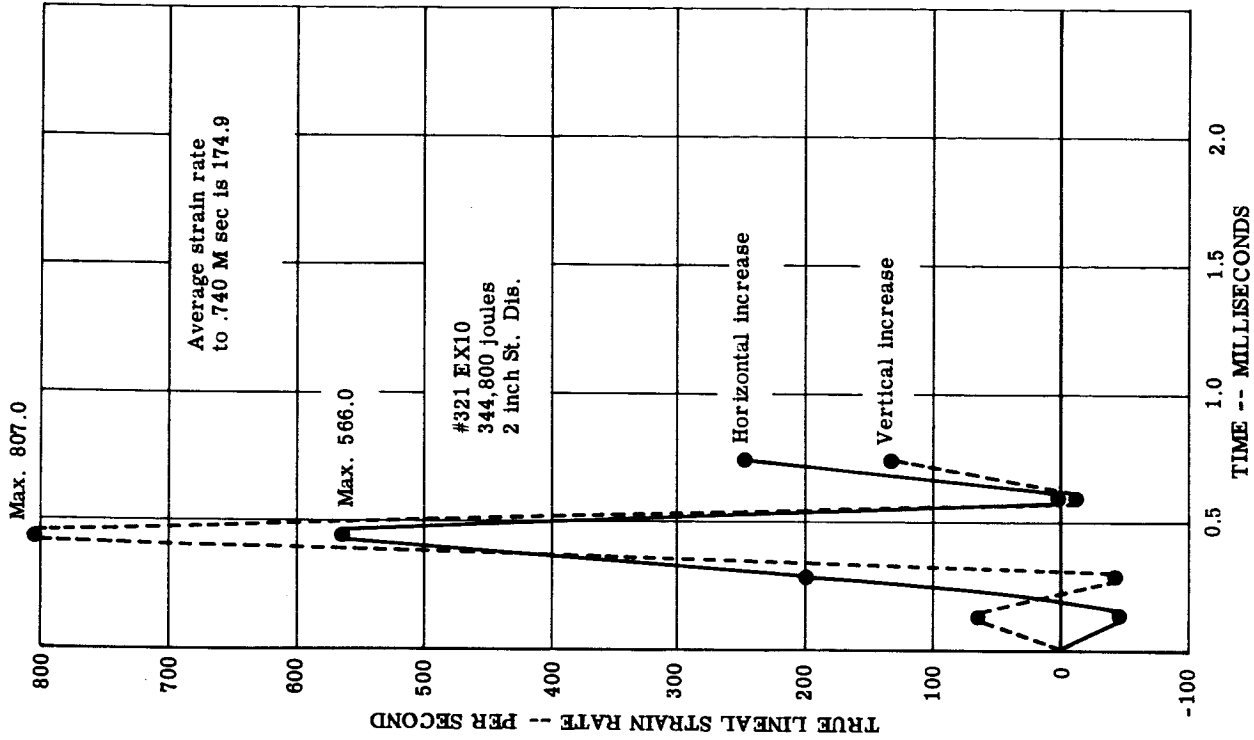


FIGURE 52 TOTAL LINEAL AREA, STRAIN, AND RATE OF STRAIN OF ORIGINAL .5" x .5" CENTER SQUARE FOR .092", 321 STAINLESS STEEL

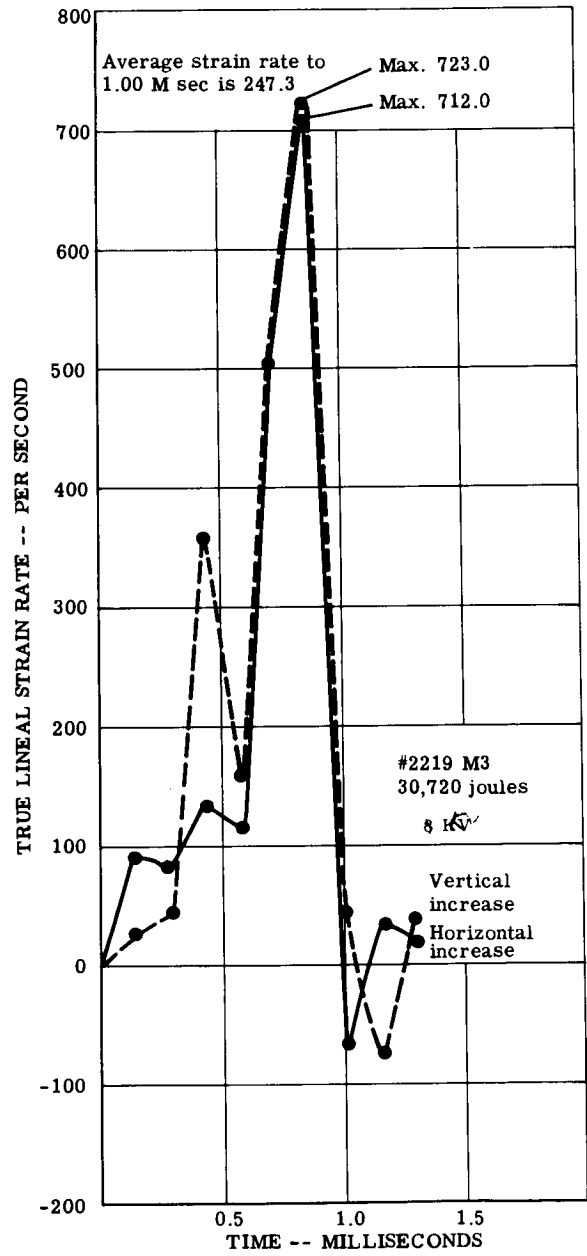
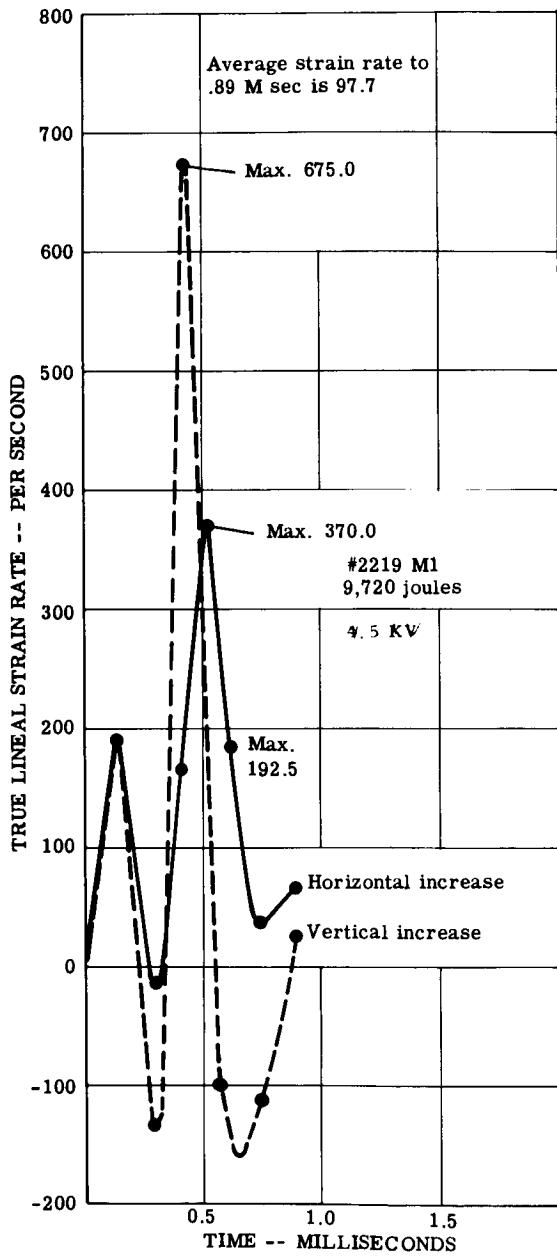


FIGURE 56 TRUE LINEAL STRAIN RATE OF .5" x .5" CENTER SQUARE FOR .092", 2219-0 ALUMINUM

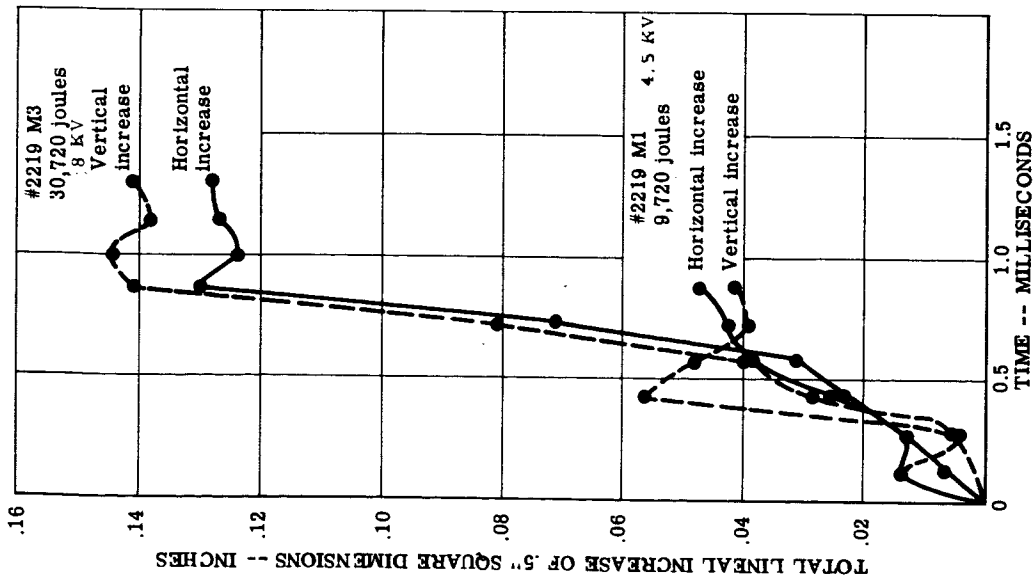
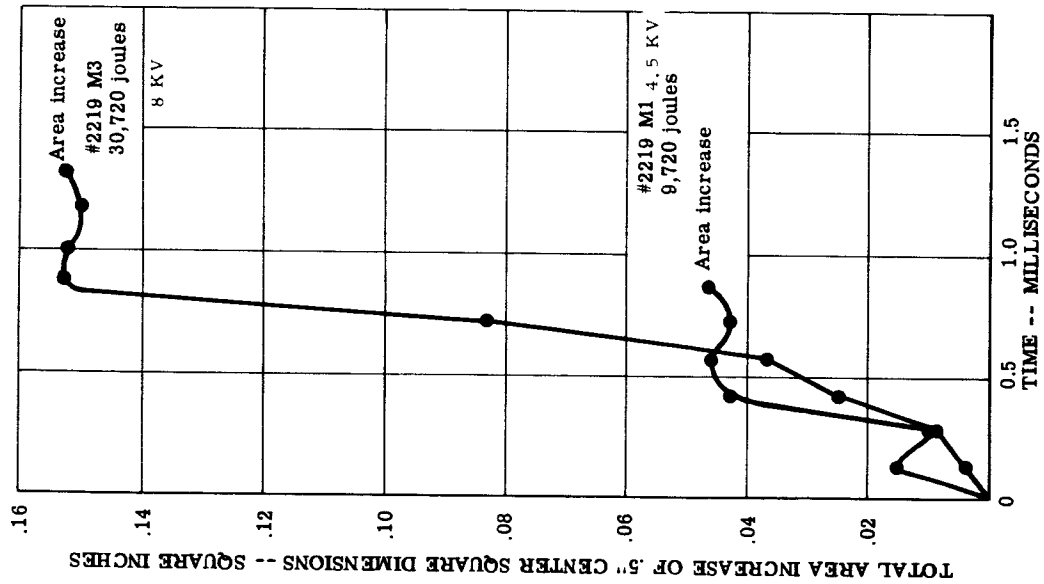


FIGURE 57 TRUE LINEAL STRAIN RATE OF .5" x .5" CENTER SQUARE FOR 092" 2219-0 ALUMINUM

MAGNETIC



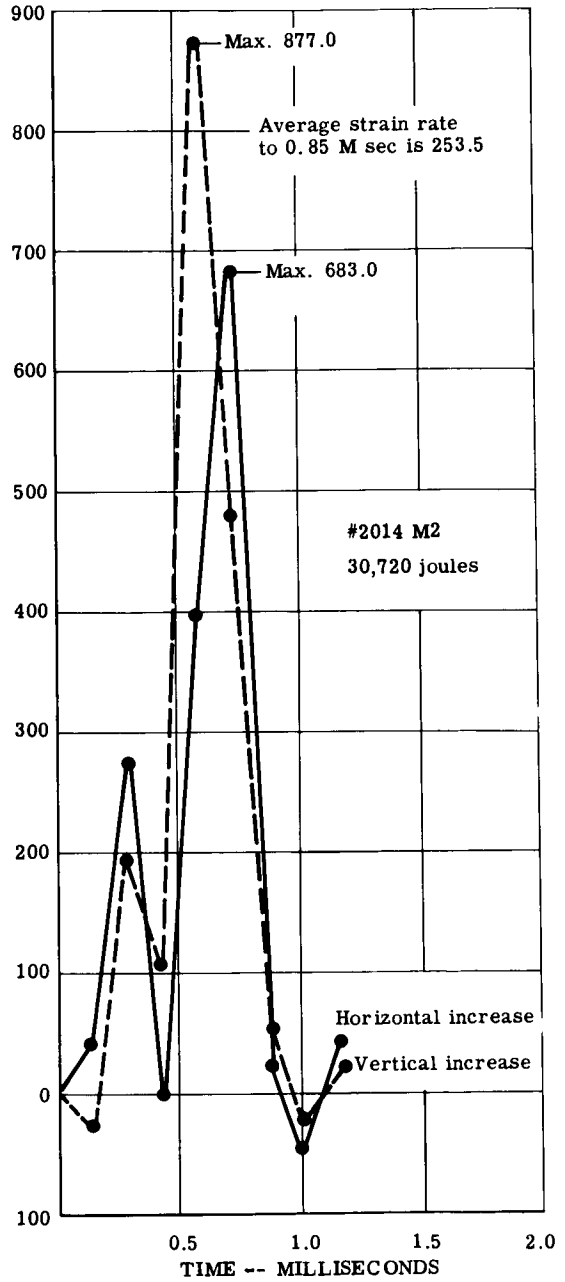
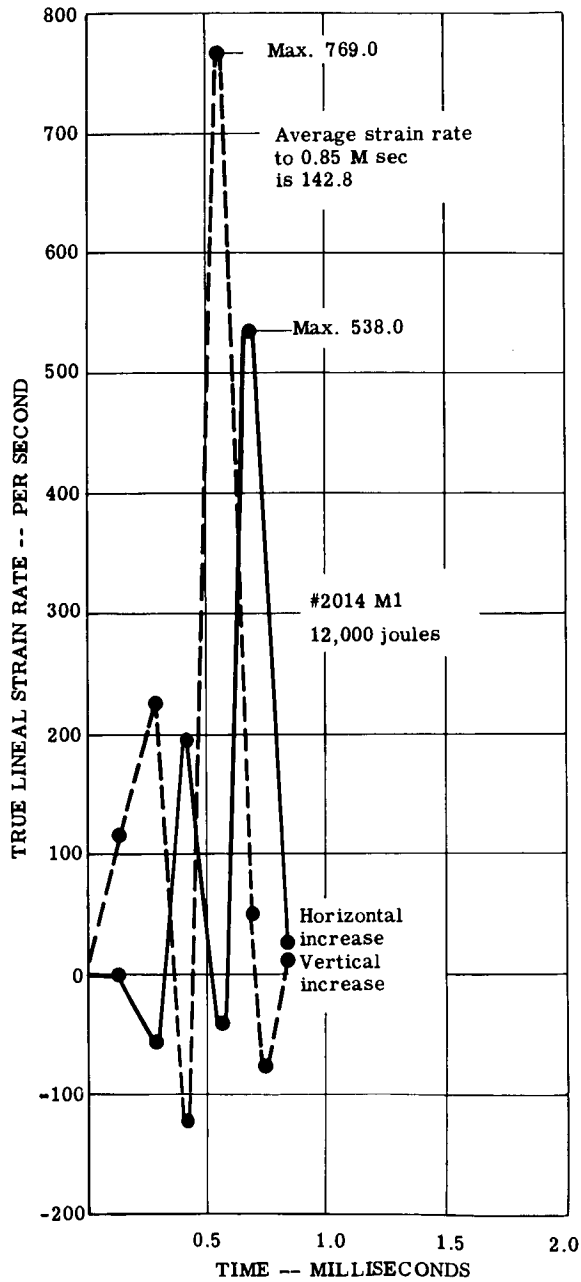


Figure 58 True Lineal Strain Rate of .5" x .5" Center Square for .092", 2014-0 Aluminum

MAGNETIC

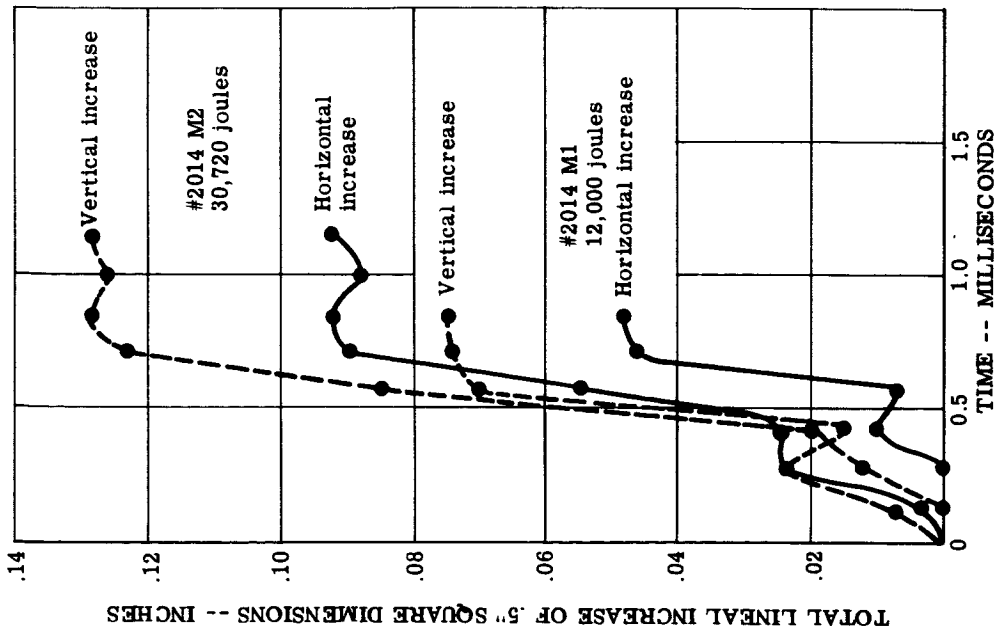
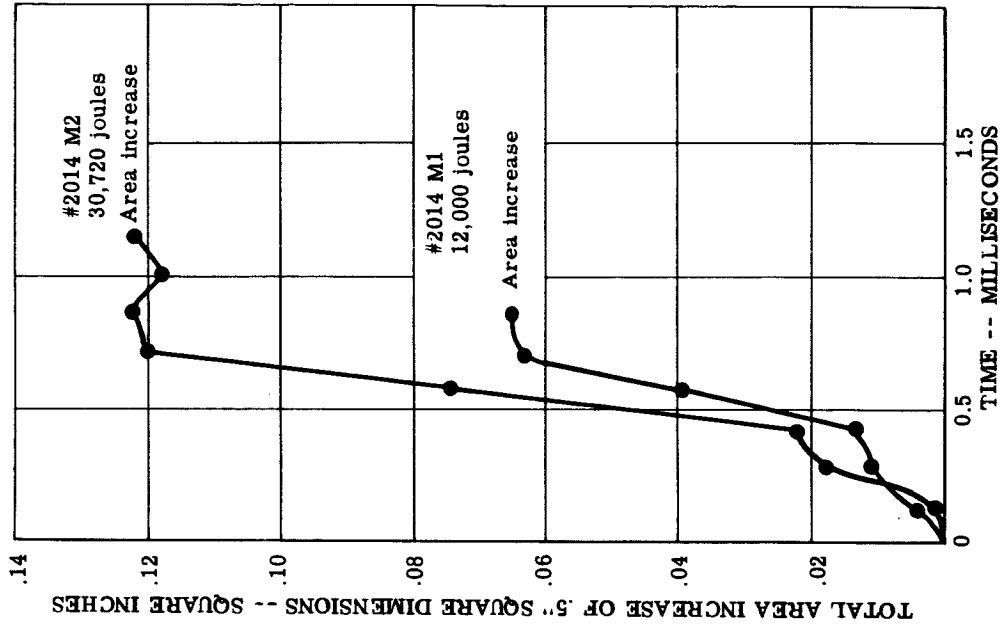
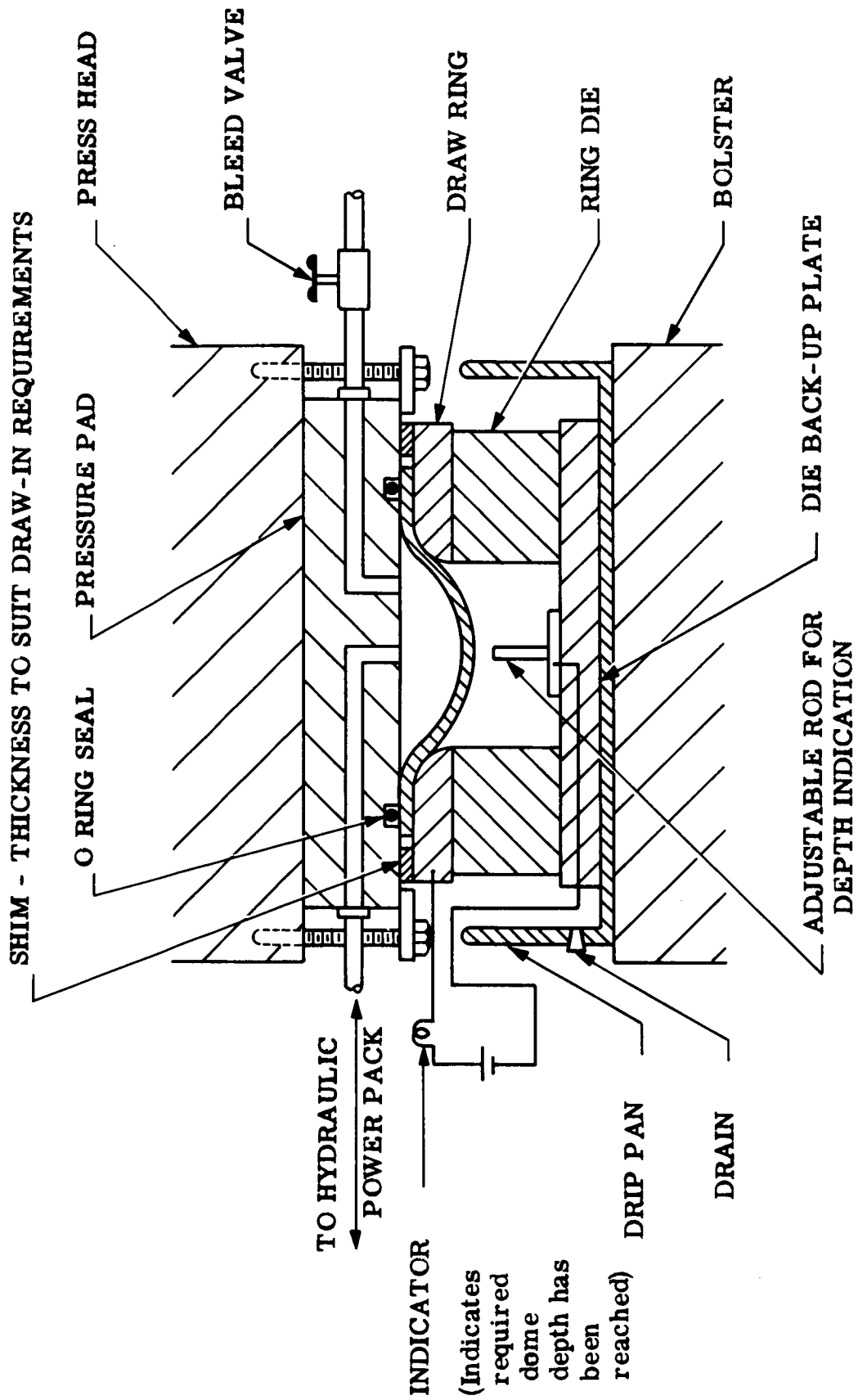


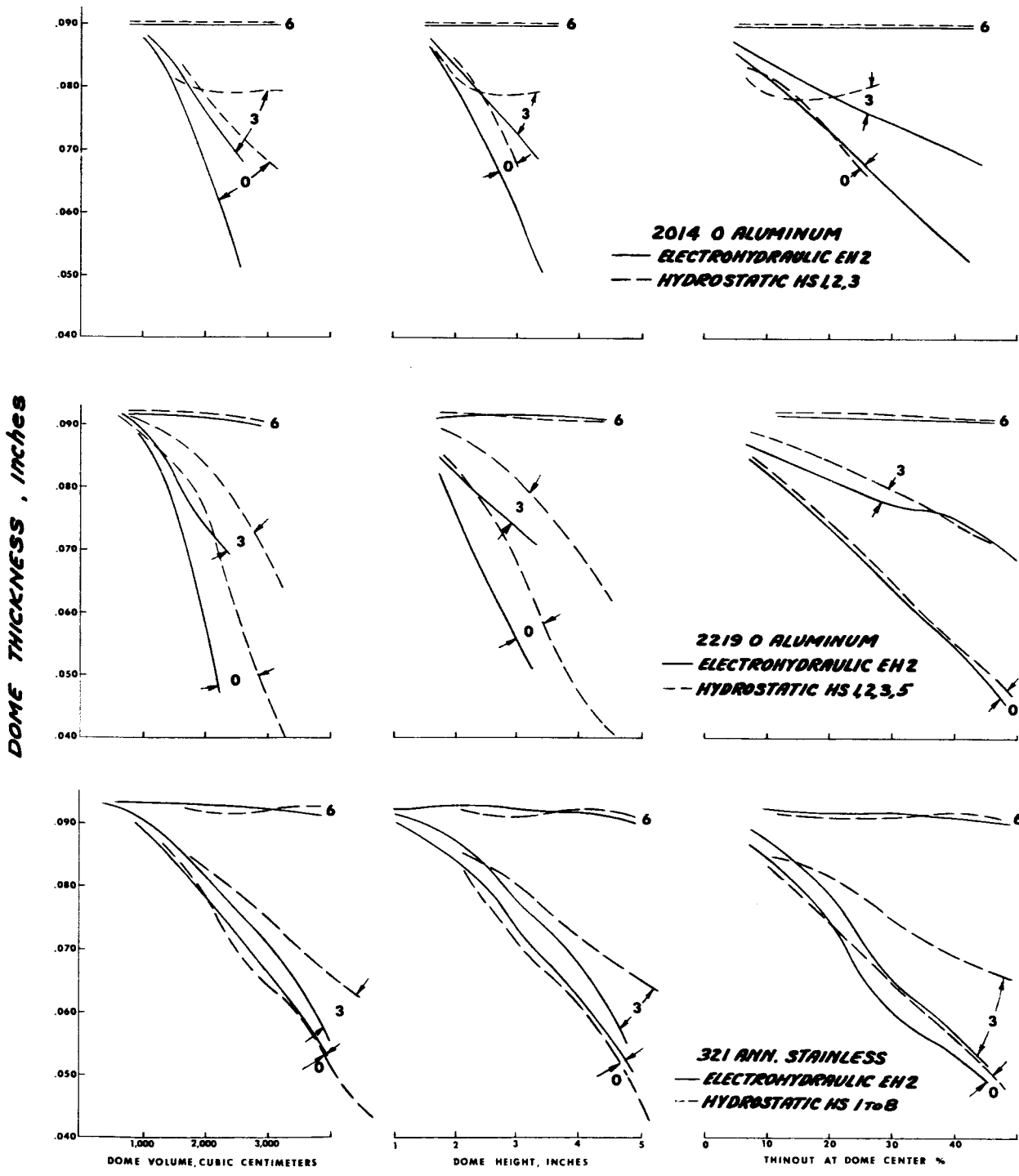
FIGURE 59 TRUE LINEAL STRAIN RATE OF .5" x .5" CENTER SQUARE FOR .092" 2014-0 ALUMINUM

MAGNETIC



Schematic Sketch of Hydrostatic Dome Forming Experiments  
On Lake Erie Press

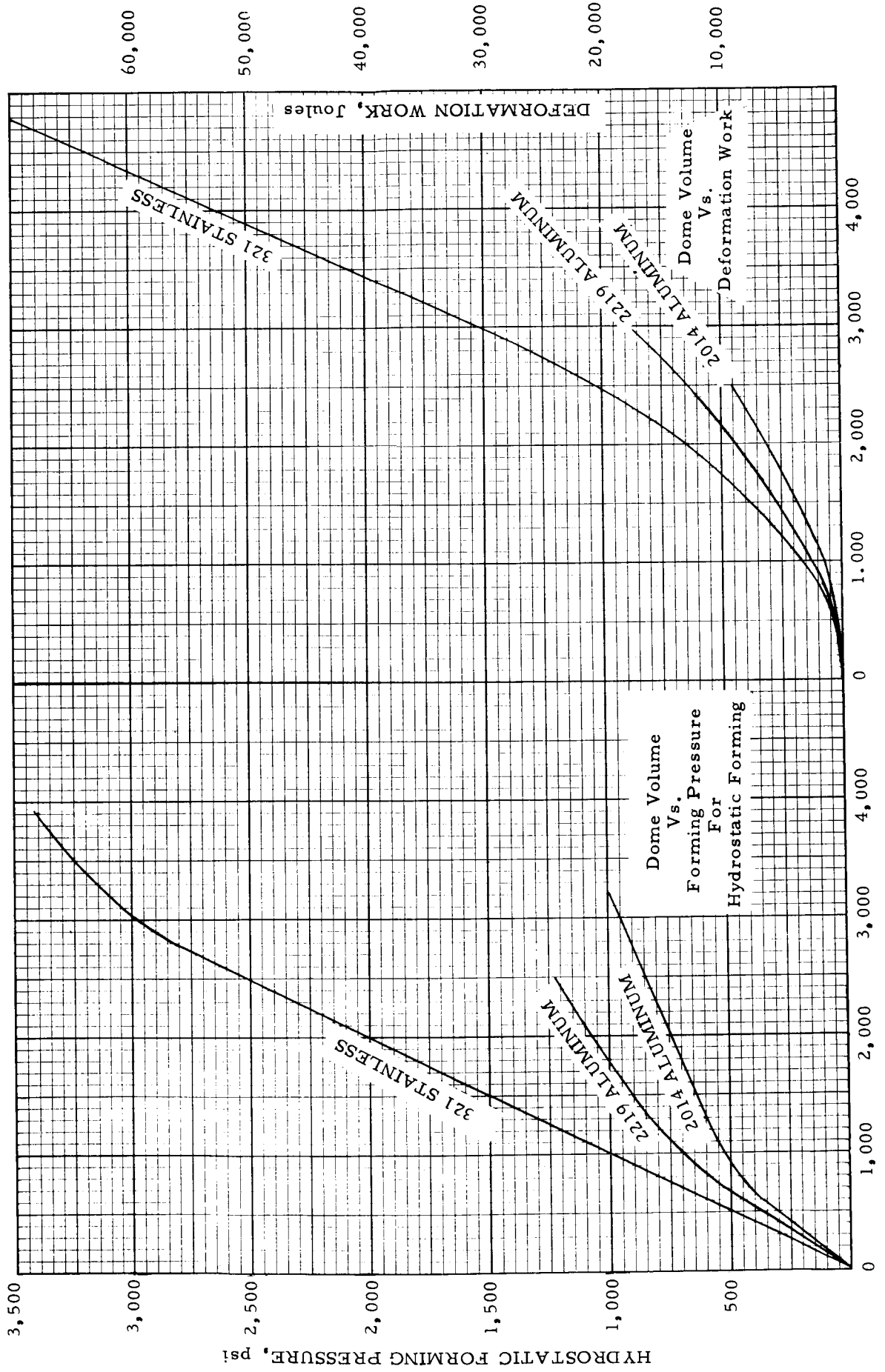
FIGURE 60



NOTE: 0, 3 & 6 ARE MEASUREMENT POSITIONS FROM DOME CENTER FROM TABLE 4

DIFFERENCE OF ELECTROHYDRAULIC AND HYDROSTATIC THINOUT GRADIENT IN TERMS OF VOLUME, HEIGHT & CENTER THINOUT

FIGURE 61



DOME VOLUME, cubic centimeters,

FIGURE 62

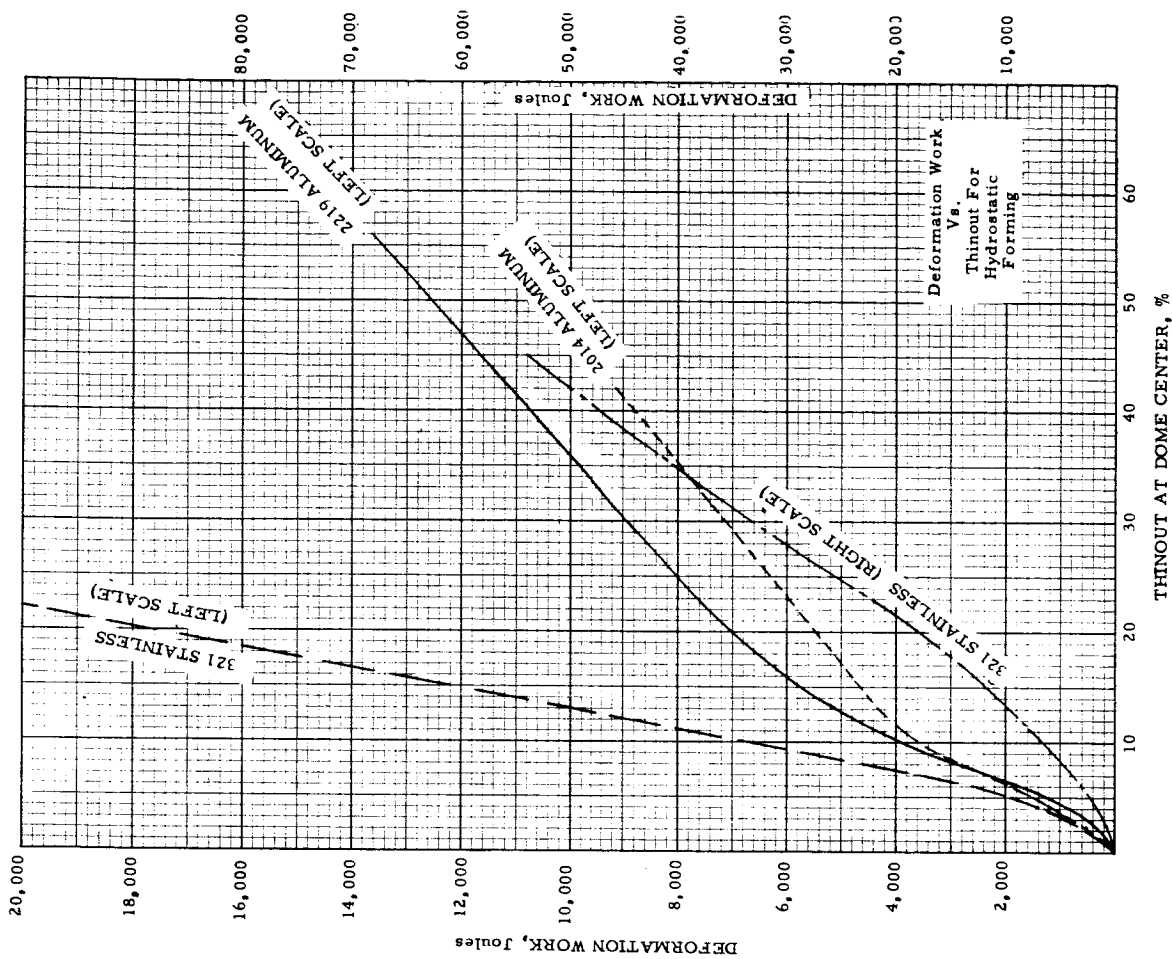


FIGURE 64

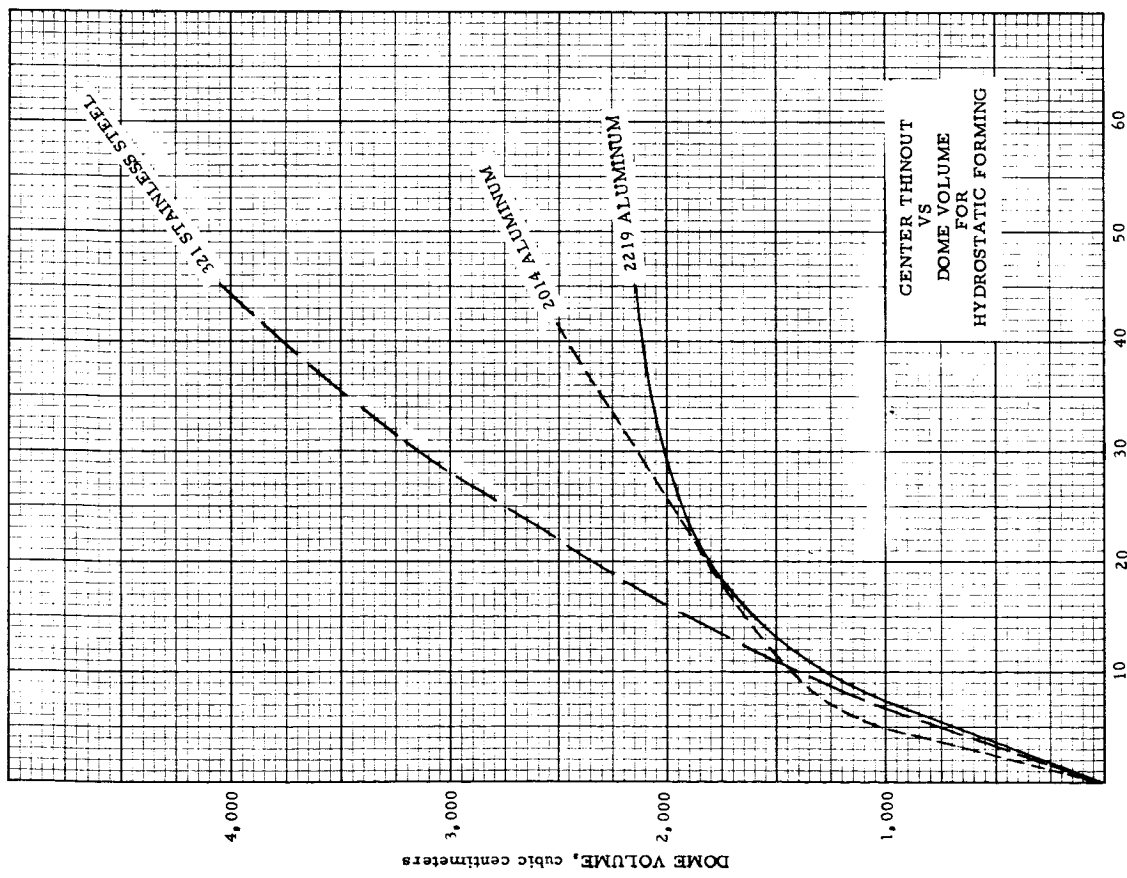


FIGURE 63

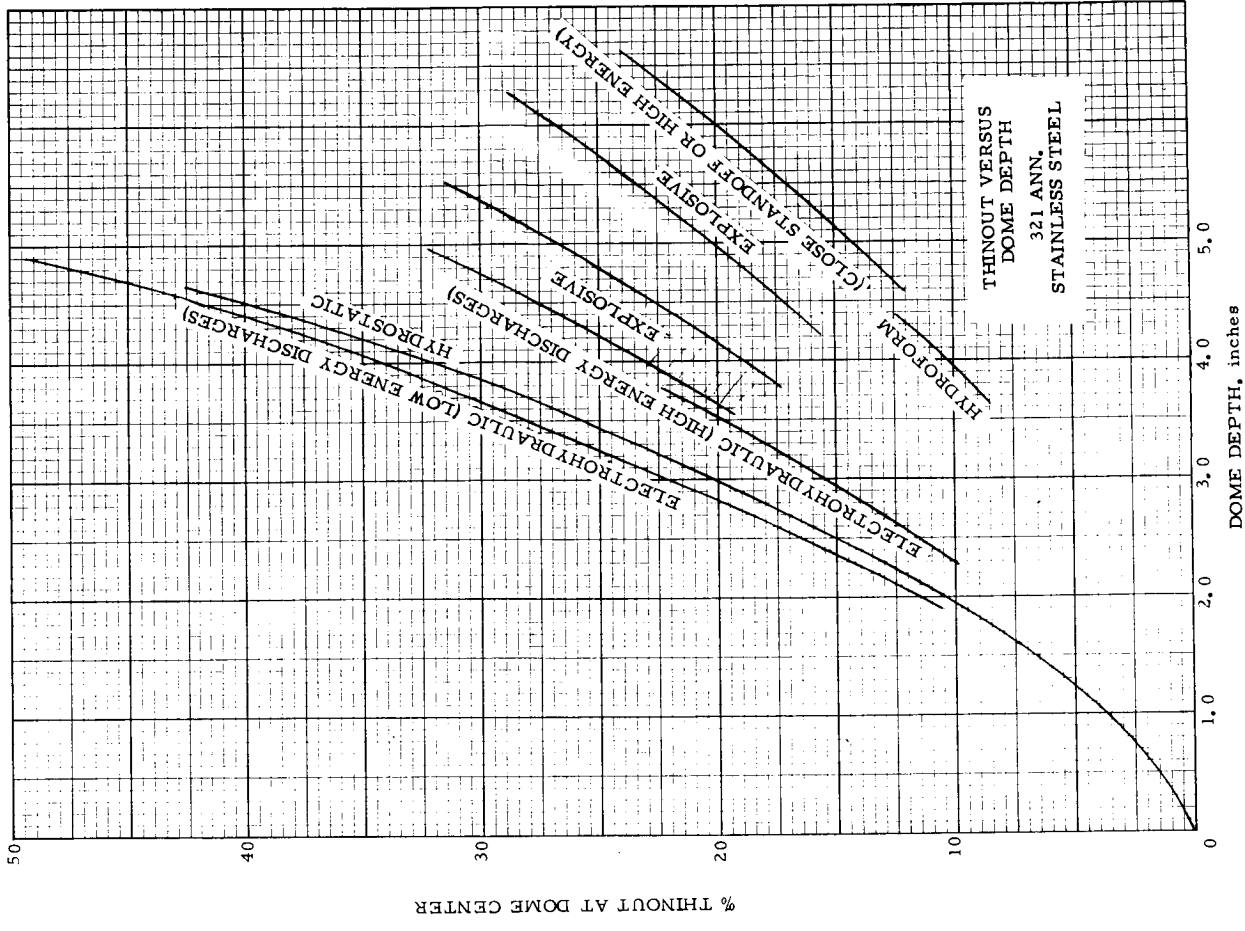


FIGURE 66

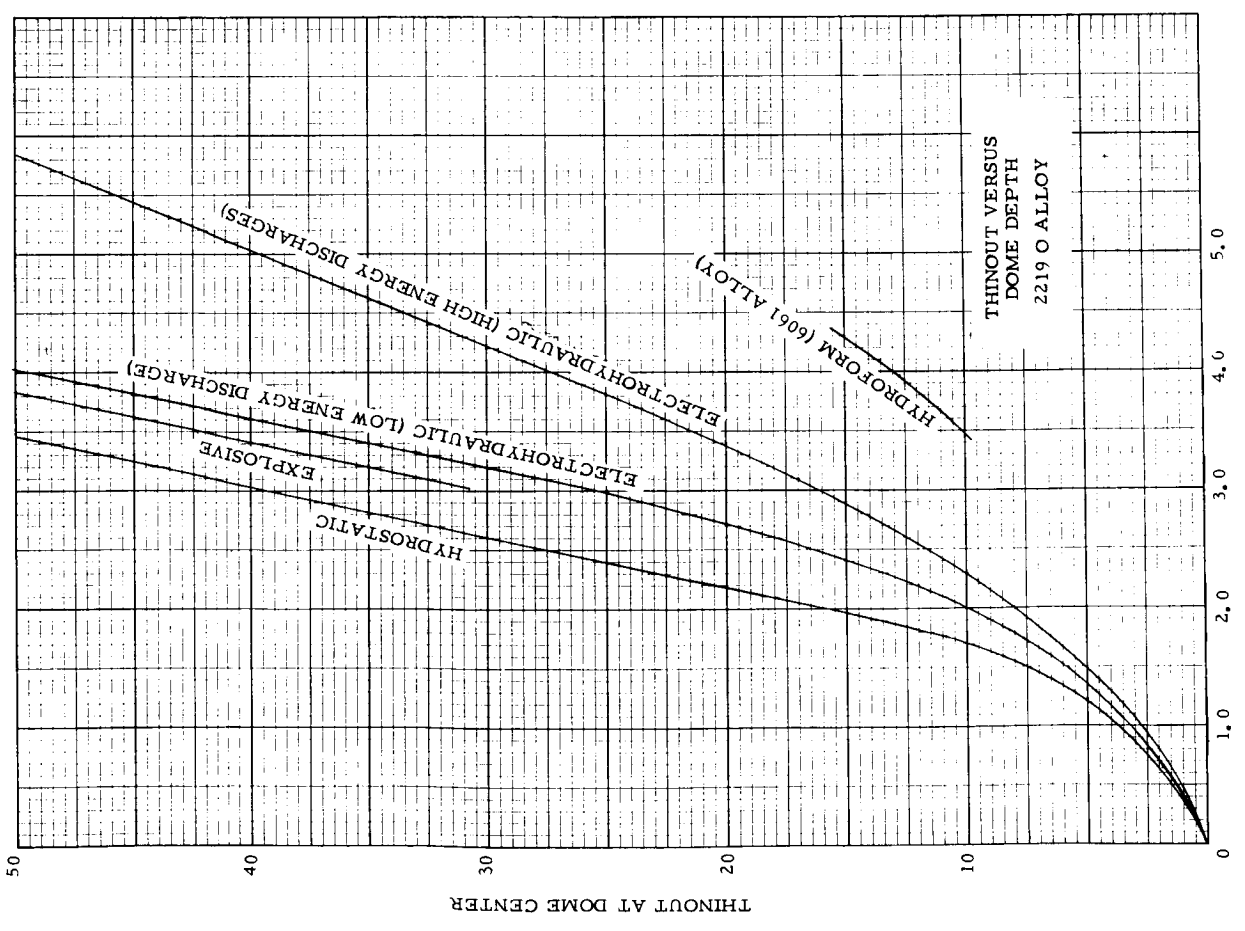


FIGURE 65

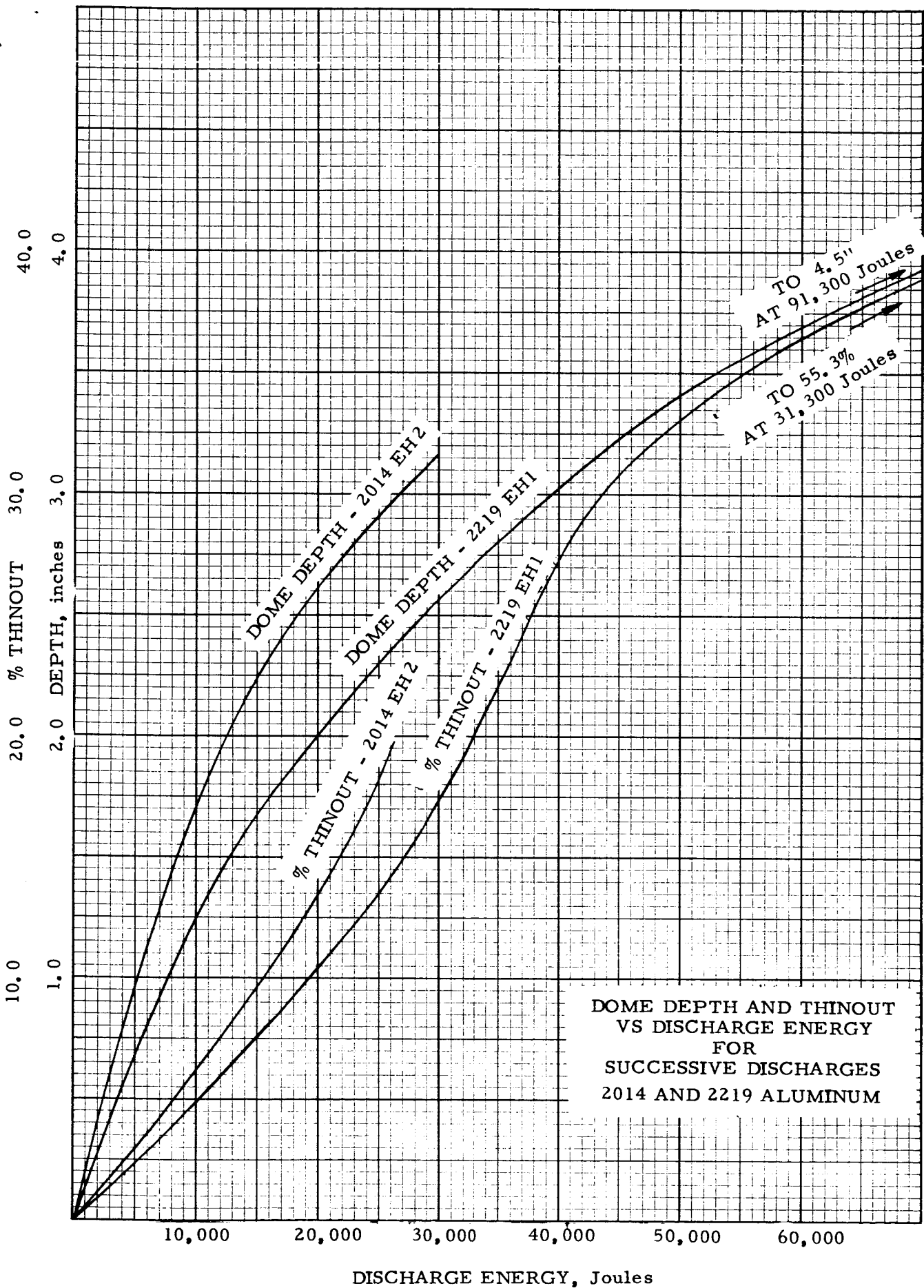


FIGURE 67



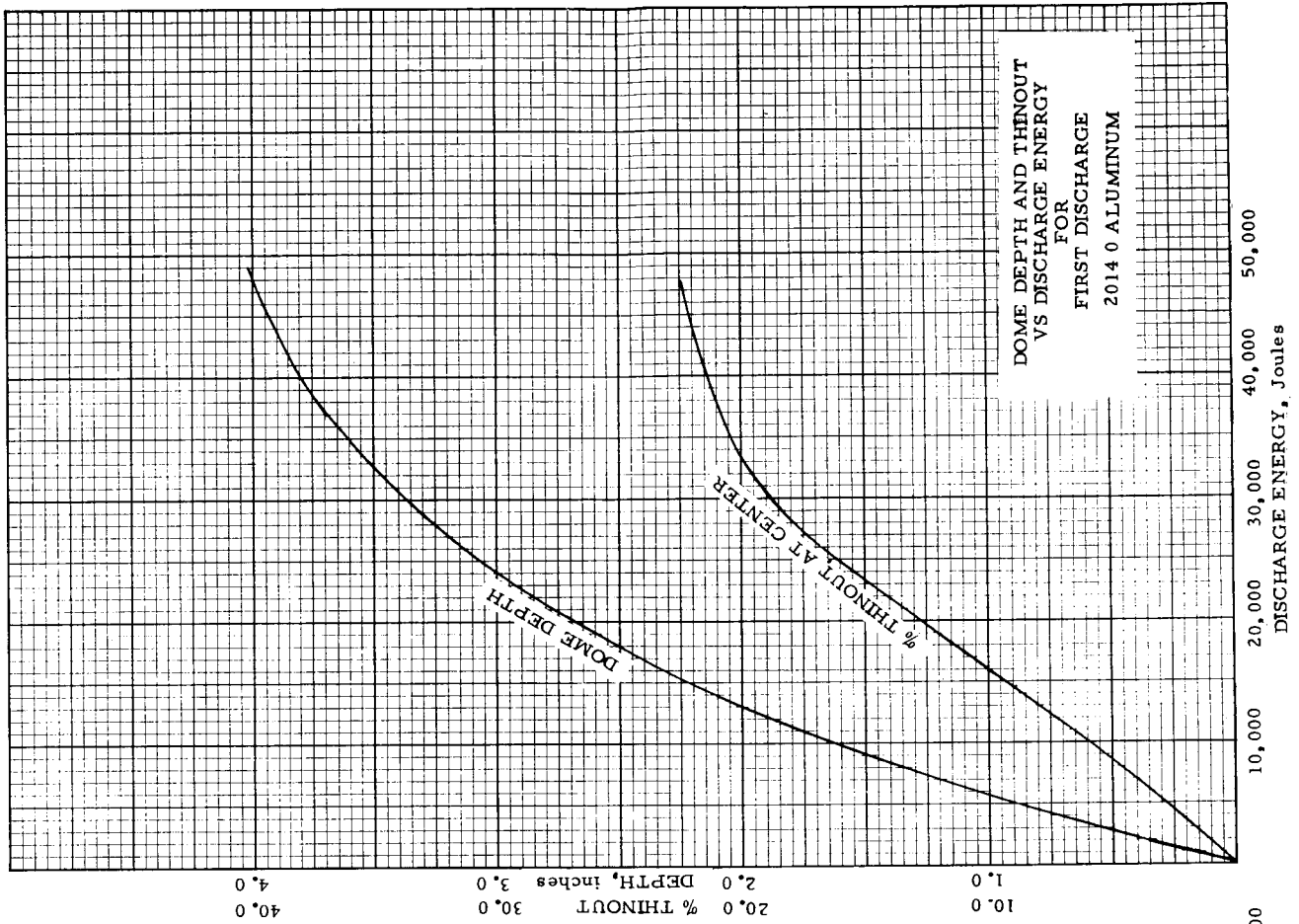


FIGURE 65

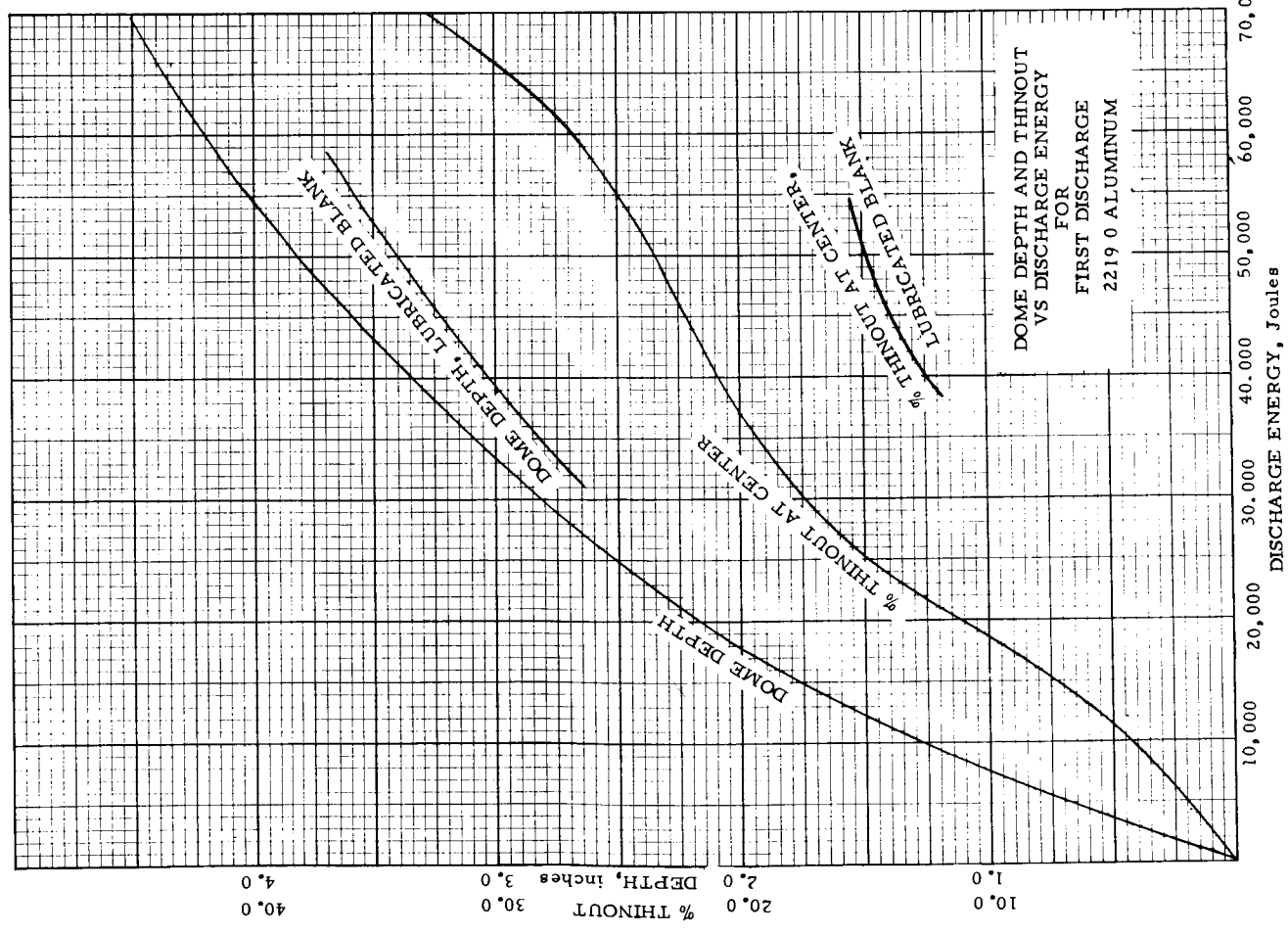


FIGURE 68

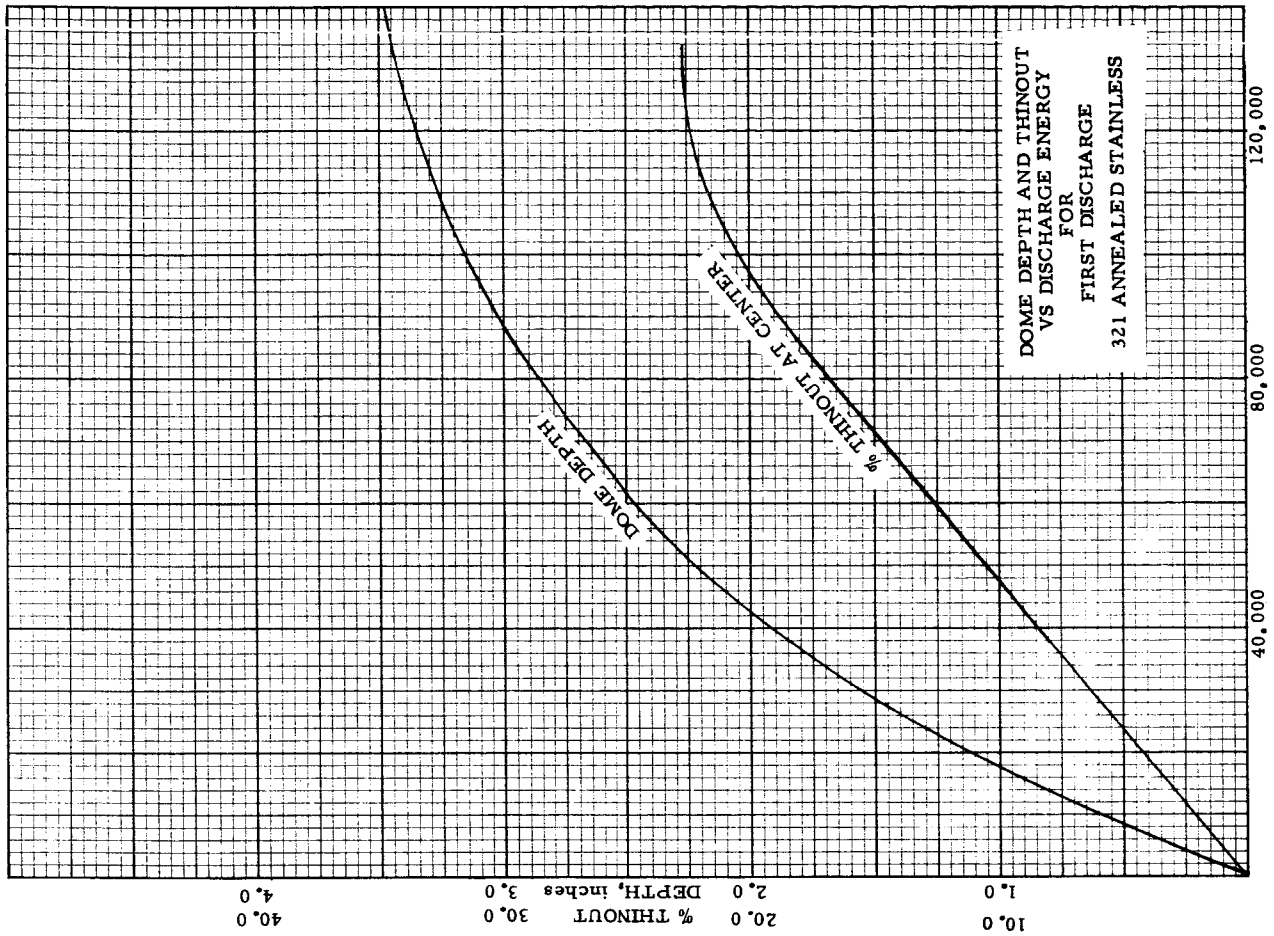


FIGURE 71

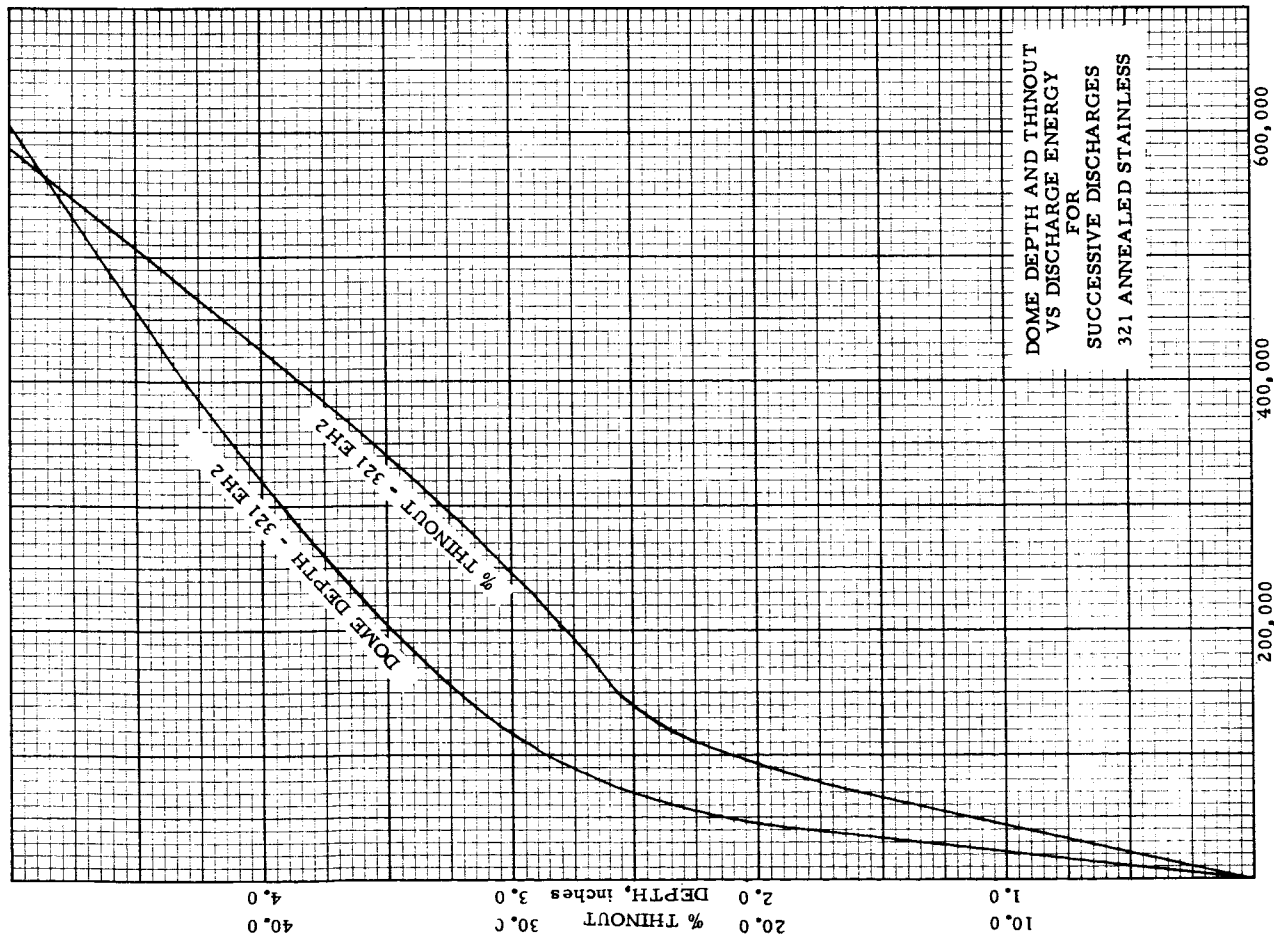
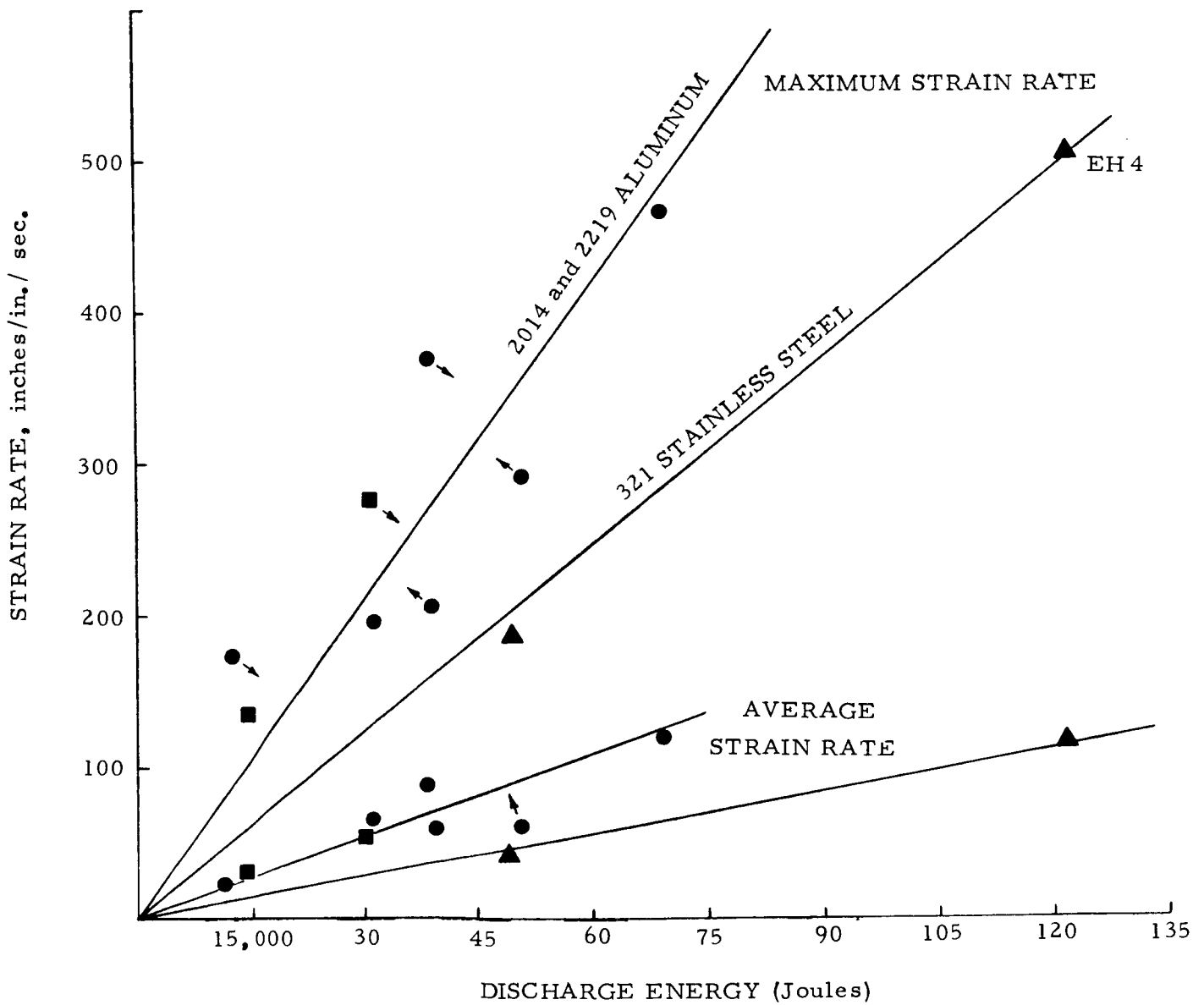


FIGURE 70

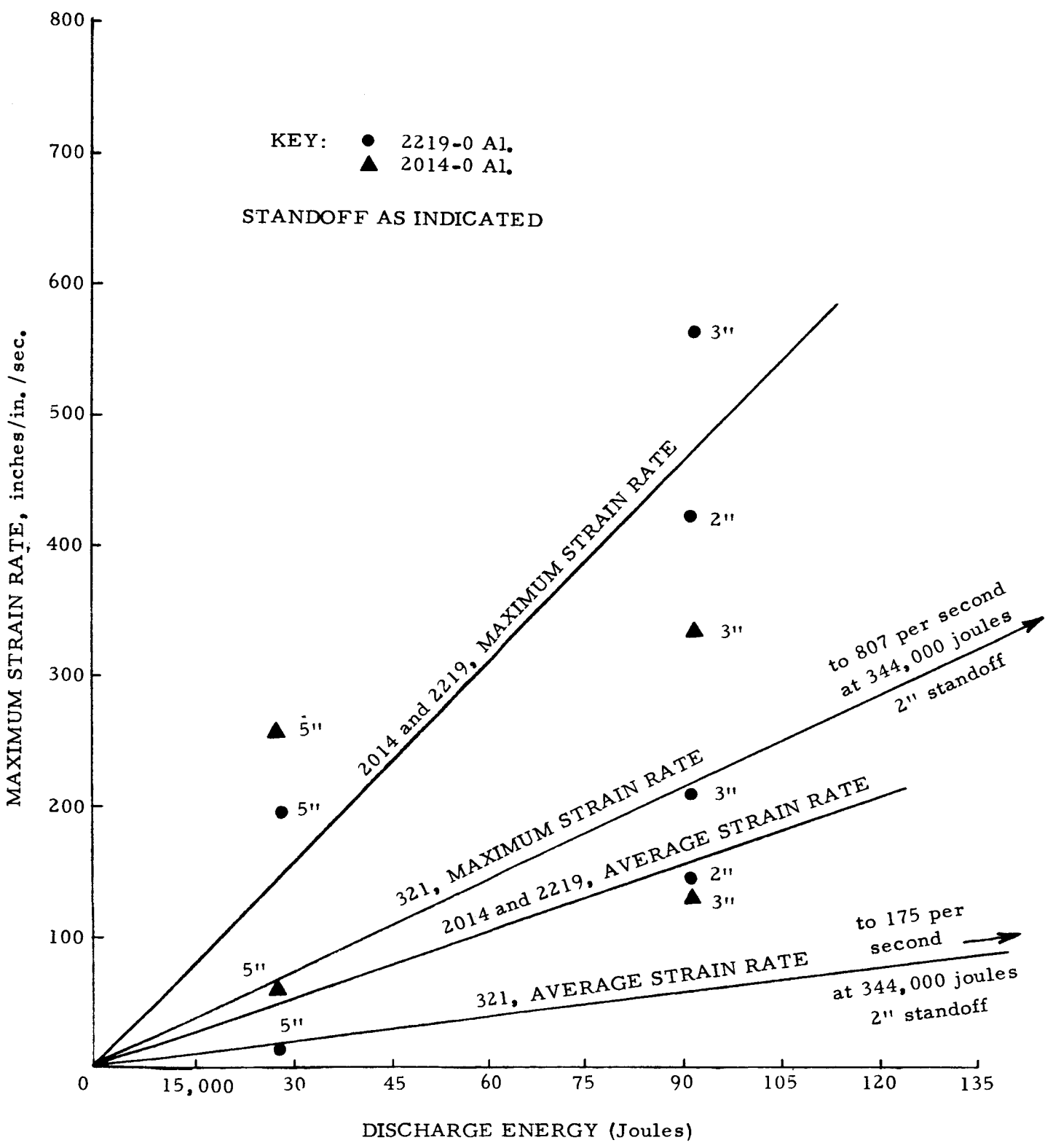
KEY: ● 2219-0, Al  
 ■ 2014-0, Al  
 ▲ 321 St. St. Ann.

STANDOFF 1 1/4" FOR ALL POINTS



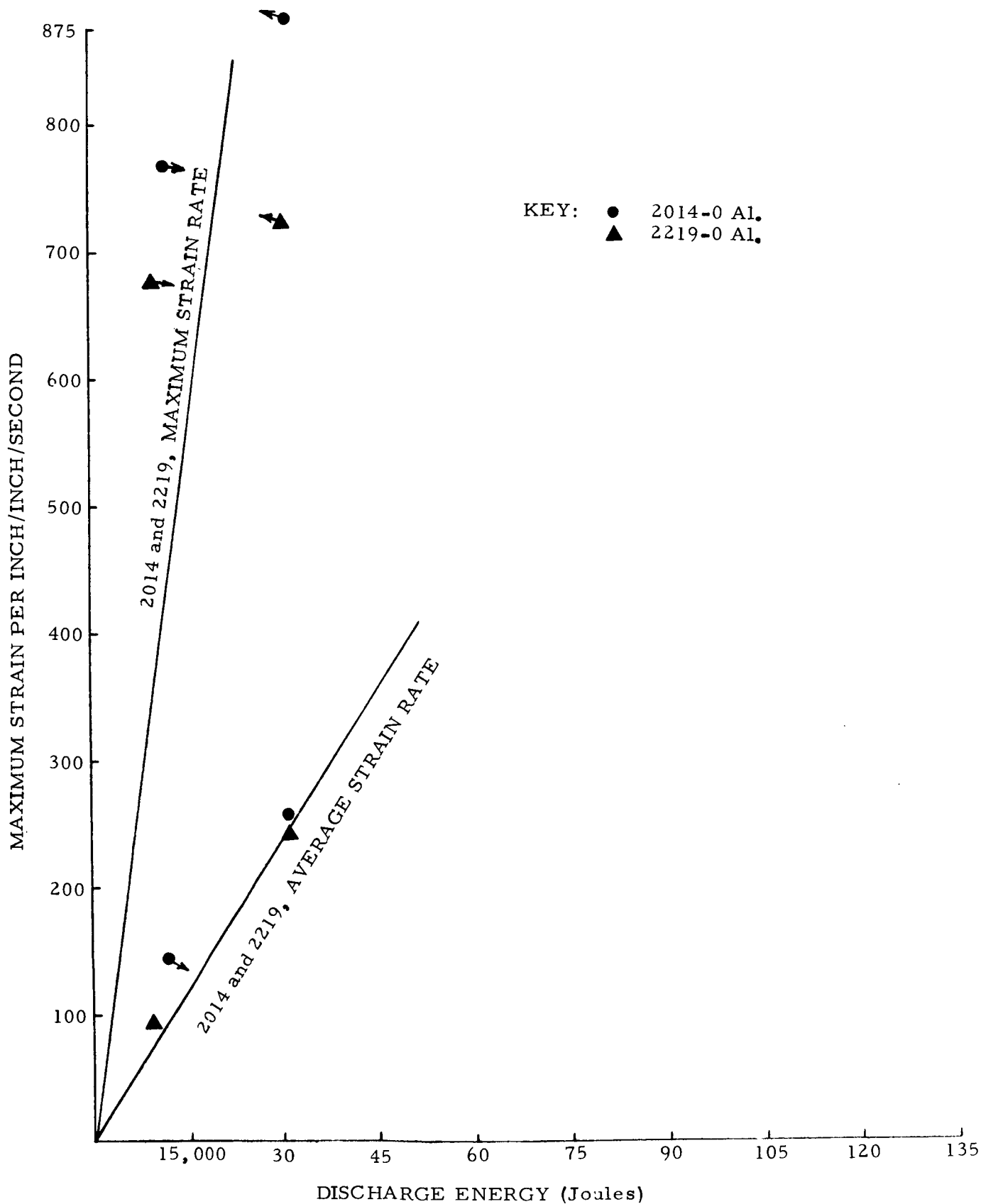
RELATIONSHIP BETWEEN STRAIN RATE AND DISCHARGE ENERGY FOR THE ELECTROHYDRAULIC PROCESS

FIGURE 72



RELATIONSHIP BETWEEN STRAIN RATE AND DISCHARGE ENERGY FOR THE EXPLOSIVE PROCESS

FIGURE 73



RELATIONSHIP BETWEEN STRAIN RATE AND DISCHARGE ENERGY FOR THE MAGNETIC PROCESS

FIGURE 74

## DISCUSSION OF RESULTS

### A. Mechanical Property Testing

The conditions under which all mechanical properties were obtained in this program are listed below for reference to the discussion that follows:

- |         |  |
|---------|--|
| Table 1 | Test results of 2219-0, 2014-0 and 321 stainless parent stock to establish a reference.  |
| Table 3 | Test results of specimens from flat and round bottom domes which were electrohydraulically formed using the strain hardenable 2219-0 alloy to determine if the mechanical properties of curved tensile specimens differ significantly from flat tensile coupons of equal material thickness. |
| Table 5 | Test results to compare free formed domes by the high energy rate and hydrostatic forming processes.   |
| Table 7 | Test results from domes impacted against the die surface.  |

Yield strength, ultimate strength, and percent elongation are plotted against percent thinout for each of the three materials in Figures 15, 16, 17. Only the 2219 material is markedly influenced by the forming method. For given dome deformation (thinout) work hardening is appreciably less for the high strain rate processes as a group in comparison with the hydrostatic (zero strain rate) process. This can be seen in the large difference (5,000 to 10,000 psi) between respective yield and ultimate strengths for hydrostatic forming and the high strain rate processes. Microstructural examinations in the Appendix, however, indicate that a degree of difference may be due to the size of Cu Al<sub>2</sub> in the matrix rather than strain rate alone.

Test conditions in Table 5 were selected to produce two strain rates for each material in the electrohydraulic and explosive processes which differed by a factor of at least 2. In general, the maximum strain rates ranged from 100 to 877. No significant difference in mechanical properties from specimens formed in this range of strain rates was discerned. Consequently, the small differences are taken as scatter and only one curve for each high strain rate process has been drawn through the experimental points in Figure 15.

## B. X-Ray Diffraction

### Stress Measurement

When a polycrystalline piece of metal is deformed elastically in such a manner that the strain is uniform over relatively large distances, the lattice plane spacings in the constituent grains change from their stress-free value to some new value corresponding to the magnitude of the applied stress. The new spacing is essentially constant from one grain to another for any particular set of planes. If the metal is deformed plastically, the lattice planes usually become distorted in such a way that the spacing of any particular set of planes varies from one grain to another or from one part of a grain to another.

The uniform strain occurring in the case of elastic deformation causes a shift of x-ray diffraction lines to new positions. On the other hand, the non-uniform strain caused by plastic deformation causes broadening of the corresponding x-ray diffraction line.

The shift of the diffraction line may be used to calculate the strain, and the stress can be determined by a calculation involving the elastic constants of the material. For example, assume that a cylindrical rod of cross-sectional area  $A$  is stressed elastically in tension by a force  $F$ . The stress  $\sigma_y = \frac{F}{A}$  acts in the  $y$ -direction (along the axis), but there are no stresses in the  $x$ - or  $z$ -directions (x-ray diffraction does not measure the shear stresses present). The stress  $\sigma_y$  produces a strain  $\epsilon_y = \frac{L_f - L_o}{L_o}$  in the  $y$ -direction ( $L_f$  and  $L_o$  are final and original lengths of the rod). Strain is related to stress by relation  $\sigma_y = E\epsilon_y$ , where  $E$  is Young's modulus. Since the elongation of the rod is accompanied by a decrease in its diameter  $D$ , the strains in the  $x$ - and  $z$ -directions are  $\epsilon_x = \epsilon_z = \frac{D_f - D_o}{D_o}$ . If the rod is isotropic,  $\epsilon_x = \epsilon_z = \gamma\epsilon_y$ , where  $\gamma$  is Poisson's ratio.

The measurement of  $\epsilon_y$  by x-rays would require diffraction from planes perpendicular to the axis of the rod. Since this may be physically impossible, reflecting planes which are parallel, or almost parallel, to the axis of the rod are utilized to take a back-reflection photograph at normal incidence. (Normal incidence is used to gain precision in the measurement of the plane spacing,  $d$ .) In this way, a measurement of strain in the  $z$ -direction is obtained from  $\epsilon_z = \frac{d_n - d_o}{d_o}$ , where  $d_n$  is the spacing of the stressed plane reflecting at normal incidence, and  $d_o$  is the spacing of the same plane in the absence of stress. Since  $\epsilon_z = \gamma\epsilon_y$  and  $\sigma_y = E\epsilon_y$ , the relationship  $\sigma_y = \frac{E}{\gamma} \left( \frac{d_n - d_o}{d_o} \right)$  is obtained, which gives the required stress in terms of known and observed quantities.

In the more general case, there will be stress components in two or three directions at right angles to one another. However, the stress at right angles to a free surface is always zero. Therefore at the surface of body, as in the measurements in this report, we have to deal with no more

than 2 stress components lying in the plane of the surface. At the free surface, the strain normal to the surface is not zero. It is given by  $\epsilon = -\frac{\gamma}{E} (\sigma_1 + \sigma_2) = \frac{dn - d_0}{d_0}$  where  $(\sigma_1 + \sigma_2)$  is the sum of the principal stresses. The x-ray measurements done for this report were used to obtain  $(\sigma_1 + \sigma_2)$ .

The values used to determine the sum of the principal stresses were:

- |                |   |                              |
|----------------|---|------------------------------|
| 321 SS Samples | - | E = 28 x 10 <sup>6</sup> psi |
|                |   | γ = 0.35 (assumed)           |
| Al Samples     | - | E = 10 x 10 <sup>6</sup> psi |
|                |   | γ = 0.33                     |

The unstressed values of the spacings were obtained from parent stock samples submitted and were found to be (by the x-ray diffraction methods described below):

- |         |   |                                |
|---------|---|--------------------------------|
| 321 SS  | - | spacing of 420 plane = .80333A |
| Al 2014 | - | spacing of 511 plane = .77946A |
| Al 2219 | - | spacing of 511 plane = .77923A |

#### Method of Lattice Measurement

Several x-ray diffraction methods of determining the desired lattice spacings were investigated. These were back reflection techniques and are listed below:

- |   |              |
|---|--------------|
| 1. Precision focusing back reflection camera    |              |
| 2. Flat plate camera with focusing pinhole tube | Film Methods |
| 3. Flat plate camera with beam collimating tube |              |
| 4. Diffractometer                               |              |

Method 1 is capable of high precision measurements in 1-2 hour exposures with proper sample conditions, which occur when the sample conforms to the circumference of the camera. The method can be (and was) satisfactory for a very small portion of a small, flat sample as in the case of the parent stock coupons. However, the dome-shaped samples curved away from the circumference of the camera and were too large for the camera.

Methods 2 and 3 differ in the type of tube through which the x-ray beam passes. Method 3 requires very long exposures (approximately 8 hours) thus making it impossible to finish the work in the allotted time with the existing equipment. Method 2 is very similar to Method 1, but samples as large as 6" in diameter can be handled with 1-2 hour exposures. The x-ray beam covers a circular area on the sample with a diameter of about 0.30" for stainless and about 0.44" for aluminum.



Method 4 utilizes the diffractometer which can be considered a back reflection method only when operated at very large diffraction angles. The diffractometer will not accommodate anything other than small flat samples without modification of the equipment.

In view of the above considerations, Method 2 was chosen to obtain the lattice measurements. The part of the sample to be measured was positioned at a known, fixed distance from the film. 3.3" and 2" were selected for aluminum and steel respectively to obtain a reflected diameter within the film size.

## Results

Typical diffraction patterns are shown in Figures 24, 25 and 26, and Table 13 contains the residual stress calculations from the patterns.

For the 2014 alloy (Figure 24), the characteristic sharp  $K\alpha_1$  and  $K\alpha_2$  lines of an annealed, stress free microstructure can be observed. The normal line broadening with strain is observed although little difference due to degree of strain (thinout) is observed.

For the 2219 alloy (Figure 25), the parent stock diffraction lines are quite broad indicating the anneal was not adequate to produce a stress free microstructure. Further broadening occurs with strain but considerable difference in the degree of broadening in individual specimens of equal strain is observed. Some patterns are too diffuse to permit measurement of the center of the broadened "line." It is believed, based on the electron transmission microscopy observation of decided difference in  $\text{Cu Al}_2$  precipitate size, that all 2219 blanks were not similarly annealed. These observations, as discussed in the appendix, indicate that for samples with small precipitate, the precipitate and matrix atomic lattices were coherent at their interfaces, thereby producing stress on a microscopic scale. Such structure would be stronger than an annealed structure with precipitates too large to permit coherency over the longer interface length. In Figure 25, it is believed that the photographs in the left column represent structure with initial coherency stress and the photographs at the right were initially stress free. This hypothesis is borne out in Figure 15 where EX 6 (the formed specimen in the left column of Figure 25) is on the higher curves of ultimate and yield strength.

For 321 stainless steel all of the diffraction patterns are poor in that the lines are broad and the center is not well defined. In several photographs the lines are not distinguishable from the background. Stress measurements which were obtained were discounted since the accuracy at best would be  $\pm .020''$  which corresponds to stress values of  $\pm 40,000$  psi. An improvement in measurement accuracy may be possible with cobalt rather than copper radiation since the reduction in background intensity would increase line definition. However, cobalt radiation was not available at the time of the experimental work.

Since most of the aluminum alloy diffraction lines were more clearly defined, measurement to an accuracy of  $\pm .010$  is possible. For the 3.33" distance employed, this is an accuracy of about  $\pm 3,000$  psi. When several readings were taken at positions about 1" apart the scatter of readings was somewhat greater. Five readings about a 2" diameter around the dome center as shown in Table 13 for 2014 EHCD12 have a total variation range of 15,000 psi. Since the total range of all aluminum stress measurements is hardly greater than this variation, there is really no basis of sufficient accuracy to attempt to ascribe meaning to the differences in stress values between specimens

formed under various conditions. It is more meaningful to state that the stress measurements were all small (less than 20,000 psi) in comparison with the combined yield stress which would be  $1.4 (30,000 + 30,000) = 84,000$  psi. (The 1.4 factor is the increase in balanced biaxial stress over uniaxial tensile stress)

A stress measurement of -6,500 psi was obtained on the inside dome surface of specimen 2014 EHCD 12. This value does not differ appreciably from the -13,900 psi average of the outside surface measurements. This is a reasonable result since both surfaces stretch during forming, and the ratio of thickness to curvature radius is not large enough to produce appreciable differences in elastic relaxation on the two surfaces. In this sense a dome configuration differs considerably from a specimen such as a beam with a longitudinal bend where the inner surface compressive stress is balanced by tension stress in the outside surface.

### C. Electron Transmission Microscopy

This technique was employed with a limited number of samples to observe the effect of strain upon the internal structure. The resulting micrographs and discussion are rather voluminous and are, therefore, included as an appendix to this report for convenience.

#### D. Stress Corrosion

Stainless steel domes selected for stress corrosion testing included 0 to 800 per second strain rate, low and high impact, and free formed specimens. (See Table 14) Nine of these specimens were tested as formed by either the electrohydraulic explosive or hydrostatic process. An additional nine specimens were stress relieved to provide reference data.

Results of the tests revealed no stress corrosion failures in any of the 18 specimens. Some light pitting and rust staining developed on a number of specimens, but not preferentially. This behavior would be deemed normal for an 18-8 stainless grade even in an unfabricated condition. During the course of testing, frequent cracking failures occurred in the stainless steel safety wire used to suspend the domes in the tank, at points of high plastic deformation, testifying to the aggressiveness of the corrosive environment employed.

After the rather extended exposures imposed (288 hours), several metallographic specimens were taken at random from areas indicating general corrosion. These were examined for the presence of transgranular network cracking, characteristic of stress corrosion attack in austenitic stainless steel, and found completely unaffected. A photomicrograph of a typical section is shown on Page 15.

On the basis of these results, it appears that for the dome configuration employed in this program, stress levels are not sufficient to produce stress corrosion. Also, neither strain rate or die impact affected stress corrosion susceptibility.

## E. Pressure Measurement

Pressure-time relationships were obtained for the electrohydraulic forming process under a variety of conditions. The equipment and instrumentation employed to obtain the traces are described in the Experimental Procedure and Techniques section of this report.

The four different tooling arrangements utilized for the experimentation are shown in sketches A, B, C & D of Figure 31. The pressure profiles obtained with each tooling arrangement are shown above the sketches for various conditions of energy level and gage distance. Data obtained from the traces are listed in Table 15 with the experimental conditions employed for the traces. The data is plotted in the graphs of Figure 32.

Examination of the pressure profiles in Figure 31 reveals several interesting aspects. The first pulse shown on all the traces is due to extraneous voltage pickup in the transducer from the expansion and collapse of the magnetic field. This first trace is an indication of the initiation of discharge and also is an indication of the vaporization time of the wire. Pressure traces for various wire diameter sizes are shown in Figure 31 as traces 21, 22 and 23. It can be seen that the period of wire vaporization for the various wires vary depending upon diameter. Generally, the larger the diameter, the longer the time required for vaporization for a given energy level. For the .096", .062" and .032" diameter wires, the vaporization periods were 120 u secs, 60 u secs, and 30 u secs respectively. It can be seen from Graph C of Figure 32 that the most efficient wire size for 5KV is .062". The .096" wire is least efficient compared to the others with its initial pulse occurring approximately 60 u secs. late due to the longer vaporization period.

The traces at the top of Figure 31 for 2" gage distances show an initial pulse starting 100 u secs from the initiation of discharge followed by secondary pulses at approximately 100 u sec intervals. This appears to be the primary pulse from the discharge source followed by reflected pulses from the tank walls. The regularity and uniformity of the reflected pulses are difficult to reconcile with the tank configuration used. The first pulse is unquestionably the primary pulse from the discharge gap. The decay of the first pulse with increasing gage distance is shown graphically in Graph E of Figure 32. This profile was obtained by superimposing the first pulse of traces 1 through 5 of Figure 32 on one time base. The graph indicates both the amplitude decay and the delay time for the pulse to register at the transducer. The pulse travels at approximately acoustic velocity (4800 ft/sec.). At this velocity, a distance of 5.76 inches requires a time period of 100 u secs. The long time period before the first pulse occurs is due to the time required for complete vaporization of the wire and buildup of the pressure pulse.

The second pulse occurs approximately 100 u secs later than the first pulse at the 2" gage distance. This pulse could be due to either a reflection from the blank behind the electrode gap which would be a longitudinal wave in the same direction as the primary wave or a circumferential wave from the inner diameter of the tank. Comparison of trace 11 (rigid backup plate) with traces 17 and 18 (non-rigid backup plate) reveal that the second pulse is almost identical in all three cases. If the second pulse were reflected from the backup plate, it would seem that the pulse reflecting from the non-rigid plate would have a lower amplitude due to the absorption of energy by the moving plate.

Because of the proximity of the backup plate to the initiating wire, it appears that the bubble is formed against the backup plate and the pressure wave travels outward from the large gas ball down the tank. The proximity of the workpiece to the initiation wire is discussed further in the next section.

The increase in amplitude of the third and fourth pulses as the gage distance is increased is attributed to reflections from the tank walls which are closer to the transducer at the longer gage distances. The trend is seen graphically in Graphs A, B, and D. They show that the first pulse decreases with increasing gage distance, the second pulse is relatively unaffected but increases slightly and the third and fourth pulse increase considerably at the longer gage distances.

Again comparing trace 11 with 17 and 18, it is observed that the third pulse seen in trace 11 is missing from traces 17 and 18. This is attributed to the rarefaction wave emitted by the moving workpiece which cancels out the pulse occurring at the transducer at that time.

Graph F shows that the peak pressure is proportional to the discharge energy under a variety of forming conditions. The three materials of interest, 2219-0 aluminum, 2014-0 aluminum and 321 stainless steel were formed at 5, 6 and 7 KV respectively. Plotting the peak pressure from the first discharge in each instance versus the discharge energy reveals that the pressure is directly proportional to the discharge energy under these conditions.

## F. Dimensional Evaluation

### 1. Efficiency

When a workpiece shape of compound curvature such as a dome shape is formed largely by stretch (rather than draw) the thickness varies considerably over the formed surface. Consequently, the amount of strain work per unit surface area varies since strain work and change in thickness are closely related. To very accurately obtain the amount of strain work performed in forming a dome, it would be necessary to note the change in area shape and thickness of each unit square on a dome formed a grid marked blank. Comparison of shape and thickness of each formed grid square with a variety of calibration cylinders biaxially strained in a range of axial strain ratios and in a range of strains would give the strain work for each grid. The total strain work per dome is then the sum of work of all squares.

The above is a tedious process and is not justifiable for the purposes of this program. A somewhat less accurate but much simpler method of strain work measurement was employed. The procedure used was to measure the dome depth, thickness and volume as the pressure was increased during hydrostatic forming. The total work done upon such a dome is the incremental sum of pressure multiplied by volume increase. Either the dome thinout, dome volume or dome depth measurements may now be used to equate the work done with a dome of equal thinout, volume or depth but formed by another process. The accuracy of this method of strain work calibration suffers only when the thinout gradients of the workpiece dome and calibration dome differ. It is, therefore, necessary to establish whether the thinout gradient for the workpiece and its calibration counterpart are similar. This was done graphically in Figure 61

Figure 62, left, is a plot of hydrostatic pressure versus dome volume. The area under the curve for each material is therefore the deformation work, and this work as graphically obtained is shown in Table 16, and plotted versus dome volume in Figure 62, right. This data and the use of volume versus thinout curves in Figure 63 gives deformation work versus thinout in Figure 64.

With the use of the above figures the deformation work and efficiency in successive electrohydraulic discharges for each of the three materials was calculated. Note that results are valid only if the thinout gradient curves in Figure 61 are reasonably close. In this regard, for the aluminum alloys, deformation work obtained by dome volume comparison is invalid and erroneously too high since the curves of Figure 61, left indicate appreciably greater thinout for both #0 (center) and #3 positions for hydrostatic domes.

Table 17 indicates that the efficiency of electrohydraulic dome forming to hemisphere depth is 15% and 10% for 2219 aluminum and 321

stainless steel, respectively. Based on an average flow stress midway between annealed yield and ultimate of 20,000 and 66,000 psi for 2219 and 321, a greater difference in efficiency might be expected. The principal reason that efficiencies do not differ to a greater degree is that the available energy for each workpiece material does not differ since the peak electrohydraulic pulse pressure greatly exceeds the hemispherical yield pressure of both workpieces.

## 2. Thinout

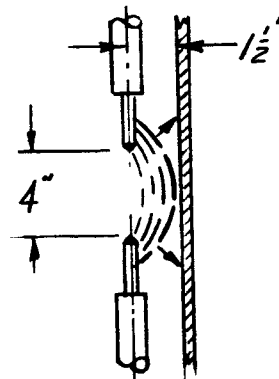
The thinout across the dome contour is shown in Figures 19, 20, 21, and 22 for the three materials as formed by several processes. All processes show appreciable thinout except for the hydroform process in which forming is almost entirely by draw. Low and high energy curves in Figures 65 and 66, and 19, 20, 21, 22, also show that as the forming energy (power) is increased, center thinout is not as great as is observed in explosive forming at close standoff, as the photograph in Figure 20 shows. It appears that the overall thinout gradient in a cross section can, therefore, be minimized by shifting the maximum thinout away from the dome center by high forming energy and close standoff. Note the thickness measurements of 321 EX 6 in Table 8.

It is of interest to compare thinout at rupture with various forming conditions which influence the size of the gas bubble as in the table below. Data is presented for 2219 alloy only since domes in the other materials were not formed to rupture for all cases.

Free Formed 2219-0 Domes

<u>Forming Method</u>	<u>Forming Energy (Joules)</u>	<u>Standoff Distance (in. )</u>	<u>Thinout at Rupture</u>	<u>Type of Rupture</u>
Hydrostatic			44.6%	Split at dome center
Electrohydraulic	17,280	1 1/2	57.2	Split at dome center
Electrohydraulic	69,120	1 1/2	40.0	6" circular ring
Explosive	27,600	5	48.9	Split at dome center
Explosive	92,000	3	44.5	6" circular ring

The 6 inch circular type of rupture indicated in the above table can be attributed to the influence of the gas ball acting on the workpiece. It appears that for high energies at small standoff distances, the workpiece becomes quickly engulfed by the expanding gas ball. The low pressure gaseous products contained in the spherically expanding gas ball "breaks" over the workpiece and does not contribute to workpiece deformation as much as the pressure wave front just ahead of it as shown below.





Phase I experiments in which a 13 cavity hemispherical die was used to determine energy distribution (energy profile across workpiece), revealed that for small standoff distances pressure was greatest in a circular ring at some distance from the center of the workpiece. That is, the depth of the cavities located away from the center of the workpiece were greater than the center cavity depth. Conversely, at greater standoff distances, the peak energy profile was obtained for the center cavity which at that time was attributed to reflections from the bridge electrode used. However, it would appear that the Phase I experiments support the theory of gas ball to work-piece proximity presented here.

### 3. Discharge Energy and Dome Depth

Dome depth and center thinout with increasing electrohydraulic discharge energy are plotted in Figures 67, 68, 69, 70, 71. It is observed that for given energy expended, depth is slightly greater in single discharges than for multiple discharges indicating that high energy discharges are somewhat more efficient.

Expectedly, the dome depth for given energy decreases with material strength in the order 321, 2219, 2014.

As previously discussed, the thinout for given energy is greater for lower energy (multiple) discharges.

The amount of drawin in the three stretch processes (electrohydraulic, explosive and hydrostatic) was quite similar (2 to 8% of the original blank diameter.) However, deeper domes were obtained electrohydraulically and explosively than by hydrostatic forming since in high strain processes the forming time is too short for lateral redistribution of stress in the metal. Consequently, necking occurs over a wider area rather than in a single failure line. The onset of non-uniform elongation (in the tensile specimen sense) is therefore delayed permitting either greater thinout at failure or relatively more uniform thinout gradient. Both of these factors produce deeper domes.

Coupon No.	Alloy	Yield* PSI	Ultimate PSI	Elongation % in 2"	Hardness Rockwell F	Handbook Values
PST-1	2219-0 ↑ ↓	13,100	28,100	20.0	RH 88	Yield = 10,000 PSI
PST-2		12,700	28,200	20.0	RH 87	Ult. = 25,000 PSI
PST-3		12,600	28,100	20.0	RH 87	Elong. = 20%
PSL-1		12,300	27,800	20.0	RH 87	
PSL-2		12,300	27,800	20.0	RH 88	
PSL-3		2219-0	12,300	28,000	20.0	RH 87
PST-1	2014-0 ↑ ↓	9,200	24,900	21.5	RH 80	Yield = 16,000 PSI
PST-2		10,000	25,000	20.0	RH 81	Ult. = 32,000 PSI
PST-3		10,000	25,100	21.5	RH 80	Elong. = 16%
PSL-1		9,700	25,600	24.5	RH 79	
PSL-2		10,200	25,900	22.5	RH 79	
PSL-3		2014-0	10,000	25,900	21.5	RH 80
PST-1	321-Ann.St.St. ↑ ↓	43,000	88,000	57.0	RH 84	Yield = 35,000 PSI
PST-2		43,900	86,900	56.0	RH 81	Ult. = 90,000 PSI
PST-3		45,100	86,600	54.0	RH 83	Elong. = 50%
PSL-1		43,100	87,900	50.0	RH 83	
PSL-2		43,700	88,800	60.0	RH 83	
PSL-3		321-Ann.St.St.	44,100	89,300	53.5	RH 82

NOTES - PSL denotes Parent Stock "Longitudinal Grain Direction"  
\* Extensometer yield, 0.2% offset, 2" gage length.

PST denotes Parent Stock "Transverse Grain Direction"

2219-0 material was annealed from a T31 condition at 775°F for 1 hr. and cooled 50°F/hr. to 500°F

Hardness to type 321 stainless is given only for information and the values are not to be construed as being indicative of the tensile strength.

See Figure 23 for typical tensile coupons.

TENSILE PROPERTIES OF .093"  
MATERIALS BEFORE FORMING

TABLE 1

INPUT ENERGY		VOLUME (CC)	SPECIMEN NUMBER	DOME CONFIGURATION (FLAT OR ROUND BOTTOM)	ALLOY	SHOT NO.	DU DE (I
KV	JOULES						
7	23,520	2,050	EH 3	Flat	2219-0	1	2.
6	17,280	2,520	↑			2	3.
6	17,280	2,940	↓			3	3.
6	17,280	3,260	↑			4	3.
8	30,720	-	EH 3 <sup>(1)</sup>			5	3.
7	23,520	1,960	EH 4			1	2.
6	17,280	2,460	EH 4			2	3.
6	17,280	2,840	EH 4			3	3.
4	7,680	740	EH 5			1	0.
5	12,000	1,440	↑			2	2.
6	17,280	2,280	↓	3	3.		
5	12,000	2,340	↑	4	3.		
5	12,000	2,420	↓	5	3.		
6	17,280	2,980	EH 5 <sup>(1)</sup>	6	3.		
10.5	53,000	-	EH 6 <sup>(1)</sup>	1	3.		
10	48,000	-	EH 7 <sup>(1)</sup>	1	3.		
10	48,000	2,820	EH 8	1	3.		
7	23,520	1,800	EH 9	1	1.		
5	12,000	1,860	EH 9 <sup>(1)</sup>	2	1.		
6	17,280	2,040	EH 9 <sup>(1)</sup>	3	1.		
6	17,280	1,760	EH 10 <sup>(1)</sup>	Round	2219-0	1	2.
8	30,720	2,300	EH 11			1	3.
4	7,680	2,300	EH 11 <sup>(1)</sup>			2	3.
5	12,000	2,550	EH 11 <sup>(1)</sup>			3	3.
12	69,120	3,790	EH 12			1	4.
6	17,280	3,950	↑	2	4.		
7	23,520	4,180	↓	3	4.		
7	23,520	-	EH 12 <sup>(1)</sup>	4	5.		



DOME SPECIMENS NOS. 2219-EH 9 AND 2219-EH 10 FORMED TO EQUAL GAGE REDUCTION FOR COMPARISON OF MECHANICAL PROPERTIES.

(5)

DEPTH (IN)	THINOUT AT DOME CENTER (%)	THICKNESS MEASUREMENTS									
		POSITION NUMBER									
		8	7	6	5	4	3	2	1	Center	1
65	15.1	.094	.093	.093	.089	.082	.078	.078	.079	.079	.079
45	35.5	.094	.093	.092	.087	.074	.071	.066	.065	.060	.065
49	39.7	.093	.092	.091	.087	.076	.068	.060	.058	.056	.059
49	42.0	.093	.092	.091	.086	.072	.061	.055	.054	.054	.054
49(2)	49.5	.093	.093	.092	.078	.064	.050	.042	.047	.047	.050
12	12.9	.093	.092	.092	.088	.079	.075	.078	.081	.081	.082
45	35.5	.093	.092	.091	.081	.072	.073	.071	.067	.060	.062
50	39.7	.093	.092	.092	.079	.075	.067	.062	.059	.056	.059
97	3.2	.093	.093	.093	.092	.091	.090	.090	.090	.090	.090
18	18.3	.094	.094	.093	.090	.088	.086	.083	.079	.076	.080
12	38.7	.093	.093	.092	.087	.080	.073	.070	.066	.057	.065
09	39.7	.093	.093	.092	.086	.079	.072	.066	.062	.056	.062
15	43.0	.093	.093	.092	.086	.078	.070	.064	.060	.053	.059
50(2)	50.6	.093	.093	.092	.084	.073	.063	.055	.054	.046	.051
50(2)	30.0	.093	.093	.092	.085	.074	.057	.053	.064	.065	.064
50(2)	25.8	.094	.092	.092	.086	.078	.063	.064	.067	.069	.067
48(2)	23.6	.094	.093	.092	.085	.067	.061	.067	.073	.071	.072
85	9.7	.093	.092	.092	.086	.078	.073	.074	.080	.084	.083
85	10.8	.093	.092	.091	.083	.077	.073	.074	.080	.083	.083
91(5)	12.9	.093	.092	.091	.083	.075	.071	.073	.079	.081	.080
29	12.9	.094	.094	.093	.089	.083	.081	.082	.082	.081	.082
03	21.5	.095	.095	.093	.087	.076	.070	.071	.073	.073	.073
05	22.6	.096	.095	.094	.087	.076	.070	.072	.072	.072	.073
32	26.9	.096	.095	.093	.085	.076	.071	.071	.070	.068	.070
46	32.3	.097	.095	.091	.084	.073	.070	.072	.068	.063	.065
49	34.5	.097	.095	.090	.083	.072	.066	.066	.063	.061	.064
74	41.0	.097	.095	.090	.080	.070	.062	.063	.061	.055	.059
00(4)	44.1	.097	.095	.091	.081	.066	.056	.060	.057	.052	.055

ELECTROHYDRAULICALLY FORMED ROUND  
DOME DATA OBTAINED FOR .092" 22

TABLE 2

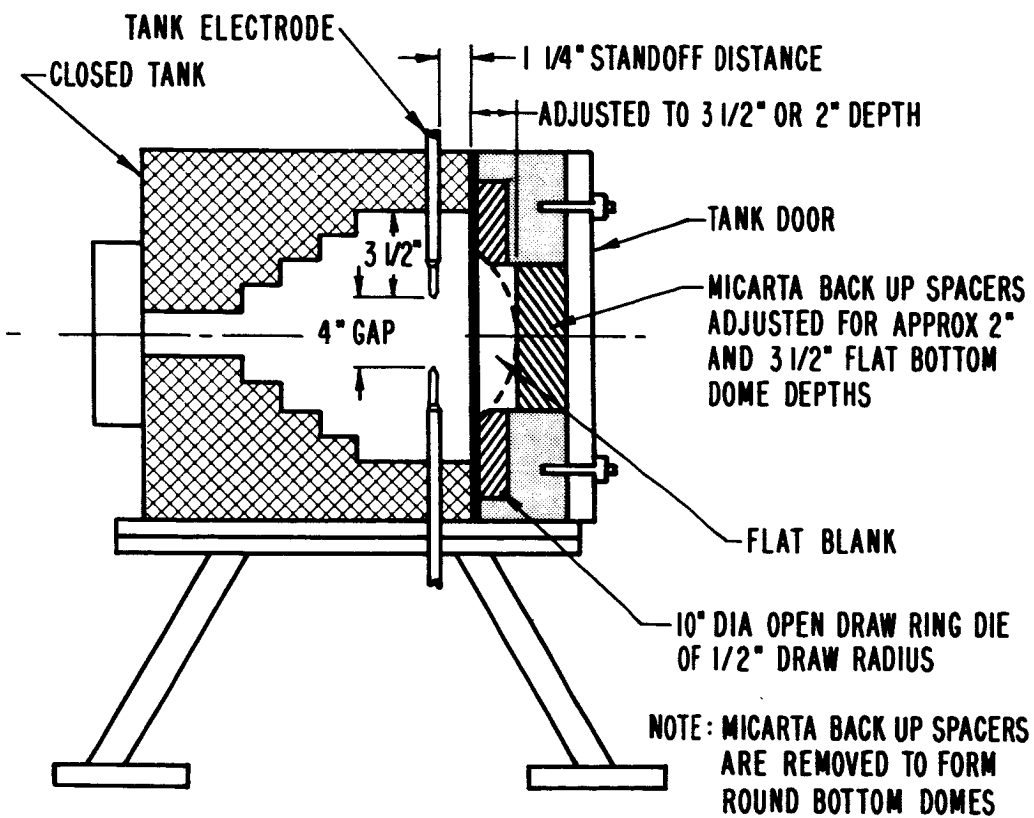
	2	3	4	5	6	7	8
.078	.077	.079	.090	.095	.096	.096	
.071	.074	.076	.086	.093	.095	.095	
.060	.065	.073	.084	.093	.095	.095	
.056	.059	.067	.082	.042	.094	.095	
.046	.048	.059	.076	.093	.094	.095	
.079	.075	.074	.084	.093	.094	.095	
.071	.073	.074	.081	.092	.094	.095	
.062	.064	.070	.081	.092	.094	.095	
.090	.090	.091	.092	.093	.093	.093	
.084	.087	.089	.091	.093	.094	.094	
.068	.072	.080	.087	.093	.093	.093	
.066	.072	.078	.086	.093	.093	.093	
.064	.070	.072	.086	.093	.093	.093	
.053	.063	.073	.085	.093	.093	.093	
.054	.060	.075	.086	.094	.096	.097	
.059	.057	.073	.086	.093	.096	.097	
.067	.056	.070	.085	.093	.095	.096	
.081	.078	.079	.087	.093	.094	.095	
.081	.077	.078	.086	.093	.094	.095	
.079	.073	.075	.084	.093	.094	.094	
.081	.081	.083	.089	.092	.093	.093	
.068	.068	.076	.086	.092	.092	.093	
.068	.068	.076	.086	.092	.093	.094	
.067	.069	.077	.087	.092	.093	.093	
.066	.062	.072	.082	.089	.099	.102	
.065	.061	.068	.073	.083	.098	.101	
.062	.061	.068	.072	.090	.099	.102	
.058	.055	.065	.071	.094	.099	.102	

Common Forming Conditions

.092" 2219-0 flat blank of 17 $\frac{1}{2}$ " dia.  
 Closed tank housing the 10" dia. open draw  
 ring die of  $\frac{1}{2}$ " draw radius.  
 Micarta back-up spacers placed behind  
 10" dia. open die to form flat bottom  
 domes.  
 960 ufd capacitor bank  
 .096" dia. magnesium initiating wire for  
 discharges less than 10 kv.  
 .125" dia. magnesium initiating wire for  
 discharges 10 kv or greater.  
 4" electrode gap, axial in-line  
 (opposing) electrodes mounted in a vertical  
 plane.  
 1 $\frac{1}{4}$ " standoff distance.

NOTES

- (1) Tensile coupons obtained from dome center for Mechanical Property tests. See Figure 33 . Also see Table 3 and Figure 34 for tensile values and plots of tensile values versus percent thinout, respectively.
- (2) Denotes rupture of flat bottom domes. Ruptures have generally occurred at shoulder of dome where metal strain is greatest.
- (3) See Figures 35, 36, 37 for plot of thickness change versus dome position no.
- (4) Round bottom dome ruptured, depth estimated.
- (5) Micarta back-up spacers adjusted for approx. 2" of flat bottom dome depth - all other flat bottom domes have a 3 $\frac{1}{2}$ " depth.



Closed Tank Showing Method Used to Obtain Flat and Round Bottom Domes of Varying Depths

4

Coupon No.	Coupon Center Thickness (in.)	Yield (psi)	Ultimate (psi)	Elongation (% in 2")	Hardness Rockwell F
3TF-A	.046	32,700	36,800	1.5	75
3TF-B	.042	34,300	38,300	1.5	75
3TF-C	.047	33,400	38,900	2.0	74
12TR-A	.053	30,500	35,600	2.5	73
12TR-B	.056	31,900	35,800	2.5	73
12TR-C	.052	34,300	37,400	2.0	73
7TF-A	.070	29,800	33,500	3.5	73
7TF-B	.070	30,500	33,200	4.0	74
7TF-C	.069	30,000	33,900	4.0	75
11TR-A	.072	26,600	32,100	5.5	70
11TR-B	.070	27,300	32,900	5.0	70
11TR-C	.068	27,500	32,800	4.0	72
9TF-A	.080	26,100	30,200	7.5	69
9TF-B	.081	27,000	30,200	8.0	68
9TF-C	.081	27,400	30,200	7.5	69
10TR-A	.081	25,900	29,800	8.5	67
10TR-B	.083	25,900	29,300	11.0	65
10TR-C	.081	25,400	30,100	8.5	66

NOTE - For size, source, and location of all tensile coupons, see Figure 33  
For Common Forming Conditions, see Table 2

MECHANICAL PROPERTIES OF 2219-0  
TENSILE COUPONS OBTAINED FROM  
FLAT AND ROUND BOTTOM DOMES  
FORMED ELECTROHYDRAULICALLY

TABLE 3

INPUT ENERGY		VOLUME (CC)	SPECIMEN NUMBER	ALLOY	SHOT NO.	AVERAGE STRAIN INCHES/IN/SEC/	MAX. STRAIN INCHES/IN/SEC/	DOMED DEPTH (IN)	THINOUT AT DOME CENTER (%)
KV	JOULES								
3	4,320	600	EH 1	2219-0	1	10-20 <sup>(6)</sup>	75-150 <sup>(6)</sup>	0.66	1.9
5	12,000	1,360	↑	↑	2	-	-	1.79	7.6
5	12,000	1,920	↓	↓	3	-	-	2.45	15.2
6	17,280	2,370	↓	↓	4	-	-	3.28	31.5
6	17,280	2,870	↓	↓	5	-	-	3.84 <sup>(2)</sup>	46.7
7	23,520	-	EH 1	↑	6	-	-	4.50 <sup>(2)</sup>	55.3
10	48,000	2,610	EH 2	↑	1	50-100 <sup>(6)</sup>	250-300 <sup>(6)</sup>	3.24	12.9
8.5	34,600	3,900	↑	↑	2	-	-	4.76	39.8
5	12,000	4,020	↓	↓	3	-	-	4.77	38.7
6	17,280	4,510	↓	↓	4	-	-	5.18	46.2
6	17,280	4,950	EH 2	↓	5	-	-	5.67 <sup>(2)</sup>	57.2
6	17,280	1,760	EH 10	↓	1	25-100 <sup>(6)</sup>	150-250 <sup>(6)</sup>	2.29	12.9
8	30,720	2,300	EH 11	↓	1	62.0	192.0	3.03	21.5
4	7,680	2,300	EH 11	↓	2	-	-	3.05	22.6
5	12,000	2,550	EH 11	↓	3	-	-	3.32	26.9
12	69,120	3,790	EH 12	↓	1	117.0	457.0	4.46	32.3
6	17,280	3,950	EH 12	↓	2	-	-	4.49	34.5
7	23,520	4,180	EH 12	↓	3	-	-	4.74 <sup>(2)</sup>	41.0
7	23,520	-	EH 12	↓	4	-	-	5.00 <sup>(2)</sup>	44.1
6	17,280	1,640	EH 13	↓	1	25-100 <sup>(6)</sup>	150-250 <sup>(6)</sup>	2.07	8.7
7	23,520	2,560	EH 13	↓	2	-	-	3.60 <sup>(2)</sup>	38.0
6	17,280	-	EH 13	↓	3	-	-	4.10 <sup>(2)</sup>	46.7
5	12,000	1,150	EH 14	↓	1	24.4	174.1	1.48	4.4
5	12,000	1,640	EH 14	↓	2	-	-	2.38	17.6
9	38,880	2,420	EH 16 <sup>(7)</sup>	↓	1	88.7	372.2	3.025	17.4
9	38,880	2,520	EH 17 <sup>(7)</sup>	↓	1	58.3	202.8	2.99	12.0
10.5	53,000	2,940	EH 18 <sup>(7)</sup>	↓	1	50-100 <sup>(6)</sup>	250-300 <sup>(6)</sup>	3.41	15.2
10.5	53,000	3,120	EH 19 <sup>(7)</sup>	↓	1	61.1	284.0	3.58	15.2
9	38,880	-	EH 20	↓	1	75-100 <sup>(6)</sup>	350-400 <sup>(6)</sup>	3.26	21.7
8	30,720	-	EH 1	2014-0	1	25-75 <sup>(6)</sup>	250-300 <sup>(6)</sup>	3.46 <sup>(2)</sup>	20.8
6	17,280	-	EH 1	↑	2	-	-	4.48	40.6
5.5	14,520	1,730	EH 2	↑	1	25.8	130.2	2.20	8.9
5	12,000	3,100	EH 2	↑	2	-	-	2.96	24.4
10	48,000	-	EH 3	↑	1	50-100 <sup>(6)</sup>	300-400 <sup>(6)</sup>	4.00 <sup>(2)</sup>	20.9
8	30,720	2,580	EH 4	↑	1	50.7 <sup>(6)</sup>	276.5	3.33	20.9
7.5	25,900	-	EH 5	↑	1	25-75 <sup>(6)</sup>	250-300 <sup>(6)</sup>	3.08	16.1
10	48,000	-	EH 1	321 Ann.St.St.	1	25-50 <sup>(6)</sup>	150-200 <sup>(6)</sup>	2.19	12.0
12.5	75,000	-	↑	↑	2	-	-	3.25	28.3
14	94,080	-	↑	↑	3	-	-	4.020	33.7
14	94,080	-	↑	↑	4	-	-	4.080	39.2
14	94,080	-	EH 1	↑	5	-	-	4.230 <sup>(2)</sup>	39.2
10	48,000	1,725	EH 2	↑	1	25-50 <sup>(6)</sup>	150-200 <sup>(6)</sup>	2.125	10.8
12.5	75,000	2,400	↑	↑	2	-	-	3.16	24.7
12.2	71,200	2,870	↑	↑	3	-	-	3.45	28.0
13.8	91,500	3,240	↑	↑	4	-	-	3.88	32.3
14	94,080	3,620	↑	↑	5	-	-	4.27	37.6
14	94,080	3,925	↑	↑	6	-	-	4.59	43.0
14	94,080	4,280	↑	↑	7	-	-	4.90	49.4
14	94,080	5,290	EH 2	↑	8	-	-	5.29 <sup>(2)</sup>	56.9
10	48,000	1,760	EH 3	↑	1	39.0	181.7	2.16	10.9
10	48,000	2,200	↑	↑	2	-	-	2.88	19.6
8	30,720	2,440	↑	↑	3	-	-	3.02	19.6
8	30,720	2,520	↑	↑	4	-	-	3.16	20.6
9	38,880	2,700	EH 3	↑	5	-	-	3.35	22.8
16	122,880	2,670	EH 4	↑	1	119.7	503.0	3.42	25.8
17	138,720	-	EH 6	↑	1	200-300 <sup>(6)</sup>	500-600 <sup>(6)</sup>	3.54	19.6
17	138,720	-	EH 7	↑	1	200-300 <sup>(6)</sup>	500-600 <sup>(6)</sup>	3.42	17.4
16.5	130,680	-	EH 9	↑	1	200-300 <sup>(6)</sup>	500-600 <sup>(6)</sup>	3.29	20.9
10	48,000	1,760	EH 5	↑	1	25-50 <sup>(6)</sup>	150-200 <sup>(6)</sup>	2.26	9.91
12	69,120	2,420	EH 5	↑	2	-	-	3.04	20.9
14	94,080	3,010	EH 5	↑	3	-	-	3.63	25.3
16	122,880	-	EH 5	↑	4	-	-	4.05	27.5
10	48,000	-	EH 8	↑	1	25-50 <sup>(6)</sup>	150-200 <sup>(6)</sup>	2.17	7.6
12	69,120	-	EH 8	↑	2	-	-	3.00	19.6
14	94,080	-	EH 8	↑	3	-	-	3.40	23.9
16	122,880	-	EH 8	321 Ann.St.St.	4	-	-	4.08	30.2



## THICKNESS MEASUREMENTS (IN) (8)

## POSITION NUMBER

8	7	6	5	4	3	2	1	Center	1	2	3	4	5	6
.092	.092	.092	.092	.092	.092	.092	.092	.091	.092	.092	.092	.092	.092	.092
.094	.094	.094	.092	.092	.090	.089	.086	.085	.086	.088	.088	.090	.091	.092
.095	.095	.093	.091	.089	.086	.083	.079	.078	.081	.034	.086	.089	.090	.093
.095	.094	.090	.097	.083	.078	.073	.065	.063	.071	.076	.080	.085	.086	.092
.095	.094	.089	.083	.078	.070	.064	.053	.049	.061	.066	.072	.080	.088	.093
.095	.095	.089	.081	.072	.062	.054	.045	.041	.050	.056	.063	.076	.083	.092
.095	.094	.094	.093	.089	.087	.086	.084	.081	.080	.082	.081	.084	.090	.095
.096	.096	.096	.095	.080	.081	.075	.070	.056	.063	.070	.077	.081	.082	.092
.097	.096	.095	.092	.080	.080	.074	.066	.057	.060	.069	.074	.080	.079	.098
.098	.097	.096	.092	.079	.079	.072	.064	.050	.056	.066	.072	.079	.080	.101
.098	.098	.096	.091	.080	.076	.068	.059	.040	.053	.063	.070	.077	.078	.110
.094	.094	.093	.089	.083	.081	.082	.082	.081	.082	.081	.081	.083	.089	.092
.095	.095	.093	.087	.076	.070	.071	.073	.073	.073	.068	.068	.076	.086	.092
.096	.095	.094	.087	.076	.070	.072	.072	.072	.073	.068	.068	.076	.086	.092
.096	.095	.093	.085	.076	.071	.071	.070	.068	.070	.067	.069	.077	.087	.092
.097	.093	.091	.084	.073	.070	.072	.068	.063	.065	.066	.062	.072	.082	.089
.097	.095	.090	.083	.072	.066	.066	.063	.061	.064	.065	.061	.068	.073	.083
.097	.095	.090	.080	.070	.062	.063	.065	.055	.059	.062	.061	.068	.072	.090
.097	.095	.091	.081	.066	.056	.060	.057	.052	.055	.058	.055	.065	.071	.094
.094	.093	.093	.090	.085	.084	.084	.085	.084	.085	.084	.084	.086	.089	.092
.095	.094	.093	.088	.083	.079	.074	.064	.057	.067	.074	.080	.083	.087	.092
.095	.094	.094	.085	.078	.070	.061	.057	.049	.058	.064	.071	.079	.086	.092
.093	.092	.092	.090	.087	.086	.088	.088	.087	.088	.087	.085	.086	.090	.091
.093	.093	.092	.089	.086	.084	.079	.076	.075	.079	.082	.084	.086	.089	.091
.097	.096	.092	.086	.076	.070	.072	.076	.076	.075	.070	.067	.075	.087	.092
.098	.097	.094	.089	.086	.080	.080	.082	.081	.082	.081	.080	.085	.088	.094
.101	.098	.092	.088	.082	.075	.078	.079	.078	.079	.078	.077	.084	.088	.092
.107	.098	.092	.088	.082	.076	.079	.079	.078	.080	.078	.077	.084	.088	.093
					.068			.072			.065			
.092	.092	.090	.086	.081	.077	.076	.074	.072	.073	.076	.077	.080	.084	.090
.092	.092	.090	.083	.076	.067	.062	.060	.054	.057	.057	.065	.074	.082	.090
.093	.092	.091	.087	.080	.080	.082	.083	.082	.083	.082	.079	.080	.086	.090
.093	.092	.091	.088	.080	.080	.078	.073	.068	.072	.078	.079	.079	.086	.090
.097	.095	.087	.083	.092	.062	.078	.074	.072	.074	.066	.060	.075	.086	.090
.095	.094	.092	.083	.068	.064	.070	.073	.072	.074	.068	.055	.068	.083	.091
								.078						
.093	.093	.092	.089	.084	.081	.083	.082	.081	.082	.082	.081	.083	.088	.091
.094	.093	.092	-	.080	.078	.075	.071	.066	.070	.078	.079	.081	-	.091
.095	.093	.091	-	.075	.072	.069	.066	.061	.065	.069	.073	.076	-	.089
.094	.093	.091	-	.072	.070	.066	.062	.056	.062	.066	.070	.073	-	.089
.094	.092	.090	-	.070	.067	.064	.061	.056	.061	.065	.068	.071	-	.089
.093	.093	.093	-	.087	.086	.085	.084	.083	.084	.083	.084	.086	-	.092
.094	.093	.092	-	.084	.080	.076	.073	.070	.073	.076	.079	.081	-	.091
.094	.093	.092	-	.082	.077	.072	.070	.067	.071	.073	.076	.078	-	.092
.094	.093	.092	-	.080	.074	.070	.066	.063	.066	.069	.071	.074	-	.092
.095	.094	.093	.078	.074	.070	.065	.062	.058	.061	.065	.069	.073	.080	.093
.095	.094	.092	.076	.073	.068	.062	.058	.053	.058	.062	.067	.070	.077	.093
.096	.094	.091	.076	.073	.066	.060	.054	.047	.054	.060	.065	.069	.074	.091
.095	.094	.091	.072	.067	.064	.057	.051	.040	.051	.057	.063	.066	.072	.090
.092	.092	.091	.088	.084	.082	.083	.085	.082	.084	.083	.082	.086	.089	.092
.093	.092	.091	.087	.082	.081	.080	.078	.074	.079	.080	.081	.084	.089	.092
.092	.092	.091	.086	.081	.079	.077	.077	.074	.076	.078	.080	.083	.087	.092
.093	.092	.091	.087	.080	.078	.076	.075	.073	.075	.077	.079	.082	.088	.092
.093	.092	.091	.085	.079	.077	.075	.073	.071	.074	.076	.079	.081	.088	.092
.093	.092	.091	.084	.079	.074	.071	.075	.069	.075	.072	.073	.078	.084	.092
								.074						
								.076						
								.076						
.094	.094	.093	.090	.086	.083	.082	.083	.082	.083	.083	.084	.086	.090	.093
.094	.094	.092	.088	.083	.082	.078	.075	.073	.076	.079	.082	.084	.090	.093
.095	.094	.090	.085	.079	.076	.074	.070	.068	.072	.075	.078	.080	.087	.092
								.066						
								.085						
								.074						
								.070						
								.064						

2

TESTING (1)  
PERFORMED

Common F

7 8

92 .092  
93 .093  
94 .094  
94 .094  
94 .094  
94 .094  
98 .098  
03 .102  
06 .107  
08 .105  
11 .113  
93 .093  
92 .093  
93 .094  
93 .093  
99 .102  
98 .101  
99 .102  
99 .102  
92 .093  
93 .094  
94 .094  
91 .092  
92 .092  
93 .094  
96 .097  
96 .099  
97 .099

Mechanical Properties<sup>(9)</sup>

Mechanical Properties<sup>(9)</sup>

Mechanical Properties<sup>(9)</sup>

Mechanical Properties<sup>(9)</sup>

Mech. Prop. & Electron Microscopy<sup>(9)</sup>

X-ray Diffraction<sup>(9)</sup>

Mechanical Properties<sup>(9)</sup>

Mechanical Properties<sup>(9)</sup>

Mech. Prop. & Electron Microscopy<sup>(9)</sup>  
X-ray Diffraction<sup>(9)</sup>

Mechanical Properties<sup>(9)</sup>

Mechanical Properties<sup>(9)</sup>

Mech. Prop. & Electron Microscopy<sup>(7)</sup>  
Stress Corrosion<sup>(4)</sup>  
Stress Corrosion<sup>(5)</sup>  
X-ray Diffraction

Stress Corrosion<sup>(4)</sup>

Stress Corrosion<sup>(5)</sup>

.092" ir  
17 $\frac{1}{2}$ " dia  
20 $\frac{1}{2}$ " dia  
Closed t  
draw rac  
960ufd c  
.096" di  
.125" di  
4" elect  
vertical  
1 $\frac{1}{4}$ " Star

NOTES:  
specimen

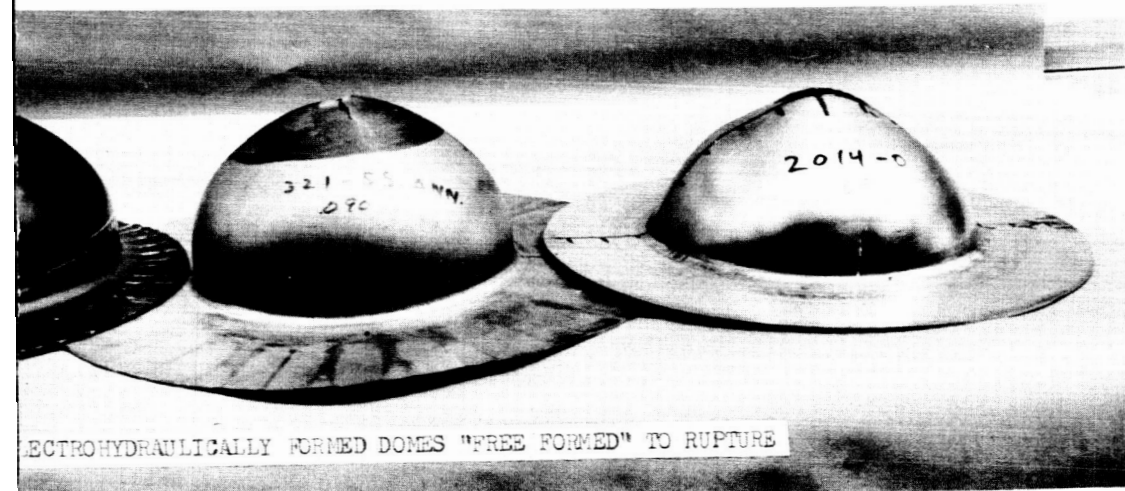


3

Forming Conditions

- initial thickness = all materials
- . blank for 2219-0 and 2014-0 al. alloys
- . blank for 321 stainless
- blank housing the 10" dia. open draw ring die of  $\frac{1}{2}$ " radius.
- capacitor bank
- a. magnesium initiating wire for discharges less than 10 kv.
- a. magnesium initiating wire for discharges 10 kv or greater.
- rode gap, axial in-line (opposing) electrodes mounted in a plane.
- doff distance.

- (1) For the size, source, and location of all test specimens obtained for the indicated tests, see Figure 23
- (2) Depth estimated, dome ruptured.
- (3) High speed motion pictures taken of metal strain.
- (4) Entire dome tested as - "as formed". See Table 11
- (5) Entire dome tested as - "Stress relieved" (1,850°F - 2,050°F for 1/2 hr. and air cooled). See Table 11
- (6) Approximate range of strain rate based on experimental data obtained from the electrohydraulic and explosive processes - not actually measured.
- (7) Cimcool lubricant used on both sides of blank.
- (8) See Figure 19 for plot of thickness change versus dome position no.
- (9) For test results, see Tables 5, 13 & Appendix A.
- (10) Original thickness values have measured .090" to .094".



ELECTROHYDRAULIC FREE FORMING DOME DATA OBTAINED AT VARYING ENERGY LEVELS FOR .092" 2219-0, 2014-0 AND 321 STAINLESS.

**TABLE 4**

4

Coupon No.	Alloy	Original Thickness (in.)	Coupon Center Thickness (in.)	Thinout (%)
HS 1	2219-0	.092	.081	11.0
HS 2	↕	"	.065	29.40
HS 3L	↕	"	.053	42.40
HS 4	2219-0	"	.051	44.60
HS 1	2014-0	.091	.083	8.80
HS 2	↕	"	.071	22.00
HS 3L	2014-0	"	.051	44.00
HS 1	321-Ann.St.St.	.094	.088	6.40
HS 2	↕	.094	.081	13.80
HS 3	321-Ann.St.St.	.092	.068	26.10
EH 10	2219-0	.093	.081	12.90
EH 14	↕	.091	.076	16.50
EH 16	↕	.092	.076	17.40
EH 11	↕	.093	.068	26.90
EH 12	2219-0	"	.052	44.10
EH 2B	2014-0	.090	.083	7.8
EH 4	↕	.091	.073	19.80
EH 2A	↕	.090	.068	24.40
EH 11	2014-0	.091	.054	40.60
EH 3B	321-Ann.St.St.	.092	.083	10.80
EH 3A	↕	"	.074	19.60
EH 4	↕	.093	.071	23.60
EH 2	321-Ann.St.St.	"	.047	49.50
M 1	2219-0	.092	.082	10.90
M 3B	↕	"	.072	21.80
M 2L	↕	"	.059	35.90
M 3A	2219-0	"	.058	37.00
M 1	2014-0	.090	.075	16.70
M 3B	↕	"	.072	20.00
M 2L	↕	"	.058	35.60
M 3A	2014-0	"	.051	43.40

Yield* (psi)	Ultimate (psi)	Elongation (% in 2")	Rockwell Hardness RF Scale	Forming Process
34,400	40,900	8.5	80	Hydrostatic ↑
37,800	43,800	5.5	83	
39,100	44,400	4.5	84	
38,400	44,300	3.5	84	
22,500	26,000	12.0	49	↓ Hydrostatic
26,900	30,100	4.0	59	
32,400	34,600	2.0	69	
60,000	90,400	45.5	-	
79,500	102,900	35.0	-	Electrohydraulic ↑
99,100	121,300	18.0	-	
25,400	30,100	8.5	66	
28,200	31,900	6.5	65.5	
28,300	32,100	6.5	70.5	↓ Electrohydraulic
27,500	32,800	4.0	72	
34,300	37,400	2.0	73	
21,500	25,000	14.5	52	
24,900	28,200	5.5	63.1	Electrohydraulic ↑
29,300	32,800	4.0	51	
30,300	33,900	3.0	66	
77,200	99,500	37.0	-	
98,400	116,500	23.0	-	↓ Electrohydraulic
103,500	119,800	16.0	-	
132,400	159,600	5.5	-	
24,200	29,400	14.0	58	
27,400	32,000	6.5	-	
28,000	33,900	3.5	71	
31,200	35,900	2.5	65	
27,300	30,700	4.5	54.5	↓ Magnetic Repulsion
27,900	30,900	4.5	56.5	
29,000	31,500	3.5	66	
29,300	29,600	2.0	57	

EX 1	2219-0	.092	.079
EX 3	↑	.091	.071
EX 2	↓	.092	.068
EX 6	↑	"	.065
EX 5	2219-0	"	.050
EX 1	2014-0	.093	.087
EX 2	↑	"	.071
EX 3	↓	"	.058
EX 6	2014-0	.093	.058
EX 1	321-Ann.St.St.	.092	.086
EX 2	↑	.093	.075
EX 3	↓	.092	.075
EX 6	↑	.093	.075
EX 5	↓	"	.063
EX 4	321-Ann.St.St.	.090	.054

- NOTES:
1. All coupons taken in the transverse grain number contains letter L for "Longitudinal"
  2. \* Denotes Extensometer yield, 0.2% offset
  3. For size, source, and location of all tests
  4. For the Electrohydraulic recorded data and forming  
For the Explosive recorded data and forming  
For the Magnetic recorded data and forming  
For the Hydrostatic recorded data and forming
  5. Plots of yield, ultimate and elongation vs. strain for the above forming processes can be seen

3

14.10	27,700	30,700	7.5	63
22.00	28,500	32,400	5.0	70
26.10	28,400	33,100	5.0	68
29.40	39,700	44,300	5.0	84
45.60	32,600	42,900	3.0	73
6.45	22,900	27,200	11.5	51
23.65	27,900	31,200	4.0	60
37.70	29,600	33,400	3.0	67
37.70	29,400	32,800	2.5	67
6.50	64,300	97,400	47.5	-
19.70	94,400	115,000	25.5	-
18.50	87,400	114,300	24.0	-
19.70	90,500	107,500	23.0	-
32.30	121,100	144,900	8.5	-
40.00	131,000	150,900	6.5	-



direction except where coupon identification  
 1 grain direction".  
 t, 2" Gage length.  
 file coupons, see Figure 23  
 d forming conditions, see Table 4  
 ng conditions, see Table 8  
 g conditions, see Table 10  
 ming conditions, see Table 11A  
 alues versus % thinout  
 en in figures 15, 16 and 17.

MECHANICAL PROPERTIES OF .090" 2219-0, 2014-0 AND  
 304 STAINLESS TENSILE COUPONS OBTAINED FROM  
 PROCESSES "FREE FORMED" BY THE ELECTROHYDRAULIC,  
 EXPLOSIVE, MAGNETIC AND HYDROSTATIC FORMING PROCESSES

4

**TABLE 5**

Coupon No.	Alloy	Orig. Thkns. (in.)	Center Coupon Thkns. (in.)	Thinout %	Impact Condition	Yield* (psi)	Ult. (psi)	Elong. (% in 2")	Rockwell Hardness (RF Scale)	Forming Process
EHCD 24	2219-0	.092	.072	21.8	High	31,700	34,100	3.5	74	Electrohydraulic
EHCD 26	"	"	.070	23.9	Low	31,700	34,800	3.0	73.5	
EHCD 7	2014-0	.090	.056	37.8	High	31,600	33,800	2.0	70	Electrohydraulic
EHCD 9	"	"	.051	43.4	Low	31,300	33,300	2.0	68	
EHCD 15	321-Ann. St. St.	.091	.056	38.5	Low	130,100	153,100	6.0	-	Electrohydraulic
EHCD 17	"	.092	.065	29.4	High	124,000	147,000	6.0	-	
EXCD 1	2219-0	.093	.053	43.0	Low	32,700	36,500	3.5	73	Explosive
EXCD 3	"	.092	.057	38.0	High	32,400	36,000	3.5	74	
EXCD 1	2014-0	.091	.045	50.6	Low	31,400	33,900	2.0	65	Explosive
EXCD 4	"	"	.044	51.6	High	31,600	33,000	2.0	65	
EXCD 1	321-Ann. St. St.	.092	.068	26.1	Low	111,700	134,000	12.0	-	Explosive
EXCD 4	"	.090	.072	20.0	High	104,100	123,200	12.0	-	

NOTES: 1. All coupons taken in the transverse grain direction.

2. # Denotes Extensometer yield, 0.2% offset, 2" gage length.

3. For size, source and location of all tensile coupons, see Figure 23

4. For the electrohydraulic and explosive recorded data and forming conditions, see Tables 6 & 9

MECHANICAL PROPERTIES OF .092" 2219-0, 2014-0, AND 321 STAINLESS TENSILE COUPONS OBTAINED FROM JONES "DIE IMPACTED" BY THE ELECTROHYDRAULIC AND EXPLOSIVE PROCESSES.



INPUT ENERGY		SPECIMEN NUMBER	ALLOY	SHOT NO.	DIE IMPACT CONDITION
KV	JOULES				
9	38,880	EHCD 22	2219-0	1	-
9	38,880	EHCD 22		2	High
9	38,880	EHCD 24		1	-
11	58,080	EHCD 24		2	High
9	38,880	EHCD 27		1	-
11	58,080	EHCD 27		2	High
9	38,880	EHCD 21		1	-
9	38,880	EHCD 21		2	Low
9	38,880	EHCD 26		1	-
11	58,080	EHCD 26		2	Low
7	23,520	EHCD 7	2014-0	1	-
8	38,880	EHCD 7		2	High
7	23,520	EHCD 11		1	-
8	38,880	EHCD 11		2	High
6	17,280	EHCD 12		1	-
5	12,000	↕		2	-
5	12,000	↕		3	-
7	23,520	EHCD 12		4	High
6	17,280	EHCD 9		1	-
5	12,000	↕		2	-
↕	↕	↕		3	-
↕	↕	↕		4	-
5	12,000	EHCD 9		5	Low
6	17,280	EHCD 10		1	-
5	12,000	↕		2	-
↕	↕	↕	3	-	
5	12,000	EHCD 10	4	-	
↕	↕	↕	5	Low	
12	69,120	EHCD 12	321 Ann.St.St.	1	-
13	81,120	EHCD 12		2	-
17	138,720	EHCD 12		3	High
12	69,120	EHCD 13		1	-
13	81,120	EHCD 13		2	-
17	138,720	EHCD 13		3	High
13	81,120	EHCD 16		1	-
14	94,080	EHCD 16		2	-
16	122,880	EHCD 16		3	High
13	81,120	EHCD 17		1	-
14	94,080	EHCD 17		2	-
16	122,880	EHCD 17		3	High
10	48,000	EHCD 10		1	-
12	69,120	↕		2	-
14	94,080	↕		3	-
16	122,880	EHCD 10		4	Low
10	48,000	EHCD 11		1	-
12	69,120	↕		2	-
14	94,080	↕		3	-
16	122,880	EHCD 11		4	Low
10	48,000	EHCD 14	1	-	
12	69,120	↕	2	-	
13	81,120	↕	3	-	
13	81,120	EHCD 14	4	Low	
10	48,000	EHCD 15	1	-	
12	69,120	↕	2	-	
13	81,120	↕	3	-	
13	81,120	↕	4	-	
13	81,120	EHCD 15	5	Low	

DOME DEPTH (IN)	THINOUT AT DOME CENTER (%)	THICKNESS MEASUREMENTS (IN)																			
		POSITION NUMBER																			
		8	7	6	5	4	3	2	1	Center	1	2	3								
3.50	-																				
4.02	29.4												.065								
3.43	-																				
4.02	25.0												.069								
3.56	-																				
4.04	24.7	.095	.094	.092	.082	.079	.064	.060	.064	.070	.061	.058	.065								
2.97	-																				
4.02	35.6	.098	.097	.094	.087	.077	.069	.067	.069	.061	.068	.064	.067								
3.57	-																				
4.03	21.7												.072								
3.02	-																				
4.05	41.1												.053								
2.93	-																				
4.05	32.2	.093	.092	.091	.083	.074	.067	.061	.060	.050	.058	.061	.067								
2.84	-																				
3.14	-																				
3.48	-																				
4.04	36.7												.057								
2.62	-																				
2.90	-																				
3.26	-																				
3.62	-																				
3.94	-																				
4.05	53.3												.042								
2.79	-																				
3.21	-																				
3.58	-																				
3.93	-																				
4.05	45.6	.094	.092	.091	.084	.079	.069	.061	.054	.049	.054	.060	.069								
2.70	-																				
3.32	-																				
4.04	24.4												.068								
2.59	-																				
3.29	-																				
4.05	38.8												.055								
2.79	-																				
3.49	-																				
4.05	33.7												.061								
2.81	-																				
3.55	-																				
4.04	33.7	.092	.091	.091	.078	.073	.066	.061	.061	.061	.061	.062	.064								
2.36	20.0												.072								
3.05	22.8												.065								
3.74	38.8												.055								
4.03	44.4												.050								
2.33	17.8												.074								
3.01	26.7												.066								
3.71	32.2												.061								
4.03	32.2	.093	.092	.090	.082	.076	.068	.062	.063	.061	.065	.063	.064								
2.43	-																				
3.17	-																				
3.72	-																				
4.04	32.2												.061								
2.26	-																				
3.05	-																				
3.57	-																				
4.00	-																				
4.04	37.8												.056								

2

TESTING (1)  
PERFORMED

4 5 6 7 8

X-ray Diffraction (2)

Mechanical Properties (2)

.080 .082 .092 .091 .096

X-ray Diffraction (2)

.079 .085 .094 .095 .096

Mechanical Properties (2)

Mechanical Properties (2)

.073 .081 .090 .091 .092

X-ray Diffraction (2)

Mechanical Properties (2)

.080 .084 .091 .092 .093

X-ray Diffraction (2)

Stress Corrosion (4)

Stress Corrosion (3)

X-ray Diffraction (2)

.076 .077 .088 .092 .093

Mechanical Properties (2)

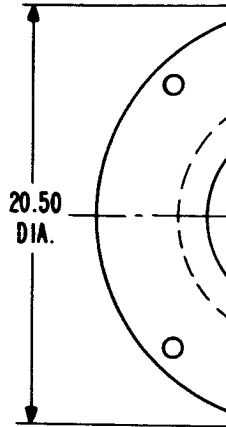
Stress Corrosion (3)

.073 .082 .090 .092 .093

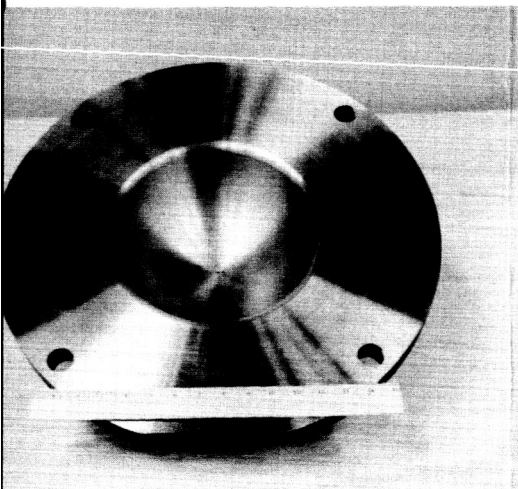
Stress Corrosion (4)

X-ray Diffraction (2)

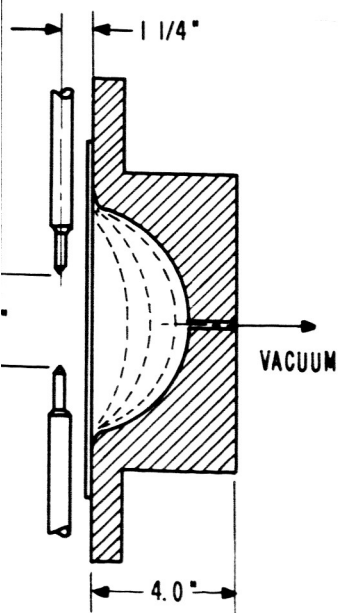
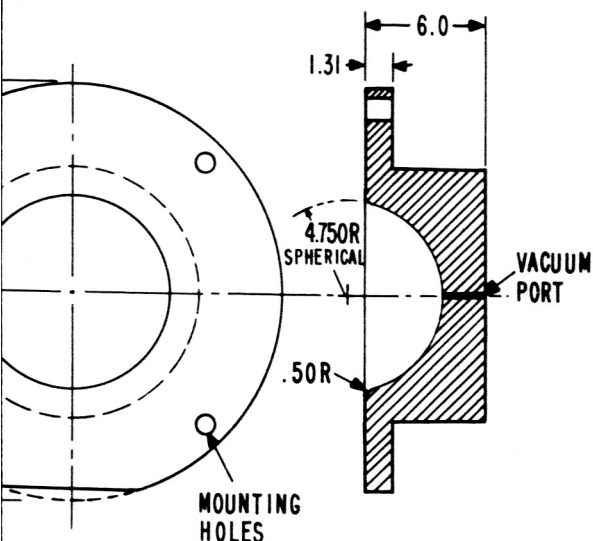
Mechanical Properties (2)



3



Hemispherical Die



Common Forming Conditions

- .092" initial thickness - all materials
- 17½" dia. blank for 2219-O and 2014-O al. alloys.
- 20½" dia. blank for 321 stainless
- Closed tank housing the Hemispherical die.
- 960 ufd capacitor bank.
- .096" dia. magnesium initiating wire for discharges less than 10 kv.
- .125" dia. magnesium initiating wire for discharges 10 kv or greater.
- 4" electrode gap, axial in-line (opposing) electrodes mounted in a vertical plane.
- 1¼" standoff distance
- Cimcool lubricant used on both sides of blank.
- 28" Hg. vacuum behind workpiece.

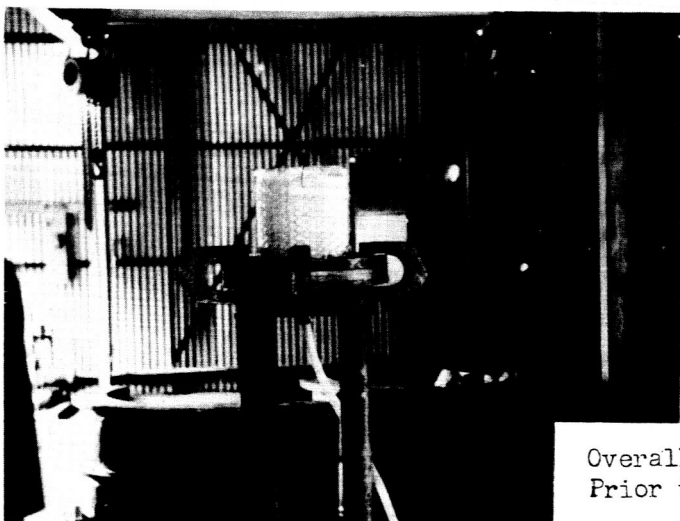
NOTES

- (1) For the size, source, and location of all test specimens obtained, see Figure 23 for the indicated tests.
- (2) For test results, See Tables 13, and 7.
- (3) Entire dome tested as - "As formed". See Table 14.
- (4) Entire dome tested as - "Stress relieved". (1,850°F - 2,050°F for ½ hr. and air cooled) See Table 14.

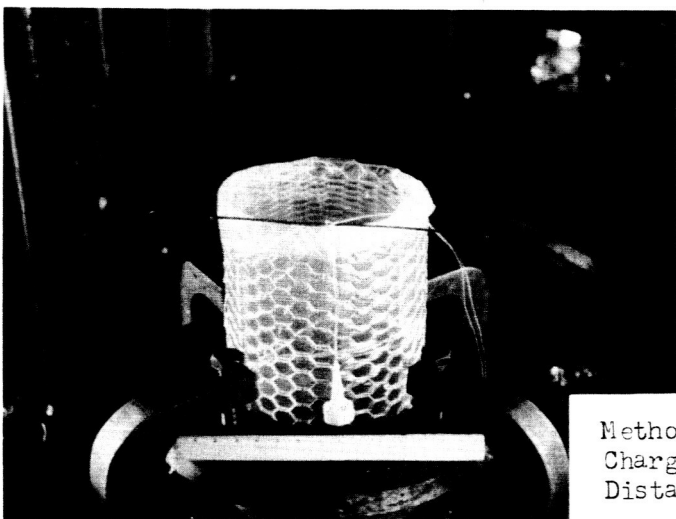
ELECTROHYDRAULIC DIE IMPACTING DOME  
 DATA OBTAINED AT VARYING ENERGY LEVELS  
 FOR .092" 2219-O, 2014-O AND 321 STAINLESS.

TABLE 6

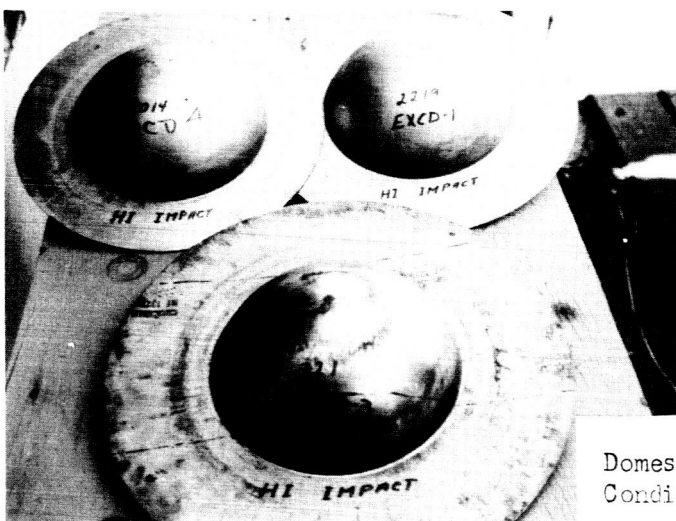
4



Overall View of Test Setup  
Prior to Detonation



Method Employed to Position  
Charge and Adjust Standoff  
Distance



Domes Explosively Formed Under  
Conditions of High Die Impact

6

INPUT ENERGY

PELLET			STANDOFF DISTANCE (IN)	SPECIMEN NO.	ALLOY	SHOT NO.	AVERAGE STRAIN INCHES/ IN/ SEC/
WT. (GR)	DIA. (IN)	JOULES					
20	1.0	92,000	2	EX 3	2219-0	1 <sup>(3)</sup>	147.3
20	1.0	92,000	3	EX 4		1 <sup>(3)</sup>	203.6
20	1.0	92,000	4	EX 2		1	200 - 300 <sup>(6)</sup>
12	1.12	55,200	5	EX 1		1	100 - 200 <sup>(6)</sup>
6	0.75	27,600	5	EX 5		1	20 - 50 <sup>(6)</sup>
↑	↑	↑	2.5	EX 5		2	-
↓	↓	↓	2.5	EX 5		3	-
↓	↓	↓	5	EX 6		1 <sup>(3)</sup>	20.1
↓	↓	↓	2.5	EX 6		2	-
6	0.75	27,600	2.5	EX 6		3	-
20	1.0	92,000	3	EX 3	2014-0	1 <sup>(3)</sup>	100 - 200 <sup>(6)</sup>
20	1.0	92,000	3	EX 4		1 <sup>(3)</sup>	130.4
20	1.0	92,000	5	EX 2		1	100 - 200 <sup>(6)</sup>
5	0.75	22,990	5	EX 1		1	50 - 75 <sup>(6)</sup>
6	0.75	27,600	5	EX 6		1	"
↑	↑	↑	3	EX 6		2	-
↑	↑	↑	3.5	EX 6		3	-
↑	↑	↑	5	EX 7		1 <sup>(3)</sup>	63.4
↓	↓	↓	3	EX 7		2	-
↓	↓	↓	3.5	EX 7		3	-
6	0.75	27,600	5	EX 5	1	50 - 75 <sup>(6)</sup>	
30	1.25	138,000	3	EX 5	2	-	
			2	EX 5	3	-	
			3	EX 8	1	200 - 300 <sup>(6)</sup>	
75	2.0	344,850	2	EX 6	321 Ann.St.St.	1	150 - 200 <sup>(6)</sup>
75	2.0	344,850	2	EX 7		1	"
75	2.0	344,850	2	EX 9		1	"
75	2.0	344,850	2	EX 10		1 <sup>(3)</sup>	174.9
50	1.5	229,900	3	EX 3		1	100 - 200 <sup>(6)</sup>
50	1.5	229,900	4	EX 2		1	50 - 100 <sup>(6)</sup>
12	1.12	55,200	4	EX 1		1	20 - 50 <sup>(6)</sup>
20	1.0	92,000	4	EX 4		1	"
35	1.5	160,930	3	EX 4		2	-
35	1.5	160,930	2	EX 4		3	-
30	1.5	137,940	3	EX 5		1	50 - 100 <sup>(6)</sup>
35	1.5	160,930	3	EX 5		2	-
35	1.5	160,930	3	EX 5		3	-
20	1.0	92,000	4	EX 8		1	20 - 50 <sup>(6)</sup>
35	1.5	160,930	3	EX 8		2	-
35	1.5	160,930	3	EX 8		3	-
20	1.0	92,000	4	EX 11	1	20 - 50 <sup>(6)</sup>	
35	1.5	160,930	3	EX 11	2	-	
35	1.5	160,930	3.5	EX 11	3	-	
20	1.0	92,000	4	EX 12	1	20 - 50 <sup>(6)</sup>	
35	1.5	160,930	3	EX 12	2	-	
35	1.5	160,930	3	EX 12	3	-	
150	2.0	689,700	3	EX 13	321 Ann.St.St.	1	200 - 300 <sup>(6)</sup>

MAX. STRAIN INCHES/IN/SEC/	DOME DEPTH (IN)	THINOUT AT DOME CENTER (%) <sup>(9)</sup>	THICKNESS MEASUREMENT POSITION									
			8	7	6	5	4	3	2	1	0	
424.0	4.00 <sup>(2)</sup>	22.0	.094	.093	.090	.083	.065	.057	.064	.070	.070	
563.0	3.04	31.5	.093	.093	.092	.088	.080	.072	.067	.066	.066	
0 - 600 <sup>(6)</sup>	3.12	27.2	.093	.092	.092	.086	.082	.077	.073	.069	.069	
0 - 400 <sup>(6)</sup>	2.15	15.2	.092	.092	.091	.090	.087	.086	.083	.081	.079	
0 - 300 <sup>(4)</sup>	1.29	-	-	-	-	-	-	-	-	-	-	
-	2.50	-	-	-	-	-	-	-	-	-	-	
-	3.71	48.9	.093	.093	.092	.082	.070	.059	.053	.051	.049	
193.8	1.17	-	-	-	-	-	-	-	-	-	-	
-	2.09	-	-	-	-	-	-	-	-	-	-	
-	3.12	29.7	-	-	-	-	-	-	-	-	.066	
0 - 400 <sup>(6)</sup>	4.05	45.2	.094	.093	.092	.089	.077	.066	.060	.056	.055	
330.0	3.74	36.2	.094	.093	.092	.084	.071	.060	.058	.060	.059	
0 - 400 <sup>(5)</sup>	2.62	24.7	.093	.093	.093	.087	.084	.080	.075	.073	.072	
0 - 300 <sup>(6)</sup>	1.31	6.45	.093	.093	.093	.092	.091	.090	.089	.088	.088	
"	1.38	-	-	-	-	-	-	-	-	-	-	
-	2.74	-	-	-	-	-	-	-	-	-	-	
-	3.66	37.7	-	-	-	-	-	-	-	-	.055	
265.0	1.56	-	-	-	-	-	-	-	-	-	-	
-	2.70	-	-	-	-	-	-	-	-	-	-	
-	3.45	43.5	-	-	-	-	-	-	-	-	.055	
0 - 300 <sup>(6)</sup>	1.44	-	-	-	-	-	-	-	-	-	-	
-	2.69	-	-	-	-	-	-	-	-	-	-	
-	4.00 <sup>(2)</sup>	41.3	-	-	-	-	-	-	-	-	.055	
0 - 500 <sup>(6)</sup>	4.70 <sup>(2)</sup>	-	-	-	-	-	-	-	-	-	-	
0 - 900 <sup>(6)</sup>	4.56	13.3	.095	.094	.088	.079	.069	.067	.072	.076	.076	
"	4.38	17.2	-	-	-	-	-	-	-	-	.076	
"	4.68	-	-	-	-	-	-	-	-	-	-	
807.0	4.44	-	-	-	-	-	-	-	-	-	-	
0 - 500 <sup>(6)</sup>	3.24	20.6	.094	.093	.091	.088	.081	.078	.077	.076	.076	
0 - 300 <sup>(6)</sup>	2.80	20.4	.094	.094	.093	.087	.084	.083	.080	.076	.076	
0 - 200 <sup>(6)</sup>	1.52	5.43	.095	.095	.094	.093	.092	.090	.087	.086	.086	
"	1.95	-	-	-	-	-	-	-	-	-	-	
-	3.46	-	-	-	-	-	-	-	-	-	-	
-	5.22	41.2	-	-	-	-	-	-	-	-	.055	
0 - 300 <sup>(5)</sup>	2.50	-	-	-	-	-	-	-	-	-	-	
-	3.75	-	-	-	-	-	-	-	-	-	-	
-	4.67	33.3	-	-	-	-	-	-	-	-	.055	
0 - 200 <sup>(6)</sup>	1.80	-	-	-	-	-	-	-	-	-	-	
-	3.25	-	-	-	-	-	-	-	-	-	-	
-	4.70 <sup>(2)</sup>	26.1	-	-	-	-	-	-	-	-	.055	
0 - 200 <sup>(6)</sup>	1.89	-	-	-	-	-	-	-	-	-	-	
-	3.49	-	-	-	-	-	-	-	-	-	-	
-	4.49	30.4	-	-	-	-	-	-	-	-	.055	
0 - 200 <sup>(6)</sup>	1.89	-	-	-	-	-	-	-	-	-	-	
-	3.55	-	-	-	-	-	-	-	-	-	-	
-	4.78 <sup>(2)</sup>	35.5	-	-	-	-	-	-	-	-	.055	
0 - 1000 <sup>(6)</sup>	5.50 <sup>(2)</sup>	30.4	.094	.092	.085	.076	.065	.059	.067	.066	.066	

2

EMENTS (IN) (7)

NUMBER

	1	2	3	4	5	6	7	8	TESTING (1) PERFORMED
1	.069	.065	.051	.072	.083	.091	.092	.093	Mechanical Properties (10)
3	.065	.065	.071	.080	.090	.092	.093	.093	X-ray Diffraction & Electron Micro
7	.068	.072	.077	.083	.086	.092	.093	.094	Mechanical Properties (10)
3	.073	.081	.083	.086	.089	.090	.092	.093	Mechanical Properties (10)
9	.051	.050	.057	.069	.081	.091	.092	.093	Mechanical Properties (10)
4									X-ray Diffraction (10)
1	.060	.063	.071	.081	.087	.093	.093	.094	Mechanical Properties (10)
3	.061	.060	.059	.068	.079	.091	.092	.093	X-ray Diffraction (10)
0	.072	.075	.079	.082	.085	.092	.092	.092	Mech. Prop. & Electron Microscopy (10)
7	.087	.088	.089	.090	.091	.093	.093	.093	Mechanical Properties (10)
8									Mechanical Properties (10)
2									X-ray Diffraction (10)
4									
8	.076	.072	.066	.065	.077	.088	.093	.094	Mech. Prop. & Electron Microscopy (10)
7									X-ray Diffraction (10)
									Stress Corrosion (4)
									Stress Corrosion (5)
3	.074	.075	.078	.081	.087	.092	.093	.093	Mechanical Properties (10)
4	.076	.078	.082	.084	.087	.092	.093	.093	Mechanical Properties (10)
7	.086	.087	.088	.090	.090	.091	.091	.091	Mechanical Properties (10)
3									Mechanical Properties (10)
2									Mechanical Properties (10)
8									X-ray Diffraction (10)
4									Stress Corrosion (4)
8									Stress Corrosion (5)
4	.066	.062	.061	.066	.077	.086	.093	.095	

TABLE 8

3



copy (10)

### COMMON FORMING CONDITIONS

.092" initial thickness - all materials.  
17½" Dia. blank for 2219-0 and 2014-0 al. alloys.  
20½" Dia. blank for 321 stainless.  
4 ft. Die support test stand housing the .10" dia. open  
draw ring die of ½" draw radius.  
Eight special "C" clamps for blank hold down.  
Cylindrical "chicken wire-plastic bag" water container  
of 4½ gal. capacity.  
97½/2½% RDX/WAX High Explosive Pellet  
"Hercules Powder Co." #8 Blasting Cap  
"Hercules Powder Co." Blasting Generator  
and Galvanometer.

### NOTES

- (1) For the size, source, and location of all test specimens obtained, see Figure 23 for the indicated tests. Stress corrosion tests performed only on the 321 stainless domes.
- (2) Depth estimated, dome badly ruptured.
- (3) High speed motion pictures taken of metal strain.
- (4) Entire dome tested as - "As formed".
- (5) Entire dome tested as - "Stress relieved".  
(1,850°F - 2,050°F for ½ hr. and air cooled)
- (6) Approximate range of strain rate based on experimental data obtained from the electrohydraulic and explosive processes - not actually measured.
- (7) See Figure 20 for plot of thickness change vs. dome position no.
- (8) For field photos of Explosive forming experiments, see Figure 41
- (9) Original thickness values have measured .090" to .094".
- (10) For test results, see Tables 5, 13, 14, & Appendix A.

EXPLOSIVE, FREE FORMING DOME DATA OBTAINED AT VARYING ENERGY LEVELS  
FOR .092", 2219-0, 2014-0 AND 321 STAINLESS

4

WT. (GMS)	INPUT ENERGY		STANDOFF DISTANCE (IN.)
	DIA. (IN.)	JOULES	
20	1.0	92,000	3
6	0.75	27,600	4
20	1.0	92,000	2.5
6	0.75	27,600	4
20	1.0	92,000	3
6	0.75	27,600	5
20	1.0	92,000	3
6	0.75	27,600	5
20	1.0	92,000	4
6	0.75	27,600	3
20	1.0	92,000	4
6	0.75	27,600	
6	0.75	27,600	
20	1.0	92,000	
6	0.75	27,600	
20	1.0	92,000	4
6	0.75	27,600	5
75	2.0	344,850	4
35	1.5	160,930	3
50	1.5	229,900	2.5
35	1.5	160,930	3
50	1.5	229,900	3.5
35	1.5	160,930	2
50	1.5	229,900	2.5
35	1.5	160,930	5
36	1.12	165,528	4
35	1.5	160,930	2
36	1.12	165,528	4
35	1.5	160,930	2
50	1.5	229,900	3.5
35	1.5	160,930	2
50	1.5	229,900	2.5
35	1.5	160,930	5

#### Common Forming Conditions

.092" initial thickness - all materials.  
 17 $\frac{1}{2}$ " dia. blank for 2219-0 and 2014-0 al. al.  
 20 $\frac{1}{2}$ " dia. blank for 321 stainless.  
 4 ft. Die support test stand housing the  
 Hemispherical die.  
 Four special "C" clamps for blank hold down.  
 Cylindrical "chicken wire - plastic bag" wat  
 container of 4 $\frac{1}{2}$  Gal. capacity.  
 97 $\frac{1}{2}$ /2 $\frac{1}{2}$ % RDX High Explosive Pellet  
 "Hercules Powder Co." #8 Blasting Cap.  
 "Hercules Powder Co." Blasting Generator  
 and Galvanometer

SPECIMEN NO.	ALLOY	SHOT NO.	DIE IMPACT CONDITION	DOMESTIC DEPT. (IN.)	
EXCD 2	2219-0	1	-	3.80	
EXCD 2	↕	2	High	4.05	
EXCD 3		1	-	3.65	
EXCD 3		2	High	4.05	
EXCD 1		1	-	3.77	
EXCD 1		2	Low	4.05	
EXCD 4		1	-	3.79	
EXCD 4		2219-0	2	Low	4.05
EXCD 2		2014-0	1	-	3.32
EXCD 2	↕	2	High	4.05	
EXCD 4		1	-	3.27	
EXCD 4		2	-	4.02	
EXCD 4		3	High	4.05	
EXCD 1		1	-	3.46	
EXCD 1		2	Low	4.05	
EXCD 5		1	-	3.61	
EXCD 5		2014-0	2	Low	4.05
EXCD 3	321 Ann.St.St.	1	-	3.41	
EXCD 3	↕	2	High	4.01	
EXCD 4		1	-	3.51	
EXCD 4		2	High	4.01	
EXCD 6		1	-	3.06	
EXCD 6		2	High	4.05	
EXCD 8		1	-	3.93	
EXCD 8		2	High	4.05	
EXCD 1		1	-	2.30	
EXCD 1		2	Low	3.96	
EXCD 2		1	-	2.52	
EXCD 2		2	Low	4.02	
EXCD 5		1	-	3.12	
EXCD 5		2	Low	4.05	
EXCD 7		1	-	3.93	
EXCD 7	321 Ann.St.St.	2	Low	4.05	

loys.

er

2

THINOUT (6)  
AT DOME  
CENTER  
(%)

THICKNESS MEASUREMENT

POSITION NUMBER

	8	7	6	5	4	3	2	1	Center	1
-										
47.3	.093	.093	.092	.082	.070	.059	.053	.051	.049	.051
-										
38.0									.057	
-										
51.1									.045	
-										
45.6	.092	.092	.091	.078	.067	.057	.052	.051	.050	.051
-										
50.0									.045	
-										
53.8	.092	.091	.090	.080	.070	.064	.058	.053	.042	.047
-										
50.0									.045	
-										
27.8	.091	.091	.090	.085	.079	.074	.069	.068	.065	.067
-										
-										
22.2	.091	.090	.088	.080	.073	.066	.068	.071	.070	.068
-										
-										
-										
28.2	.093	.093	.090	.080	.072	.067	.068	.067	.066	.067
-										
-										
-										
-										

3

EXPLOSIVE DIE IMPACTING DOME DATA OBTAINED  
AT VARYING ENERGY LEVELS FOR .092" 2219-C,  
2014-0, AND 321 STAINLESS.

TABLE 9

3 (IN.)

TESTING (1)  
PERFORMED

2	3	4	5	6	7	8	
.050	.057	.069	.081	.091	.092	.093	X-ray Diffraction (2) Mechanical Properties (2) Mechanical Properties (2)
.052	.058	.069	.082	.092	.092	.093	X-ray Diffraction (2) X-ray Diffraction (2)
.055	.064	.071	.079	.083	.091	.093	Mechanical Properties (2) Mechanical Properties (2)
.070	.074	.080	.085	.083	.092	.093	X-ray Diffraction (2) X-ray Diffraction (2)
.063	.065	.074	.079	.089	.090	.091	Mechanical Properties (2) Stress Corrosion (4) Stress Corrosion (3)
.067	.067	.072	.081	.091	.093	.094	Mechanical Properties (2) X-ray Diffraction (2) Stress Corrosion (4) Stress Corrosion (3)

5

NOTES

- 1) For the size, source and location of all test specimens obtained, see Figure 23 for the indicated tests. Stress corrosion tests performed only on the 321 stainless domes.
- 2) For test results, see Tables 7 & 13
- 3) Entire dome tested as - "As formed". See Table 14
- 4) Entire dome tested as - "Stress relieved". (1,850°F - 2,050°F for 1/2 hr. and air cooled). See Table 14
- 5) For field photos of Explosive forming experiments, see Figure 41
- 6) Original thickness values have measured .090" to .094".

INPUT ENERGY		VOLUME (CC)	SPECIMEN NUMBER	ALLOY	SHOT NO.	AVERAGE STRAIN RATE IN/IN/SEC
KV	JOULES					
8	30,720	1,590	M2	2219-0	1	200-3
8	30,720	1,580	M3	2219-0	1 (2)	247.
4.5	9,720	900	M1	2219-0	1 (2)	97.
8	30,720	1,740	M2	2014-0	1 (2)	253.
7.5	25,900	1,660	M3	2014-0	1	100-2
5	12,000	1,100	M1	2014-0	1 (2)	142.

Common Forming Conditions

.092" thick flat blank of 17½" dia.  
 10" dia. Open Draw Ring Die of ½" draw radius.  
 6 turn spirally wound flat coil of 139 uhs.  
 inductance housed in closed die.  
 960 ufd capacitor bank.

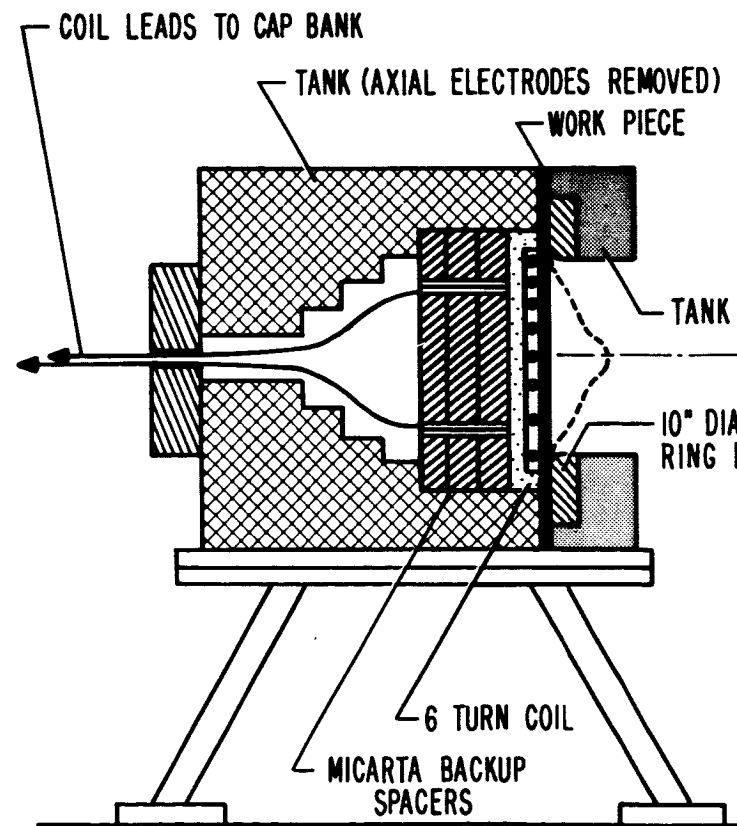


**Figure 54 Method Used to House Six Turn Co  
Strain Rate Measurements**

TEST NO.	MAX. STRAIN INCHES/IN/SEC.	DOME DEPTH (IN)	PEAK COIL CURRENT (AMPS)	DISCHARGE FREQUENCY	THINOUT AT DOME CENTER (%)
00(3)	700-800(3)	3.065	21,000	1.4 kc	37.0
3	723.0	3.145	21,000	1.14 kc	37.0
7	675.0	1.445	11,700	-	10.88
5	877.0	3.365	21,000	1.4 kc	36.7
00(3)	700-800(3)	3.14	19,300	-	35.6
3	769.0	1.825	13,100	1.25 kc	16.67

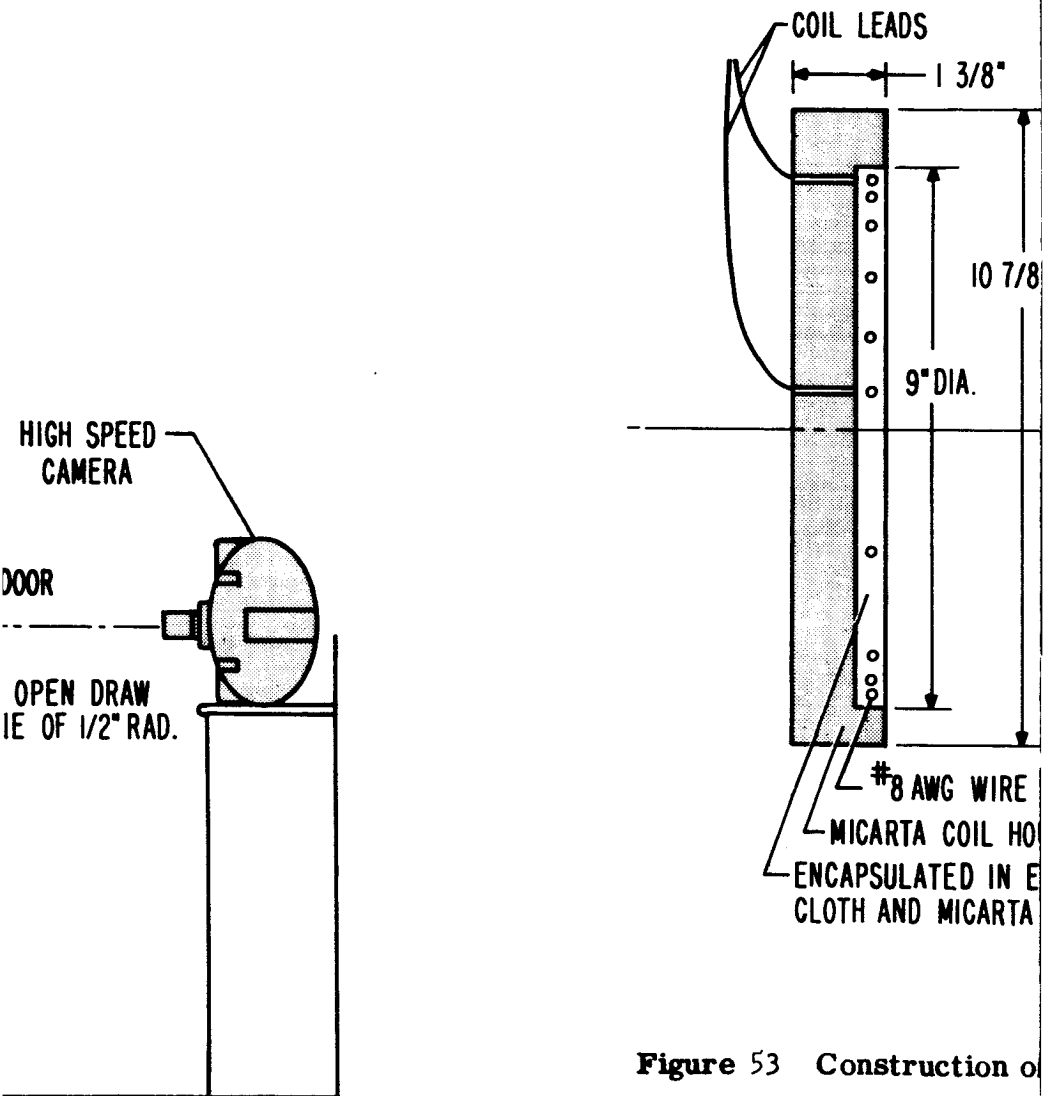


Figure 53 Construction of

MAGNETIC FREE FORM  
WITH A SIX TURN,  
AT VARYING ENERGY  
AND 2014-0 ALLOYS

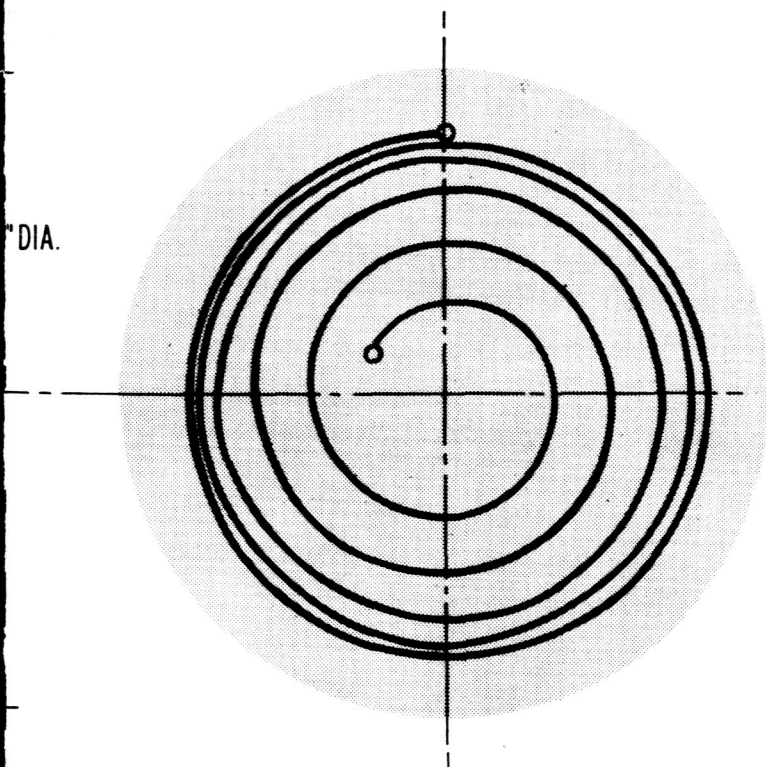
1 in Closed Tank for

*Handwritten mark resembling a stylized '2' or checkmark.*

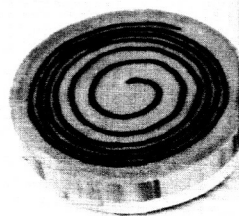
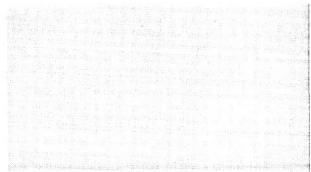
TAB

THICKNESS MEASUREMENTS (IN) (4)  
POSITION NUMBER

8	7	6	5	4	3	2	1	Center	1	2	3	4	5
.093	.093	.092	.085	.086	.083	.080	.055	.058	.069	.081	.085	.086	.081
.092	.092	.092	.085	.085	.083	.079	.056	.058	.064	.081	.084	.086	.081
.092	.092	.092	.090	.090	.089	.088	.086	.082	.088	.089	.090	.090	.091
.091	.091	.090	.082	.083	.080	.076	.057	.057	.068	.080	.083	.084	.081
.091	.090	.090	.083	.083	.082	.073	.063	.058	.064	.079	.082	.084	.081
.090	.090	.090	.087	.087	.086	.085	.081	.075	.034	.086	.087	.088	.081



USING  
EPOXY BETWEEN PLEXIGLASS  
BACKING



Six Turn Spirally Wound Coil of 139 Microhenries

MEASURING DOME DATA OBTAINED  
FROM SPIRALLY WOUND FLAT COIL  
AT SEVERAL LEVELS FOR .092", 2219-0

SIX TURN FLAT  
FREE FORM DOME  
OF DOME CENTER

FIG

LE 10

2

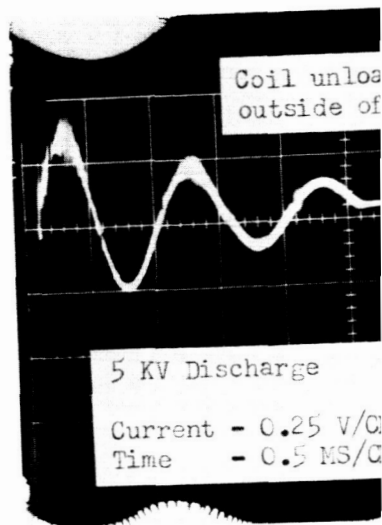


TESTING PERFORMED

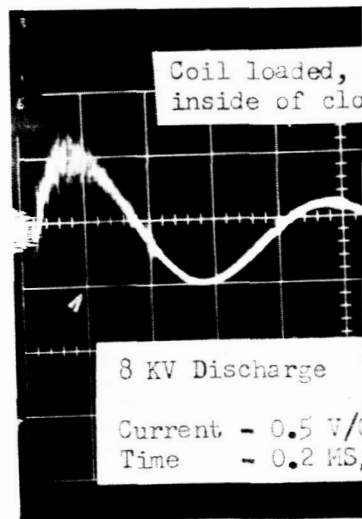
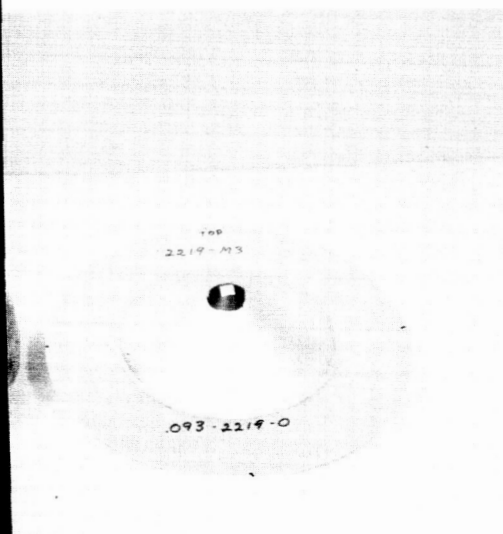
	6	7	8	
7	.092	.092	.092	Mechanical Properties (6)
8	.092	.092	.092	Mechanical Properties (6)
1	.092	.092	.092	Mechanical Properties (6)
5	.090	.091	.091	Mechanical Properties (6)
5	.090	.090	.090	Mechanical Properties (6)
9	.090	.090	.090	Mechanical Properties (6)

NOTES

- (1) For the size, source, and location tensile specimen, see Figure 23
- (2) High speed motion pictures taken of metal strain.
- (3) Approximate range of strain rate based on experimental data obtained - not actually measured.
- (4) See Figure 21 for plot of thickness change vs. dome position no.
- (5) Original thickness values have measured .090" to .094".
- (6) For test results, see Table 5



1/4 cycle frequency

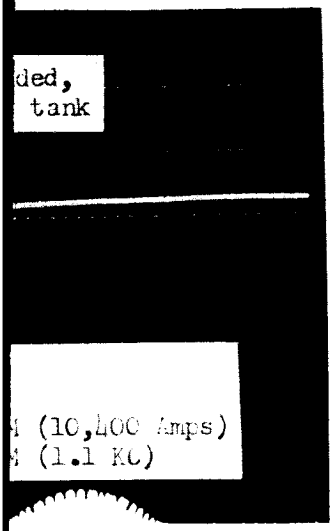


1/4 cycle frequency

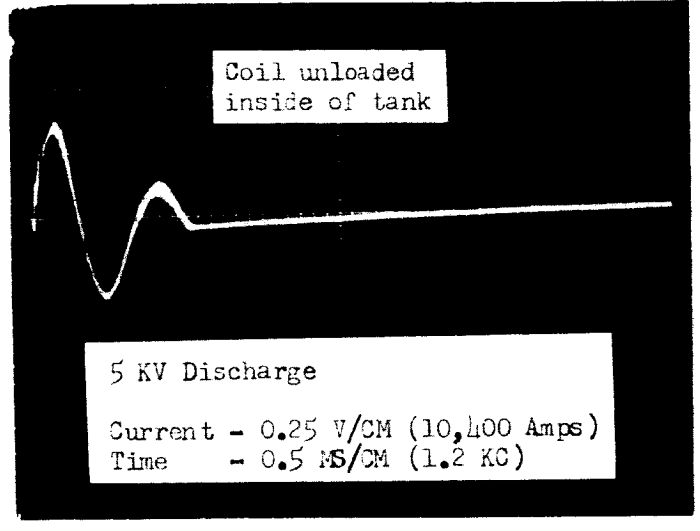
OIL USED TO MAGNETICALLY FOR STRAIN RATE MEASUREMENTS SQUARE.

URE 55

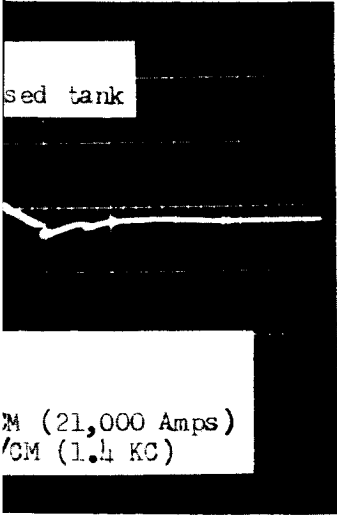
4



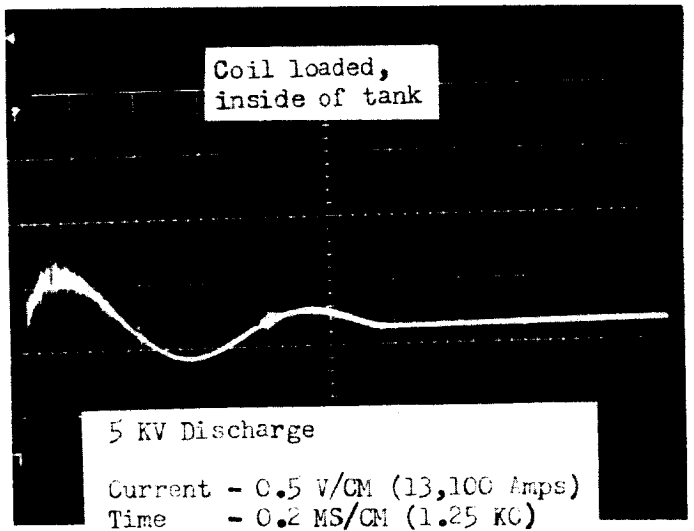
q. - 4 kc



1/4 cycle freq. - 5 kc



. - 10 kc



1/4 cycle freq. - 10 kc

5

FORMING PRESSURE (PSI)	VOLUME (CC)	SPECIMEN NUMBER	ALLOY	DOME DEPTH (IN.)	THINOUT AT DOME CENTER (%)	THICKNESS (%)						
						8	7	6	5	4	3	2
1,100	2,140	HS 3	2219-0	3.22 <sup>(2)</sup>	44.6	.092	.091	.091	.089	.080	.071	.062
1,050	2,150	HS 4	↑	3.13 <sup>(2)</sup>	45.6	.092	.092	.091	.086	.083	.074	.065
1,100	2,080	HS 5	↓	2.84	37.0	.093	.093	.092	.090	.085	.078	.070
1,000	1,800	HS 2	↓	2.52	29.38	.092	.092	.092	.090	.084	.078	.071
850	1,330	HS 1	2219-0	1.76	10.88	.092	.091	.091	.090	.088	.085	.083
1,100	2,460	HS 3	2014-0	3.40 <sup>(2)</sup>	45.0	.091	.091	.090	.087	.077	.070	.062
850	2,500	HS 4	↑	3.32	41.75	.091	.090	.090	.082	.078	.070	.062
700	1,900	HS 2	↓	2.53	23.1	.091	.091	.090	.088	.081	.078	.074
600	1,300	HS 1	2014-0	1.78	7.69	.091	.091	.090	.090	.088	.086	.085
3,400	3,920	HS 4	321 Ann.St.St.	4.75	42.4	.096	.095	.092	.080	.065	.059	.054
3,200	3,920	HS 8	↑	4.70	43.5	.092	.091	.090	.075	.060	.052	.048
3,200	3,840	HS 7	↓	4.60	41.5	.095	.094	.092	.079	.064	.057	.053
3,000	3,040	HS 3	↓	3.71	28.3	.096	.095	.093	.085	.076	.072	.069
2,150	2,140	HS 6	↓	2.77	18.10	.092	.092	.091	.089	.083	.080	.078
2,150	2,120	HS 5	↓	2.71	19.15	.091	.091	.090	.088	.082	.079	.077
2,000	1,940	HS 2	↓	2.53	14.90	.095	.095	.094	.090	.086	.084	.082
1,100	1,180	HS 1	321 Ann.St.St.	1.60	7.45	.094	.094	.093	.092	.091	.089	.088

Common Forming Conditions

.092" Thick flat blank of 17 $\frac{1}{2}$ " diameter

10" Dia. Open Draw Ring Die of  $\frac{1}{2}$ " draw radius

HYDROSTATIC FREE FORMING DOME  
OBTAINED AT VARYING PRESSURE  
.092" 2219-0, 2014-0 AND 321 STAIN

TABLE IIA

FORMING PRESSURE (PSI)	SPECIMEN NUMBER	ALLOY	ORIGINAL THICKNESS	DOME DEPTH (IN.)	THINOUT AT DOME CENTER (%)	THICKNESS (%)						
						8	7	6	5	4	3	2
2,300	HF 1	6061-0	.063	3.99	12.7	.066	.065	.064	.061	.061	.059	.055
7,400	HF 1	304-L	.040	3.98	10.0	.043	.043	.042	.037	.039	.039	.036
7,400	HF 2	304L	.040	3.98	10.0	.043	.043	.042	.037	.039	.039	.036

Common Forming Conditions

16.4" Dia. blank

10" Dia. Open Draw Ring Die of  $\frac{1}{2}$ " draw radius

9  $\frac{3}{4}$ " Dia. full hemispherical die punch.

NOTES

- (1.) For the size, source, and location of all test specimens obtained, see Figure 23 for the indicated tests. Stress corrosion tests performed only on the 321 stainless domes.
- (2.) Depth estimated, dome ruptured.
- (3.) Entire dome tested as - "As formed".
- (4.) Entire dome tested as - "Stress relieved".
- (5.) See Figure 21 for plots of thickness change versus dome position number.
- (6.) Original thickness values have measured .090" to .094".

HYDROFORM DOME DATA OBTAINED AT VARYING PRESSURES FOR .063" 6061-0 AND .040" 304L STAIN

TABLE IIB

Frame Number (1)	Film Image Dimensions (inches)			Apparent Area Inc. (%) (5)	Corrected Area Inc. (%) (6)
	Horiz. (2)	Vert. (3)	Area (4)		
1	.0240	.0233	.000559	0.0	0.0
2	.0239	.0237	.000567	1.4	0.8
3	.0261	.0253	.000662	18.2	10.8
4	.0261	.0262	.000685	22.6	13.4
5	.0270	.0267	.000720	29.0	17.3
6	.0265	.0272	.000720	29.0	17.3
7	.0268	.0270	.000723	29.6	17.6
8	.0276	.0284	.000784	40.4	25.1
9	.0275	.0278	.000765	36.8	21.9
10	.0279	.0278	.000776	39.0	23.2

Measured dimensions of square before forming - Horiz., .495 in.

Measured dimensions of square after forming - Horiz., 550 in.,

Final depth of formed dome - 3.03 in.

Distance from camera to subject - 48 in.

Film speed at time of event - 6,960 frames per sec.

Estimated Dome Depth (inches) (7)	Correction Factor (8)	Actual Square Dimensions (inches)		
		Horiz. (9)	Vert. (10)	Area (11)
0.0	1.00	.507	.482	.245
.25	.994	.505	.500	.252
1.80	.959	.532	.517	.274
2.30	.947	.533	.536	.285
2.60	.941	.548	.542	.296
2.60	.941	.538	.552	.297
2.65	.940	.544	.548	.298
3.10	.929	.542	.576	.311
2.92	.933	.542	.547	.296
3.03	.931	.550	.548	.301

, Vert., .495 in.

Vert., .550 in.

TYPE

2

Total Dimensional Increase (inches)			Dimensional Increase by frames (inches)		Strain Rate (in/in/sec.)	
Horiz. (12)	Vert. (13)	Area (14)	Horiz. (15)	Vert. (16)	Horiz. (17)	Vert. (18)
.000	.000	.000	.000	.000	0.0	0.0
-.002	.018	.007	-.002	.018	- 27.5	260.0
.025	.035	.029	.027	.017	372.2	237.0
.026	.054	.040	.001	.019	11.6	255.5
.041	.060	.051	.015	.006	221.0	77.8
.031	.070	.052	-.010	.010	- 12.7	111.7
.037	.068	.053	.006	-.002	87.7	- 28.6
.035	.094	.066	-.002	.026	- 25.6	313.0
.035	.065	.051	.000	-.029	0.0	- 350.0
.043	.066	.056	.008	.001	91.2	12.7

3

ICAL VALUES OBTAINED AND USED IN THE CALCULATION  
OF STRAIN RATE FOR SPECIMEN NO. 2219-EH16

TABLE 12

SPECIMEN NUMBER	ALLOY	FORMING PROCESS	FORMING CONDITIONS	SPECIMEN THICKNESS (IN)	SUM OF PRINCIPAL STRESSES (PSI)
EH 20	2219-0	Electrohydraulic	Free formed (5)	.072	$\left[ \begin{array}{l} -21,900 \\ -7,300 \\ -10,000 \\ -16,900 \\ -14,600 \end{array} \right]$ average
EHCD 21	2219-0	↖	Die impacted (4)	.061	
EHCD 22	2219-0		Die impacted (3)	.065	
EH5	2014-0		Die impacted (5)	.071	
EHCD 10	2014-0		Die impacted (4)	.049	
EHCD 12	2014-0		Die impacted (3)	.057	
EH 9	321 Ann.St.	↖	Free formed (5)	.074	$\left[ \begin{array}{l} -17,900 \\ -9,800 \\ -8,700 \\ -2,300 \\ -6,500 \end{array} \right]$ average
EHCD 14	321 Ann.St.		Die impacted (4)	.061	
EHCD 16	321 Ann.St.	Electrohydraulic	Die impacted (3)	.064	
EX 4	2219-0	Explosive	Free formed (5)	.064	$\left[ \begin{array}{l} -16,200 \\ -15,300 \\ -11,500 \end{array} \right]$ average
EX 6	2219-0	↖	Free formed (3)	.071	
EXCD 2	2219-0		Die impacted (6)	.052	
EXCD 4	2219-0		Die impacted (4)	.053	
EX 4	2014-0		Free formed (5)	.057	
EX 7	2014-0		Free formed (6)	.054	
EXCD 2	2014-0		Die impacted (3)	.060	
EXCD 5	2014-0		Die impacted (4)	.072	
EX 7	321 Ann.St.		Free formed (5)	.078	
EX 8	321 Ann.St.		Free formed (6)	.064	
EXCD 2	321 Ann.St.	↖	Free formed (4)	.064	
EXCD 3	321 Ann.St.	Explosive	Die impacted (3)	.065	
HS 5	2219-0	Hydrostatic	Free formed (5)	.058	$\left[ \begin{array}{l} -18,900 \\ -15,300 \\ -11,500 \end{array} \right]$ average
HS 4 (2)	2014-0	↖	Free formed (3)	.053	
HS 1 (2)	321 Ann.St.		Free formed (4)	.088	
HS 3 (2)	321 Ann.St.		Free formed (5)	.068	
HS 4	321 Ann.St.	↖	Free formed (4)	.053	
HS 6	321 Ann.St.	Hydrostatic	Free formed (3)	.077	

NOTES:

- (1) X-ray pattern could not be measured.
- (2) 1" x 1" test specimens used. All other test specimens measure 6" in diameter and were also obtained from dome apex. (See Figure 23)
- (3) Highly impacted against die surface.
- (4) Lightly impacted against die surface.
- (5) Formed in one shot for a maximum rate of strain.
- (6) Formed in multiple shots for a minimum rate of strain.
- (7) Original thickness values measured .090" to .094".
- (8) All measurements on outside dome surface.

RESULTS OF X-RAY DIFFRACTION ANALYSIS OF SPECIMENS TAKEN FROM DOMES FORMED UNDER VARIOUS CONDITIONS

TABLE 13

SPECIMEN NO.	FORMING PROCESS	FORMING CONDITIONS	DOME DEPTH (IN.)	IMMERSION (HOURS)	DOME CONDITION
EH-6	Electrohydraulic ↕	Free Formed	3.54	216	Some Pitting
EH-5		Free Formed	4.05	288	No Defects
EH-7		Free Formed	3.42	288	No Defects
EH-8		Free Formed	4.08	288	No Defects
EHCD-13		Die Impacted	4.05	216	Some Pitting
EHCD-10		Die Impacted	4.03	288	No Defects
EHCD-12		Die Impacted	4.04	216	No Defects
EHCD-11		Die Impacted	4.03	216	No Defects
EX-9	Explosive ↕	Free Formed	4.68	288	No Defects
EX-11		Free Formed	4.49	216	Some Pitting
EX-10		Free Formed	4.44	288	Some Pitting
EX-12		Free Formed	4.78	288	General Surface Attack
EXCD-8		Die Impacted	4.05	216	Some Pitting
EXCD-7		Die Impacted	4.05	288	No Defects
EXCD-6		Die Impacted	4.05	216	Some Pitting
EXCD-5		Die Impacted	4.05	216	No Defects
HS-7	Hydrostatic	Free Formed	4.60	192	Some Pitting
HS-8		Free Formed	4.70	192	Some Pitting

RESULTS OF STRESS CORROSION TESTS PERFORMED  
FOR .092" - 321 STAINLESS STEEL DOMES IN A  
BOILING 25% AQUEOUS MAGNESIUM CHLORIDE SOLUTION

TABLE 14



Pressure (3) (psi)				Input Energy		Gage Distance (In.)	Remarks
1st Pulse	2nd Pulse	3rd Pulse	4th Pulse	KV	Joules		
4,480	11,650	13,500 <sup>(1)</sup>	11,650	5	12,000	11	Hemispherical surface (preformed dome of 1/4" depth) used to focus pressure wave energy.
5,470	8,960	11,700 <sup>(1)</sup>	11,600	↑	↑	8	
5,740	8,700 <sup>(1)</sup>	5,740	900			6	
5,740 <sup>(1)</sup>	9,000 <sup>(1)</sup>	2,690	4,480			4	
9,900	8,070	3,940	3,140			2	
7,170 <sup>(1)</sup>	5,740	8,950 <sup>(1)</sup>	5,400	↓	↓	11	Flat surface used to reflect pressure wave energy.
8,600 <sup>(1)</sup>	6,250	7,350	3,750			8	
5,360 <sup>(1)</sup>	5,360	5,360	5,360			6	
6,280 <sup>(1)</sup>	4,500	4,300	2,700			4	
7,170 <sup>(1)</sup>	2,300	2,300	2,300			2	
8,060	20,600	21,500 <sup>(1)</sup>	12,200	6	17,280	11	Flat surface used to reflect pressure wave energy.
11,600	21,200 <sup>(1)</sup>	10,700	6,300	↑	↑	8	
17,000 <sup>(1)</sup>	18,850 <sup>(1)</sup>	5,400	5,200	↓	↓	5.5	
34,000 <sup>(1)</sup>	18,000	9,000	7,200	6	17,280	2	
9,860	27,800	29,600 <sup>(1)</sup>	15,200	7	23,520	11	Flat surface used to reflect pressure wave energy.
19,300 <sup>(1)</sup>	32,300 <sup>(1)</sup>	12,500	6,300	7	23,520	5.5	
37,600 <sup>(1)</sup>	1,600	-	-	7	23,520	2	

Peak Pressure (3) (psi)	Input Energy		Wire Dia. & Material	Blank Dia. & Material	Gage Distance (In.)	Dome Depth (In.)	Remarks
	KV	Joules					
34,000	6	17,280	.063" Mg.	17 1/2" 2014-T6	2	2.50 <sup>(2)</sup>	Blanks free formed into dome in one shot.
28,600	6	17,280	.092" Mg.	17 1/2" 2014-0	2	2.80	
19,700	5	12,000	.096" Mg.	17 1/2" 2219-0	2	2.03	
37,600	7	23,520	.092" Mg.	20 1/2" 321 St. St.	2	1.76	
7,170	5	12,000	.096" Mg.	-	11	-	Flat surface used to reflect pressure wave energy.
21,500	5	12,000	.062" Mg.	-	11	-	
19,700	5	12,000	.032" Mg.	-	11	-	

#### Common Conditions

960 ufd Capacitor Bank  
 Closed tank containing axial inline electrodes of 1/4" gap  
 .096" dia. magnesium initiating wire except where indicated otherwise  
 1 1/4" workpiece standoff distance  
 Kistler 617 gage with sensitivity of 0.0557 V/1000 psi  
 Kistler amplifier - calibrator, Model 655  
 Type 555 Tektronix oscilloscope with type K preamp plug-in  
 Rogowski pickup coil used to provide sweep trigger signal for pressure measurements.

#### NOTES:

- (1) Peak pressure at the indicated gage distance
- (2) Part ruptured into 4 pcs., depth estimated.
- (3) See Figures 31 and 32 for pressure pulse traces and graphs respectively.

ELECTROHYDRAULIC PRESSURE PULSE  
 DATA OBTAINED WITH THE KISTLER 617 TRANSDUCER  
 IN THE CLOSED TANK

TABLE 15

Volume, cc	2014			2219			321		
	<u>Squares</u> △	Total	Total Joules	<u>Squares</u> △	Total	Total Joules	<u>Squares</u> △	Total	Total Joules
500	15	15	516	19	19	654	25	25	860
1000	42.5	57.5	1461	56	75	2580	75	100	3440
1500	58.5	116	3990	81	156	5330	125	225	7745
2000	68.0	184	6330	99	255	8760	150	375	12,900
2500	79	263	9050	115	370	12,740	225	600	20,640
3000							274	874	30,400
3500							318	1192	41,000
4000							335	1527	52,500

Work in joules obtained graphically from figure 62

1 square = 50,000 lb. inch<sup>-2</sup> cm<sup>3</sup> = 305 inch lbs. = 34.4 joules

TABLE OF DEFORMATION WORK PER DOME VOLUME  
IN HYDROSTATIC FORMING

TABLE 16

SPECIMEN 2219-0 EH 1

TOTAL ENERGY, JOULES	DOME DEPTH, INCHES
4,320	.66
16,320	1.79
28,320	2.45
45,600	3.28
67,880	3.84
91,300	4.50

% CENTER THINOUT	WORK, JOULES	% EFFICIENCY
1.9	400	9.25
7.6	2,600	15.9
15.2	5,850	20.6
31.5	9,200	20.8
46.7	11,950	17.6
55.3	13,500	14.8

DOME VOLUME CC	WORK, JOULES	% EFFICIENCY
600	900	20.8
1,360	4,500	27.6
1,920	8,200	29.0
2,370	11,700	25.6
2,870	16,200	23.9



SPECIMEN 321 STAINLESS EH 2

TOTAL ENERGY, JOULES	DOME DEPTH, INCHES
48,000	2.13
133,000	3.16
204,200	3.45
295,700	3.88
389,780	4.27
483,860	4.59
577,940	4.90
672,020	5.29

% CENTER THINOUT	WORK, JOULES	% EFFICIENCY
10.8	7,600	15.8
24.7	25,000	18.8
28.0	30,400	14.9
32.3	36,700	12.4
37.6	44,200	11.4
43.0	51,400	10.6
49.4	62,200	10.7
56.9	69,000	10.3

DOME VOLUME CC	WORK, JOULES	% EFFICIENCY
1,725	9,800	20.4
2,400	19,000	14.3
2,870	27,800	13.6
3,240	35,500	12.0
3,620	44,000	11.3
3,925	51,000	10.6
4,280	58,600	10.1
5,290	70,000	10.3



SPECIMEN 2014 0 EH 2

TOTAL ENERGY, JOULES	DOME DEPTH, INCHES
14,520	2.20
26,520	2.96

% CENTER THINOUT	WORK, JOULES	% EFFICIENCY
8.9	3,360	23.1
24.4	7,900	29.8

DOME VOLUME CC	WORK, JOULES	% EFFICIENCY
1,730	6,800	46.8
3,100	9,800	36.9



The above data gives deformation work and efficiency based on thinout or dome volume in comparison with the pressure volume work of hydrostatic forming. The data is valid only if thinout gradient of the electrohydraulic and hydrostatic specimens are similar. Based on the comparisons in Figure 61, the data marked by arrow is considered accurate within  $\pm 20\%$ . The data marked X is invalid due to poor thinout correlation in Figure 61

ELECTROHYDRAULIC DOME FORMING EFFICIENCY

## CONCLUSIONS

1. Neither high strain rates nor die impacting in electrohydraulic and explosive forming of 321 stainless steel domes produced susceptibility to stress corrosion cracking.

2. X-ray diffraction measurements of residual strain perpendicular to the surface of the dome center of 2219 and 2014 specimens indicate that combined surface stress is less than 20,000 psi for all dome depths and forming conditions. Difference in stress between individual domes were within the 10,000 psi range of experimental accuracy.

Residual stress measurements of stainless steel could not be validly made due to diffraction line broadening and background reflection caused by deformation.

3. Mechanical properties (ultimate, yield and elongation) responded similarly with strain for all strain rates and processes in dome forming of 2014-0 aluminum and 321 annealed stainless steel.

The ultimate and yield strengths of 2219 alloy for a given strain were considerably higher when formed hydrostatically (zero strain rate) than for most domes formed at high strain rate. However, electron transmission microscopy indicates that the strength difference may be attributable to Cu Al<sub>2</sub> precipitate size and distribution in the grain matrix of the blank material rather than due to the strain rate used in forming.

4. Direct photographic observation of the expanding workpiece surface during forming produces a more accurate record of changes in strain rate during the event than possible with indirect methods such as contact probes. Strain-time relationships obtained graphically for the three materials in three high strain processes show that complex fluctuations in strain rate occur during forming. Maximum strain rates as high as 877 in./in./sec. and as low as 130 in./in./sec. were employed.

The efficiency of conversion of stored capacitor energy to deformation work in electrohydraulic forming .093" x 10" diameter 321 annealed stainless steel and annealed aluminum alloy hemispheres was about 10% and 15%, respectively.

5. Insufficient data and experimental scatter do not permit exact expression of strain rate in terms of forming energy. However, the relationship appears linear. This result is reasonable since

neither the duration of the forming energy or forming time change markedly with the magnitude of forming energy. The strain rates of 2219-0 and 2014-0 aluminum alloys are similar for given energy. Curves presented for these materials show that at the dome center maximum strain rates are in the ratio 5.4 : 1.2 : 1 and average strain rates are in the ratio 4.5: 1: 1 for magnetic: electrohydraulic: explosive processes. Curves presented for 321 annealed stainless steel show the maximum strain rates to be 1.2: 1 and 1.5 :1 for electrohydraulic and explosive processes, respectively. In summary, the latter processes are quite similar in strain rate whereas magnetic forming is significantly faster.

Although the discharge current is lower and discharge time is longer in magnetic forming, higher strain rates are obtained since the magnetic force is directly upon the workpiece whereas the electrohydraulic impulse is transmitted through the water medium. The strain of the workpiece can be considered to result from workpiece kinetic energy which is produced by such force. Two considerations can account for the difference in strain rate. First, although the short (20 u second) duration of electrohydraulic pressures agrees with the effective time of electric discharge power and, therefore, indicates no time extension, the pressure decreases approximately inversely with distance traveled to the workpiece. Second, a portion of deformation work may be attributable to the kinetic energy of water moving toward the workpiece under the influence of "cylindrical bubble" expansion of the arc products. This kinetic energy is effective later and over considerably longer time than the pressure pulse, thereby implying a lower force of longer duration upon the workpiece and consequent lower strain rate.

6. At equal strain (as indicated by thinout at dome center), lubricated blanks produce deeper domes since draw-in of metal from the flange is increased. Consequently, lubrication reduces the strain rate since the dome shape is obtained with less stretch of the metal. Strain-time observations show that the erratic pulsating strain behavior of electrohydraulic forming was not ascribable to forming without lubrication.
7. Graphs of dome depth and corresponding discharge energy were obtained for 2219-0, 2014-0 aluminum, and 321 annealed stainless steel. Expectedly, for given energy the depth is less for higher yield strength material.
8. A procedure to determine efficiency of dome forming of various processes by calibration to the pressure work in hydrostatic

dome forming was developed. Accuracy is contingent on adjustment of flange clamping pressure during hydrostatic forming to produce thinout gradients similar to the process being evaluated.

9. Techniques for the preparation of specimens of about 2 millionths of an inch in thickness were successfully employed for electron transmission microscopy. Sufficient experimental effort could not be expended to obtain quantitative results, but unique differences in dislocation behavior between specimens was observed. The technique was specifically useful in pointing out that difference in precipitate size rather than strain rate may be responsible for differences in the mechanical strength of 2219 alloy aluminum domes.
10. Pressure time relationships were established during the first discharge in forming 2219-0 aluminum, 2014-0 aluminum and 321 annealed stainless steel at discharge energy levels of 5KV, 6KV and 7KV respectively. The pressure profiles were obtained with a Kistler 617 transducer.

Pulse pressures up to 37,600 psi were observed. This pressure was obtained with a 23,520 joule discharge at a distance of 2" from the transducer.

Peak pressure of the electrohydraulic pulse was found to increase directly with discharge energy. For a given energy level, an optimum wire diameter exists. This conclusion corroborates previous data obtained concerning initiating wire sizes.

11. In the electrohydraulic and explosive forming processes, the type of rupture and consequently the amount of thinout obtained at rupture are influenced by the size of the gas ball and proximity of the gas ball to the workpiece.

APPENDIX A

PRELIMINARY ELECTRON MICROSCOPIC  
STUDY OF METALS DEFORMED AT  
HIGH STRAIN RATES

## ABSTRACT

A preliminary transmission electron microscope study was made of the internal microstructure of aluminum alloys 2219, 2014 and stainless alloy 321 deformed at high strain rates. Comparisons have been made between alloys and between samples of each alloy hydrostatically, electrohydraulically and explosively formed, as well as the parent stock of each. The simple criteria for comparison were dislocation cell size, dislocation characteristics, dislocation-particle interactions and deformation modes. Dislocation dynamics are shown to differ according to the grossly different stacking fault energies of the aluminum alloys and the stainless sample. It is indicated that a satisfactory understanding of the effects of different strain rate processes on work hardening properties will require further studies of this type under more complete experimental control. High rate forming is shown to favor twinning as a deformation mode in the 321 alloy. Recommendations are presented for future studies of this type.



## INTRODUCTION

This report is of a preliminary nature. A thorough study would have been time consuming, requiring the implementation of a number of crystallographic analysis techniques and an analysis in depth of a large number of detailed observations.

The problem presented was to make a microstructural study of three alloys (2014 aluminum, 2219 aluminum, 321 stainless) deformed at high and low strain rates so as to characterize each and to develop, if possible, an explanation for the work hardening properties of each alloy under the different strain conditions.

The twelve samples received, which included pieces of parent stock, are listed in Tables I, II and III. The conditions of forming the specimens are included. They were selected so as to provide the optimum basis for comparison.

Electron microscopy is obviously the logical tool to use on this problem. Neither light microscopy nor x-ray diffraction have the sensitivity necessary to provide information at the subgrain level at which differences will be manifested. It is now well known that the plastic properties of metals must ultimately be based upon dislocations, how they operate in different crystals, how they interact with themselves, and how they interact with foreign structures. In recent years there has been a shift from the study of these crystal defects at the surface of metals by replica techniques to the direct study of them by transmission directly through thin foils. This trend has resulted in enormous advances in understanding of microstructures and the micromechanics of deformation processes (1). In working with thin foils and dislocations, there are three important considerations which must be dealt with.

(1) The preparation of samples is an extremely delicate matter since fairly large areas with thicknesses of the order of  $500\text{\AA}$  must be produced. The preparation process must be clean and introduce no new artifacts into the internal features.

(2) Thinning bulk materials to this level inevitably introduces certain changes in the dislocations and their arrangements in the bulk material through the relief of local microstresses. These changes have not been found to be serious by other workers but they must be considered.

(3) Dislocations are in effect the "trees" in the "forest" that is the bulk material. Inferences about bulk properties based upon the observed character of some dislocations and some dislocation tangles must necessarily remain inferences until supported by a broad body of evidence. Details of dislocation micromechanics must also, logically, have a quantitative relationship with bulk properties. This represents a considerable difficulty because of the great variety of dislocation mechanics that must first be described at least qualitatively.

Insofar as the literature has been surveyed, there does not appear to have been much work done on the analysis of metals deformed at high strain rates. Some meaningful single crystal studies are noted but practically no data is available on the behavior of individual dislocations or their interactions (2).

## METHODS

### A. Preparation of Thin Foils of Aluminum Alloys

The technique described below follows in part that described by Nicholson, Thomas and Nutting (3). Advantage was taken of the natural curvature of most of the specimens which were one-inch squares cut from hemispherical domes. Both the 2219 and the 2014 alloys were thinned in the described manner. The 2014 alloy in general produced less satisfactory foil specimens. This could be attributed mainly to the fact that this is a "dirtier" alloy containing many gross inclusions. The following are a list of the preparative steps found necessary to obtain suitable foils:

1. The convex side of the specimens, which were about .075" thick, were ground flat in flowing water conditions until a center thickness of .025" was obtained. This established an initial taper of less than arctan 3/100 from the center outwards. No further grinding was permissible since it could disturb the internal structure that was to be examined.

2. Chemical thinning was performed to reduce sample thickness to .010". Reference (4) recommends electro-machining in nitric acid electrolyte down to .002" thickness, but it was found that ordinary immersion in a strong solution of NaOH was simpler and less time consuming since a quantity of samples could be treated simultaneously. It was necessary to hold this operation at .010" to avoid having an etch roughness of such dimension that subsequent electropolishing could not remove it. The black surface smudge could be removed by a short immersion in concentrated nitric acid.

3. A rapid electropolishing step was then employed to reduce thickness to .001". Lenoirs Solution (92 cc ortho phosphoric acid 85%, 13cc conc.  $H_2SO_4$ , 16 gms,  $CrO_3$  and 14 cc  $H_2O$ ) was employed in the temperature range 50-90°C at 10-20 volts and approximately 4 amps/sq. in. current density. In general, old and nearly exhausted solutions could be used at this step. The cathode was a simple sheet of aluminum and no stirring of the electrolyte was necessary.

4. Final electropolishing was always carried out in fresh electrolyte in the temperature range 65°-80°C at 10-14 volts potential. The sample was handheld with tweezers and inspected every 10 seconds until a breakthrough or hole developed in the center of the sample.

5. The sample was then washed in water, given a short immersion in a cold solution of phosphoric and chromic acids (70 ml 85% orthophosphoric acid, 32 g chromic acid, 130 ml water) to remove residual surface oxides,

and further washed in distilled water and alcohol. Samples were dried by pressing between lens tissue on a flat surface.

6. Suitable specimens of electron transparent metal could then usually be cut from the areas surrounding the center hole with a scalpel or scissors.

7. The thin foils were mounted for examination on 60 mesh nickel screens which had been lightly coated with a pressure sensitive adhesive material.

#### B Preparation of Thin Foils of Stainless Steel 321

These samples were also obtained as 1" squares. When these were flat or of small curvature, it was found advantageous to cold grind a concavity on one side to insure that the thinnest section was in the center of the piece. Preferential electropolishing at the edges of the samples was so pronounced that production of suitable foils would otherwise be much more difficult. The preparative steps are as follows:

1. The specimens were wet ground on the convex or flat side to a center thickness of .018". This additional thinning at this stage was acceptable because of the much greater strength of this metal compared to aluminum. Strains from surface deformation are not likely to penetrate .009" into the central area.

2. No attempts were made to use a chemical or electromachining step since the limited number of samples did not justify the effort. Rather a rapid electropolishing step was used to thin to .001" center thickness. A solution of 60% orthophosphoric acid (85%) and 40% concentrated sulfuric at 50-80°C was employed for electropolishing at 10-20 volts and approximately 4 amps/sq. in. (4). Cathode material was also stainless steel and no stirring was required.

3. Fresh electrolyte was used during the final polishing step at a temperature of 55-70°C and 10-12 volts potential. Samples were again hand-held in unstirred solution and periodically inspected until breakthrough occurred at the center of the specimen.

4. Thorough rinsing was carried out in running water and alcohol before drying against lens tissue.

5. As with the aluminum alloys, the thin areas suitable for electron transmission were cut free with scalpels and mounted with adhesive to 60 mesh nickel screens.

#### C. Electron Microscopy

The various techniques and methods of study with the electron microscope on thin foils are well developed (1) and there is no need to

discuss them at length. However, since this is a preliminary study and to some extent a survey of twelve specimens, definite approaches had to be established for the examination so that comparable data would result. The limited time did not permit complete freedom of approach for each sample.

In general, intermediate magnifications were employed (1,000 - 10,000 X on the film) to obtain reasonable fields of view. No efforts were made to operate under high resolution conditions. Stereo-micrographs were made whenever possible and selected area electron diffraction patterns were obtained of many of the regions shot in stereo. These SAD patterns provide Laue type diffraction data on small local areas of interest in the micrographs.

Very little "in microscope" examination or analysis could be made. It was necessary to make micrographs of reasonably interesting areas and to leave analysis and interpretation to the examination of the micrographs. As a consequence, well designed tilt and darkfield experiments could not be conducted at this time.

## OBSERVATIONS AND RESULTS

An attempt has been made to summarize some descriptive parameters for each examined specimen of each of the three alloys in Tables I, II, and III. In addition, an average of two representative micrographs are attached of each specimen for illustration of some of the factors to be discussed. All the effects described may not be illustrated or convincingly established with these 24 micrographs. However, they are the summarized result of examining the 300 odd micrographs that were taken. Print quality is not high since careful development with dodging was not possible in the scheduled time. Except for special cases, it has been necessary to neglect electron diffraction data. For the most part, one superficially observes only a minor arcing of the single crystal spots as a result of all deformations. Twin patterns of the 321 alloy are exceptions to this observation.

For the sake of ready comparison by the reader, the % thin out, yield strength and principal residual stresses as determined by X-ray diffraction have been added to the tables.

### Alloy 2219

#### A. Parent Stock (2219)

This sample was examined as a reference for the strained samples. Table I and Figure 1 reveal that it is a 2 phase structure consisting of  $\Theta$  ( $\text{CuAl}_2$ ) plates having a Widmanstaetten orientation in the matrix. It has not been determined whether these are  $\Theta$  or  $\Theta'$  plates since the phase structure

is not known and electron diffraction analysis is incomplete. Few dislocations and no dislocation loops are seen in this material. The micrograph was taken in an area with a strong Bragg reflection operating. The particles are apparently completely coherent with the matrix; i. e. there is at the interface, a complete matching of the lattices. Since these lattices do not normally match, a significant strain develops in both near the interface and the strain field cloud can be visualized around some properly oriented particles. In other orientations, a stacking fault type of interference fringe, which also is characteristic of coherent particles, is vividly seen.

#### Hydrostatically Formed at Low Strain Rate (2219)

Reference to Table I and Figs. 2 & 3 will provide a general description of this alloy deformed at low strain rates. This sample was undoubtedly formed from the parent stock since the precipitate size is consistent. There are enormous numbers of dislocations present and their abundance can only be appreciated by tilting a particular area of a sample so that many of the otherwise invisible dislocations are revealed. It would seem in this sample that the inter particle spacings defined the size of the subgrain structure. Because each particle has dislocations contacting it, it was not possible to see well defined subgrain boundaries or dislocation free areas between boundaries. At the interface of a great many plates, it is possible to discern what are apparently Moire patterns; i. e. lines defining the periodic coincidence of rows of atoms of the matrix and precipitate lattices in the direction of viewing. This effect necessarily reflects a loss of the complete lattice coherency that was seen in the parent stock. It would appear that this loss of coherency of the particles is general, but that is not yet completely established. Loss of coherency is associated with the formation of dislocation networks at the matrix-particle interfaces to various degrees. Particles viewed edge-on frequently appear fuzzy due to the many dislocations surrounding them. Those dislocations that extend for any length in the matrix are reasonably clear of kinking and no free dislocation loops are seen there.

#### Electrohydraulically Formed at High Strain Rates (2219)

Again Table I with Figures 4, 5 and 6 will provide a general description of the internal structure of this sample. A most significant feature of this description is the size of the particles compared to those in the parent stock and the hydrostatically formed sample. Volume-wise they are about 30 times as large and, obviously, there is a much greater separation of these particles in the matrix. In the interparticle spaces, it is possible to see many well-defined subgrain boundaries of both tilt and twist types. More complex types of apparent subboundaries or line regions of accumulated damage are also plentifully apparent. Dislocation loops are occasionally seen in the matrix and long dislocations are frequently jogged or stepped in character. There is a tendency for dislocation clouds to appear at particular parts of the particle-matrix interface as can be seen in the micrographs. In addition, there is a common tendency for broad diffuse Bragg reflection bands to appear in the  $\Theta$

plates indicating that they are bent. Both of these effects may arise because of the large blocking factor of the particles to the movement of dislocations and the distortion of the metal. It is not clear whether the  $\Theta$  plates are coherent, partially coherent or incoherent since it has not been possible to discern Moire patterns, interference bands or strain fields. Special note should be taken of the stereo pair of micrographs Figures 4 and 5 which were taken with the specimen at two angles to the beam. They illustrate the manner in which the appearance of microstructural effects are sensitive to tilt and thereby to the delicate interaction of the electron beam with the crystal lattice. These photos can be arranged for stereo viewing in a suitable stereo print-viewer. The three dimensional viewpoint and the general overlap of structures, visible on one and invisible in the other, provide significant improvements in the perspectives that can be gained of the internal structure.

#### Explosively Formed at High Strain Rates (2219)

Figures 7 and 8, as well as Table I, should be referred to for evaluating this sample. The data obtained indicate that it is in most essential features similar to the sample formed electrohydraulically. The parent metal stock that was deformed is undoubtedly of the same origin as the electrohydraulic sample. The subgrain size appears to be incrementally larger and the subgrains seem to have less internal damage; i. e. the dislocations are more clearly accumulated into subgrain boundaries.

#### B. Alloy 2014

##### Parent Stock (2014)

This alloy is somewhat more complex in its phase structure than alloy 2219. It contains considerable amounts of silicon, magnesium and manganese and is found to be quite a "dirty" material in that many large particles and inclusions were encountered. This "dirtyness" made it difficult to obtain satisfactory thin foils, of reasonable area, since the inclusions tended to produce large holes and pits during electropolishing. Although a wide variety of particle sizes appeared, the principle phase present was a type of pseudo-cubic particle with an edge dimension of about  $1000\text{\AA}$ . No attempt was made to identify this phase. No evidence could be found that it was coherent with the matrix. It is assumed that during growth there may have been a coherent stage during which the cubic character developed, but that, on later growth, coherency was broken and the rounding of the particle edges began. No strain fields could be seen about the particles and there was no consistent evidence that a Widmanstaetten orientation existed within the matrix. The precipitate particle size was consistent through all these samples and it is therefore probable that a common source of the alloy stock was used throughout. Figure 9 is a micrograph of the internal structure.

### Hydrostatically Formed at Low Strain Rate (2014)

Reference to Table II and Figures 10 and 11 will provide a description of this sample. A great number of dislocations are present, interacting with the precipitate particles and each other. The dislocation density is by quick estimation in excess of  $7 \times 10^{10}/\text{cm}^3$ . The dislocation tangles around the particles are so dense that it is the infrequent case where one can see singular interactions as in Figure 11. Tilt and twist boundaries are seen periodically but they are short, and poorly defined for the most part. Estimation of subgrain size is therefore subject to a large error.

### Electrohydraulically Formed at High Strain Rate (2014)

Refer to Table II and Figures 12, 13 for a summary description. This sample has rather well defined subgrains which are almost all formed by the generation of tilt boundaries (i. e. boundaries containing parallel edge dislocations). Dislocations, as usual, are interacting with precipitate particles, but a tendency is also noted for groups of dislocations to line up in a narrow band connecting two particles. This effect is not clearly developed in the other samples of this alloy that were evaluated. It may be that this indicates that the directions of shear strain are more directly resolved than in the other samples. A few dislocation loops as well as a number of jogs in ordinary dislocations were observed. The tilt boundaries usually are anchored at particles and it appears that they are generated as the metal shears past the particles.

### Explosively Formed at High Strain Rate (2014)

Refer to Table II and Figures 14, 15 for descriptive data. It will be noted this sample is largely similar to the electrohydraulic sample except that in general the features are less well defined. The subgrain size seems marginally larger but this is the only direct distinction. Dislocation densities qualitatively seem lower also. Dislocation jogging and loop formation are again only occasionally observed.

## C. Alloy 321

### Parent Stock (321)

This sample was examined as a reference for the strained samples. During the grinding stage of thinning, the thickness was inadvertently reduced to .005". As a result, the polishing step did not remove all damaged metal before breakthrough occurred. The display of dislocations seen as a result of this damage was, however, found to be advantageous. This alloy was found to be effectively a single phase material although some occasional spheroidized particles are seen. Dislocations tend to move along simple slip planes and occasionally they are found clustered about the spheroidal particles. Dislocation loops apparently form readily since even at these small strains they were fairly common. No clear evidence of dislocation dissociation into

into partials with a separating stacking fault could be found. At best, one could see only stacking fault type fringes modulating the density of the dislocations. No nodes with stacking fault fringes could be seen either. The absence of clear cut stacking fault effects establishes that the stacking fault energy is not extremely low. The only twins observed were obviously growth twins such as is seen in Figure 16. Figure 17 is an electron diffraction pattern of just such a twin showing the relationship between the matrix and twin spots. It can be shown by indexing that this pattern is due to the overlap of two spot displays each taken down a zone axis (110) and is characteristic of twinning on the (111) planes.

#### Hydrostatically Formed at Low Strain Rates (321)

Reference to Table III and Figures 18, 19, 20 will provide an abbreviated description of this sample. Transmission examination reveals that the sample has an enormous quantity of dislocations present - most of which are aggregated in complex tangles. In a few areas it was possible to observe a few dissociated dislocations as in Figure 18 with the characteristic stacking fault fringes apparent between them. Some small loops are scattered throughout but they are difficult to discern amidst the tangles. A good many fine and some large deformation twins are seen throughout. While they, in total, represent only a few percent of the deformed material, it is of considerable interest to note that this mode of deformation operates. The twins are produced by a dislocation mechanism and one can see as in Figure 19 the partial dislocations moving in the plane of the twin. The twins seemingly form by the coherent motion of parallel oriented dislocations. Figure 20 is an electron diffraction pattern of the area displayed in Figure 19. By comparison with Figure 17 it is obvious, without even indexing, that this array of spots reflects the presence of twins. The streaking of the twin spots in the pattern reflects the fact that the twins are extremely thin in the streaked directions. In other words, the thin dimension causes a relaxation of the Laue condition in that direction and a poor wave interference condition of the diffracted electrons in that direction.

#### Electrohydraulically Formed at High Strain Rates (321)

Reference to Table III and Figures 21 and 22 will provide a summary description of this sample. Except for a few considerations, the internal structure is basically similar to that of the hydrostatically formed sample. The degree of twinning is greatly increased and the formation of twins on different (111) planes does lead to twin intersections. The twins are generally of a large size with many dislocations present in them probably at the twin interfaces. No dissociated dislocations were seen but they occurred so infrequently in the other samples of this series that one cannot be sure they are not present in a similar degree. The dislocations are so uniformly distributed in the general matrix that it is difficult to assess the subgrain size. The impression is gathered that it is somewhat smaller than in the hydrostatic sample. Twins were again readily identified by electron diffraction



analysis. Loops are seen to be left in the matrix probably by the anchoring of dislocations at point defects, their distortion into dipoles and the subsequent release of the dislocation leaving a pinched off loop. Dipoles can be seen periodically.

#### Explosively Formed at High Strain Rate (321)

Reference to Table III and Figures 23, 24, will provide a summary description of this sample. The sample is in all features very similar to that produced by electrohydraulic forming. The only point of difference, which is probably of minor significance, is the observation in a number of twins of an interference and/or Moire effect not previously observed. In Figure 23 can be seen a number of twin ends which display patterns of alternating density variation in several directions. In these areas there are only limited numbers of associated dislocations which apparently permits the effect to be observed. Some of the interference effects (Fig. 24) are undoubtedly due to a stacking fault type fringe which depends upon the angle and the thickness of the twins. Moire effects are in some manner caused by the overlap of twins.

## DISCUSSION

### A. General

Smith<sup>19</sup> has proposed that the passage of a shock produces a compressive wave in metal which is bounded on the forward and trailing sides by a group of dislocations which accommodate the compressive strain. Theoretically after passage of the shock the dislocations of the forward edge should be annihilated by those of the trailing side. Hornbogen<sup>20</sup> suggests that dislocation loops which distort into pairs of screw dislocations would be formed and that these would only annihilate if they were of opposite sign and close together. In high rate forming operations, shocks are present but an analysis is necessary to determine how rapidly the shock is dampened by the physical system and how rapidly they are converted to mechanical motion. The passage of acoustic shocks during the early part of the forming operation may have significant effects on the later, massive deformation of the metal. Particular types and numbers of dislocation sources may appear, as a result of these initial shocks, and serve to establish the nature of the deformation process. A thorough understanding of the deformation process would have to include information on shocked but relatively undeformed metal.

In the type of study reported here, one is dealing with such complex dislocation phenomena that visualization of their 3-dimensional arrangements cannot adequately be inferred from 2-dimensional micrographs. Even ordinary stereo micrographs are limited since in most cases the separate micrographs sample different zones of the specimen and therefore different slip systems. Basinski's method<sup>21</sup> would be more helpful in this type of work since it is more carefully designed for 3-D evaluation. The value of good 3-D studies cannot be over-rated since dislocation phenomena are difficult to visualize even when their population is low.

An additional point must be made about visualizing the internal damage caused by the various strain methods. In all the present samples, the direction of view has been perpendicular to the plane of the sheet specimens and therefore perpendicular to the principle directions of straining. It is entirely possible that the damage displayed by viewing parallel to the plane of the sheet and parallel to the principle strain directions will be different in both qualitative and quantitative senses. Technical difficulties of obtaining thin foils of such cross sections are appreciable, but it is obvious that the effort should be made in future work in order to obtain the maximum of available information.

There were basic problems in these present experiments in attempting to correlate physical properties (i. e., yield strength) with the internal features of the metals (i. e., microstructural features) because one cannot readily assess what are the most significant features. Work hardening theories relating dislocation mechanics to yield strength are not yet adequate to serve as guides. Samples strained at different rates to the same percent thinout tended to have nearly common yield strengths. Yet it is expected from prior work that the samples deformed at slow rates

are closer to failure than those at high rates. There is a need to either characterize how close one is to failure or else to work with samples that are known to be failing. In this way the criteria for judging internal dislocation dynamics and their importance in contributing to failure could be better established.

## B. Aluminum Alloys Compared to Stainless

A special point must be made that the alloys studied in this investigation were all face-centered cubic crystals. This apparently unifying feature of the three alloys is, however, illusory. In recent years it has become abundantly clear that the deformation characteristics of fcc metals can be divided into three reasonably distinct groups based upon whether they have a high, intermediate or low stacking fault energy (SFE)<sup>1,5,6,7</sup>. In studies based on pure metals and low or moderate strain rates, it has been found that those having a high SFE deform with the aggregation of dislocations into well-ordered cell or subgrain boundaries. Tilt boundaries, which are parallel arrays of edge dislocations, and twist boundaries, which are the result of interacting groups of screw dislocations, are both very often formed. Between boundaries there are regions which are largely dislocation free. In metals of low SFE the tendency to form subgrains is minimal. Dislocations are nearly uniformly distributed but form some loose networks of undefined character. Because of the tendency of dislocations on the primary slip planes to break up into "ribbon" dislocations (i. e. two partial dislocations separated by a stacking fault), it is energetically difficult for them to cross slip around obstacles and they will tend to pile up. In some cases they form twins<sup>8,9</sup>. In metals of intermediate SFE there is as may be expected, a tendency for the dislocations to aggregate in a manner intermediate between the high and low SFE metals. Dislocation networks are somewhat better defined and twinning tends to occur more readily than the extension of stacking faults.

The foregoing discussion of literature data provides the basis for distinguishing between the behavior of the aluminum alloys and the stainless steel samples. All aluminum alloys are known to have high SFE's whereas stainless steels are usually of low or low-intermediate energies. Another distinction is that both of the aluminum alloys have precipitate phases present while the stainless sample is nearly particle-free.

It is to be expected therefore that the deformation and work hardening properties of the aluminum and stainless alloys will arise through basically different dislocation mechanisms whether at low or at high strain rates. The results have clearly confirmed this. Whereas subgrains or cells are often clearly defined in the aluminum alloys, there are only poorly defined complex dislocation networks in the low SFE stainless alloy. The aluminum alloys display significant interactions between dislocations and the precipitate particle phase, while the 321 alloy demonstrates the presence of significant numbers of twins in all strained samples. In work hardening, the loss of plasticity is associated with an increased difficulty of propagating dislocations through the grains of the sample. In the stainless alloy, the less flexible types of dislocations tend to pile up against each other and to establish low energy locks between themselves so that dislocation movements are made increasingly difficult. In the aluminum alloys, although the disloca-

tion interaction barriers are not so great, there is the additional presence of particle barriers to inhibit their movement.

It is of considerable interest that the importance of SFE which has only been established for ideal metal systems is also found to apply in these commercial alloys.

### C. Alloy 2219 Compared to Alloy 2014

Both of these materials contain a second, precipitate phase dispersed in the matrix. According to Thomas<sup>10</sup> the addition of alloying elements does not appreciably reduce the exceptionally high stacking fault energy of aluminum. It is, therefore, to be expected that no fundamental differences in simple dislocation mechanics will be seen in these two alloys. This expectation is readily confirmed by reference to the results. In both alloys reasonably well defined subgrains were formed by straining at high or low rates and no unanticipated types of dislocation-dislocation interactions were detected in either.

The differences that might develop will then more probably be based upon dislocation-particle or dislocation-point defect interactions. The latter interaction may be of significance since it is known that solute content and type will influence the characteristics of at least the vacancy type of point defect.<sup>1</sup> It is not possible, however, to expect that sub-structural differences based on the difference of solute content could be detected in the type of study conducted for this report.

A difference, based upon the interaction of dislocations with the pseudo-cubic particles of 2014 and the plate like  $\Theta$  particles of 2219, could perhaps be expected in the work hardening properties. The  $\Theta$  plates grow on (100) planes while slip occurs on (111) planes. The capacity of the plates to block dislocation movement should therefore be fairly good. The pseudo-cubic particles in the 2014 alloy should also be effective since they present nearly a common dimension in all directions. No attempts were made to count particles and compare overall blocking potential of the dispersions in these alloys.

A more fundamental difference in the particle dispersions of the two alloys is the fact that the  $\Theta$  plates are initially coherent with the matrix while the pseudo-cubic particles are not. It has already been established that dislocations can pass through coherent or semi-coherent particles, at least, in the narrow dimensions. Nutting<sup>11</sup> reported and illustrated the passage of dislocations through coherent  $\Theta$  plates in an Al-4% Cu alloy. The shear force associated with a dislocation in the matrix would be directly transmitted to matching atomic planes in the coherent plates. In non-coherent plates the shear forces are not so directly coupled to the possible slip planes of the particles and the dislocations will be held up until sufficient energy is developed to activate another mechanism for bypassing the particles. From the actual results obtained in this study, it is difficult to assess any correlation with the coherency factor for two reasons. The mechanical properties do not suggest any fundamental difference in the work hardening of the two alloys and in addition there were two different annealing treatments employed in the 2219 samples.

A further question arises when one considers how important the particle-matrix interfaces may be as sources of dislocations during deformation. Wilsdorf<sup>12</sup> has demonstrated that incoherent particles act as dislocation sources as well as grain boundaries, twin boundaries, polygonization walls and simple dislocation interactions (i. e. Frank-Read sources). Particles that remain coherent cannot nucleate dislocations but the situation on semicoherent particles is different. In a simple Al-4% Cu alloy Wilson<sup>13</sup> found that the  $\Theta$  plates generated dislocations while Bonar and Kelly<sup>14</sup> in a similar alloy only considered them to be obstacles to dislocation movement. It is impossible to evaluate at this time whether the availability of dislocation sources in the two alloys is a matter that contributes to the work hardening properties. It is of considerably interest that the results show that in Alloy 2219, the coherent particles lose their coherency after hydrostatic straining. The strain energy in the coherent interface is apparently released so that the particles are thereafter only semicoherent at best.

#### D. Comparison of Strain Rates in 2219 Alloy

As pointed out in the results, the stock used for hydrostatic straining was different from that used during the electrohydraulic and explosive forming operations. This apparently came about through different annealing treatments of the 2219 stock which was received in the T-6 condition. As a result of this unfortunate experimental situation, it is impossible to know whether the lower work hardening values of the strain rate samples is due to the difference in strain rate or whether it is due to the differences in the interparticle spaces in the two stocks employed. Only a repeat of these experiments on consistent stock will resolve the uncertainty.

In this discussion, both the electrohydraulic and explosively formed samples will be treated as similar high rate samples since no significant distinctions between them have appeared in this study.

In the hydrostatic sample, the only basis for estimating subgrain size was the space between the particles about which many dislocation clouds had accumulated. The estimated cell size in the high rate samples were nearly three times greater and in the much larger interparticle spaces there were well defined tilt and twist boundaries. This effective difference of cell size may correlate with the work hardened properties of these materials through the inverse square root relationship between grain size and flow stress<sup>15</sup>. This rule, which has experimental support, states that, as subgrain or cell size is decreased, flow stress or yield strength will increase. It is not unreasonable to substitute interparticle spacing for cell size in this relationship and on this basis alone one might expect the material of large interparticle spacing to even have an initial lower yield strength than that having the small interparticle space.

The fact that the results show a greater amount of dislocation loop formation and dislocation jogging in the high rate samples than in the low rate suggests that the detailed dynamics of dislocation motion in the two cases are probably different. Wilsdorf and Wilsdorf<sup>16</sup> have shown that point defects arise during slip, through dislocation interactions, and that these may then interact with other dislocations to form jogs or they may

anchor dislocations so that, on breakaway, loops remain. These detailed dynamics of dislocations cannot be dealt with in the present experimental situation but undoubtedly they influence the deformation-work hardening relationship in high strain rate forming. An understanding of their importance would require a larger, more controlled set of experiments. It is possible to speculate that the loops and jogs represent a type of dispersed residual damage left after intensive dislocation-dislocation cross-pinnings and breakaways. In the slow rate sample, because of the general low stress prevailing, such breakaways may not be common and damage may tend to gather together and to accumulate more in local concentrations.

#### E. Comparison of Strain Rates in 2014 Alloy

Sample consistency presents a better situation for comparison of rates in this alloy, but again, it is to be noted that this was a "dirty" alloy which presented difficulties in thinning and, therefore, in evaluating.

The mechanical property data is not broad enough to establish that the work hardening by a slow rate is significantly greater than by a high rate. It is probable that studies made of materials deformed by these different rate methods at points where they are closer to failure will allow better correlation of the work hardened state with substructural damage.

In the present samples it is observed that the dislocation cell structure is both larger and more perfectly defined in the high rate samples. This would in itself indicate that internal damage is more perfectly distributed in these. Long range stress build up in the hydrostatic samples is suggested by the x-ray data and also by the micrographs. In Figure 10 (Hydrostatic) one observes a characteristic concentration of dislocations piled up around particles while in Figure 13 (electrohydraulic) the pile-ups appear to be more resolved into defined slip modes between particles. One gathers the impression that the metal is rotating in blocks about various particle lever points in the latter figure but that the lever points are not so well defined during low-rate hydrostatic straining. Additional studies would be needed to verify these different modes of internal deformation. Tilt experiments in the electron microscope whereby one may look down more than one zone axis would enable one to map out the dislocation damage and its relationship to particle lever points more perfectly. A better understanding of the operative slip systems would also develop.

The possible significance of loops and jogs in the high rate samples was discussed with respect to the 2219 alloy and no other obvious implications of these arise with respect to the 2014 alloy.

#### F. Comparison of Strain Rates in 321 Alloy

It is apparent from the results and the earlier discussion that this particular type of stainless steel has an intermediate or low-intermediate stacking fault energy. This alloy is basically an 18% Cr-10.5% Ni stainless steel and it is surprising that it deforms by twinning. The literature<sup>1,5,7</sup> indicates that the 18-8 composition does not twin but deforms with wide ribbon

dislocations reflecting its low stacking fault energy. The difference in SFE may, however, be simply a result of the presence of other elements such as carbon which has been found by Roberts<sup>17</sup> to raise SFE in Hadfields steels.

The mere existence of twins in an fcc metal is a matter of some interest since Birchenall<sup>18</sup> in his book published in 1959 states that such metals do not deform by twinning. However, Venables in 1960<sup>3</sup> and 1962<sup>9</sup> discusses twinning in fcc Cu-Al alloys (0-8% Al) as does Thomas<sup>1</sup> for Cu-2% Be. The critical feature is found to be the SFE; for, if it is low enough for the development of stacking faults, twins will not readily propagate amidst them.

Subgrain or cell size is so difficult to assess especially with twins present that the data listed in Table 3 are not very meaningful. There is, indeed, some question whether a true subgrain or cell is present in the sense that there are regions of undeformed metal surrounded by boundaries of dislocation networks.

The considerably greater amount of twinning present in the samples deformed at high rates is clear and is evidence that the method of deformation is nucleated by the higher stress conditions. Since there is evidence of a greater stacking fault appearance at lower rates (hydrostatic), it is safe to assume that the initial development of ribbon dislocations at low internal stresses is sufficient to inhibit twin formation and propagation. At high rates the coherent dislocation motions required for twin formation probably initiate very rapidly under the high strain before there is a general production of singular dislocations in the matrix. As a consequence twinning is not inhibited.

The yield strengths listed are not indicative of any trend which would suggest that deformation by twinning leads to a greater or lesser work hardening. In one sense the formation of twins leads to a larger effective subgrain size which would suggest a lower work hardened condition while in another sense the subgrains which result are more effectively misoriented and would cause greater work hardening because of the greater difficulty of passing dislocations from one to the other. More careful study and correlation of data is required to decide these questions.

The significance of loop formation and jogged dislocations could not be ascertained or considered in these various samples although it is clear that the formation and behavior of point defects are important parameters in deformation studies.

## CONCLUSIONS

1. It is amply demonstrated that the transmission electron microscopic method of study is an extremely pertinent method for developing fundamental information on the internal structure of metals deformed at high rates of strain.
2. A basic distinction in deformation behavior exists between the two aluminum alloys and the stainless steel alloy. The dislocation dynamics of the aluminum group basically reflects the known high stacking fault energy of these alloys and the dislocation dynamics of the stainless sample reflects its low SFE.
3. No obvious basis was found for distinguishing between work hardening mechanisms in the 2219 and 2014 alloys. However, there are doubtlessly detailed subtle differences based upon point defect behavior and precipitate-coherency differences which are peculiar to each alloy.
4. No real distinctions could be made, in the three alloys examined, between the samples electrohydraulically and explosively formed. The two high rate methods are obviously in a similar class of deformation rates.
5. The use of 2219 alloy stock, annealed to different final conditions obscured the comparison of these samples deformed at high and low strain rates. Differences of particle size and distribution could account for differences of work hardening experienced. The greater presence of dislocation loops and jogs is considered a significant feature of high rate forming.
6. In the 2014 alloy, the subgrain cell size is larger after high rate forming than after hydrostatic forming. This plus the presence of dislocation loops and jogs suggests that at high rates the build up of internal stress conditions is slower. There is as yet no significant correlation indicated between these features and yield strength after work hardening.
7. Deformation twinning is a significant mode of deformation in all strained samples of the 321 stainless alloy. At the higher rates of strain the proportion of twins is increased by at least an order over the low rate. This is believed to result not only from the higher stress conditions but also because of the lower availability of dislocations that could block the propagation of twins.
8. Additional significant information, which may improve both the control and the application of high rate forming methods, can be readily projected from an expanded study of this type based upon more carefully designed experiments.



## RECOMMENDATIONS

1. It must first be recommended that transmission electron microscopic examination be continued and extended in the study of high rate forming processes since they are uniquely capable of describing the microstructural features of metals which are directly involved in the plastic deformation process.

2. In view of the fact that there have been practically no studies of dislocation mechanics as a function of strain rate (7), except at low levels, it is recommended that a foundation of understanding for high rates be based upon a graded series of samples subject to different rates from the lowest to the highest possible.

3. It is recommended that future studies include samples subject to acoustic shocks with the minimum of deformation in order to understand the state of the metal prior to massive deformation.

4. The criteria for distinguishing between the internal features of metals deformed at high and low strain rates should be based upon samples which are more appropriately characterized in terms of physical properties. Thus future studies should include samples at failure and those nearing failure. The unique features of high rate forming processes might then be more apparent.

5. Since there is some suggestion that coherency effects between precipitates and matrix can be important factors in deformation behavior, it is recommended that this effect be studied with at least one alloy demonstrating coherency such as 2219 alloy. Controlled aging to known particles sizes, distributions and coherency strains would provide samples suitable for resolving these questions after controlled deformation and electron microscopic evaluation.

6. Future studies should be based upon more sophisticated electron microscopic techniques than it has been possible to apply here. They should include where applicable, particle and dislocation counts, trace analysis to establish Burgers vectors and operating slip systems, in-microscope tilt experiments and refined stereomicrography.

7. In a different vein, consideration should be given to the concept of employing an alloy which has been deformed at high rates as a special matrix in which to bring about a precipitation reaction. It is now established that the high strengths of both the normal tempering carbon steels and the age hardening maraging steels<sup>22</sup> are a result of the growth of a highly dispersed phase upon the dislocation networks in a martensite matrix. Since high rate forming produces a similar density of dislocations, it is entirely feasible to project new alloy precipitation systems of exceptional properties where a martensitic or diffusionless transformation is not required to develop the required high degree of dispersion. Distinct advantage over normal strain-aging processes would be expected based

upon a superior distribution of dislocations produced at high rates compared to those produced during low rate straining. Since a martensitic transformation would not be required, new alloy systems would be dealt with, where there is no upper temperature limits imposed by the A-s temperature (i. e., the austenite reversion temperature).

## REFERENCES

1. Thomas, G., "Transmission Electron Microscopy of Metals," John Wiley and Sons, New York 1962.
2. DMIC Report 179, December 1962, "A Guide to the Literature on High-Velocity Metalworking," Battelle Memorial Inst., Columbus 1, Ohio.
3. Nicholson, R.B., Thomas, G. and Nutting, J., Brit. J. App. Phys., Vol. 9, p. 25, January 1958.
4. Kelly, P.M. and Nutting, J., J. of Inst. Metals, Vol. 87, p. 385, 1959.
5. Hirsh, P.B., Partridge, P.G., and Tomlinson, H., 4th Intern. Kong. Elektronenmikroskopie, Springer-Verlag, Berlin 1958, p. 536.
6. Howie, A., Proceedings of the European Regional Conf. on Electron Microscopy, Delft, 1960, p. 383.
7. Swann, P.R., "Electron Microscopy and Strength of Crystals," Interscience, New York 1963, pp 131-181.
8. Venables, J.A., Proceedings of the European Regional Conf. on Electron Microscopy, Delft 1960, p. 443.
9. Venables, J.A., 5th Intern. Cong. for Electron Microscopy ("Electron Microscopy"), Academic Press, New York 1962, J-8.
10. Thomas, G., Phil. Mag., 1959, 4, p. 1213.
11. Nutting, J., 4th Intern. Kong. Elektronenmikroskopie, Springer-Verlag, Berlin 1958, p. 574.
12. Wilsdorf, H.G.F., "Structure and Properties of Thin Films," John Wiley and Sons, New York 1959, p. 151.
13. Wilson, R.N., 5th Intern. Cong. for Electron Microscopy ("Electron Microscopy"), Academic Press, New York 1962, K-3.
14. Bonar, L.G. and Kelly, A., 5th Intern. Cong. for Electron Microscopy ("Electron Microscopy"), Academic Press, New York 1962, K-11.
15. Warrington, D.H., Proceedings of the European Regional Conf. on Electron Microscopy, Delft 1960, p. 354.
16. Wilsdorf, H.G.F. and Kuhlman-Wilsdorf, D., 5th Intern. Cong. for Electron Microscopy ("Electron Microscopy"), Academic Press, New York 1962, J-2.

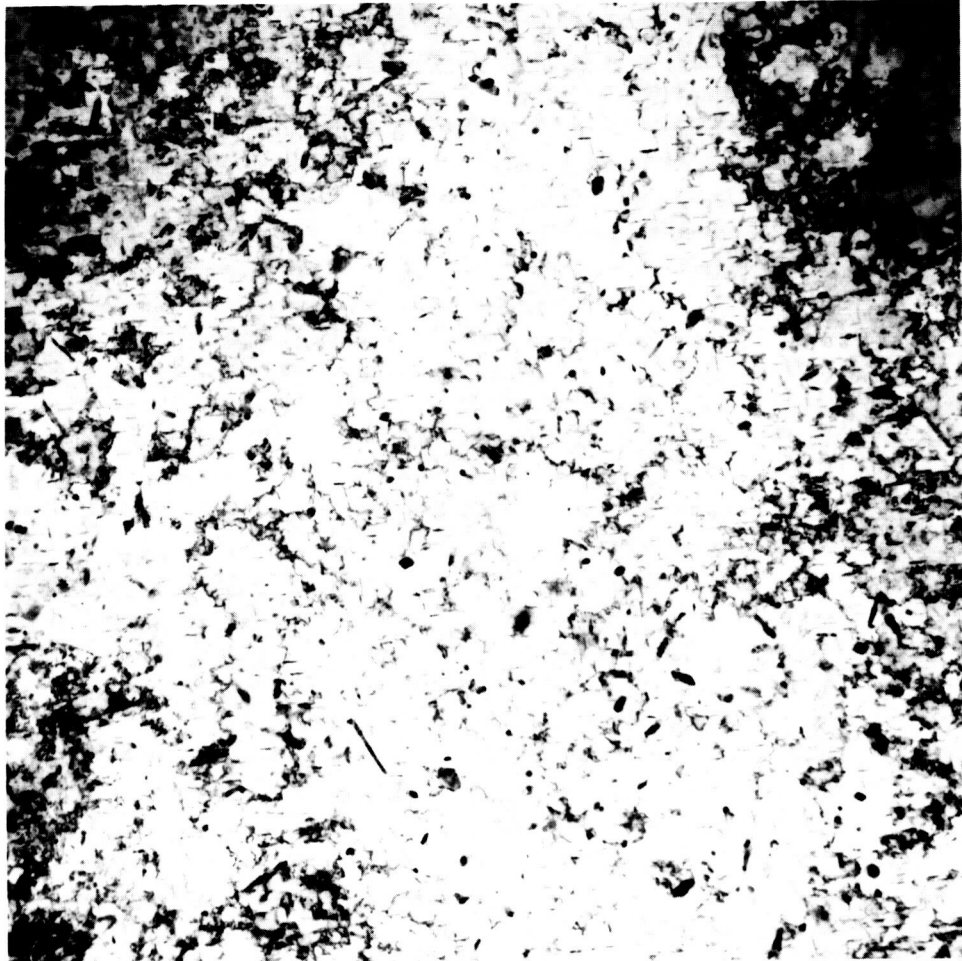
17. Roberts, W.N., 5th Intern. Cong. for Electron Microscopy ("Electron Microscopy"), Academic Press, New York 1962, p.2.
18. Birchenall, C.E., "Physical Metallurgy", McGraw-Hill, New York 1959 p. 133.
19. Smith, C.S., Trans Aime 212, 574, 1958.
20. Hornbogen, E., Acta Met., #10 Vol. 10, 1962, p. 978.
21. Basinski, Z.S., 5th Intern. Cong. for Electron Microscopy ("Electron Microscopy"), Academic Press, New York 1962, B-13.
22. Ence, E. and Renshaw, T., RAC 1661, 2 August 1963, Republic Aviation Corporation, Farmingdale, New York.



26,500x

Precipitated plates can be seen on the three (100) planes. The large dark band is due to bending of the thin foil and the operation of a Bragg reflection. Within and at the edge of the band a series of modulated "stacking fault" type interference fringes can be seen in many of the particles. Strain fields can be seen to be connected to particles to the right of S and in several other areas.

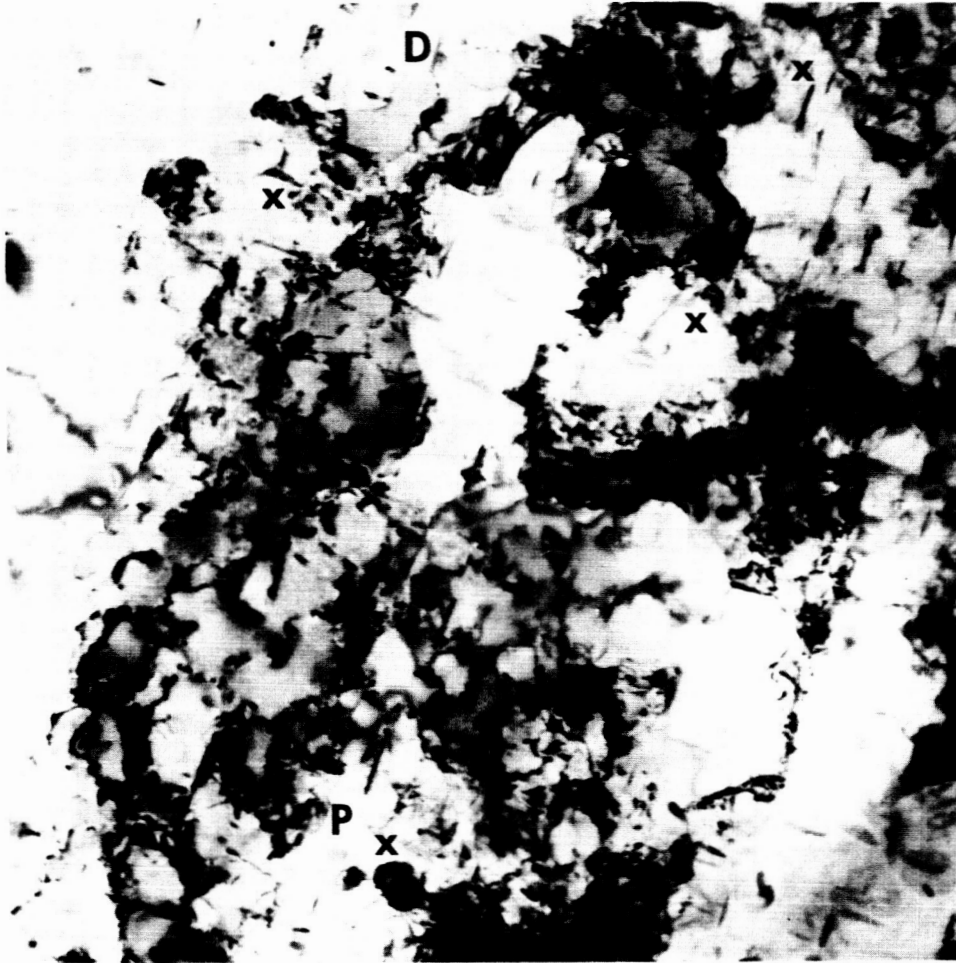
Figure 1 Parent Stock of Alloy 2219



9,000x

A low magnification view. Individual dislocations cannot be clearly seen but their presence is discerned in cloudy arrays. Darkening in some areas is due not only to dislocation clouds but also to the partial rotation of the metal into Bragg reflection conditions.

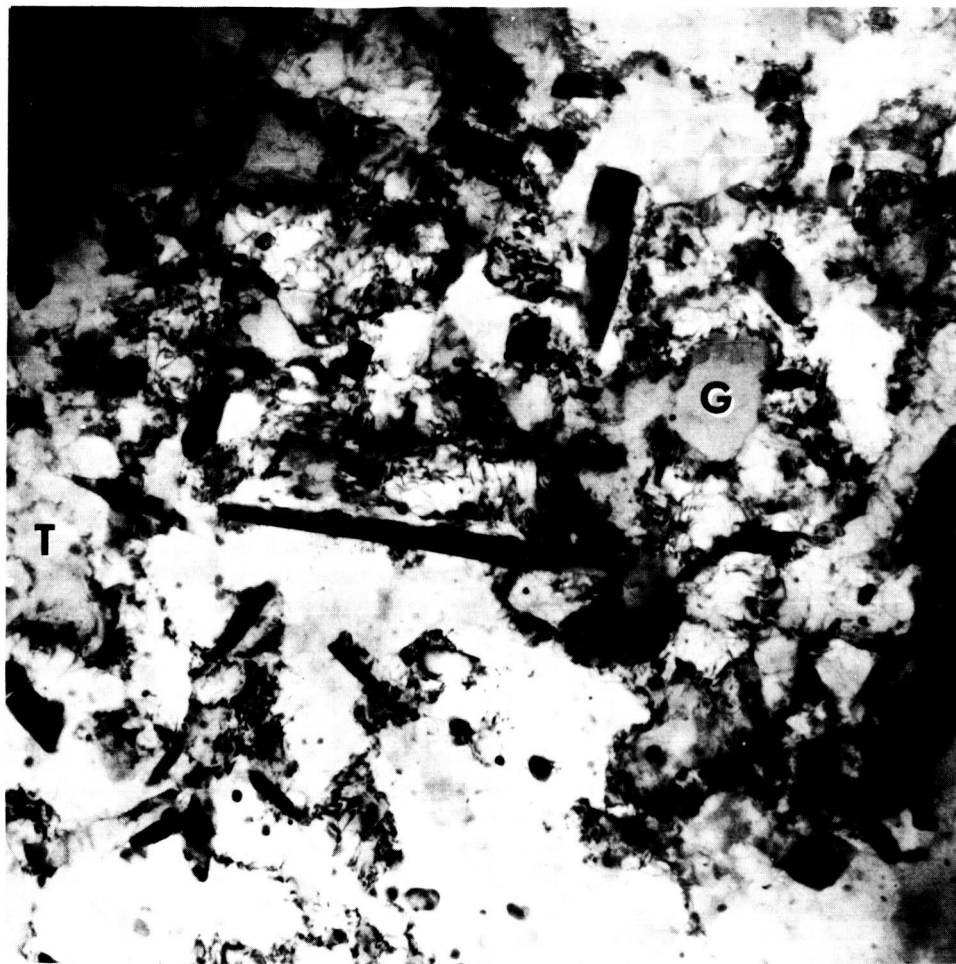
Figure 2 Alloy 2219 - Hydrostatically Formed



26,500x

Heavy clouds of dislocations tend to obscure individual interactions. Above P several dislocations have wrapped a  $\theta$  particle and confused its outline. At particles parallel to the plane of the foil and marked X, there can be seen faint Moire fringes indicating loss of coherency. A group of filamentary singular dislocations connecting between particles can be seen near D.

Figure 3 Alloy 2219 - Hydrostatically Formed

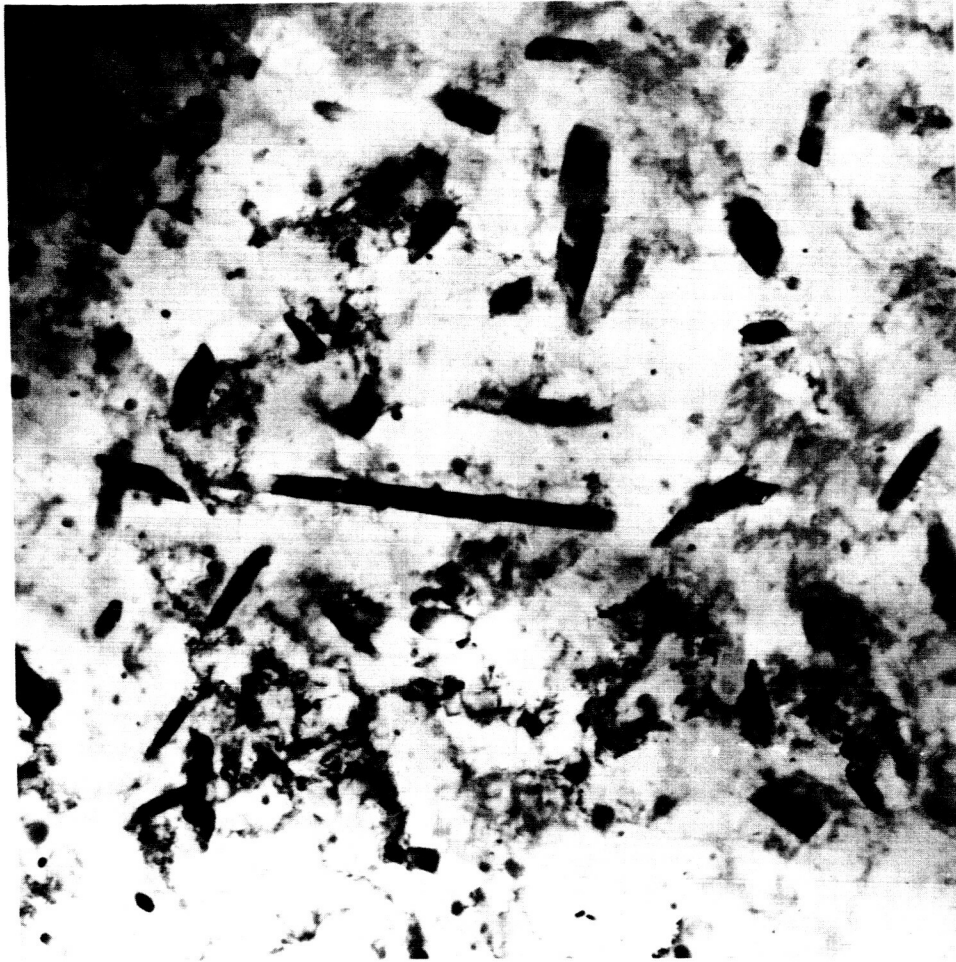


16,000x

In most features, this sample is similar to that hydrostatically formed. The  $\theta$  particles are larger and subgrains free of dislocations such as G are more evident. Below T is an ill defined twist boundary. Many primitive tilt boundaries emanate from particle ends. Compare to Figure 5.

Figure 4 Alloy 2219 - Electrohydraulically Formed

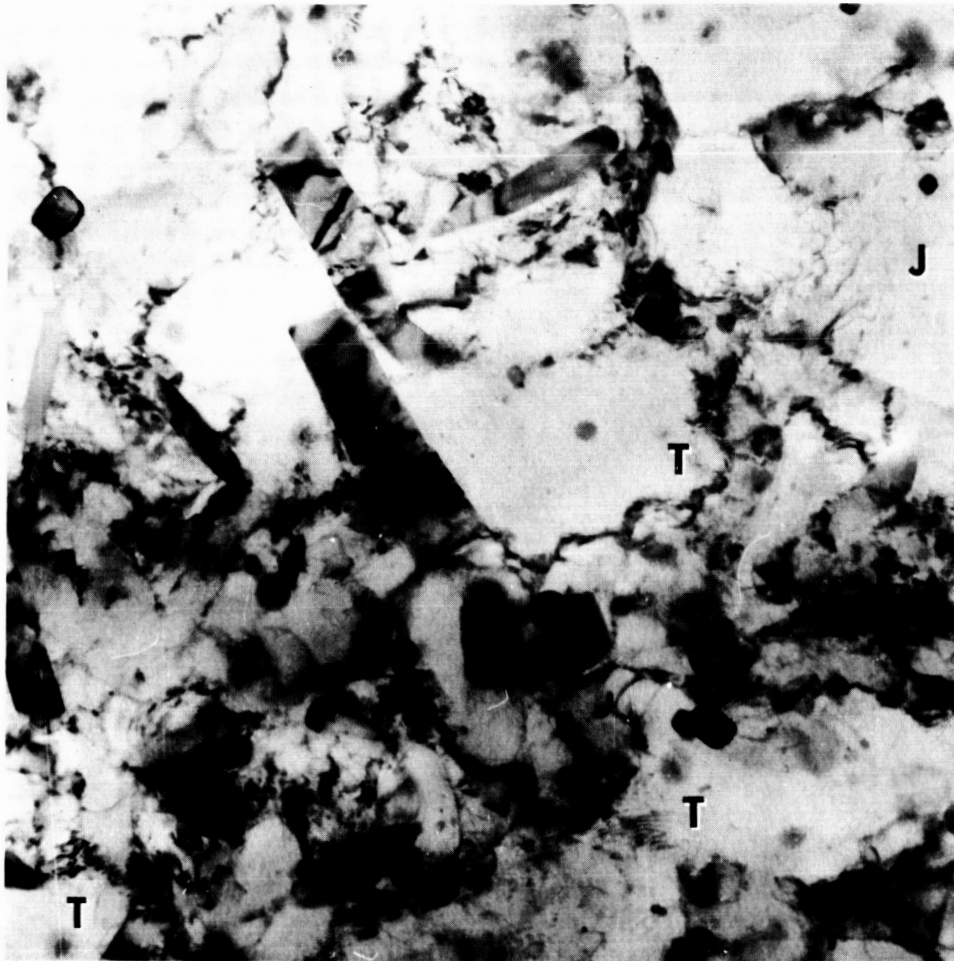




16,000x

This shot was taken after  $10^\circ$  tilt of the area seen in Figure 4 and is part of a stereo pair. The same particle features can be seen but the dislocation arrays are almost all different.

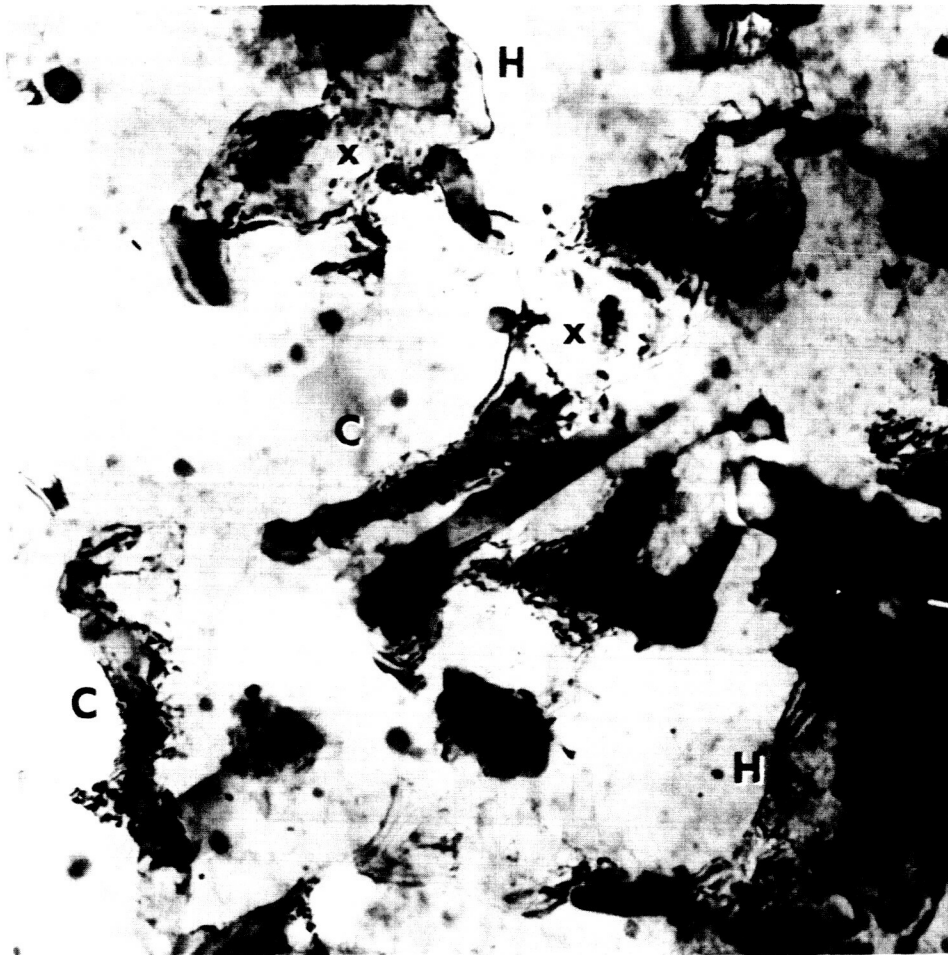
Figure 5 Alloy 2219 - Electrohydraulically Formed



26,500x

The largest  $\theta$  plates all have Bragg reflection bands traversing them indicating that they are bent during deformation. Sections of tilt boundaries or arrays of edge dislocations are seen at T. Jogging or sharp direction changes can be seen in the dislocations around J.

Figure 6 Alloy 2219 - Electrohydraulically Formed



26,500x

Dislocations are largely confined to limited regions connecting particles. Sub-boundaries are often complex as at C. Often they are of a high angle type where individual dislocations cannot be seen as at H. Dot-like edge dislocations can be seen on end at X.

Figure 7 Alloy 2219 - Explosively Formed



26,500x

Abundant dislocation-particle interactions are seen in the central area. The formation of subgrains in connection with the particles is also evident.

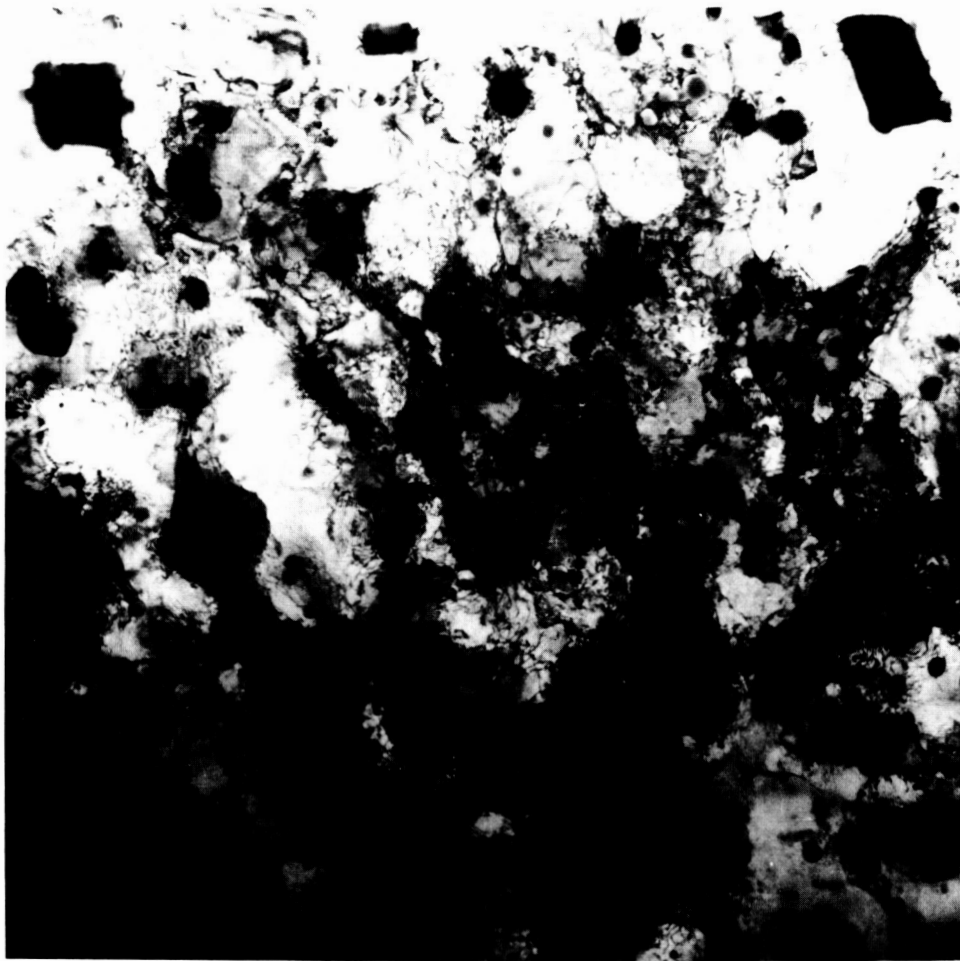
Figure 8 Alloy 2219 - Explosively Formed



9,000x

Small pseudo-cubic particles are seen as well as the large "inclusion" type particles. A simple grain boundary which has a wedge or "stacking fault" type interference fringe at F traverses the area in an irregular manner. The few dislocations present near D are seen to be bending around the small particles.

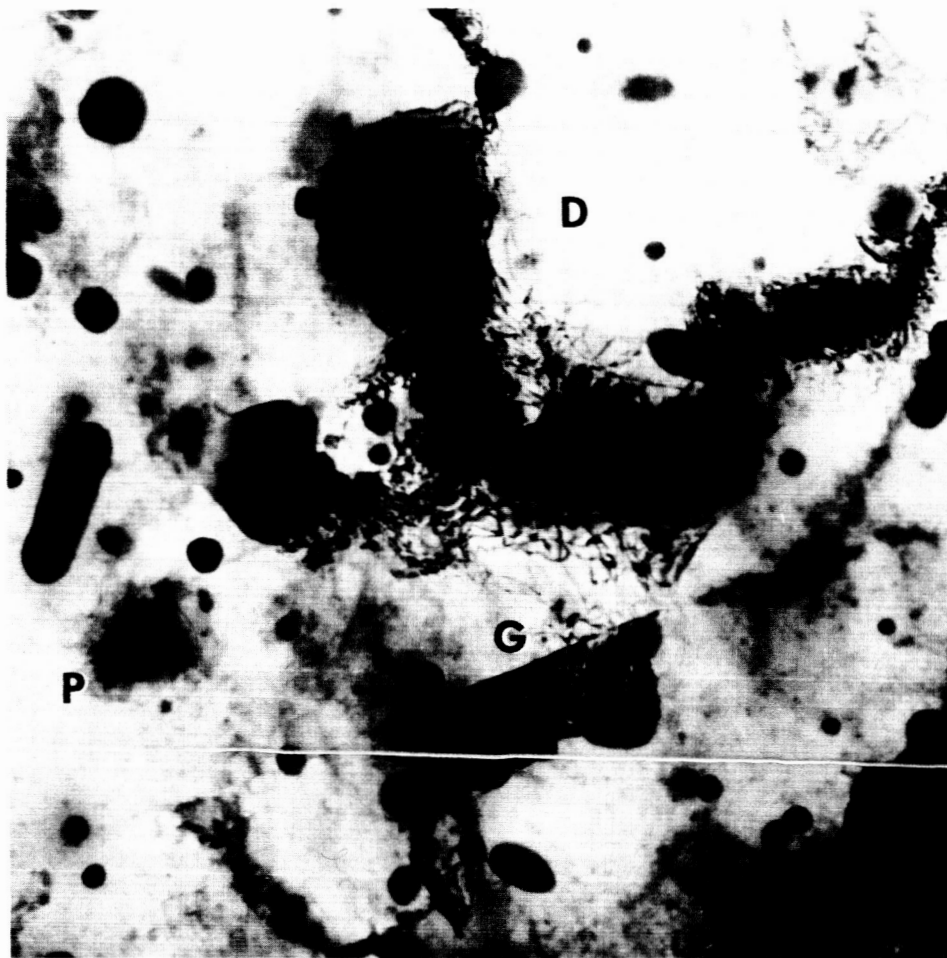
Figure 9 Alloy 2014 - Parent Stock



16,000x

Enormous clouds of dislocations heavily concentrated around particles are seen. Sub-grain blocks are discernable also.

Figure 10 Alloy 2014 - Hydrostatically Formed



26,500x

It is generally noted that larger particles as in picture center have a greater amount of dislocation damage associated with them. Dislocation damage also develops at grain boundaries as at G. A dislocation dipole is seen at D. A cloud of poorly resolved dislocations is seen around the particle at P.

Figure 11 Alloy 2014 - Hydrostatically Formed

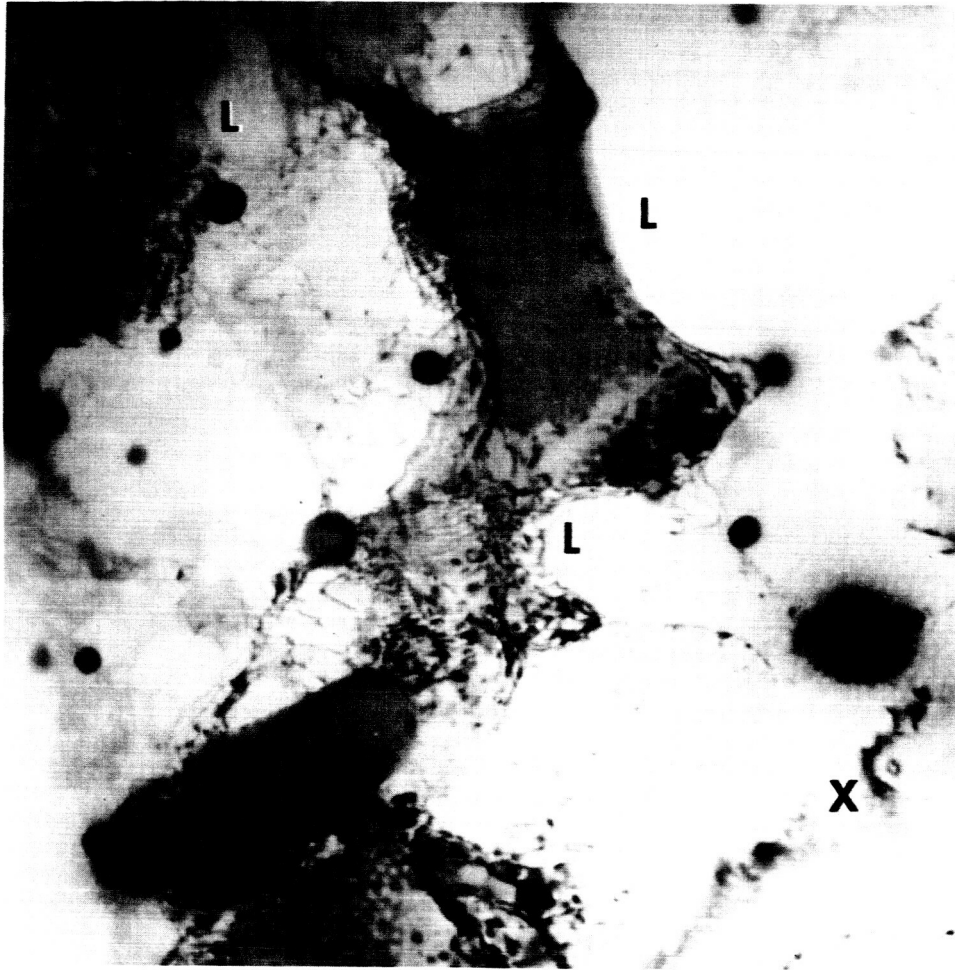


26,500x

Particles which do not have dislocations around them are often on the surface of the thin metal foil having been freed by the electro polish. The dislocations are rather heavily disturbed or jogged and only infrequently smoothly drawn.

Figure 12 Alloy 2014 - Electrohydraulically Formed

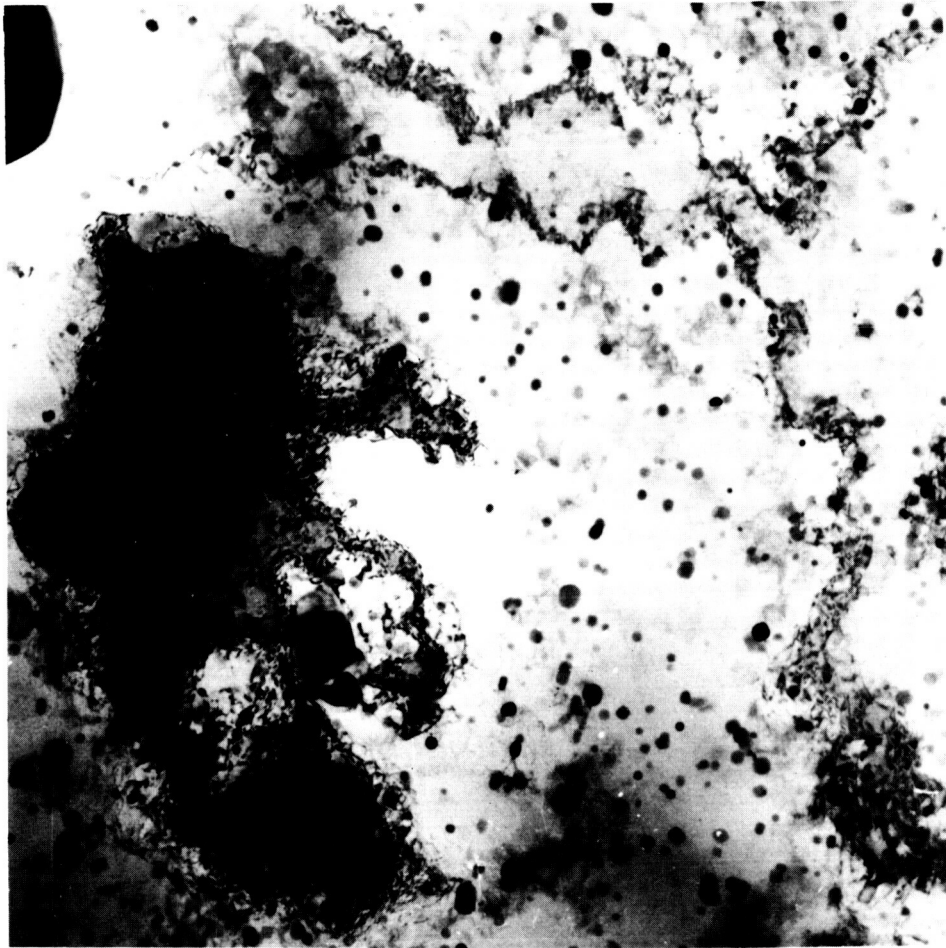




26,500x

The dislocations do not encompass the particles as completely as in hydrostatic samples. On either side of X are seen well defined dislocation loops while to the left of the L's are seen irregularly defined loops.

Figure 13 Alloy 2014 - Electrohydraulically Formed



16,000x

The dark area has been rotated to a considerable degree from the remaining metal since a distinct Bragg condition operates only there. Dislocations are very irregular and combined in a complex fashion.

Figure 14 Alloy 2014 - Explosively Formed



26,500x

Singular shots such as these provide only limited information. Tilt experiments and electron diffraction analysis would indicate what slip systems operate and allow better understanding of the complex area to the right of P. The poorly resolved dislocations in the area left of the grain boundary could also be brought into better contrast.

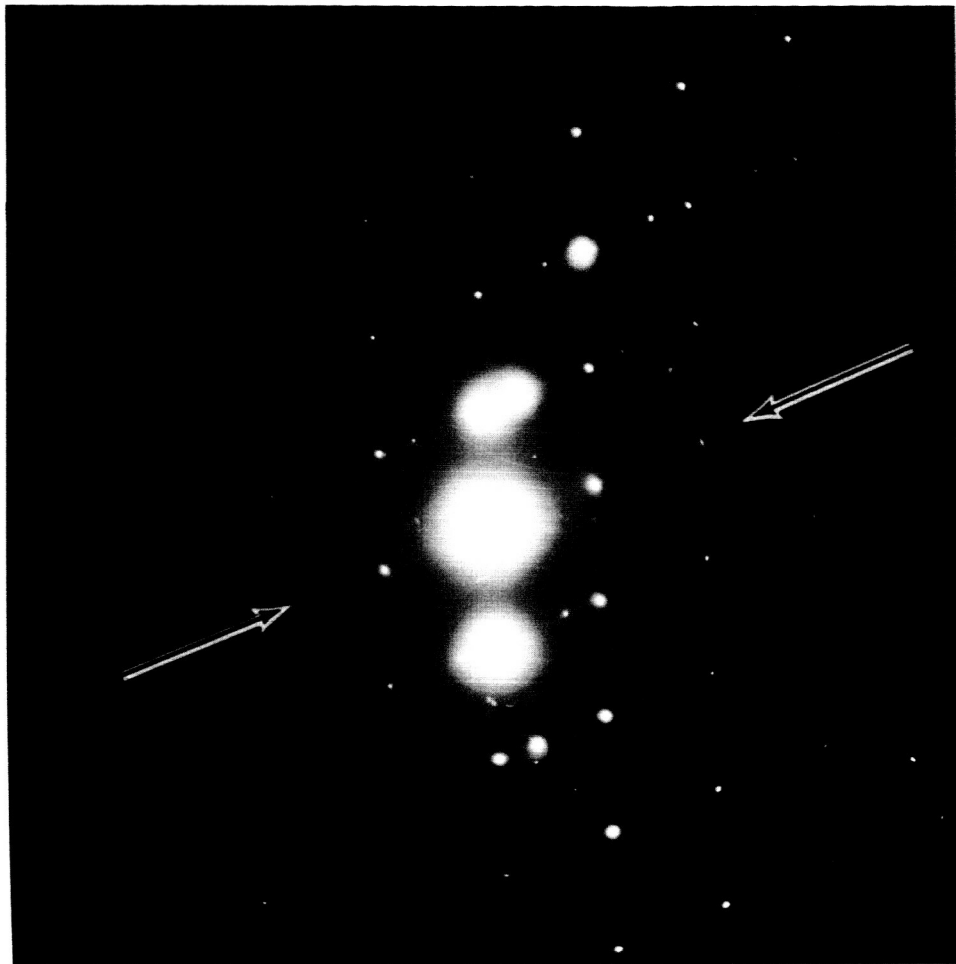
Figure 15 Alloy 2014 - Explosively Formed



21,000x

A limited distribution of dislocations is seen which resulted from the excessive grinding of this sample. They tend to be accumulated around the isolated globular particles. At D, a slight fringing of the dislocations indicates that a stacking fault of small width is present. T locates a large growth twin which traverses the area. A variety of nodes and other dislocation-dislocation interactions are visible throughout.

Figure 16 Alloy 321 - Parent Stock With Minor Working



An electron diffraction pattern of the large growth twin seen in Figure 16. This pattern indexes as two overlapping patterns from two Zone Axis (110) spot displays of the austenite lattice. The two displays coincide at one group of (111) spots and have a symmetry about a line through these spots as indicated. It is typical of twin relationships.

Figure 17 Alloy 321 - Parent Stock



32,000x

In this area are seen a great many dislocations which are steeply inclined to the foil and therefore shortened. A few very small narrow twins are visible left of T. Note that these always terminate at dislocations operating on other slip planes. Stacking faults can be seen near the S's indicating that stress has caused the partial dislocations on either side of them to spread.

Figure 18 Alloy 321 - Hydrostatically Formed



16,000X

Extensive deformation twinning is seen in this area. Note that most of the twins end at their intersection with other twins in the upper portion of the micrograph. It is difficult to define subgrains amidst the clouds of dislocations between twins. The group of curved bands which turn about the upper left corner are Bragg extinction contours formed by bending of the foil and the local formation of a Bragg reflection condition.

Figure 19 Alloy 321 - Hydrostatically Formed



The electron diffraction pattern obtained from the sample area shown in Figure 19. It can be seen by inspection that this pattern is of the same type as Figure 17. It has also been indexed as two  $\{110\}$  zone axis patterns with a common  $(111)$  pole being the axis of symmetry. It should be noted that all the twin spots are streaked out reflecting the twins thin dimension perpendicular to the  $(111)$  twin plane interfaces.

Figure 20 Alloy 321 - Hydrostatically Formed

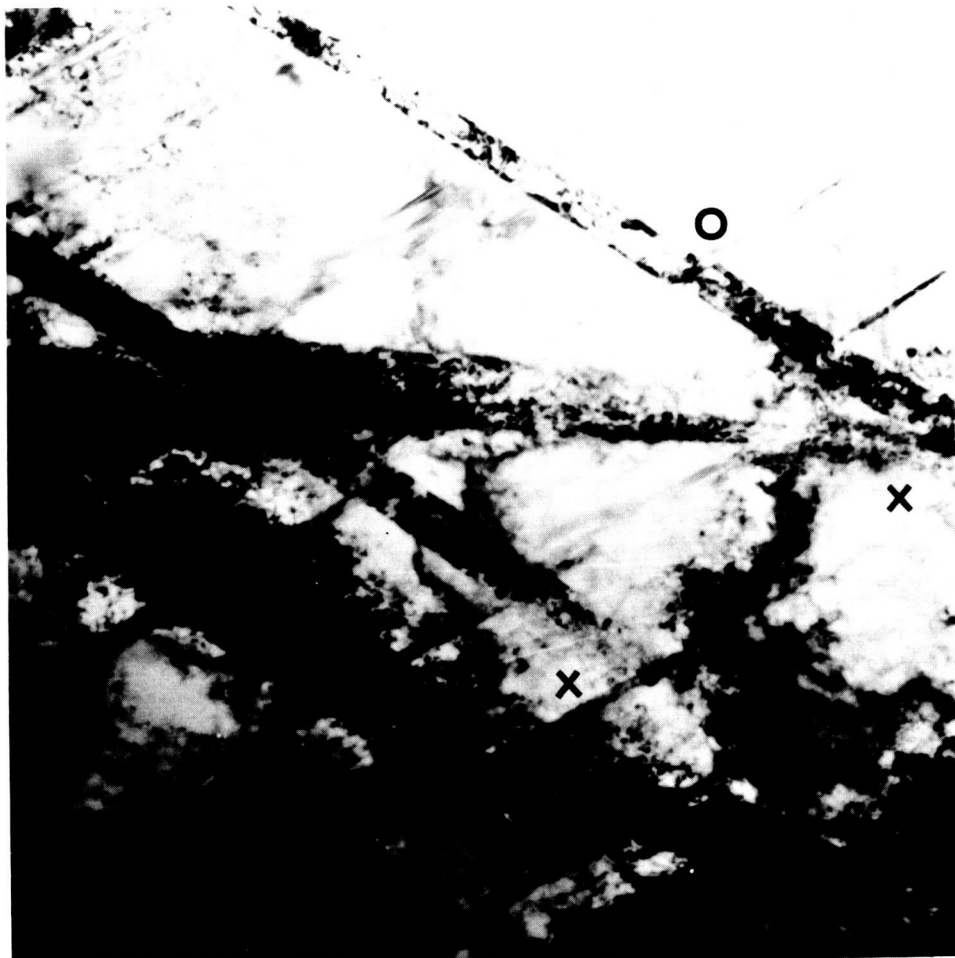




9,000X

A low magnification micrograph illustrating to some extent the high degree of deformation twinning manifest in this sample. Since the appearance of twins is orientation dependent, not all that are present in this area can be seen. There could be as many as 9 twinning systems which are not visible here. Note that the section indicated by A is a large growth twin which itself contains deformation twins.

Figure 21 Alloy 321 - Electrohydraulically Formed



37,500X

It is interesting that so very much dislocation damage is associated with the twins produced at high strain rates. The dislocations in these twins may be intrinsic or they may have accumulated there after they had formed. Dislocation loop formation is extensive throughout, but can be difficult to see. Note them at X. The very thin twin at O has apparently caused the intersecting large twin to un-twin locally.

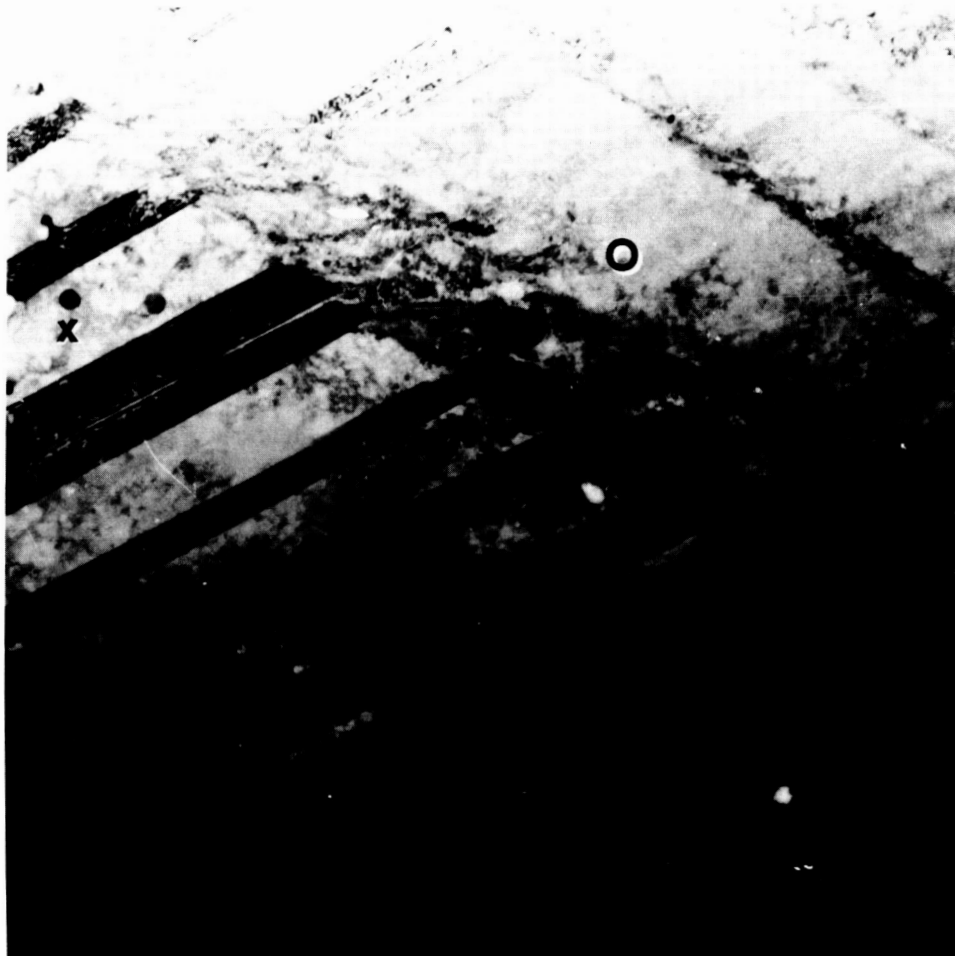
Figure 22 Alloy 321 - Electrohydraulically Formed



21,000X

The extreme density of dislocations seen here inhibits examination of them individually. Higher magnifications and resolutions would be required. Note the Moiré type patterns in the twins below the X.

Figure 23 Alloy 321 - Explosively Formed



16,000X

An interesting feature of the twins below X are the stacking fault type fringes seen in them. This type of interference fringe occurs when two wedges of metal are separated by a thin inclined interface. Below O is a gross example of twin intersections. The penetration of one twin through another is doubtlessly difficult and it testifies to the high stresses operating during high strain rate deformation.

Figure 24 Alloy 321 - Explosively Formed

Samples	% Thinout and Yield Strength	Precipitate	
2219 Parent Stock	- 12,700 psi	Coherent $\Theta$ plates size 2800A° x 1100A° x 240A°	nor
2219-HS3 Hydrostatically Formed Low Strain Rate	20% 39,400 psi	Coherent $\Theta$ plates size 2800A° x 1900A° x 200A°	ap 1/
2219-EH16 Electrohydraulically Formed High Strain Rate	16% 28,300 psi	$\Theta$ plates size 1000A° x 2000A° x 15,000A°	Ap 3/
2219-EX2 Explosively Formed High Strain Rate	20% 28,400 psi	$\Theta$ plates size 1000A° x 2000A° x 15,000A°	Ap l r

TABLE I ALLOY 2219 ALUMINUM

Subgrain Size	Matrix Dislocation Loops	Character of Subgrain Boundaries	Dislocation Particle Interaction
none present	none present	none present	Very few dislocations present
prox. 1 micron	none present	Undefined except by interparticle spaces	Very extensive interaction between particles at the particle interface. Dislocations bowed out from particles
prox. 2 micron	Occasional loops present	Often well defined. Tilt and twist boundaries.	Dislocations arise at isolated points on the particle interface. Dislocations tend to concentrate at subboundaries
prox. 3 micron	Similar to above	Similar to above	Similar to above



n is	Sum of Principal Residual Stresses (By X-ray Diffraction)	Remarks
locations	- -	⊖ plates are coherent with matrix and strain field can be seen in the matrix around them.
ve icles and e-matrix oops are om	-12, 000 psi	Most ⊖ particles have lost their complete coherence with matrix. Very little distortion of particles. Dislocations are not heavily jogged.
frequently ated points le-matrix slocations ntrate in s	-1, 000 psi	⊖ particle apparently retain coherence or partial coherence with matrix, considerable bending of particles is noted. Dislocations are highly jogged.
ove	-10, 600 psi	Similar to above, plus damage seems more confined to subgrain boundaries and the boundaries are more clearly defined than in the electrohydraulic sample

3

Samples	% Thinout and Yield Strength	Precipitate
2014 Parent Stock	10,000 psi	Principally pseudo-cubic particles 1000A° on the edge
2014-HS3 Hydrostatically Formed	19% 32,400 psi	Principally pseudo-cubic particles 1000A° on the edge
2014-EH4 Electrohydraulically Formed	15% 24,900 psi	Principally pseudo-cubic particles 1000A° on the edge
2014-EX4 Explosively Formed	19% 27,900 psi	Principally pseudo-cubic particles 1000A° on the edge



TABLE II ALLOY 2014 ALUMINUM

Subgrain Size	Matrix Dislocation Loops	Character of Subgrain Boundaries	Dislocation Pattern Intensity
none present	none present	none present	Very pres
approx. 1/2 microns	none present	Poorly defined tilt & twist boundaries are seen occasionally, but otherwise subgrain areas are not clearly separated	Much partic catio plex deta parti mor
approx. 3/4 microns	occasionally present	Very often large and well defined tilt boundaries are seen. Clean areas between boundaries are often seen.	Part of th matr the f dislo tilt b
approx. 1 micron	occasionally present	A certain number of well defined subgrain tilt boundaries are seen, not as often as in the electro-hydraulic sample.	Simi but l defin

2


Dislocation particle interactions	Sum of Principal Residual Stresses (By X-ray Diffraction)	Remarks
few dislocation ent	- -	Precipitate pseudo-cubic phase is apparently not coherent with the matrix
interaction of cles & dislo- ns but too com- to evaluate in l. Larger cles collect e dislocations.	-18,900 psi	Dislocations pile up and bow around particles forming complex tangles. No jogging of dislocations observed
icular portions e particle- ix interface are ocus of many cations and oundaries.	-4,200 psi	Groups of dislocations often connect with separated particles by one narrow path. Jogging of dis- locations observed.
lar to above, ess well ed.	-2,300 psi	Similar to above, but less well defined.

	% Thinout and Yield Strength	Subgrain Size	
321 Parent Stock	- - 43,500 psi	-	S t
321-HS3 Hydrostatically formed at low strain rate	17% 99,100 psi	Estimate sub- grain size due to dislocations to be 1 micron on the edge, and smaller	S s t n K d a
321-EH4 Electro- hydraulically formed at high strain rates	18% 103,500 psi	Estimation difficult but 1/3 - 3/4 microns	L r n i u d s k
321-EX6 Explosively formed at high strain rate	17% 90,500 psi	Estimate 1/2 microns	L r n i u  k

TABLE III ALLOY 321 STAINLESS

Matrix Dislocation Loops	Deformation Modes	Character of Subgrain Boundaries	Nature and Size of Deformation Twins
Some present throughout	Isolated dislocations	-	-
Small loops are scattered throughout but not abundant. Linking and dipole formation are seen	Abundant dislocations. scattered stacking faults considerable deformation twinning.	Ill defined, no tilt or twist boundaries seen, only masses of tangled dislocations.	Narrow spear shaped twins vary in length from 1/6 to 10 microns
Loops are reasonably common but content is hard to evaluate. Many dipoles also seen as well as linking.	Abundant dislocation tangles, no stacking faults, much deformation twinning	Ill defined, no tilt or twist boundaries seen, only masses of tangled dislocations.	Many wedge shaped twins crossing grains. Size varies 1/2 to 10 <sup>+</sup> microns in length but most are on large size.
Loops are reasonably common but content is hard to evaluate. Many dipoles also seen as well as linking.	Abundant dislocation tangles, no stacking faults, much deformation twinning	Ill defined, no tilt or twist boundaries seen, only masses of tangled dislocations.	Many wedge shaped twins crossing grains. Size varies 1/2 to 10 <sup>+</sup> microns in length but most are on large size.



Estimated % of Deformation Twins	Sum of Principal Residual Stresses (by X-Ray Diffraction)	
-	-	Annealing twins and dislocation content. partials.
1 - 4%	+109,000 psi	Operation of slip planes.
10 - 30%	+136,000 psi	Twins pass through dislocations incoherent with matrix planes.
10 - 30%	+94,000 psi 	Moire and interference patterns.

---

Remarks

---

are present. Excessive grinding developed a high internal dis-  
Only a slight indication of dislocation dissociation into

---

planes when seen is often associated with twin formation.

---

each other with apparent ease. Twins are relatively  
matrix - having large numbers of dislocations in the twin

---

ence effects can be seen in some twins.

---

4